

A Thesis Submitted for the Degree of PhD at the University of Warwick

Permanent WRAP URL:

<http://wrap.warwick.ac.uk/102985/>

Copyright and reuse:

This thesis is made available online and is protected by original copyright.

Please scroll down to view the document itself.

Please refer to the repository record for this item for information to help you to cite it.

Our policy information is available from the repository home page.

For more information, please contact the WRAP Team at: wrap@warwick.ac.uk



MONASH University

New materials for cancer imaging and therapy

Robbin Ralf Vernooij

Bachelor of Science, Master of Science

Thesis submitted for the degree of Doctor of Philosophy at
Monash University in 2017

Joint PhD

School of Chemistry, Monash University

Department of Chemistry, the University of Warwick

Copyright notice

© Robbin Ralf Vernooij 2017. I certify that I have made all reasonable efforts to secure copyright permissions for third-party content included in this thesis and have not knowingly added copyright content to my work without the owner's permission.

Abstract

Metal-based photoactivated chemotherapy (PACT) involves a class of metal-based prodrugs, which may overcome the limitations and side effects of current metal-based chemotherapeutic agents on account of their novel mechanism(s) of action. In this thesis, a number of vibrational spectroscopic methods were developed and applied to study the mechanisms of metal-based PACT agents upon activation with light.

A particularly promising PACT agent is the diazido Pt(IV) anticancer prodrug, *trans,trans,trans*-[Pt(N₃)₂(OH)₂(py)₂] (**1**, py = pyridine), in which photoinduced cleavage of ligands from platinum yields reactive species, which are likely implicated with the observed biological activity. However, monitoring the azido and hydroxido ligands, and the metal centre simultaneously remains challenging. Vibrational spectroscopy is a potentially powerful tool to study both metal and ligand vibrations without the requirement of labelling and is non-destructive at the same time. The essential first step was the screening of **1** by a range of vibrational spectroscopic methods, including Attenuated Total Reflection Fourier Transform Infrared (ATR-FTIR), Raman and synchrotron radiation far-infrared (SR-FIR), aided by Density Functional Theory (DFT). This yielded an extensive vibrational fingerprint of **1** containing individual ligand (pyridine, hydroxide and azide) and platinum to ligand vibrations. The established methodologies provided the necessary basis for elucidating further photodecomposition and photoreaction pathways.

Successive ATR-FTIR studies allowed for examinations of the photodecomposition of **1** complemented by transient electronic absorption and UV-Vis spectroscopy under 420 nm or 310 nm irradiation. Chemometric data evaluation using Principal Component Analysis (PCA) and Multi Curve Resolution Alternating Least Squares (MCR-ALS) on the steady state UV-Vis and ATR-FTIR spectra captured the formation of a Pt(II) intermediate, *trans*-[Pt(N₃)(py)₂(OH/H₂O)] and a final product, *trans*-[Pt(py)₂(OH/H₂O)₂], in which the *trans* pyridine scaffolds were retained. Upon irradiation, the rapid removal of the hydroxido stretching vibration was found to correlate to a shift in the anti-symmetric azido vibration, indicative of a possible second intermediate.

Experimental evidence of subsequent azido dissociation from platinum suggests that at least one hydroxyl radical is formed in the reduction of Pt(IV) to Pt(II) under such conditions. Additionally, photoproducts formed upon irradiation of **1** in the presence of the DNA nucleotide 5'-guanosine monophosphate (5'-GMP) could be systematically studied using ATR-FTIR, mass spectrometry and DFT calculations.

Underpinning methodologies were subsequently applied to study a series of photoactivatable ruthenium-based CO releasing complexes of the formula $[\text{RuLCl}_2(\text{CO})_2]$ (L = 2,2'-bipyridine with 4' methyl and/or carboxyl substituents). A three-step mechanism involving the sequential formation of $[\text{RuL}(\text{CO})(\text{CH}_3\text{CN})\text{Cl}_2]$, $[\text{RuL}(\text{CH}_3\text{CN})_2\text{Cl}_2]$ and $[\text{RuL}(\text{CH}_3\text{CN})_3\text{Cl}]^+$ was deduced upon 350 nm irradiation in acetonitrile. Rapid removal of the first CO ligand ($k_1 \gg 3 \text{ min}^{-1}$) and a modest rate for the second CO ligand ($k_2 = 0.099 - 0.17 \text{ min}^{-1}$) was observed, with slowest rates found for the electron-withdrawing carboxyl substituents. Aqueous media considerably slowed down the photodecarbonylation ($k_1 = 0.46 - 1.3 \text{ min}^{-1}$ and $k_2 = 0.026 - 0.035 \text{ min}^{-1}$) and the carboxyl groups were shown to have a less pronounced effect on the rate constants, revealing the possible implications for the design of such candidates intended for clinical application.

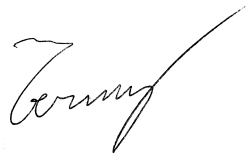
State-of-the-art synchrotron based infrared spectroscopy was utilised with continued focus on the mechanism of action of **1**. ATR-FTIR and synchrotron radiation far-infrared were combined (SR-ATR-FIR) to enable the rapid screening of samples, exposing changes to the metal to ligand vibrations of **1**. Additionally, *in situ* irradiation using liquid transmission SR-FIR revealed the removal of in the platinum to oxygen (hydroxide) and platinum to nitrogen (azide) vibrations simultaneously. Moreover, a mid-infrared live single cell study of **1** on acute myeloid leukaemia cells (K562) by Synchrotron Radiation Infrared Microspectroscopy revealed significant changes to DNA base stacking and lipid vibrations after only four hours of low dose irradiation at 350 nm (2.58 J cm^{-2}).

Lastly, the low wavelength excitation of the earlier described photoactivatable metal-based anticancer prodrug candidates was considered, which commonly hamper their clinical feasibility. A range of lanthanide-doped upconverting nanoparticles (UCNPs) were synthesised, allowing for near-infrared light excitation and visible light emission as a potential platform for wavelength activation of PACT agents in a clinically-relevant window.

Declaration

This thesis contains no material which has been accepted for the award of any other degree or diploma at any university or equivalent institution and that, to the best of my knowledge and belief, this thesis contains no material previously published or written by another person, except where due reference is made in the text of the thesis.

Signature:

A handwritten signature in black ink, appearing to read 'Robbin Ralf Vernooij', written in a cursive style.

Print Name: Robbin Ralf Vernooij

Date: 02/11/2017

Thesis including published works declaration

I hereby declare that this thesis contains no material which has been accepted for the award of any other degree or diploma at any university or equivalent institution and that, to the best of my knowledge and belief, this thesis contains no material previously published or written by another person, except where due reference is made in the text of the thesis.

This thesis includes three original papers published in peer reviewed journals. The core theme of the thesis is metal-based photoactivated chemotherapy and their mechanism(s) of action. The ideas, development and writing up of all the papers in the thesis were the principal responsibility of myself, the student, working within the School of Chemistry at Monash University and the Department of Chemistry at the University of Warwick under the supervision of the late Leone Spiccia, Bayden R. Wood, Peter J. Sadler, and Vasilios G. Stavros.

The inclusion of co-authors reflects the fact that the work came from active collaboration between researchers and acknowledges input into team-based research.

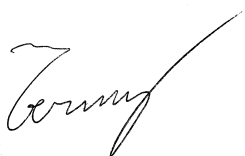
In the case of Chapter 2 and 3 my contribution to the work involved the following:

Thesis chapter	Publication title	Status	Nature and extent (%) of student contribution ^a
Chapter 2	Comprehensive Vibrational Spectroscopic Investigation of <i>trans,trans,trans</i> -[Pt(N ₃) ₂ (OH) ₂ (py) ₂], a Pt(IV) Diazido Anticancer Prodrug Candidate	Published	<i>60%. Concept and collecting data and writing first – final drafts</i>
Chapter 3.1	Spectroscopic Studies on Photoinduced Reactions of the Anticancer Prodrug, <i>trans,trans,trans</i> -Pt(N ₃) ₂ (OH) ₂ (py) ₂]	Published	<i>60%. Concept and collecting data and writing first – final drafts</i>
Chapter 3.5	Studies of Carbon Monoxide Release from Ruthenium(II) Bipyridine Carbonyl Complexes upon UV-Light Exposure	Published	<i>25%. Collecting DFT data, writing corresponding parts of first draft and data analysis towards mechanism of action</i>

^a Non of the co-authors are Monash or Warwick students.

I have not renumbered sections of submitted or published papers in order to generate a consistent presentation within the thesis.

Student signature:



Date: 02/11/2017

The undersigned hereby certify that the above declaration correctly reflects the nature and extent of the student's and co-authors' contributions to this work. In instances where I am not the responsible author I have consulted with the responsible author to agree on the respective contributions of the authors.

Main Supervisor signature:



Date: 02/11/2017

Acknowledgements

My sincerest appreciation goes to all of those involved in the support and guidance from start to end of this PhD candidature.

Leone Spiccia has been my supervisor throughout my candidature and stood at the centre of my development by challenging me when necessary and leaving space to choose my own direction. His extensive network of internationally renowned experts has supported and inspired me to pursue research at the highest level. Leone's presence drove me to work hard, explore the unknown and dig deep in order to convince him of my findings. Whether it was science or social, he was always there to support me. Thank you Leone for being the strong Leone I knew and the one I will always remember you as.

Peter J. Sadler never ceased to amaze me with his extensive scientific knowledge, enthusiasm, ideas and necessary means to overcome challenges. I would like to thank you for your guidance throughout my PhD: it has been a great honour to work with you.

Bayden R. Wood has had a strong influence on the direction my research took by instigating interest in the work I carried out at the start, despite not having any official requirement to do so. His on going input and teaching has been incredibly valuable, which transpired into a fruitful candidature. My sincerest thanks go to him for all his support.

Vasilios J. Stavros provided valuable guidance and advice during my time at the University of Warwick necessary to carry out cutting edge research and has positively shaped my scientific undertaking.

Bim Graham and Ekaterina I. Izgorodina (Katya Pas) have equally provided tremendous amount of time introducing and guiding me in their respective fields of research. A great deal has been learnt from them and has been incredibly valuable.

Synchrotron work is by any means not straightforward and it is scientifically as well as mentally challenging at times. This is, however, why it is very exciting work to me and I would gratefully thank the beamline scientists for their help and support during and outside beamtime. In particular, Dom R. T. Appadoo, Keith R. Bambery and Mark J. Tobin from the Australian Synchrotron.

Tanmaya Joshi, David Perez-Guaita and Manja Kubeil have been excellent mentors during my time at Monash University, without whom I would not have been able to reach the position I am in today.

I would also like to thank my fellow colleagues at Monash University: Shannon A. Bonke, Steffen Braunger (Meyer) and Leena Bird as close friends and keen sources of discussion. Likewise, my colleagues at the University of Warwick are kindly acknowledged for their persisting support: Isolda Romero-Canelón, Carlos Sanchez-Cano, James P. C. Coverdale and Hannah E. Bridgewater.

Monash University is gratefully acknowledged for the Faculty of Science Dean's International Postgraduate Research Scholarship. The author further thanks the Monash Warwick Alliance for their support and travel funding as part of the Monash University and the University of Warwick Joint PhD program.

Reka Hollos has been the most supportive person by my side at all times, even when times got tough when we were far apart. Thank you so much for always believing in me, you are an incredible person and the one I want to spend the entirety of my life with.

Lastly, special thanks go to my parents, Harry and Petra Vernooij for their encouragement, everlasting support and unconditional love over the years. Thank you mom and dad.

Publications during enrolment

Spectroscopic Studies on Photoinduced Reactions of the Anticancer Prodrug, *trans,trans,trans*-[Pt(N₃)₂(OH)₂(py)₂]

Robbin R. Vernooij, Tanmaya Joshi, Michael D. Horbury, Bim Graham, Ekaterina I. Izgorodina, Vasilios G. Stavros, Peter J. Sadler, Leone Spiccia[†] and Bayden R. Wood

Chem. Eur. J., **2018**, published online, awaiting issue assignment (front cover).

DOI: 10.1002/chem.201705349

Probing the action of a novel anti-leukaemic drug therapy at the single cell level using modern vibrational spectroscopy techniques

Joanna L. Denbigh, David Perez-Guaita, Robbin R. Vernooij, Mark J. Tobin, Keith R. Bambery, Yun Xu, Andrew D. Southam, Farhat L. Khanim, Mark T. Drayson, Nicholas P. Lockyer, Royston Goodacre and Bayden R. Wood

Sci. Rep., **2017**, 7, 2649.

DOI: 10.1038/s41598-017-02069-5

Contribution: carried out synchrotron beamtime experimental work and assisted with revision of the manuscript text.

Studies of carbon monoxide release from ruthenium(II) bipyridine carbonyl complexes upon UV light exposure

Manja Kubeil, Robbin R. Vernooij, Clemens Kubeil, Bayden R. Wood, Bim Graham, Holger Stephan and Leone Spiccia

Inorg. Chem., **2017**, 56, 5941-5952

DOI: 10.1021/acs.inorgchem.7b00599

Contribution: acquired, processed and analysed DFT data including the writing and revision of the associated manuscript text.

Supramolecular Photoactivatable Anticancer Hydrogels

V. Venkatesh, Narendra Kumar Mishra, Isolda Romero-Canelón, Robbin R. Vernooij, Huayun Shi, James P. C. Coverdale, Abraha Habtemariam, Sandeep Verma and Peter J. Sadler

J. Am. Chem. Soc., **2017**, *139*, 5656-5659

DOI: 10.1021/jacs.7b00186

Contribution: acquired, processed and analysed ATR-FTIR data including the writing and revision of the associated manuscript text.

Comprehensive Vibrational Spectroscopic Investigation of *trans,trans,trans*-[Pt(N₃)₂(OH)₂(py)₂], a Pt(IV) Diazido Anticancer Prodrug Candidate

Robbin R. Vernooij, Tanmaya Joshi, Evyenia Shaili, Manja Kubeil, Dominique R. T. Appadoo, Ekaterina I. Izgorodina, Bim Graham, Peter J. Sadler, Bayden R. Wood and Leone Spiccia

Inorg. Chem., **2016**, *55*, 5983-5992

DOI: 10.1021/acs.inorgchem.6b00476

Conferences, scientific presentations and workshops during enrolment

April 2017 **Clircon17, Manchester Institute of Biotechnology, Manchester, UK.**

Attendance of conference

October 2016 **Final NanoTracking Meeting, Helmholtz Virtual Institute NanoTracking, Dresden, Germany.**

Scientific discussions on outcomes of NanoTracking and future collaborations.

September 2016 **Data Analysis for Reproducible Research in R, WDSI Vacation School, University of Warwick, UK.**

Five day workshop on R Studio software, including work discussion on thesis data.

July 1 2016 **CLIRSPEC Summer Shool, Windermere, UK.**

Fundamentals of spectroscopy, clinical applications and implications, interactive workshops for data handling and clinical applications.

March 2016 **Dalton 2016, Coventry, UK.**

Poster: Vibrational spectroscopic studies of photoactivatable diazido Pt(IV) anticancer complexes.

March 2016 **Advanced vibrational spectroscopy for biomedical applications, RSC Faraday Discussion, Cambridge, UK.**

Poster: Vibrational spectroscopic studies of photoactivatable diazido Pt(IV) anticancer complexes.

November 2015 **RACI Inorganic Chemistry Symposium, Melbourne, Australia.**

Poster: Vibrational spectroscopic studies of photoactivatable diazido Pt(IV) anticancer complexes. (Best poster award).

October 2015 **11th Australian Conference on Vibrational Spectroscopy (ACOVS11) and 5th Asian Spectroscopy Conference (ASC5), Sydney, Australia.**

Conference talk: Vibrational spectroscopic studies of photoactivatable diazido Pt(IV) anticancer complexes.

Synchrotron THz and IR workshop, invited talk: Synchrotron Far-IR: Exploration of new techniques towards measurement of metal-based drugs and their biomolecular interactions.

September 2015 **Fourth Annual NanoTracking Meeting, Helmholtz Virtual Institute NanoTracking, Lipari, Italy.**

Talk: New Materials for Cancer Imaging and Therapy.

April 2015 **The University of Warwick. Prof. Peter Sadler & Dr. Vas Stavros Groups.**

Invited talk: Vibrational spectroscopy: a tool for studying metal-based anticancer drugs and new nanomaterials.

December 2014 **7th Asian Biological Inorganic Chemistry Conference (AsBIC7), Gold Coast, Australia.**

Poster: Vibrational spectroscopic studies of diazido Pt(IV) anticancer complexes.

Table of contents

Copyright notice	i
Abstract.....	ii
Declaration.....	iv
Thesis including published works declaration	v
Acknowledgements	vii
Publications during enrolment.....	ix
Conferences, scientific presentations and workshops during enrolment	xi
Chapter 1.....	1
Scientific Introduction	1
1.1 Cancer	1
1.2 Chemotherapy.....	4
1.2.1 Metal-based Chemotherapy	4
1.3 Photoactivatable Anticancer Complexes	9
1.3.1 Photoactivatable Anticancer Prodrug Candidates.....	9
1.3.2 Photophysical and Photochemical Properties of PACT Complexes.....	11
1.3.3 Platinum Redox Chemistry to Exploit in PACT.....	15
1.4 <i>Trans,trans,trans</i> -[Pt(N ₃) ₂ (OH) ₂ (py) ₂] (1)	16
1.4.1 DNA and <i>In Vitro</i> Work on 1	19
1.4.2 Photophysical and photochemical properties of 1.....	20
1.5 Vibrational Spectroscopy	24
1.5.1 Principles of Vibrational Spectroscopy.....	25
1.5.2 Vibrational Spectroscopic Techniques	28
1.5.3 Computational Chemistry; Theory and Experimental Methods.....	32
1.6 Addressing the Wavelength Activation of Photoactivatable Anticancer Prodrugs.....	34
1.6.1 Upconverting Nanoparticles.....	34
1.7 Research Objectives.....	38
1.8 References.....	39

Chapter 2.....	50
Comprehensive Vibrational Spectroscopic Investigation of <i>trans,trans,trans</i> - [Pt(N ₃) ₂ (OH) ₂ (py) ₂], a Pt(IV) Diazido Anticancer Prodrug Candidate.....	50
2.1 Main Manuscript	51
2.2 Supporting Information	62
2.3 ACS LiveSlides	108
Chapter 3.....	109
Photoinduced Studies of Metal-Based Anticancer Prodrug Candidates	109
3.1 Main Manuscript: Spectroscopic Studies on Photoinduced Reactions of the Anticancer Prodrug, <i>trans,trans,trans</i> -[Pt(N ₃) ₂ (OH) ₂ (py) ₂]	110
3.2 Supporting Information: Spectroscopic Studies on Photoinduced Reactions of the Anticancer Prodrug, <i>trans,trans,trans</i> -[Pt(N ₃) ₂ (OH) ₂ (py) ₂]	125
3.3 Front Cover: Spectroscopic Studies on Photoinduced Reactions of the Anticancer Prodrug, <i>trans,trans,trans</i> -[Pt(N ₃) ₂ (OH) ₂ (py) ₂]	150
3.4 Cover Profile: Spectroscopic Studies on Photoinduced Reactions of the Anticancer Prodrug, <i>trans,trans,trans</i> -[Pt(N ₃) ₂ (OH) ₂ (py) ₂]	151
3.5 Main Manuscript: Studies of Carbon Monoxide Release from Ruthenium(II) Bipyridine Carbonyl Complexes upon UV-Light Exposure.....	152
3.6 Supporting Information: Studies of Carbon Monoxide Release from Ruthenium(II) Bipyridine Carbonyl Complexes upon UV-Light Exposure	165
Chapter 4.....	186
Synchrotron Infrared Beamline Studies.....	186
4.1 Introduction	188
4.1.1 Synchrotron Radiation Far-Infrared	188
4.1.2 Synchrotron Radiation Infrared Microspectroscopy	189
4.2 Results.....	195
4.2.1 Synchrotron Radiation Attenuated Total Reflection Far-Infrared	195
4.2.2 Transmission Synchrotron Radiation Far-Infrared – Liquid cell <i>in situ</i> Irradiation ..	205
4.2.3 Synchrotron Radiation Infrared Microspectroscopy – Live Single Cell Study.....	217
4.3 Discussion.....	221
4.3.1 Synchrotron Radiation Attenuated Total Reflection Far-Infrared	221
4.3.2 Transmission Synchrotron Radiation Far-Infrared – Liquid cell <i>in situ</i> Irradiation ..	223
4.3.3 Synchrotron Radiation Infrared Microspectroscopy – Live Single Cell Study.....	227

4.4 Conclusion	230
4.5 Experimental	232
4.5.1 Chemicals	232
4.5.2 Synthesis.....	232
4.5.3 External Illumination source.....	232
4.5.4 The Australian Synchrotron.....	232
4.5.5 Far-Infrared spectroscopy	232
4.5.6 Synchrotron Infrared Microspectroscopy	233
4.5.7 Cell Culture	233
4.5.8 Cell Treatment and Irradiation	234
4.5.9 Data Processing	234
4.6 Acknowledgments	236
4.7 References	237
4.8 Supporting Information	241
4.8.1 SR-ATR-FIR – DNA Nucleobases.....	241
4.8.2 SR-ATR-FIR – Malaria Infected Red Blood Cells	244
4.8.3 Transmission Synchrotron Radiation Far-Infrared – Liquid cell <i>in situ</i> Irradiation ..	247
Chapter 5	249
Upconverting Nanoparticles	249
5.1 Introduction	251
5.1.1 Physical and (Photo)Chemical Requirements.....	252
5.2 Results and Discussion	255
5.2.1 IR-806	255
5.2.2 IR-806 dye adsorption to LiYF ₄ : Yb ³⁺ /Tm ³⁺ nanoparticles.....	256
5.2.3 Neodymium (Nd ³⁺) doped UCNPs.....	258
5.2.4 Fluorescence Spectroscopy Setup for Upconverting Nanoparticles	262
5.3 Conclusion	266
5.4 Experimental	267
5.4.1 Chemicals	267
5.4.2 Instrumentation	267
5.4.3 Synthesis.....	268
5.5 References	274
Chapter 6	277
Conclusion and Future Perspectives	277

Chapter 1

Scientific Introduction

A general scientific introduction is provided in Chapter 1. Cancer is outlined first as this is the ultimate driving force behind this research. Chemotherapy, a principal form of treatment, is discussed next with a focus on the widely used metal-based anticancer drug, cisplatin (*cis*-[PtCl₂(NH₃)₂], CDDP). The mechanism of action of cisplatin is explored in order to demonstrate the need to develop more effective drugs with significantly fewer side effects. Metal-based photoactivated chemotherapeutic agents, derived from cisplatin, may provide a solution, based on their novel mechanisms of action and an overview of the current understanding of a particularly potent diazido Pt(IV) prodrug follows, around which this thesis is centred. Subsequently, the use of vibrational spectroscopy as a potential powerful tool to deepen our understanding of the photophysical and photochemical properties of such photoactivatable metal-based prodrugs is considered. Vibrational spectroscopy allows for direct observation of oscillating nuclei without the requirement of labelling and is non-destructive at the same time. Approaches to measure both metal and ligand vibrations complemented by theoretical calculations and use of high intensity synchrotron radiation provide a broad platform to study the metal coordination environment of such drugs in great detail. Lastly, the practical boundary of requiring a light source to activate these drugs is discussed, in particular the potential use of upconverting nanoparticles as a platform for wavelength activation in a clinically-relevant window.

1.1 Cancer

Cancer, in a broad consensus, is a genetic disease caused by an accumulation of mutations in the genome of somatic cells (all except reproductive cells).^[1] Whilst the cellular origin of cancer was first deduced in 1863, it was only in 2005 when the first decrease in the total number of deaths caused by cancer was reported.^[2] Nevertheless, the global burden of cancer is estimated to rise rapidly, from an estimated amount 14.1 million new cases (and 8.2 million deaths) in 2012 to 21.7 million new cases (and 13 million deaths) in 2030.^[3] A short overview is given below on our current understanding of the disease to give the reader a better comprehension of why it is so difficult to treat cancer.

The near complete identification (~99%) of the human genome (*i.e.* the complete set of human DNA) was accomplished in 2004, capturing over 3 billion DNA basepairs.^[4] This, and the advances of DNA sequencing technologies, facilitated the rapid systematic analysis of mutations fundamentally responsible for the origin and evolution of cancer tumours.^[5] Shortly after, a census carried out by Wellcome Trust Sanger Institute in 2004, already revealed 291 human genes that are causally implicated with the development of cancer (oncogenesis).^[6] To date, this census has extended to 567 human genes with over 540,000 different genetic mutations underlying human oncogenesis.^[7] While the rapid extension of our knowledge of the underlying gene mutations is still on going, one can imagine the limitlessness of possibilities leading to different types of cancer.

A multitude of mutations can cause cancerous cells to appear and take shape in the form of tumours. The crude view of a tumour would be to imagine multiple identical cancer cells clustered together (Figure 1.1A), which could in turn become invasive cancer cells by being released from this cluster and re-entering the body's blood stream where they can form distant metastasis (secondary malignant tumour growth away from the primary tumour). This is not entirely incorrect, however, as the biology of a cancerous tumour is more complicated to rationalise. Figure 1.1B shows a better representation of the tumour microenvironment. This microenvironment consists of cancer cells and

recruited normal cells corrupted by the cancer, which as a whole is responsible for tumour growth and progression.^[8]

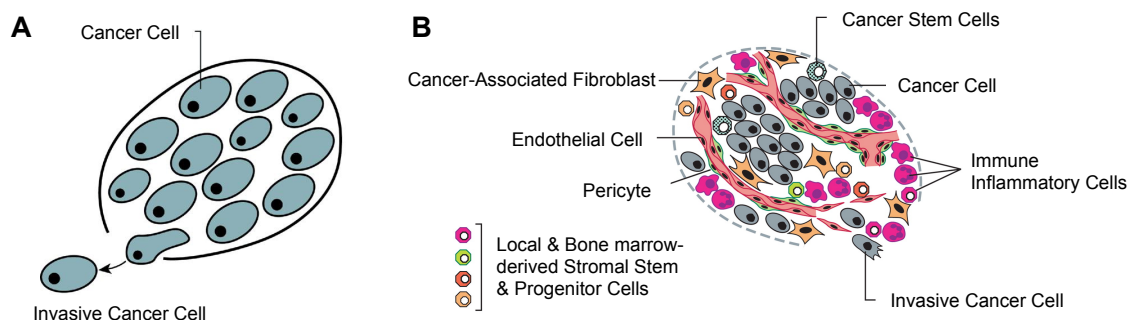


Figure 1.1. (A) Schematic view of a cancerous tumour. (B) Tumour microenvironment with recruited and corrupted normal cells. Adapted from D. Hanahan and R. Weinberg.^[8a,9] Reprinted with permission from Elsevier.

Hanahan and Weinberg proposed the hallmarks of cancer in an effort to provide a coherent framework to understand the complicated diversity of tumour microenvironments and what they are capable of, underlying the disease cancer (Figure 1.2).^[8a,9]

In short, cancer cells can sustain their proliferative signalling pathways leading to chronic proliferation, whilst normal cells carefully regulate themselves to control their cell numbers. Human cells are capable of responding to unregulated growth by activation of growth suppressor genes. However, cancers are known to sufficiently stall or inactivate these growth suppression pathways, which would otherwise lead to growth arrest, senescence (aging) or apoptosis (cell suicide program).

Additionally, obstruction or inactivation of the apoptotic cell program is often found to occur during cancer development, therefore making cancer capable of resisting cell death.^[10] Enabling replicative immortality allows the cell to continue to grow and divide, whereas normal cells are only able to cycle through a limited amount of growth and division phases. In order to sustain this growth and multiplication of cells, angiogenesis (branching of blood and lymphatic vessels) is almost always induced to allow for the supply and evacuation of increasing demand of nutrients and metabolic waste. At the same time, reprogramming of the energy metabolism allows cancer to function under aerobic (like normal human cells), anaerobic or both conditions.^[11]

One might expect the human body's immune system to reject cancer cells as a foreign entity, given its many mutations. The fact that there are clinically

detectable cancers that have avoided, evaded and/or suppressed it, is the basis of the long standing theory of the interactions of cancer with the immune system.^[12] Recent years have shown that, in many cases, there is a complex interaction between the immune system and the development of cancer, which can ultimately lead to either to eradication or evasion.^[13] In line with the above is the incorporation of immune inflammatory cells in the tumour environment, capable of supplying bioactive molecules, which can supplement the progression of other hallmarks, such as growth and survival factors as well as reactive oxygen species that can accelerate the genetic evolution of cancer.^[14] Furthermore, genome instability and mutation are the obvious, yet not to be forgotten hallmark, continuously driving cancer progression.

Lastly, the invasion and development of metastasis can occur throughout the progression of the cancer, whereby detached cancer cells enter the lymphatic or blood system, spreading throughout the body and settling in distant tissues (the start of possibly another/secondary tumour).

Most forms of human cancer develop these hallmarks to a certain degree and naturally vary between the different types of cancer. This makes them incredibly difficult to treat and while surgery and/or radiotherapy may successfully remove primary lesions of cancer, it often cannot treat the distant metastases. In such conditions, drug therapy (universally called chemotherapy) is usually considered.

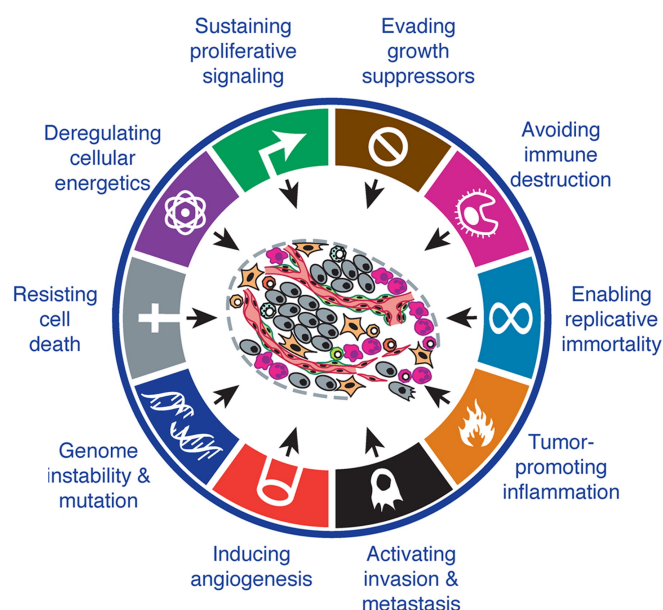


Figure 1.2. The hallmarks of cancer, providing a structured overview of acquired capabilities by developing cancers. Adapted from D. Hanahan and R. Weinberg.^[8a] Reprinted with permission from Elsevier.

1.2 Chemotherapy

The application of chemotherapy in conjunction with surgery and radiotherapy started to develop between the 1940s and 1960s.^[5,15] To date, there are over 100 different chemotherapeutic agents approved in the US alone, which can be administered in multiple combinations, depending on the type of cancer, stage and conditions of the patient.^[16] The shortcomings of most chemotherapeutic agents are unfortunately undeniable, whereby toxicity towards normal tissues of the body and inherent as well as acquired drug resistance hamper the clinical efficacy of chemotherapy. Therefore, there is on going effort to develop new and improve on long-standing chemotherapeutic agents.

One particular field of chemotherapy is metal-based anticancer agents, which was stimulated by the discovery of the antiproliferative properties of cisplatin (CDDP, *cis*-[PtCl₂(NH₃)₂]) in 1965.^[17] Metal-based anticancer agents have a broad-spectrum of application in the clinics, with approximately 50% of all patients receiving a platinum based compound.^[18]

1.2.1 Metal-based Chemotherapy

Prior to the discovery of the anticancer properties of cisplatin, the field of chemotherapy development consisted almost solely of organic and natural-product chemistry.^[19] One of the last remarks published in a paper by professor Barnett Rosenberg in 1971, the principal investigator on cisplatin as a chemotherapeutic agent, was: 'Without hesitancy I suggest it is now appropriate for inorganic chemists to join their organic brothers in submitting samples of their syntheses to appropriate Cancer Institutes for screening for anti-tumour activities'.^[20] This paper and his work are largely responsible for opening up the field of chemotherapy to metal-based agents and its rapid development.

Continuous explorations of transition metal complexes have led to a range of clinically globally approved platinum complexes to date (Figure 1.3) and complexes based on other transition metals such as ruthenium undergoing clinical trials.^[21]

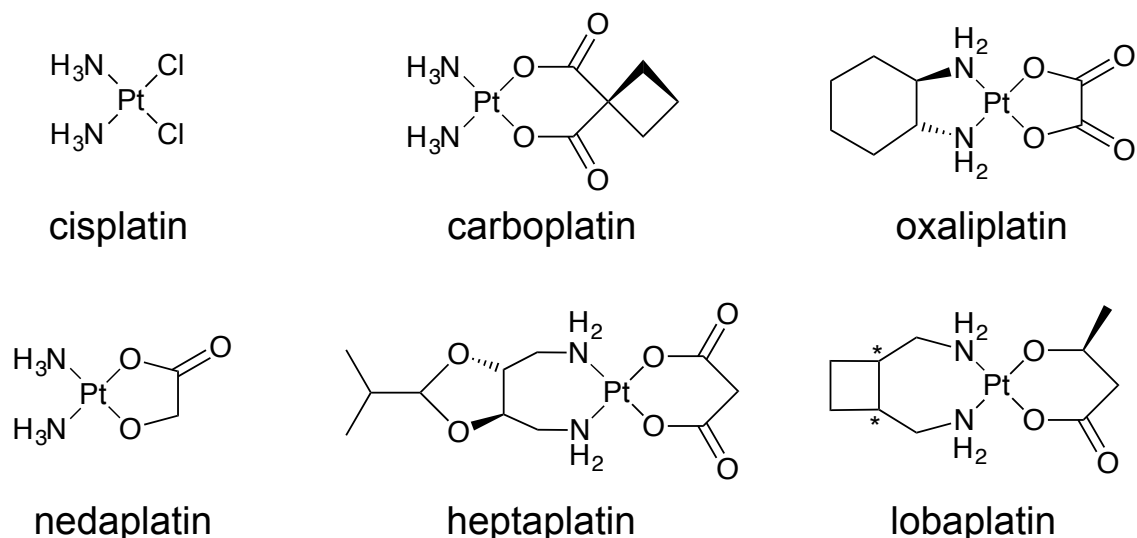


Figure 1.3. Structures of clinically approved platinum anticancer drugs.

Nevertheless, the efficacy of these drugs is limited by acquired and/or inherent resistance by cancer, restricting the applicable spectrum of chemotherapeutic agents, and the indiscriminate toxicity of drugs towards normal healthy cells, leading to severe long and short term side effects on patients.^[5,15,22]

It would be irrational to assume that each of these approved drugs has the same mechanism of action, although, one of the commonalities between them is that they rely on chemical activation. The mechanism of action of cisplatin will be used as the example below to provide a clear image, working towards new generations of anticancer drugs.

Starting with cisplatin, the mechanism of action has been studied in detail over the past decades, whereby hydrolysis of one or two chlorido ligands results in the active species of cisplatin thought to induce the observed toxicity.^[20,22b,23]

Following Figure 1.4, intravenous injection or infusion of cisplatin into the bloodstream is stabilised by the high inherent chloride concentration (~100 mM) and can be co-administered with sodium chloride solutions at adjusted pH values between 3.5 – 4.5 (Figure 1.4).^[16,19] This allows for the distribution of the relatively inactive cisplatin throughout the body, whereupon entry into the cell is attained by both active and passive uptake.^[24] Cisplatin becomes susceptible to hydrolysis inside the cytoplasm due to the relative low intracellular concentration of chloride anions (4 – 20 mM) (Figure 1.4).^[24d,25]

Stepwise hydrolysis of cisplatin yields active charged Pt(II) species capable of binding to DNA base pairs, such as the most nucleophilic position of DNA, the

N7 position of the guanine base.^[24d] The structural distortion caused by the formation of multiple intra- and interstrand DNA adducts sets in motion cell death pathways and hinders the transcription and replication of the cell (Figure 1.4).^[23],24c,25] Typically, the cell cycle is halted in the G2 stage as a response to cisplatin-DNA adducts in an effort to repair the induced DNA damage by nucleotide excision repair (NER, replacement of 30-mer oligonucleotides containing cisplatin adducts with new oligonucleotides templated from the leftover single-stranded DNA).^[22b] In the event of failed repair, for instance by the binding of high mobility group (HMG) proteins to 1,2 intrastrand (GpG) crosslinks of cisplatin blocking the NER, the cell initiates the cell death pathway referred to as apoptosis.^[26]

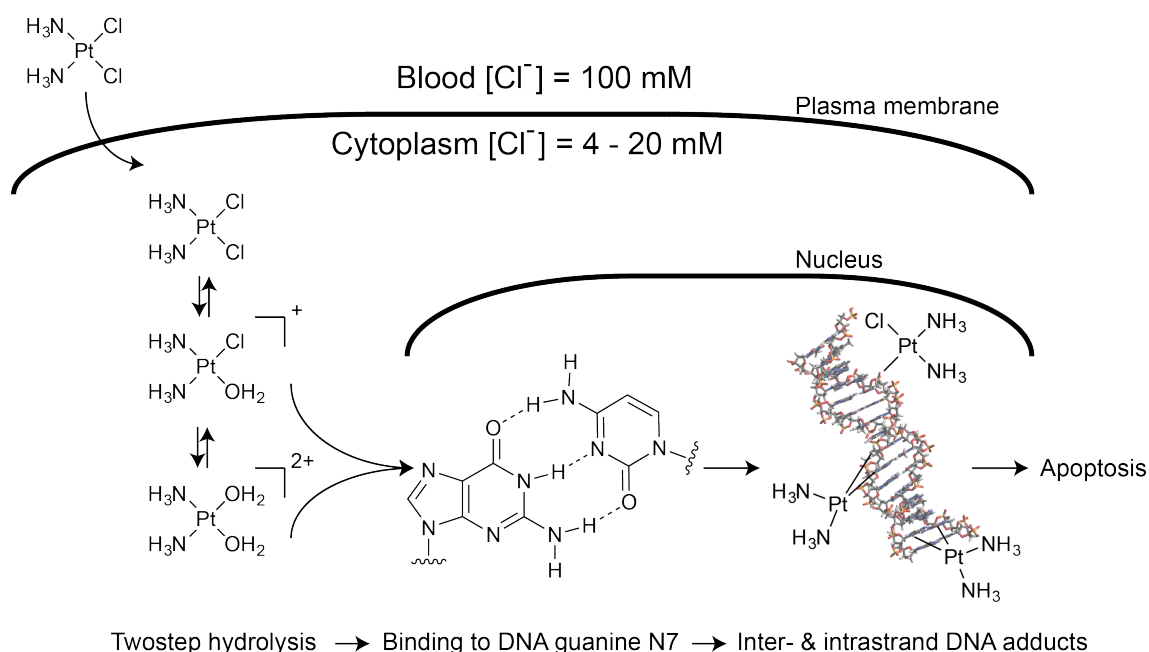


Figure 1.4. Simplified representation of the mechanism of action of cisplatin. Cellular uptake followed by stepwise hydrolysis/activation, binding of cisplatin to DNA and cellular processing leading to cell death (apoptosis).

Unfortunately, besides the unselective uptake by healthy cells leading to severe short term and long term side effects, there are also many points between the bloodstream and the nucleus where cisplatin can be deactivated, i.e. chlorido ligand release and binding of platinum to other biological targets than DNA causing unwanted side effects (Figure 1.5). First, cisplatin (and Pt(II) in general) exhibits high affinity towards sulphur containing compounds. The most abundant protein in the human bloodstream, human serum albumin, can interact with cisplatin through thiols and thioethers from cysteine and

methionine residues respectively, even though the high concentration of chloride in the bloodstream reduces reactivity by suppressing hydrolysis (Figure 1.5).^[27]

Second, the down-regulation of proteins associated with the active uptake (via copper or organic cation transporters) and up regulation of efflux by copper transports, such as ATP7B, in response to high plasma concentrations of cisplatin can lead to decreased uptake or increase efflux of (activated) cisplatin (Figure 1.5).^[24a,28]

Third, increase in DNA repair or replicative bypassing of cisplatin-DNA adducts as a response to DNA damage recognition in cancer cells leads to decrease in cell death responses.^[29]

Last, and based on the same principle of the first point, is the elevated amounts of sulphur containing compounds inside the cancer cells, such as glutathione, methionine, metallothionein and proteins. The interaction of platinum compounds with proteins is not completely understood.^[30] However, binding of the hydrolysed cisplatin to such compounds before reaching DNA causes cytoplasmic inactivation and is one of the biggest factors limiting the efficacy.^[29]

While the chemical activation by relative changes in chemical gradient is the underlying origin of the efficacy of metal-based agents like cisplatin, it is also this unselective activation that hampers the efficacy by dose limiting side effects.^[31]

Different research strategies to overcome these limitations have been formulated throughout the last decades, including exploration of metal complexes targeting intracellular proteins and biomolecular molecules outside of the nucleus, developing more kinetically inert, d^6 low-spin, metal complexes and using carriers such as polymers and nanoparticles to improve delivery.^[21,24d,32]

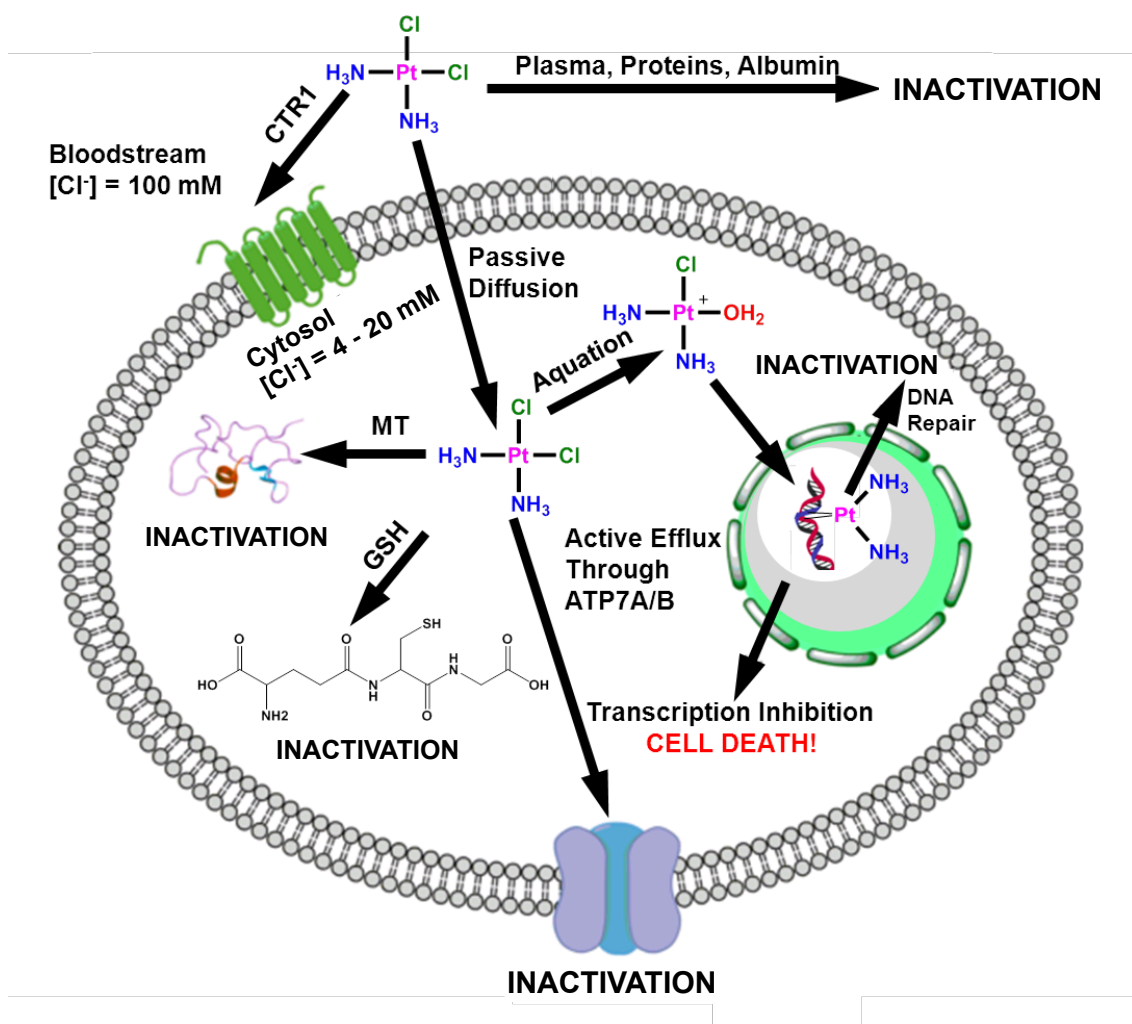


Figure 1.5. Schematic representation of possible deactivation pathways of cisplatin by intra- and extracellular conditions. Abbreviations used: CTR = copper transporters, GSH = glutathione, MT = metallothionein and OCT = organic cation transporter. Adapted with permission from Johnstone et al.^[24d] Copyright 2013 American Chemical Society.

1.3 Photoactivatable Anticancer Complexes

One particular field of research has been focussing on replacing the chlorido ligands of metal complexes (responsible for biological selectivity) with ligands to yield metal complexes that are stable and inert in the dark, but can be released locally (replaced with physical selectivity) in selected areas where cancer is located in effort to address the severe side effects and resistance on account of their novel mechanism(s) of action. Metal complexes that utilise electromagnetic radiation to induce ligand release and the subsequent formation of active species to target cancer are commonly referred to as photoactivatable anticancer complexes and give rise to the field of inorganic photoactivated chemotherapy (PACT).^[33] The temporal and spatial control over the activation of the drug has the advantages of only affecting the cancerous areas and builds on the clinically established field of photodynamic therapy (PDT), which has been used in the clinics for nearly three decades.^[34] Photosensitizers are used in PDT to transfer the energy from light to ground state triplet oxygen ($^3\text{O}_2$), subsequently producing highly reactive singlet oxygen species ($^1\text{O}_2$), which are one of the main contributors to cell death from PDT treatment.^[35] However, many malignant and most aggressive tumours are hypoxic by nature, which is a major drawback for PDT as it relies on the presence of oxygen.^[36] PACT potentially offers an advantage over PDT in hypoxic conditions, as it exploits different mechanisms to induce cell death by active binding of metal- and ligand-based species formed upon light activation.

1.3.1 Photoactivatable Anticancer Prodrug Candidates

A large variety of metal-based photoactivatable anticancer prodrugs (Co(II, III), Cu(II), Mn(I), Fe (II, III), Ir(III), Pt(II, IV), Re(I), Ru(II), Rh(III), V(IV) have been reported to date.^[33,37]

Selected examples are shown in Figure 1.6, underlining the different design approaches used for such complexes. Highlighted in red are potential leaving groups, which can be released upon photoactivation to yield metal-based and ligand species. These designs include photoreduction pathways from complexes such as the diido Pt(IV) complex (Figure 1.6A) to yield active Pt(II)

species.^[37d] Introduction of bulky conjugated ligands result in complexes, such as the biquinoline Ru(II) complex (Figure 1.6D). This yields complexes with structural distortion to facilitate rapid photochemistry using visible or near-infrared light to facilitate biquinoline release and Ru(II) species capable of binding to DNA.^[37z] Alternatively, strategies to replace the chlorido ligands with thioether ligands to afford Ru(II) complexes such as the structure depicted in Figure 1.6E. These complexes are stable in the dark due to the strong preferential binding of sulphur (“soft” base, by Pearson’s HSAB principles) to Ru(II) (intermediate/soft acid) but can be released upon light activation.^[38] Furthermore, strategies have been described using the release of toxic carbon monoxide to obtain biological activity in addition to metal-based species containing potential binding sites (Figure 1.6B, C).^[37z,39] Such complexes are generally referred to as photoactivated metal-based CO-releasing complexes (photoCORMs). While there is a strong overlap in (photo)chemistry with PACT, the application of photoCORMs has not been limited to anti-tumour activity and they have also shown promising anti-inflammatory, vasodilatory and antimicrobial properties, building on the biological interactions of carbon monoxide.^[37],40]

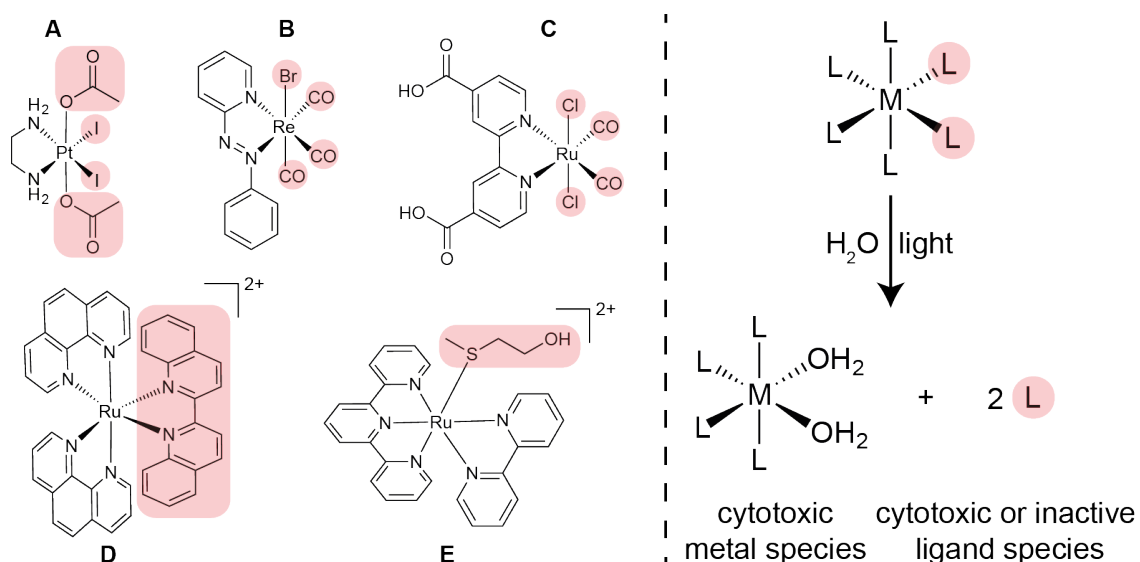


Figure 1.6 Chemical structures of PACT and photoCORMs complexes reported by the Bednarski, Mascharak, Glazer, Spiccia and Bonnet research groups (LHS).^[37d,37z,38-39,41] Schematic representation of the photoactivation of PACT or photoCORMs complexes yielding active metal and/or ligand species to act as anticancer agents (RHS).

Providing a detailed review of PACT and photoCORM compounds to date is outside of the scope of this thesis and recent reviews capture the advances in these fields.^[37k,42] Instead, the focus is placed on a potent photoactivatable diazido Pt(IV) anticancer prodrug candidate around which the majority of the work in this thesis is centred, after the brief introduction of photophysical and photochemical properties of PACT complexes and the underlying platinum chemistry of the diazido Pt(IV) complex.

1.3.2 Photophysical and Photochemical Properties of PACT Complexes

Metal-based PACT utilises the unique photochemical and photophysical properties of transition metal complexes. The photochemistry principles involving electronic transitions for organic and inorganic compounds are broadly identical. However, the unique interactions of the ligand orbitals with the metal orbitals result in the splitting of d-orbitals, as outlined by the crystal field theory (Figure 1.7A). Energy splitting (Δ) between d-orbitals gives rise to a variety of orbital energy levels, dependent on the ligands, electronic configuration of the metal and its oxidation state, and the geometry of the metal complex. These allow a range of electronic transitions to occur between or within metal, ligand and solvent orbitals, and typically fall within the visible light spectrum (Figure 1.7B).

The Beer-Lambert law, Laporte rule and spin selection rules have long helped to explain and benchmark (by extinction coefficient) the observed electronic transitions caused by the redistribution of electrons following the absorption of a photon.^[43] The extinction coefficient, ϵ ($M^{-1} \text{ cm}^{-1}$), is a measure of the strength of the electronic transition and can be derived from the Beer-Lambert law (equation 1.1), which states that the monochromatic radiation absorbed (A) by a homogenous solution is proportional to the path length (l , cm) and concentration (c , M).

Equation 1.1

$$A = \epsilon cl$$

The spin selection and Laporte rule govern the experimental probability of an electronic transition to occur, which is dependent on the transition dipole moment. Change in spin multiplicity (S) is not allowed according to the spin selection rule, whereas the Laporte rule states that transitions between states of

equal parity, such as ligand field (d-d) transitions, are not allowed in centrosymmetric molecules (Figure 1.7B). Nevertheless, relaxation of both these rules allows for forbidden transitions to be experimentally observed at low probability, hence low(er) extinction coefficients. Typically, the coupling between orbital and spin angular momenta (spin-orbit coupling) allows for spin forbidden transitions to be observed, which is more pronounced for heavier atoms. Furthermore, asymmetry or vibrational distortion in metal complexes breaks the centrosymmetry and subsequently Laporte forbidden transitions can be observed. The above translates to the general classification of the extinction coefficients by ligand field transitions ($\epsilon = \sim 500 \text{ M}^{-1} \text{ cm}^{-1}$, Laporte forbidden), metal to ligand or ligand to metal charge transfer transitions (MLCT or LMCT, $\epsilon = 10^3 - 10^6 \text{ M}^{-1} \text{ cm}^{-1}$), intraligand charge transfer transitions (ILCT, $\epsilon = 10^3 - 10^5 \text{ M}^{-1} \text{ cm}^{-1}$) and charge transfer to solvent transitions (CTTS, $\epsilon = 10 - 10^3 \text{ M}^{-1} \text{ cm}^{-1}$).

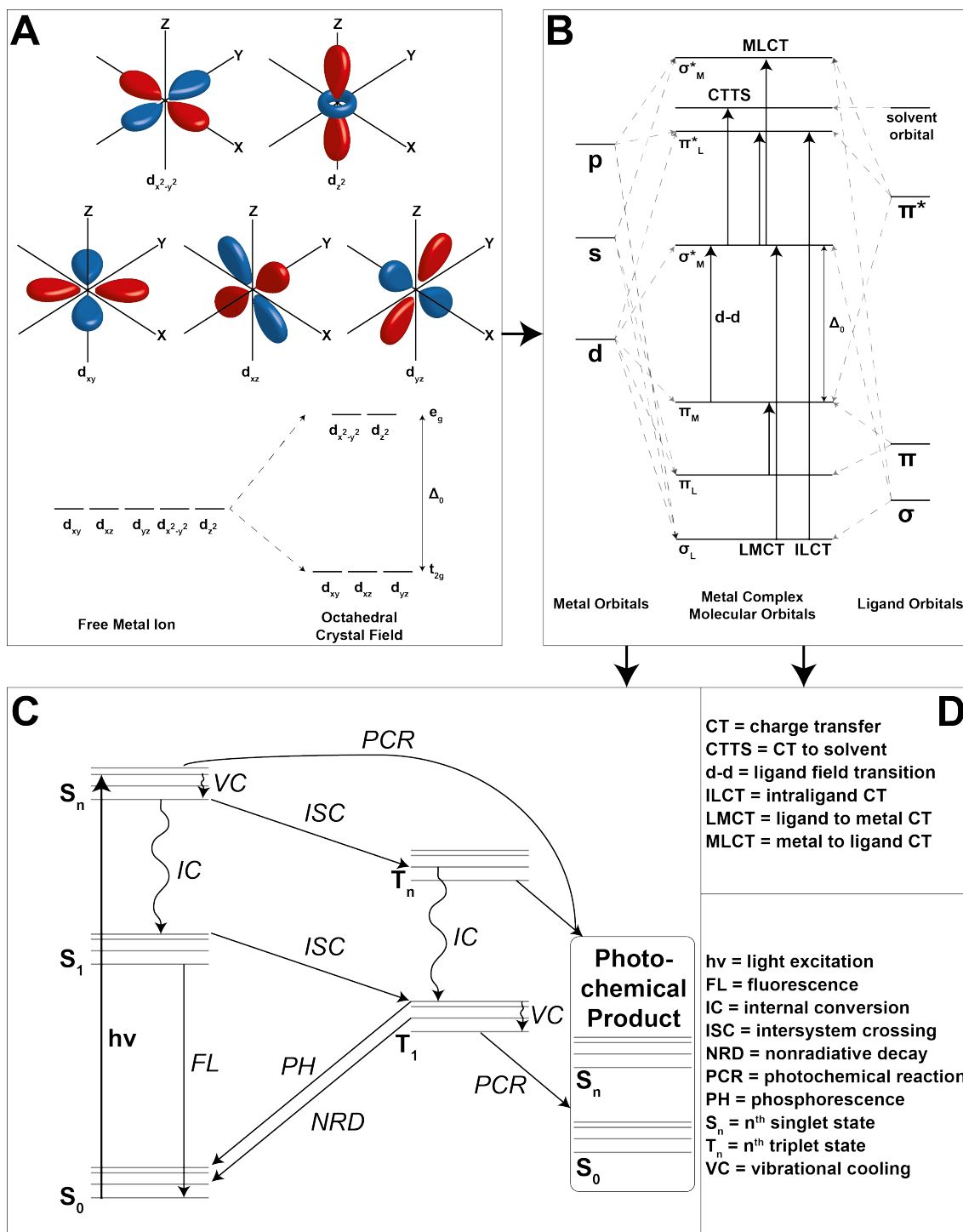


Figure 1.7. Metal-ligand orbital interactions and photochemistry of an octahedral transition metal complex. A) Crystal field splitting of the d-orbitals. B) Molecular orbital diagram outlining the possible electronic transitions between metal, ligand and solvent. C) Jablonski diagram defining the physical processes a ground state (S_0) transition metal complex can undergo following light excitation. Photochemical reactions can occur at any stage after excitation, resulting in a photochemical product. D) Abbreviations used.

In recent decades, advances in theoretical calculations, Density Functional Theory (DFT) in particular, have had great influence on elucidating the nature of electronic transitions of transition metal complexes.^[44] This allows extended elucidation to build on top of the benchmarks set for the extinction coefficients for each allowed or forbidden electronic transition, in an effort to explain the observed reactivity. This is covered in more detail in section 1.5.3.

Excitation of a ground state (S_0) transition metal complex into one or more of the electronic transition bands typically results in a singlet excited state, after which several physical processes can occur. Excited states can ultimately return to the S_0 ground state complex through radiative or non-radiative decay as shown in Figure 1.7C. However, photochemical reactions can occur at any stage during the decay, which are intertwined with the physical processes and depend on the nature of the excited state, as well as the relative energy difference between other close-lying states.^[33a]

The photochemical reactions are initiated in the excited state, whereby the promotion of an electron has the potential to weaken specific bonds within the complex. Typically, complexes exhibiting ligand field transitions undergo light-induced solvation, racemisation and isomerisation reactions, while complexes with LMCT transitions (Figure 1.7B) can undergo photoreduction at the metal centre through loss of ligands.^[33a,b]

These photochemical reactions are the foundations on which PACT relies. Intra- and intermolecular reactions such as photodissociation, photosubstitution and photoredox reactions are the favoured outcomes of such events by which active metal and/or ligand species are released to act as anticancer agents.^[33a]

1.3.3 Platinum Redox Chemistry to Exploit in PACT

The $5d^8$ Pt(II), square planar cisplatin complex owes its biological activity to the relatively slow substitution of chlorido ligands (section 1.2.1), which is a general feature in Pt(II) complexes.^[45] Low-spin $5d^6$ octahedral Pt(IV) complexes are more kinetically inert than the $5d^8$ square planar Pt(II) complexes. This has led to the development of Pt(IV) prodrugs, based on cisplatin, by oxidative addition of two axial groups to Pt(II) complexes to retain the original coordination sphere.^[46] The irreversible reduction of Pt(IV) back to Pt(II) gives the active square planar metal-based species, induced by intra- and extracellular reducing agents such as ascorbic acid, glutathione and cysteine or methionine containing proteins.^[46a] Therefore, the rate of reduction plays a critical role in the biological activity of such Pt(IV) prodrugs.

Diiodido Pt(IV) complexes were designed in an effort to eliminate the option of chemical reduction and introduce photoreduction, such as the *trans,cis*-[PtI₂(OAc)₂(en)] (Figure 1.6 I, OAc = acetate, en = ethylenediamine).^[37d,41a,47]

The photoreduction was observed through the decrease in intensity of the LMCT transition of iodide to Pt(IV) upon light activation. However, *in vitro* toxicity of *trans,cis*-[PtI₂(OAc)₂(en)] was observed in both the dark and light conditions. This was later attributed to the potential ring opening of ethylenediamine in the presence of glutathione.^[41a,47]

This inspired the next generation of photoactivatable Pt(IV) prodrugs containing azides to overcome the instability of diiodido Pt(IV) complexes in the dark, building on the unique photochemical properties of metal-azides which can undergo reduction through concomitant azide radical release.^[48]

1.4 *Trans,trans,trans*-[Pt(N₃)₂(OH)₂(py)₂] (**1**)

The diazido dihydroxo diimine platinum (IV) complex, *trans,trans,trans*-[Pt(N₃)₂(OH)₂(py)₂] (**1**, py = pyridine, Figure 1.8), is derived from a series of Pt(IV) diazido dihydroxo complexes, and has proven to be significantly more stable and potent than its predecessors and cisplatin (Figure 1.8).^[37s,37v,49]

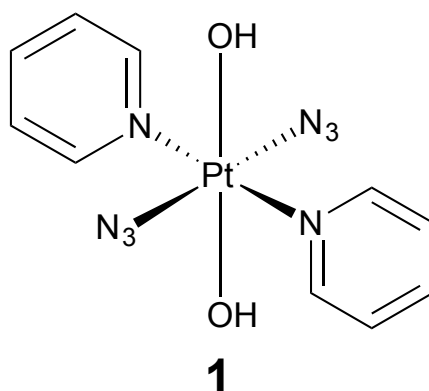


Figure 1.8. Molecular structure of *trans,trans,trans*-[Pt(N₃)₂(OH)₂(py)₂] (**1**).

The azido ligand-containing series builds on a dual targeting strategy, with photoactive release of a potentially biologically-active Pt(II) species and biologically-active ligands (such as radical [•]N₃ or the toxic N₃⁻ anion), while the Pt(IV) complexes remains inert in the dark.^[50]

Extensive screening of diazido compounds (Figure 1.9, Table 1.1) led to **1**, which holds particular advantages over its predecessors, as well as increased phototoxicity. Namely: (a) increased solubility (for *trans* Pt(IV) diazido complexes in general vs. *cis*) of (up to) ~34 mM at 298 K in aqueous solution.^[37v] (b) Pyridine ligands are retained upon irradiation whereas amine ligands were found to dissociate, which could potentially explain the reduced phototoxicity.^[37v,51] (c) Phototoxicity could be attained with wavelengths up to 500 ± 30 nm, providing a versatile range to work with.^[37v] Whilst this compound has not yet reached clinical trials and is not commercially available yet, new strategies have already been shown to be capable of extending the window of photoactivation to better suit current clinically available lasers wavelengths, whilst retaining the unique mechanism of action of **1** (section 1.6.1).^[52]

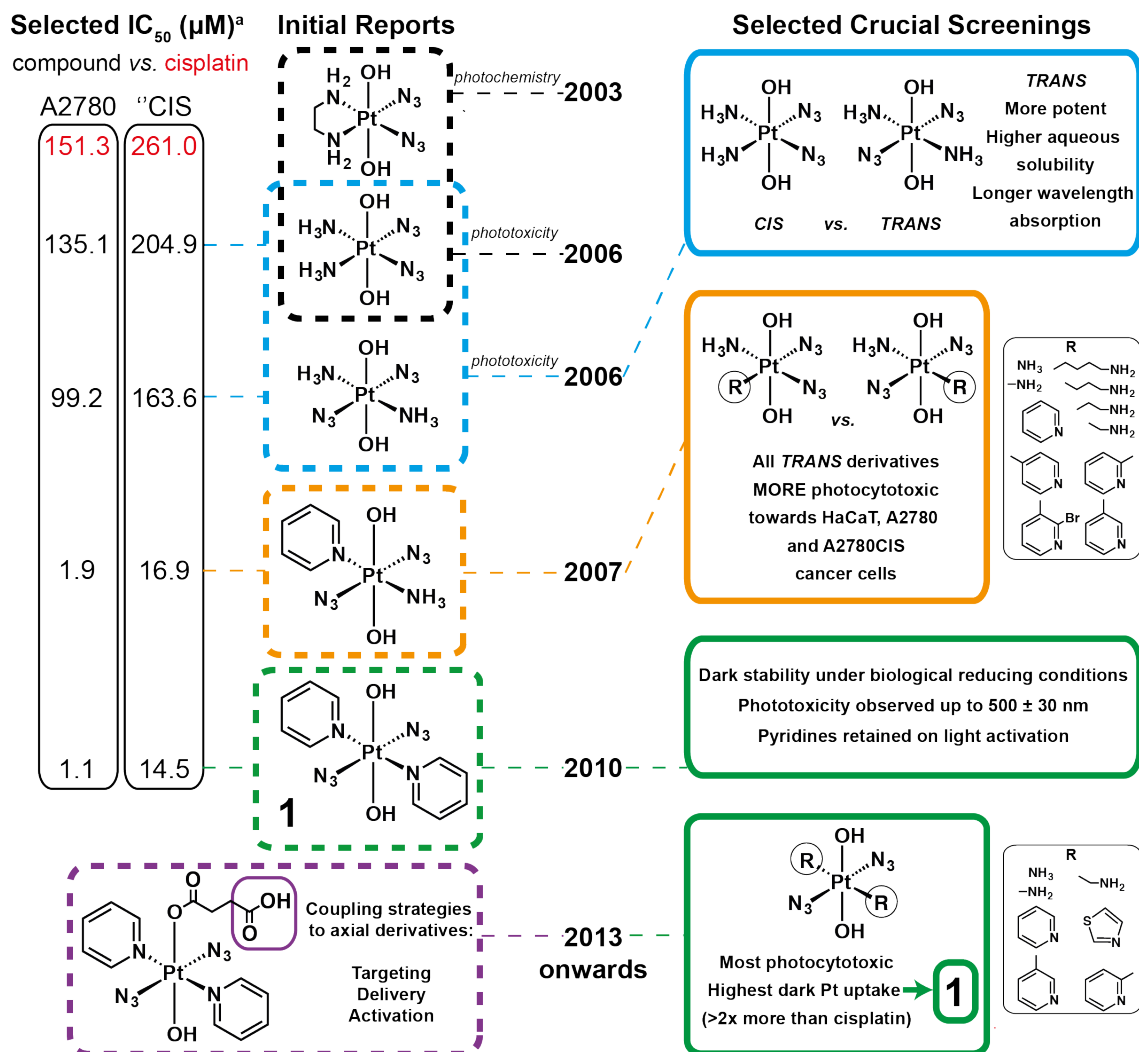


Figure 1.9. Graphical representation of the history on photoactivatable Pt(IV) diazido complexes, including selected data underlying the scientific decisions going forward. A full list of publications to date is tabulated in Table 1.1. ^a Selected IC₅₀ values after one hour of drug exposure, one hour of 365 nm irradiation (5 J cm⁻²) and 24 h recovery. Confidence intervals are omitted for clarity.^[37s,37v,49a] IC₅₀ values for cisplatin using a more common protocol of 24 h exposure and 24 h recovery without irradiation; A2780 = 1.2 μM and A2780cis = 13.4 μM.^[53] Notations used: A2780 = human ovarian carcinoma cells, "CIS" = A2780cis, cisplatin-resistant A2780 human ovarian carcinoma cells, HaCaT = human immortalised keratinocyte cells, IC₅₀ = concentration at which the complex inhibits 50% of the dye uptake in the neutral red uptake phototoxicity assay, thus the lower the value the higher the toxicity towards the cell line.

Table 1.1. Scientific publications on photoactivatable Pt(IV) diazido complexes. Review articles are omitted unless new material has been added. Colour scheme correspond to compounds in Figure 1.9, no colour = new derivative.

Title	Year	Reference
Nucleotide Cross-Linking Induced by Photoreactions of Platinum(IV)–Azide Complexes	2003	[54]
Light-activated destruction of cancer cell nuclei by platinum diazido complexes	2006	[49b]
A photoactivated trans-diammine platinum complex as cytotoxic as cisplatin	2006	[49a]
A potent cytotoxic photoactivated platinum complex	2007	[37s]
Photoactivatable Platinum Complexes	2007	[55]
Unprecedented carbon-carbon bond formation induced by photoactivation of a platinum(IV)-diazido complex	2008	[18a]
Synthesis, characterisation and photochemistry of PtIV pyridyl azido acetato complexes	2009	[37t]
Decomposition pathways for the photoactivated anticancer complex <i>cis,trans,cis</i> -[Pt(N ₃) ₂ (OH) ₂ (NH ₃) ₂]: insights from DFT calculations	2009	[51b]
Photo-cytotoxic trans diam(m)ine platinum(IV) diazido complexes more potent than their cis isomers	2010	[56]
A Potent Trans-Diimine Platinum Anticancer Complex Photoactivated by Visible Light	2010	[37v]
Probing Platinum Azido Complexes by 14N and 15N NMR Spectroscopy	2011	[57]
Insights into the Acid–Base Properties of PtIV–Diazydodiam(m)inedihydroxido Complexes from Multinuclear NMR Spectroscopy	2011	[58]
Photoreaction pathways for the anticancer complex <i>trans,trans,trans</i> -[Pt(N ₃) ₂ (OH) ₂ (NH ₃) ₂]	2011	[51a]
Ground and excited state properties of photoactive platinum(IV) diazido complexes: Theoretical considerations	2011	[59]
Tryptophan Switch for a Photoactivated Platinum Anticancer Complex	2012	[37y]
Interactions of DNA with a New Platinum(IV) Azide Dipyridine Complex Activated by UVA and Visible Light: Relationship to Toxicity in Tumor Cells	2012	[60]
Combined Theoretical and Computational Study of Interstrand DNA Guanine–Guanine Cross-Linking by <i>trans</i> -[Pt(pyridine) ₂] Derived from the Photoactivated Prodrug <i>trans,trans,trans</i> -[Pt(N ₃) ₂ (OH) ₂ (pyridine) ₂]	2012	[61]
A Computational Approach to Tuning the Photochemistry of Platinum(IV) Anticancer Agents	2012	[62]
<i>trans,trans,trans</i> -[PtIV(N ₃) ₂ (OH) ₂ (py)(NH ₃)]: a light-activated antitumor platinum complex that kills human cancer cells by an apoptosis-independent mechanism	2012	[63]
Near-Infrared Light-Mediated Photoactivation of a Platinum Antitumor Prodrug and Simultaneous Cellular Apoptosis Imaging by Upconversion-Luminescent Nanoparticles	2013	[52a]
De Novo Generation of Singlet Oxygen and Ammine Ligands by Photoactivation of a Platinum Anticancer Complex	2013	[37p]
Diazido Mixed-Amine Platinum(IV) Anticancer Complexes Activatable by Visible-Light Form Novel DNA Adducts	2013	[37n]
Cellular Accumulation, Lipophilicity and Photocytotoxicity of Diazido Platinum(IV) Anticancer Complexes	2014	[64]
Targeted delivery of photoactive diazido PtIV complexes conjugated with fluorescent carbon dots	2015	[65]
An integrin-targeted photoactivatable Pt(IV) complex as a selective anticancer pro-drug: synthesis and photoactivation studies	2015	[37o]
A Photoactivatable Platinum(IV) Anticancer Complex Conjugated to the RNA Ligand Guanidinoneomycin	2015	[37r]
Multifunctional single-drug loaded nanoparticles for enhanced cancer treatment with low toxicity in vivo	2016	[66]

Spin-labelled photo-cytotoxic diazido platinum(iv) anticancer complex					2016	[37b]
Comprehensive	Vibrational	Spectroscopic	Investigation	of	2016	[67]
<i>trans,trans,trans</i> -[Pt(N ₃) ₂ (OH) ₂ (py) ₂], a Pt(IV) Diazido Anticancer Prodrug Candidate						
Supramolecular Photoactivatable Anticancer Hydrogels					2017	[52b]
Primary photochemical processes for Pt(iv) diazido complexes prospective in photodynamic therapy of tumors					2017	[68]

1.4.1 DNA and *In Vitro* Work on **1**

The first report on **1** revealed its low micromolar doses of activity against keratinocyte (HaCaT), ovarian carcinoma (parental A2780 and cisplatin resistant A2780cis), oesophageal adenocarcinoma (OE19) and hepatoma (HepG2) cell lines, whilst only exposing them to **1** for one hour prior to light activation.^[37v] This is in contrast with cisplatin, which requires 24 hours of exposure to attain similar antiproliferative activity given the active species formation is limited by the rate of hydrolysis.^[53]

DNA platination is one of the critical events responsible for cell death by cisplatin and the studies by Pracharova et al. revealed significant higher amounts of DNA platination by complex **1** compared to cisplatin, ~16-fold, in A2780 cells after one hour of drug exposure, irradiation and a further 24 hours of incubation.^[60] This confirmed that **1** is capable of penetrating the nucleus and binding DNA after photoactivation. Importantly, no DNA platination was observed when **1** was exposed to A2780 cells when kept in the dark. Thus, the activity of **1** upon photoactivation is correlated to **1** penetrating the nucleus and binding to DNA, whilst there is no antiproliferative activity and no binding to DNA in the absence of irradiation.

Distinct differences between DNA adducts of photoactivated **1** and *cis*- and *trans*-[PtCl₂(NH₃)₂] were found, including large DNA unwinding angles, suggesting the importance of pyridine interactions with DNA-base residuals. Furthermore, using an *in vitro* model of RNA polymerase II (a RNA transcription protein inside the nucleus), it was shown that photoactivated adducts of **1** were markedly more effective^[60] at inhibiting RNA transcription.^[60] This demonstrated the likelihood that DNA adducts of **1** lead to different downstream effects compared to those formed by cisplatin.

In 2014, Pizarro et al. reported on the cellular accumulation, lipophilicity and photocytotoxicity of **1** and other diazido Pt(IV) compounds (Figure 1.8).^[64] Interestingly, after one hour in the dark, A2780 cells exposed to **1** exhibited the

highest platinum uptake (20 ± 1 ng Pt per 10^6 cells), over twice as much as cisplatin (8.1 ± 0.3 ng Pt per 10^6 cells). This supports the results of Paracharova et al. which indicated that **1** showed significantly higher amounts of DNA platination than cisplatin. Higher lipophilicity allegedly increases the passive diffusion of compounds into the cell, although, no correlation between the lipophilicity and photocytotoxicity or platinum uptake was observed between the diazido Pt(IV) compounds. This suggests that compounds such as **1** are (partially) involved in active transport into the cell.

Both these studies suggest the involvement of the *trans*-pyridine scaffold of **1** on the photocytotoxicity are unique in this diazido Pt(IV) series. However, the effect of its photochemistry and resulting photoproducts (including released ligands) on the phototoxicity is yet to be fully elucidated.

1.4.2 Photophysical and photochemical properties of 1

Early efforts studying the photophysical and photochemical properties of **1** involved the use of electronic absorption spectroscopy supported by Density Functional Theory (DFT), nuclear magnetic resonance (NMR) spectroscopy and mass spectrometry (MS) methods.^[37v]

The UV-Vis spectrum of **1** (Figure 1.10) revealed two absorption maximum at ~ 260 nm and ~ 295 nm which were assigned as dissociative LMCT (N_3 , OH \rightarrow Pt) and mixed 1 LMCT/ 1 IL (OH \rightarrow Pt, N_3 ; IL = interligand) transitions respectively, by time-dependent DFT.^[37v] Furthermore, a weak shoulder in the visible region at ~ 414 nm can be gleaned, with a similar mixed 1 LMCT/ 1 IL character. The photodecomposition of **1** by UV-Vis features the loss of 294 nm absorption at different rates, depending on the excitation wavelength. Interestingly, evolution of gas bubbles was observed throughout irradiation of **1**, although this was not further discussed at the time.^[37v] Further studies on a close derivative of **1**, *trans,trans,trans*-[Pt(N_3)₂(OH)₂(py)(methylamine)], revealed a gas evolution consisting of N_2 (likely recombination of two $\cdot N_3$) and O_2 (from the complex, rather than solvent, verified by ^{18}O -labeled water) by gas chromatography MS (GCMS).^[37p]

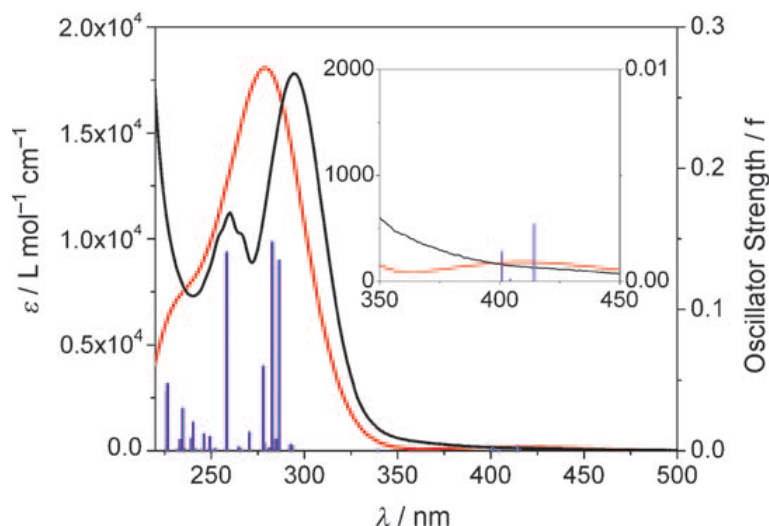


Figure 1.10. The experimental (black) and predicted (red) UV-Vis spectra of **1** in water. Inset: expansion of the 350 – 450 nm region. Blue bars indicate the calculated excited states, with heights equal to extinction coefficients. Reprinted with permission from Farrer et al.^[37v] Copyright 2010 WILEY-VCH Verlag GmbH & Co. KGaA, Weinheim.

The photoinduced binding of **1** (9 mM) to a DNA-base model, 5'-guanosine monophosphate (5'-GMP, 2 mol equiv.), was studied by ^{195}Pt NMR in D_2O under 420 nm irradiation.^[37v] Complete removal of **1** was observed within 45 min of irradiation and led to two major Pt(II) NMR signals. Synthesis allowed for the elucidation of one of the formed compounds: *trans*-[Pt(py)₂(5-GMP)₂]²⁺ (**A**), whilst the other species was reasonably assigned to *trans*-[Pt(N₃)(py)₂(5-GMP)₂]⁺ (**B**) (Figure 1.11). A third minor (PtIV) species was observed, which, after irradiation, increased in magnitude over time together with **A**, whilst **B** decreased. Subsequent monitoring of these species by electron spray ionization (ESI) MS matched this minor species to a molecular formula of: [Pt(N₃)(OH)₂(py)₂(5'-GMP)]⁺ (**C**). ^{15}N labelling of pyridine and azide allowed for further elucidation of the NMR spectra of **1**, although, no photodecomposition studies by ^{14}N or ^{15}N NMR were reported.

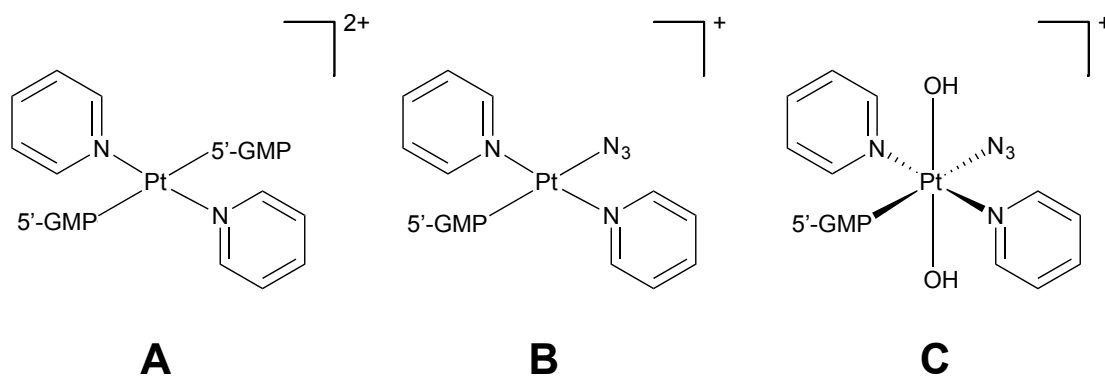


Figure 1.11. Proposed molecular structures of the formed species by photoinduced binding of **1** with 5'-GMP under 420 nm irradiation, as observed by ^{195}Pt NMR and ESI-MS.^[37v]

A combination of electron paramagnetic resonance (EPR) and ^{14}N NMR studies carried out by Butler et al. captured several important characteristic events of the azido ligands, upon irradiation of **1**.^[37y] Firstly, by using a spin trap, 5,5-dimethylpyrroline *N*-oxide (DMPO), azidyl radicals (from ^{14}N and ^{15}N azido ligands) were captured in water, phosphate-buffered saline (PBS) and growth medium for cell culture (RPMI-1640). However, the azidyl radical binding to DMPO competes with the formation of N_2 following radical dimerisation, depending on concentration and solvent, confirmed by ^{14}N NMR. Whilst PBS yielded slightly higher concentrations of trapped radicals, RPMI-1640 yielded lower concentrations. The inclusion of various amino acids, vitamins, inorganic salts, and other growth-promoting substances in RPMI-1640 is likely to compete or influence the reaction of azidyl radicals with DMPO. Furthermore, the addition of a two molar equivalent of the DNA-base model, 5'-GMP, had little effect on the capture of azidyl radicals, but did prevent the precipitation of resulting platinum species otherwise formed at such high concentrations (4 mM), likely due to binding of **1** to 5'-GMP.

Introducing known electron transfer mediators, present on the side chains of proteins, tyrosine (Tyr) and tryptophan (Trp), into the photoreactions was carried out to further investigate the possible effect of amino acids on the photocytotoxicity of **1**. Tyr $^{\bullet}$ and Trp $^{\bullet}$ are weaker oxidising agents than $^{\bullet}\text{N}_3$, thus Tyr and Trp could potentially quench the $^{\bullet}\text{N}_3$ radical to N_3^- .

The presence of L-Tyr, had little influence on the trapping of azidyl radicals, whilst L-Trp completely suppressed the capture of azidyl radicals by DMPO at

0.25 mol equiv., without substantially affecting the photodecomposition of **1**. This interestingly translated similarly to the photocytotoxic effect of **1** on the A2780 cancer cell line. Co-incubation of varying concentrations of L-Trp with **1** allowed for an increase in viability. At 500 μM L-Trp, the IC_{50} values (half maximal inhibitory concentrations) of **1** were increased by ~ 7 fold. Even at equal concentrations ($\sim 50 \mu\text{M}$, L-Trp and **1**), viable cells were observed after 24 hours, whereas 50 μM of **1** alone resulted in no viable cells.

This allowed for the first *in vitro* proof of the dual mechanism of **1**, in which the released ligands upon irradiation are responsible for a part of the observed photocytotoxicity. Additionally, the relative depletion of Trp levels in the serum of some cancer patients (breast, lung and ovarian) could be an underlying factor of the effectiveness of **1** as a chemotherapeutic agent.^[26,69]

Significant advances have been made in effort to elucidate the mechanism of action, suggesting that the cleaved ligands and platinum centres following photoactivation, act in concert to elicit the observed multi-targeted biological activity. The potential use of NMR spectroscopy to monitor the azido release of **1** was reported. However, it remains challenging to deduct significant information due to the broad resonances for quadrupolar $I=1$ ^{14}N and poorly sensitive $I=1/2$ ^{15}N resonances (due to lack the enhancement by polarisation transfer via coupled protons).^[57]

Further insights into the release of azide and, yet to be studied, hydroxido ligands as well as the changes around the platinum centre are of utmost importance to improve our understanding of these potential anticancer prodrugs in the field of chemotherapy.

1.5 Vibrational Spectroscopy

Reflecting back on Rosenberg's paper from 1971, the landscape of metal-based chemotherapy has undergone significant growth.^[20] Interestingly to mention is the remark he included after the invitation to inorganic chemists to submit samples to Cancer Institutes for anticancer activity screening: 'In addition to this chemical synthesis activity, it is desirable to know in more detail, and with greater security, the mechanisms of action of this new class of drugs, as well as their general toxicological and pharmacological properties in mammalian systems'.^[20] Already then, emphasis was placed on scientists to investigate and progress techniques to study newly synthesised compounds in order to progress in this field. A new and improved chemotherapeutic agent is very rarely revealed in the first round of discovery. Studying the mechanism of action can provide invaluable information for the development of more potent drugs in the future and can provide direct insight on how to modify screened candidates. This mechanism of action of potential anticancer prodrugs is the broad theme of this thesis, where vibrational spectroscopic techniques are utilised in order to improve upon our knowledge and develop methods to study these compounds.

Several non-invasive techniques exist to date that allow for the study of the mechanism of drug interactions with biological materials. These include radioactive and fluorescent labelling, nuclear magnetic resonance, X-ray spectroscopy and mass spectrometry.^[70] Most of these techniques provide empirical information on the drugs and their mechanism of action. While vibrational spectroscopy was the foremost used analytical tool in research and industry on chemical structures, it was consigned to mainly a qualitative functional group analysis tool throughout the late 20th century.^[71] However, recent decades have seen a resurgence of vibrational spectroscopic studies on biological specimens and biomolecular drug targets.^[72] It is now a rapidly expanding research area because of the increased throughput, spatial resolution and means to process large data sets, while at the same time being label-free and non-destructive.^[72b] Besides the fact that biomolecular changes and interactions can be examined using such techniques, another level of detection may be achieved when drugs containing distinct vibrational bands are

introduced; such as chloro (Cl), azido (N_3), hydroxido (OH) and carbonyl (CO) ligands. Specifically for the case of metal containing drugs, vibrational spectroscopy allows for monitoring changes around the metal coordination environment. This makes vibrational spectroscopy a potentially powerful tool for gaining insights into the mechanism of action of the previously discussed metal-based photoactivatable anticancer prodrug candidates (section 1.3, 1.4).

1.5.1 Principles of Vibrational Spectroscopy

Atoms are in constant motion, independent of phase, which depending on the temperature, increases or decreases in amplitude but never reaches zero. This constant motion within molecule, complex, ion etc. (further referred to as sample) can be broken down into normal modes of vibration, where all atoms oscillate at identical phase and frequency (constant translation and rotation) but with different amplitudes. All normal modes of vibration or fundamental vibrations of each sample can be deduced, which are determined by its symmetry (group theory). For example, the constant motion of a linear triatomic azide ion ($\text{D}_{\infty\text{h}}$) can be described by four normal modes of vibration (Figure 1.12), namely, ν_1 the symmetric stretching vibration, two deformations ($\nu_{2a\&b}$) and ν_3 the anti-symmetric stretching vibration. It is the frequency of these molecular vibrations that is measurable by vibrational spectroscopy.

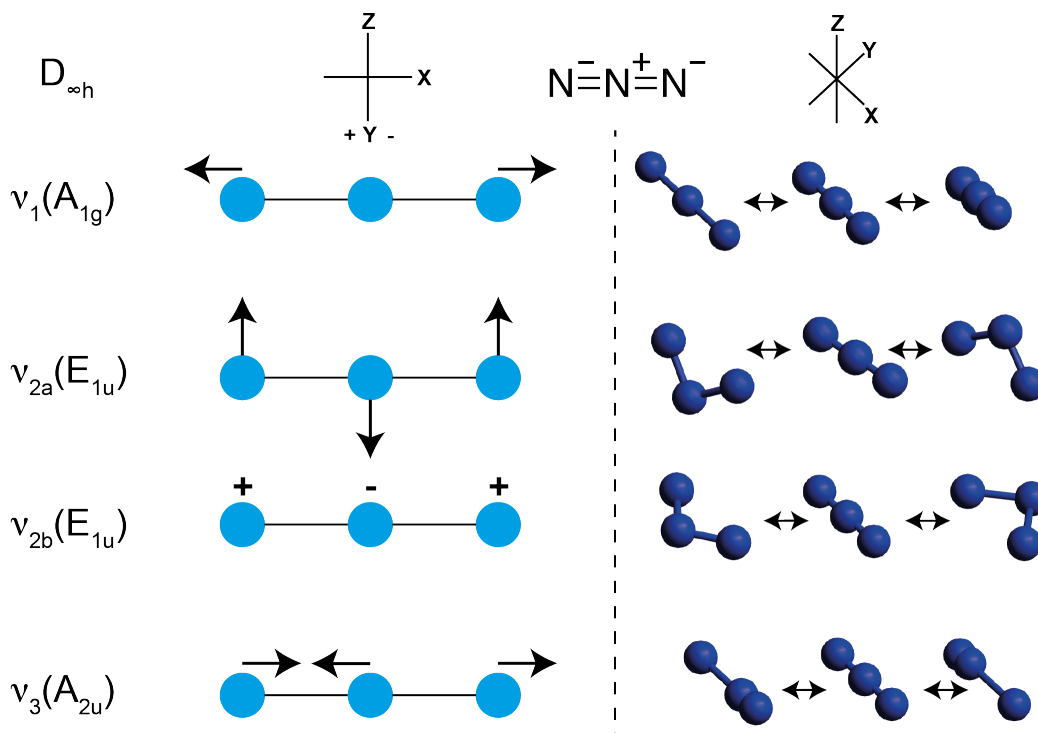


Figure 1.12. Normal modes of vibration of the triatomic linear ion, N_3^- .

Both infrared and Raman spectroscopy can measure the vibrational transitions by excitation of the vibrational ground state (ν_0) or vibrational excited states (*vide infra*). However, the physical origin of the two resulting spectra is distinctly different (exemplified by a normal of vibration in Figure 1.13). In infrared spectroscopy, the absorption of photons from the infrared source (λ_{IR}) causes transitions from the vibrational ground state (ν_0) of a sample to a vibrationally excited state (ν_1), and the energy of the photon (E_{photon}) is equal to the ΔE of the sample after absorption.^[73] In Raman spectroscopy, the excitation of a sample is the result of an incident photon (much higher in energy than in infrared spectroscopy) from a monochromatic radiation source (λ , usually an UV, Vis or near-infrared laser) inducing a transition into a virtual excited state (ν_v), followed by relaxation into either its ground vibrational state (Rayleigh scattering) or a vibrationally excited state (Stokes Raman scattering, $\nu_v - \nu_1$).^[74] Thus, Raman is a measure of loss in photon energy. Furthermore, a third scattering is possible (left out of the figure for clarity), whereby the incident photon excites the sample from ν_1 to ν_{v+1} and relaxes to the vibrational ground state ν_0 (anti-Stokes Raman, $\nu_v + \nu_1$).

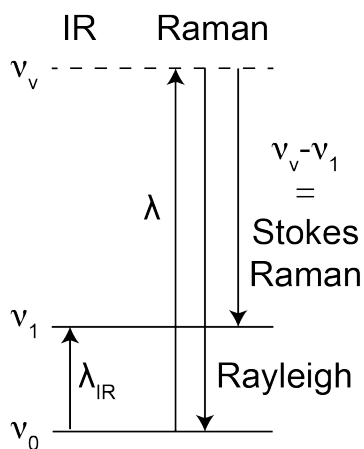


Figure 1.13. Simplified representation of infrared absorption and Raman scattering of a normal vibration. Notations used: ν_0 = ground vibrational state, ν_1 = excited vibrational state, ν_v = virtual state, λ_{IR} = infrared light excitation, λ = monochromatic laser excitation.

Both Raman and Rayleigh scattering are very weak processes, thus Raman spectroscopy benefits from laser sources capable of producing sufficient photons ($\sim 10^{15} - 10^{18} \text{ s}^{-1}$) in order to intensify the scattering and collect a (Stokes) Raman spectrum (Stokes Raman occurs with a likelihood of ~ 1 in $10^{10} - 10^{12}$).^[73b] In contrast, photon absorption by a sample in infrared spectroscopy

can occur with significantly higher probabilities, for instance, an one absorbance unit band absorbs ~90% of the photons.^[73b]

Not all normal vibrations are infrared and Raman active. A change in dipole moment of a normal vibration is required for the vibration to be infrared active, while a change in polarisation is required for a normal vibration to be Raman active. For example in Figure 1.12, the symmetric stretching vibration of the azide ion is not infrared active but Raman active and vice versa for the anti-symmetric vibration.

These principles are not straightforward and the quantum mechanical explanations are too extensive for this purpose. However, they can be visualised by imagining an infrared beam passing through one azide ion as a uniform electric field (left to right). It would be impossible to induce an symmetric stretch with any translation of the azide ion on the x,y,z coordinates. For Raman spectroscopy, the incident monochromatic laser light induces an electronic polarisation in the sample, which can couple to other existing polarisations of the sample, such as vibrational excited states. However, the polarisation of the anti-symmetric stretching vibration of an azide ion is isotropic and therefore only Rayleigh scattering will occur for this normal vibration.

This gives rise to the mutual exclusion rule, whereby normal modes of vibration cannot be both infrared and Raman active if the sample has a centre of symmetry. However, in practice, the majority of samples with multiple different atoms have several symmetry elements in addition to the centre of symmetry, influencing whether or not a transition is infrared and/or Raman active. Furthermore, inter- and intramolecular interactions in the sample add another level of complexity on top of the symmetry elements. Therefore, many vibrations can be both infrared and Raman active. A general rule applies though, whereby strong Raman bands are typically weak infrared bands, resulting in vibrations being visible in both infrared and Raman spectra, which makes them highly useful complementary techniques.

Group vibrations or characteristic vibrations are commonly identified as a particular localised vibration within a group of atoms that are dominant in a normal vibration, such as the anti-symmetric stretching vibration of azido ligands in the photoactivatable anticancer prodrug **1**. However, it is important to keep in mind that, even though the characteristic vibration is dominant, all

atoms in the sample are vibrating and involved to a certain extent. Furthermore, vibrational spectroscopy is not limited to the observation of only normal modes of vibration. Multiples of normal modes ($\nu_0 \rightarrow \nu_n, n \geq 2$), the sum or difference of two or more normal modes and excitation of a vibrational excited state ($\nu_1 \rightarrow \nu_n, n \geq 2$) can likewise be observed. These are referred to as overtones, combination bands and hot bands respectively.

1.5.2 Vibrational Spectroscopic Techniques

The main vibrational spectroscopic techniques or equipment used throughout this thesis are described briefly.

Attenuated Total Reflection – Fourier Transform Infrared (ATR-FTIR)

ATR-FTIR spectrometers are one of the most versatile infrared spectrometers, which are present in many active academic and industrial research labs. Their widespread use may be attributed to their increasing affordability, low maintenance, ease of use and ability to rapidly identify and classify any sample without prior sample preparation, so long as the sample can make physical contact with the ATR sample crystal.

ATR-FTIR is a total internal reflection technique that measures the infrared absorption of the sample at the surface of the internal reflecting element (further referred to as ATR crystal, Figure 1.14).^[75] Total internal reflection is obtained when the angle of infrared light reaching the ATR crystal surface is equal or larger than the critical angle (Equation 1.2) if the refractive index of the ATR crystal (n_2) is higher than the sample (n_1) (Snell's law). The electric field of the infrared beam under total internal reflection extends beyond the interface of reflection as it is polarised in the direction of the sample where infrared absorption can occur, which is known as the evanescent wave. The depth of penetration (d_p) of this evanescent wave is related to the wavelength (λ) and incident angle (θ_i) of the infrared beam, and the refractive index of the ATR crystal (n_2) and sample (n_1) as shown in Equation 1.3.

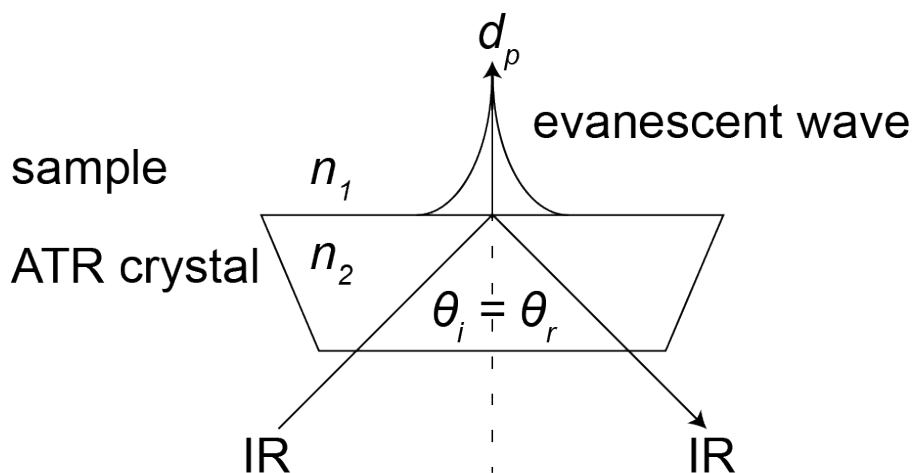


Figure 1.14. Schematic representation of ATR at $\theta_i \geq \theta_c$. Notations used: $\theta_{i/r}$ = angle of incidence/reflection, θ_c = critical angle, n_1 = refractive index of the sample, n_2 = refractive index of the ATR crystal, d_p = penetration depth of resulting evanescent wave into sample, IR = infrared beam.

Equation 1.2
$$\sin \theta_c = \frac{n_1}{n_2}$$

Equation 1.3
$$d_p = \frac{\lambda}{2\pi\sqrt{\sin^2\theta - (n_1/n_2)^2}}$$

Two different ATR crystal materials are used throughout this thesis, diamond ($n = 2.4$) and silicon ($n = 3.42$). Both of the ATR crystals are mounted into ATR accessories with the angle of incidence of the IR beam fixed to 45° . Assuming a typical refractive index of 1.5, the critical angle would be $\sim 39^\circ$ (diamond) or $\sim 26^\circ$ (silicon), meeting the requirements for ATR. The penetration depth can be calculated for the typical infrared wavenumber ranges as shown in Figure 1.15.

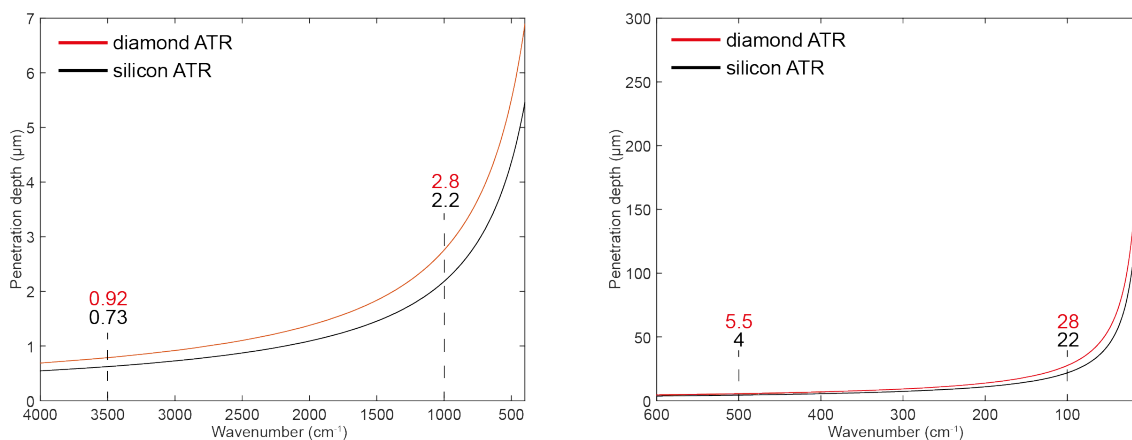


Figure 1.15. Penetration depth of the evanescent IR wave into the sample at different wavenumbers including selected peak labels with a diamond or silicon ATR crystal, IR beam incidence of 45° and a refractive index of the sample of 1.5.

Relatively low penetration depth is typically obtained in the mid-infrared region ($\sim 4000 - 400 \text{ cm}^{-1}$) between $\sim 0.5 - 6 \text{ }\mu\text{m}$, whereas the penetration depth starts to vary more significantly in the far-infrared region ($\sim 650 - 10 \text{ cm}^{-1}$). The difference in penetration depth throughout the spectral region is why ATR spectra are not directly comparable to transmission spectra with fixed path lengths. The effective path length of ATR spectra can be calculated (approximately) for quantitative analysis as described by Griffiths et al., if desired.^[75a] Nevertheless, ATR-FTIR allows for measurement of strongly absorbing samples, such as water, without having to work with short path length transmission cells.

As outlined above, ATR-FTIR spectra are dependent on the refractive index of the sample. There are samples, such as solid and crystalline materials, that exhibit anomalous dispersion, which results in rapid changes to the refractive index of the sample whilst scanning through an absorption peak.^[76] This results in asymmetric line shapes and shifts in absorption maxima to smaller wavenumber values and has to be accounted for. Such effects were observed throughout this thesis and corrections were carried out accordingly, which are outlined in Chapter 2.2.

Raman Microspectroscopy

Raman microspectroscopy is used to complement the infrared spectroscopic measurements. Raman microscopes are in general not limited to a lower wavenumber limit of $\sim 400 \text{ cm}^{-1}$ such as mid-infrared spectrometers due to the material of optics used, weak infrared sources and/or detector limits.

This lower wavenumber region ($\sim 650 \text{ cm}^{-1} - 10 \text{ cm}^{-1}$) is of particular interest to inorganic materials as it is where metal to ligand vibrations occur.^[77] Raman microspectroscopy allows one to collect spectra between $\sim 4000 \text{ cm}^{-1} - 50 \text{ cm}^{-1}$, whereas far-infrared spectrometers have to be typically used in order to obtain spectra in the lower wavenumber region. Far-infrared spectrometers have their own limitations and restrictions, which are discussed further in Chapter 4.1.

Raman scattering, as described above, is a weak process and the monochromatic lasers of different wavelengths and microscope lenses employed into the Raman microscopes allow one to minimise the unwanted scattering effects. Fluorescence can be a particular problem for many inorganic metal complexes.^[77a]

Synchrotron Radiation as Infrared Sources

Charged particle accelerators, i.e. synchrotrons, were originally used in the field of particle physics to allow the study of subatomic particle collisions. However, second and third generation synchrotrons were designed to store accelerated electrons created with strong magnetic and electric fields into electron storage rings. The electron storage ring utilises electromagnets to focus, steer and maintain the high-energy electrons in a vacuum, whereupon they emit extremely intense radiation, referred to as synchrotron radiation (SR). SR emits a wide range of electromagnetic radiation, including infrared radiation, which can be tuned by the electron energy.

The brilliance of infrared SR of a 3 GeV SR source (such as the Diamond Light Source) shows at least two orders of magnitude advantage over a typical Globar infrared source (Figure 1.16).^[78] Furthermore, this advantage increases more significantly in the far-infrared region. Apart from the high brilliance, SR is highly collimated, allowing for an effectively parallel source and its energy is intrinsically stable (directly proportional to the electron current), whereas thermal sources such as the Globar do not exhibit those properties.^[79]

This has resulted in the installation of infrared beamlines at synchrotrons, with at least 20 active infrared beamlines in 2016, continuously advancing their equipment and throughput to utilise SR.^[80] Further discussion on the particular advantages of SR and application towards the research carried out in this thesis in the far- and mid-infrared regions can be found in Chapter 4.

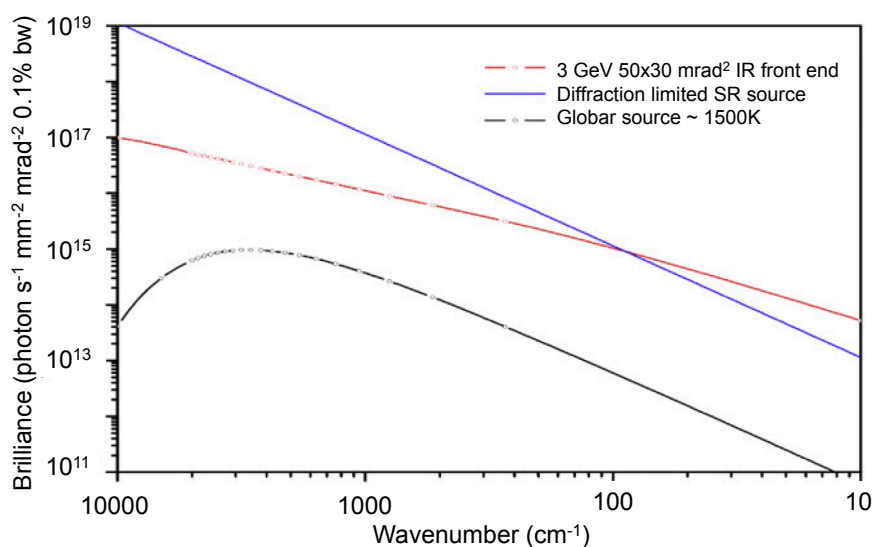


Figure 1.16. Calculated SR brilliance of a 3 GeV SR source, a typical Globar infrared source and an ideal bending magnet SR diffraction limited source. Adapted from Marcelli et al.^[78] Reprinted with permission from Elsevier.

1.5.3 Computational Chemistry; Theory and Experimental Methods

The last two decades have seen a vast increase in the amount of quantum mechanical approaches used to aid experimental observations, building on the improved reliability of models, affordable access to computational nodes and user-friendly computer codes.^[81] Density functional theory (DFT, including time-dependent DFT) is by far the most widely used method for transition metal complexes, allowing for accurate description of their ground state and excited state properties at moderate computational cost.^[44b]

DFT requires one, or several, basis set(s) and functional(s) to describe a sample, where the basis set is the set of functions describing the atomic orbitals and the functional is an approximation of the exchange-correlation energy of the overall system (sample). Multiple benchmarked basis sets and functionals (empirical and non-empirical) currently exist and have to be carefully selected to attain the appropriate ground state geometries of which the ground state and excited state properties are derived.

A complete qualitative interpretation of vibrational spectra of multi-atom metal complexes from the basic physical principles is nearly, if not, impossible. DFT allows for the prediction of vibrational frequencies, derived from the overall energy of an optimised molecular system using a harmonic approximation. This means that stretching vibrations are typically overestimated by DFT calculations and uniform scaling factors are commonly used to address the lack of anharmonicity in the DFT calculations.^[44d,82] Corresponding vibrational intensities are obtained through the description of the vibrational motion and electronic redistribution of electron density, yielding the dipole moments. Whilst accurate intensity descriptions can be obtained, the calculated intensities are largely reliant on the basis sets employed.^[83]

The DFT calculations used throughout this thesis are employed to aid the assignment of measured experimental frequencies. Likewise, time-dependent DFT (TD-DFT) calculations are used to predict the electronic absorption energies to rationalise the observed changes in the absorption spectrum upon irradiation of the photoactivatable metal complex.

The DFT method can be a very powerful tool to elucidate experimental observations. However, it remains an *ab initio* method and care has to be taken not to over-interpret results. A complete description of the chemical environment

of the metal complex, *i.e.* crystal lattice, solvent molecules, intermolecular interactions is too computationally demanding. A conductor-like polarisable continuum model (CPCM) is used throughout this thesis to better describe the electrostatic interactions between metals and ligands.^[84] This allows for better description of ground state geometries, further reflected in the better description of frequency and TD-DFT calculations, but is not to be confused with actual solvent molecules.

1.6 Addressing the Wavelength Activation of Photoactivatable Anticancer Prodrugs

The activation of metal-based photoactivatable chemotherapeutic (PACT) agents requires a light source, thus there is a practical boundary that has to be addressed in order to introduce PACT agents into the clinic. Apart from introduction light sources into the clinics, the current excitation wavelengths (UVA – blue) of PACT candidates such as **1**, is damaging to the skin (UV radiation) and does not allow for deep skin penetration due to the strong absorption of biomolecules such as haemoglobin and oxyhaemoglobin.^[85] Optimum penetration depths can be achieved between ~650 – 900 nm (*in vivo* imaging window') where the lowest extinction coefficients of haemoglobin, oxyhaemoglobin and water intersect.^[85]

Current clinical lasers are operational for the use in photodynamic therapy (PDT), the type of localised treatment of cancer with highly reactive singlet oxygen species in which the incident light energy is absorbed by a injected photosensitizer and subsequently transferred to ground state triplet oxygen (section 1.3). These PDT lasers are typically pulsed dye lasers (595 nm) and diode lasers (ranging from 630 nm to 670 nm).

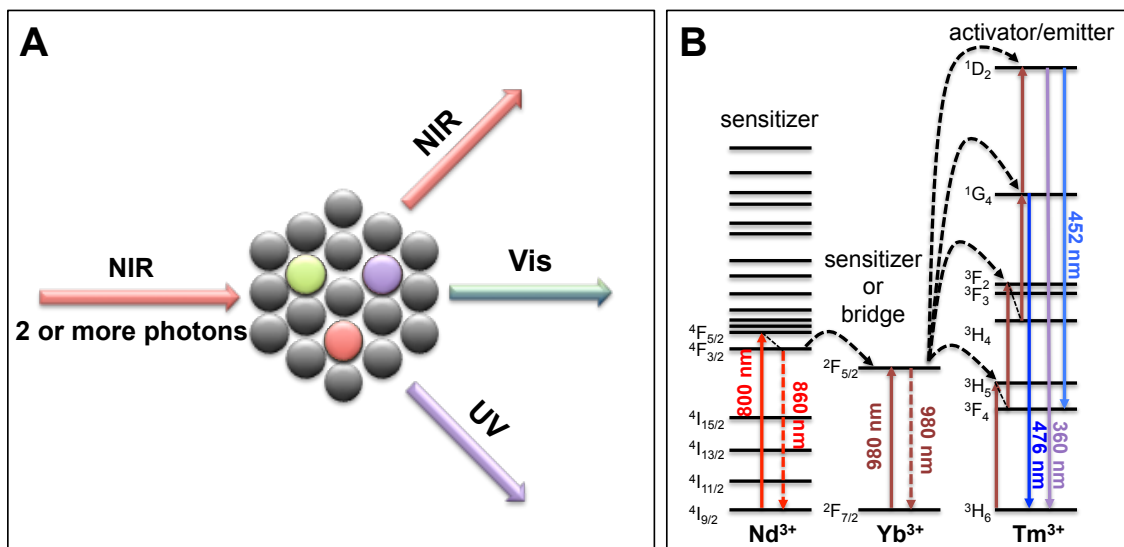
Several strategies exist to date in order to increase the absorption wavelengths of metal-based PACT candidates, such as changing the metal ion, extending aromatic ligand conjugation, conjugation to organic dyes or quantum dots and the use of upconverting nanoparticles.^[42a,65-66,86]

1.6.1 Upconverting Nanoparticles

Upconverting nanoparticles (UCNPs) have received a vast amount of attention in recent years, which exhibit a unique type emission; anti-Stokes upconversion, capable of translating near-infrared light into UV/visible emission.^[87]

UCNPs are rare earth doped nanomaterials consisting of a host lattice (e.g. NaYF₄, CaF₂, LiYF₄) doped with sensitizers and activators/emitters (lanthanides), which exhibit Stokes type downconversion and anti-Stokes type upconversion (Scheme 1.1). Photon excitation into a lanthanide (sensitizer) such as ytterbium (980 nm) and two or more subsequent Förster resonance

energy transfers (FRET) to other dopants, such as thulium (activator/emitter), allow for multiple excitations and thus multiple emission wavelengths depending on the dopants (Scheme 1.1B). Initial UCNP reports mainly consisted of ytterbium sensitizers. However, the biomedical downside of 980 nm irradiation is the strong absorption of water. Resulting thermal damage and reduced penetration depth transpired the introduction of neodymium ions into UCNPs, allowing for 800 nm excitation at which there is low absorption for both water and biomolecules.^[85,88]



Scheme 1.1. Graphical representation (A) and schematic (B) of the excitation of an UCNP by near-infrared light (800 nm or 980 nm) by two or more photons resulting in downconversion and upconversion. A) grey = host lattice, coloured = sensitizer, bridge or activator/emitter. NIR = near-infrared light, Vis = visible light, UV = UVA/B light. B) Neodymium acts as a sensitizer, ytterbium acts as a sensitizer or subsequent bridge for neodymium to an activator such as thulium. Transition energies are obtained from Shen et al. and Mahalingam et al.^[85,89]

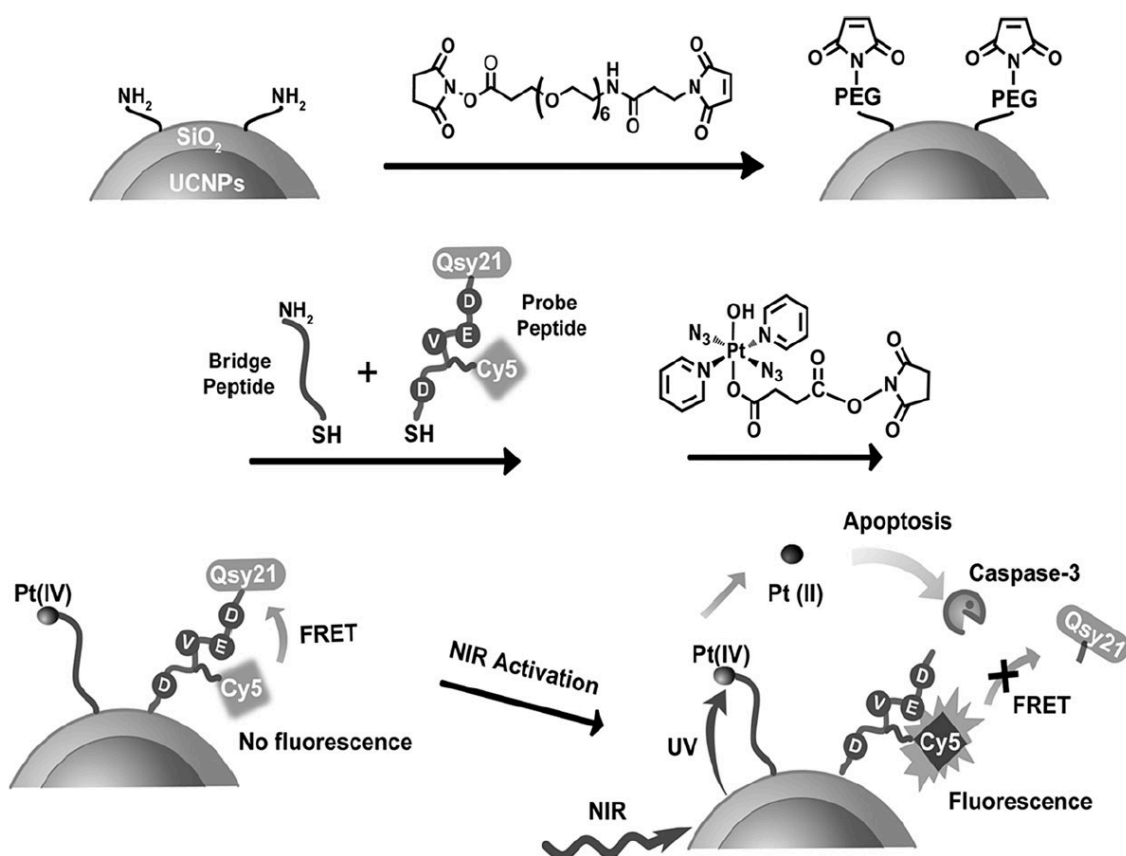
A variety of strategies exist to functionalise the surface of UCNPs, to render them water-dispersible whilst simultaneously having functional groups, such as carboxyl or amide groups, to allow covalent binding of pharmacokinetic modifiers, drugs, radionuclides, fluorescent tags, etc.^[90]

The first reports on photoactivation of metal-based PACT complexes by UCNPs were published between November – December 2013.^[52a,91]

Salassa et al. reported on the photolysis of $[\text{Ru}(\text{bpy})_2(\text{py})_2]\text{Cl}_2$ (bpy = 2,2'-bipyridine, py = pyridine) in aqueous solution by 980 nm irradiation of oleate-capped $\text{NaYF}_4:\text{Yb}^{3+}/\text{Er}^{3+}$ (20/2 mol%) UCNPs with an average size of ~80 nm.^[91a] The photolysis was monitored by UV-Vis and NMR spectroscopy and it

was suggested that covalent binding to the UCNPs surface would likely enhance the photolysis rate due to more efficient non-radiative energy transfer.

Xing et al. were the first to report on the covalent binding of an axial derivative of **1**, *trans,trans,trans*-[Pt(N₃)₂(OH)(O₂CCH₂CH₂CO₂H)(py)₂] to silica-coated NaYF₄: Yb³⁺/Tm³⁺ (30/0.5 mol%) UCNPs (~35 nm) with amino terminal groups.^[52a] The UCNPs were further functionalised with a targeting peptide (polyethylene glycol derivative) with a flanking activatable FRET pair for specific recognition of apoptosis, consisting of a fluorescence donor Cy5 and a near-infrared quencher Qsy21 cleavable by caspase-3 enzymes (Scheme 1.2).



Scheme 1.2. Graphical representation of near-infrared (NIR) light activation of a diazido Pt(IV) prodrug by UCNPs and subsequent intracellular apoptosis imaging. Reprinted with permission from Xing et al.^[52a] Copyright 2013 WILEY-VCH Verlag GmbH & Co. KGaA, Weinheim.

In vitro studies of the UCNPs (10 μM) in A2780 and A2780cis ovarian cancer cells revealed the significant reduction in viability upon one hour of 980 nm (1.5 W cm⁻²) irradiation, followed by 24 h incubation. The UCNPs exhibited equal toxicity to cisplatin in A2780 cells. However, significantly more potency was observed in A2780cis cells compared to both cisplatin and the free Pt(IV)

complex. Important to note is that 25% of the Pt(IV) complex is cleaved from the UCNPs after five hours of NIR irradiation. Promising tumour activity was observed by irradiating treated cells for only one hour. Therefore, increased photo-release efficiency might substantially increase the potency of the UCNPs. Furthermore, live cell apoptosis imaging fluorescent studies by confocal laser scanning microscopy (Cy5, DAPI and Annexin V dyes), provided proof of concept with regards to real time imaging of photoactivated cytotoxicity arising from triggered apoptosis during localised drug release. Direct introduction of caspase-3 or near-infrared irradiation of the functionalised UCNPs in cells greatly enhanced the Cy5 fluorescence.

Lastly, Lin et al. reported on the covalent bound diazido Pt(IV) complex, *trans,trans,trans*-[Pt(N₃)₂(O₂CCH₂CH₂CO₂H)₂(NH₃)(py)] (py = pyridine), to polyethylenimine coated UCNPs (NaYF₄:Yb³⁺/Tm³⁺ (40/0.5 mol%) @ NaGdF₄:Yb³⁺ (2 mol%), average size of ~65 nm).^[91b] The second carboxyl terminus of the Pt(IV) complex was coupled to polyethylene glycol. The incorporation of both a metal-based PACT complex and gadolinium ions into the UCNPs allowed for upconversion luminescence, magnetic resonance, computed tomography (trimodal) imaging and near-infrared activated platinum delivery.

In vitro studies in HeLa cervical cancer cells showed significant inhibition upon exposure to the UCNPs and 980 nm (2.5 W cm⁻²). Furthermore, significantly higher uptake of platinum was found after six hours of dark incubation when exposed to UCNPs compared to free complex. Tumour suppression in an *in vivo* model by intra-tumoural injection of the UCNPs exhibited more efficacy under 980 nm irradiation than 365 nm (UV) irradiation, despite the lower intensity of upconverted UV emission compared to the UV irradiation.

Progress in the subsequent years after have led to a few other reports of metal-based PACT complexes bound to UCNPs.^[86a,92] However, the majority of work in the field of biomedical application of UCNPs has been focused on the optimisation of quantum yield and most importantly in terms of size, shape and coating in effort to prevent accumulation in the liver or spleen whilst allowing for renal excretion, which has been hampering the effectiveness of nanoparticles *in vivo*.^[87c,93]

1.7 Research Objectives

The main objective of the work in this thesis is to provide new insight into the mechanism of action of photoactivatable platinum anticancer prodrug candidates, along with the development of new vibrational spectroscopic strategies to approach this goal and exploration of an UCNP platform to extend the excitation wavelength of such complexes. Specifically, the aims are as follows:

1. Explore the vibrational fingerprint of the photoactivatable Pt(IV) prodrug candidate, *trans,trans,trans*-[Pt(N₃)₂(OH)₂(py)₂] (**1**, py = pyridine), with a series of vibrational spectroscopic techniques as the essential first step towards monitoring the photoactivation pathways.
2. Translate the vibrational signatures to support photodecomposition and photoinduced binding studies of **1** and subsequently apply these methods to other metal-based PACT candidates.
3. Methodological plus instrumental development and utilisation of synchrotron based infrared techniques to study metal-based PACT candidates, outlined by **1**, in an effort trying to overcome the limitations of bench-top infrared equipment.
4. Synthesis and optimisation of UCNPs as a platform for addressing the wavelength activation of PACT candidates to a clinically-relevant window.

1.8 References

- [1] B. Vogelstein, K. W. Kinzler, *Nat Med* **2004**, *10*, 789-799.
- [2] a) R. L. K. Virchow, *Cellular pathology as based upon physiological and pathological histology*, J. B. Lippincott & Co, Philadelphia, **1863**; b) V. T. DeVita, S. A. Rosenberg, *New Engl. J. Med.* **2012**, *366*, 2207-2214.
- [3] S. I. Ferlay J, Ervik M, Dikshit R, Eser S, Mathers C, Rebelo M, Parkin DM, Forman D, Bray, F., GLOBOCAN 2012 v1.0, Cancer Incidence and Mortality Worldwide: IARC CancerBase No. 11 [Internet]. Lyon, France: International Agency for Research on Cancer; 2013. Available from: <http://globocan.iarc.fr>, accessed on 30 September 2017.
- [4] International, Human, Genome, Sequencing, Consortium, *Nature* **2004**, *431*, 931-945.
- [5] T. S. Lawrence, S. A. Rosenberg, I. Ovid Technologies, *Devita, Hellman, and Rosenberg's cancer principles & practice of oncology*, 10th ed., Philadelphia: Wolters Kluwer, Philadelphia, **2015**.
- [6] P. A. Futreal, L. Coin, M. Marshall, T. Down, T. Hubbard, R. Wooster, N. Rahman, M. R. Stratton, *Nat. Rev. Cancer* **2004**, *4*, 177-183.
- [7] a) Wellcome Trust Sanger Institute Cancer Genome Project, Cancer Gene Census. <http://cancer.sanger.ac.uk/census/> (28 September 2017), **2017**; b) Wellcome Trust Sanger Institute Cancer Genome Project, Catalogue Of Somatic Mutations In Cancer. <http://cancer.sanger.ac.uk/cosmic/> (28 September 2017), **2017**.
- [8] a) D. Hanahan, Robert A. Weinberg, *Cell* **2011**, *144*, 646-674; b) W. A. Flavahan, E. Gaskell, B. E. Bernstein, *Science* **2017**, *357*.
- [9] D. Hanahan, R. A. Weinberg, *Cell* **2000**, *100*, 57-70.
- [10] a) A. Strasser, S. Cory, J. M. Adams, *EMBO J.* **2011**, *30*, 3667-3683; b) S. W. Lowe, E. Cepero, G. Evan, *Nature* **2004**, *432*, 307-315; c) G. Evan, T. Littlewood, *Science* **1998**, *281*, 1317-1322; d) J. M. Adams, S. Cory, *Oncogene* **2007**, *26*, 1324-1337.
- [11] a) S. Weinhouse, O. Warburg, D. Burk, A. L. Schade, *Science* **1956**, *124*, 267; b) O. Warburg, *Science* **1956**, *123*, 309; c) O. Warburg, *British Journal of Surgery* **1931**, *19*, 168-168; d) G. L. Semenza, *J. Clin. Invest.* **2008**, *118*, 3835-3837; e) E. C. Nakajima, B. Van Houten, *Mol. Carcinog.*

- 2013**, 52, 329-337; f) K. M. Kennedy, M. W. Dewhirst, *Future Oncol* **2010**, 6, 127; g) O. Feron, *Radiother Oncol* **2009**, 92, 329-333.
- [12] a) L. Thomas, *The Yale journal of biology and medicine* **1982**, 55, 329-333; b) F. M. Burnet, *Progress in experimental tumor research* **1970**, 13, 1-27.
- [13] a) D. S. Vinay, E. P. Ryan, G. Pawelec, W. H. Talib, J. Stagg, E. Elkord, T. Lichtor, W. K. Decker, R. L. Whelan, H. M. C. S. Kumara, E. Signori, K. Honoki, A. G. Georgakilas, A. Amin, W. G. Helferich, C. S. Boosani, G. Guha, M. R. Ciriolo, S. Chen, S. I. Mohammed, A. S. Azmi, W. N. Keith, A. Bilsland, D. Bhakta, D. Halicka, H. Fujii, K. Aquilano, S. S. Ashraf, S. Nowsheen, X. Yang, B. K. Choi, B. S. Kwon, *Semin. Cancer Biol.* **2015**, 35, S185-S198; b) S. L. Topalian, J. M. Taube, R. A. Anders, D. M. Pardoll, *Nat. Rev. Cancer* **2016**, 16, 275-287; c) J. C. Becker, M. H. Andersen, D. Schrama, P. thor Straten, *Cancer Immunol., Immunother.* **2013**, 62, 1137-1148.
- [14] a) B. Z. Qian, J. W. Pollard, *Cell* **2010**, 141, 39-51; b) A. E. Karnoub, R. A. Weinberg, *Breast disease* **2006**, 26, 75-85; c) D. Hanahan, Lisa M. Coussens, *Cancer Cell* **2012**, 21, 309-322; d) S. I. Grivennikov, F. R. Greten, M. Karin, *Cell* **2010**, 140, 883-899; e) D. G. DeNardo, P. Andreu, L. M. Coussens, *Cancer Metastasis Rev.* **2010**, 29, 309-316.
- [15] B. A. Chabner, T. G. Roberts, *Nat. Rev. Cancer* **2005**, 5, 65-72.
- [16] E. Chu, V. T. DeVita, Jr., *Physicians' Cancer Chemotherapy Drug Manual 2017*, 17th ed., Jones & Bartlett Learning, **2016**.
- [17] a) B. Rosenberg, L. Vancamp, T. Krigas, *Nature* **1965**, 205, 698-699; b) B. Rosenberg, L. Vancamp, J. E. Trosko, V. H. Mansour, *Nature* **1969**, 222, 385-386.
- [18] a) L. Ronconi, P. J. Sadler, *Chem. Commun.* **2008**, 235-237; b) P. J. Dyson, G. Sava, *Dalton Trans.* **2006**, 1929-1933.
- [19] J. C. Dabrowiak, in *Metals in Medicine*, John Wiley & Sons, Ltd, **2009**, pp. 73-107.
- [20] B. Rosenberg, *Platinum Metals Rev.* **1971**, 15, 42-51.
- [21] a) U. Ndagi, N. Mhlongo, M. E. Soliman, *Drug Design, Development and Therapy* **2017**, 11, 599-616; b) T. C. Johnstone, K. Suntharalingam, S. J. Lippard, *Chem. Rev.* **2016**, 36, 1249-1262.

- [22] a) C. A. Rabik, M. E. Dolan, *Cancer Treat. Rev.* **2007**, *33*, 9-23; b) D. Wang, S. J. Lippard, *Nat. Rev. Drug Discov.* **2005**, *4*, 307-320.
- [23] a) H. J. van den Bongard, R. A. Mathot, J. H. Beijnen, J. H. Schellens, *Clin Pharmacokinet* **2000**, *39*, 345-367; b) J. Reedijk, *Chem. Rev.* **1999**, *99*, 2499-2510; c) J. Reedijk, *Chem. Commun.* **1996**, 801-806; d) J. Ma, J. Verweij, H. J. Kolker, H. E. van Ingen, G. Stoter, J. H. Schellens, *Br. J. Cancer* **1994**, *69*, 858-862; e) E. R. Jamieson, S. J. Lippard, *Chem Rev* **1999**, *99*, 2467-2498; f) T. W. Hambley, *J. Chem. Soc., Dalton Trans.* **2001**, 2711-2718; g) N. P. Farrell, *Semin. Oncol.* **2004**, *31*, 1-9; h) T. Boulikas, M. Vougiouka, *Oncol Rep* **2004**, *11*, 559-595; i) K. R. Barnes, S. J. Lippard, *Met. Ions Biol. Syst.* **2004**, *42*, 143-177; j) R. A. Alderden, M. D. Hall, T. W. Hambley, *J. Chem. Educ.* **2006**, *83*, 728; k) Z. Guo, P. J. Sadler, in *Advances in Inorganic Chemistry, Vol. 49* (Ed.: A. G. Sykes), Academic Press, **1999**, pp. 183-306; l) A. Eastman, in *Cisplatin*, Verlag Helvetica Chimica Acta, **2006**, pp. 111-134; m) B. Rosenberg, B. Lippert, *Cisplatin: Chemistry and Biochemistry of a Leading Anticancer Drug*, **1999**.
- [24] a) M. D. Hall, M. Okabe, D. W. Shen, X. J. Liang, M. M. Gottesman, *Annu. Rev. Pharmacol. Toxicol.* **2008**, *48*, 495-535; b) S. P. Binks, M. Dobrota, *Biochem. Pharmacol.* **1990**, *40*, 1329-1336; c) F. Arnesano, G. Natile, *Coord. Chem. Rev.* **2009**, *253*, 2070-2081; d) T. C. Johnstone, J. J. Wilson, S. J. Lippard, *Inorg. Chem.* **2013**, *52*, 12234-12249.
- [25] T. C. Johnstone, K. Suntharalingam, S. J. Lippard, *Phil. Trans. R. Soc. A* **2015**, 373.
- [26] A. Vaisman, S. E. Lim, S. M. Patrick, W. C. Copeland, D. C. Hinkle, J. J. Turchi, S. G. Chaney, *Biochemistry* **1999**, *38*, 11026-11039.
- [27] a) B. P. Espósito, R. Najjar, *Coord. Chem. Rev.* **2002**, *232*, 137-149; b) A. I. Ivanov, J. Christodoulou, J. A. Parkinson, K. J. Barnham, A. Tucker, J. Woodrow, P. J. Sadler, *J. Biol. Chem.* **1998**, *273*, 14721-14730.
- [28] F. Arnesano, M. Losacco, G. Natile, *Eur. J. Inorg. Chem.* **2013**, *2013*, 2701-2711.
- [29] Z. H. Siddik, *Oncogene* **2003**, *22*, 7265-7279.
- [30] a) A. Casini, J. Reedijk, *Chem. Sci.* **2012**, *3*, 3135-3144; b) G. Palermo, A. Magistrato, T. Riedel, T. von Erlach, C. A. Davey, P. J. Dyson, U. Rothlisberger, *ChemMedChem* **2016**, *11*, 1199-1210.

- [31] J. Reedijk, *Platinum Metals Rev.* **2008**, *52*, 2-11.
- [32] a) X. Wang, X. Wang, Z. Guo, *Acc. Chem. Res.* **2015**, *48*, 2622-2631; b) I. Romero-Canelón, P. J. Sadler, *Inorg. Chem.* **2013**, *52*, 12276-12291; c) P. a. Ma, H. Xiao, C. Li, Y. Dai, Z. Cheng, Z. Hou, J. Lin, *Mater. Today* **2015**, *18*, 554-564.
- [33] a) N. J. Farrer, L. Salassa, P. J. Sadler, *Dalton Trans.* **2009**, 10690-10701; b) P. J. Bednarski, F. S. Mackay, P. J. Sadler, *Anti-Cancer Agents Med. Chem.* **2007**, *7*, 75-93.
- [34] D. E. J. G. J. Dolmans, D. Fukumura, R. K. Jain, *Nat. Rev. Cancer* **2003**, *3*, 380-387.
- [35] T. Hasan, B. Ortel, A. Moor, B. Pogue, **2003**.
- [36] A. L. Harris, *Nat. Rev. Cancer* **2002**, *2*, 38-47.
- [37] a) A. Kastl, S. Dieckmann, K. Wähler, T. Völker, L. Kastl, A. L. Merkel, A. Vultur, B. Shannan, K. Harms, M. Ocker, W. J. Parak, M. Herlyn, E. Meggers, *ChemMedChem* **2013**, *8*, 924-927; b) V. Venkatesh, C. J. Wedge, I. Romero-Canelon, A. Habtemariam, P. J. Sadler, *Dalton Trans.* **2016**, *45*, 13034-13037; c) E. L. Menon, R. Perera, M. Navarro, R. J. Kuhn, H. Morrison, *Inorg. Chem.* **2004**, *43*, 5373-5381; d) N. A. Kratochwil, P. J. Bednarski, H. Mrozek, A. Vogler, J. K. Nagle, *Anticancer Drug Des* **1996**, *11*, 155-171; e) H. Brunner, H. Obermeier, *Angew. Chem. Int. Ed.* **1994**, *33*, 2214-2215; f) S. Banerjee, I. Pant, I. Khan, P. Prasad, A. Hussain, P. Kondaiah, A. R. Chakravarty, *Dalton Trans.* **2015**, *44*, 4108-4122; g) J. S. Ward, J. M. Lynam, J. W. Moir, D. E. Sanin, A. P. Mountford, I. J. Fairlamb, *Dalton Trans.* **2012**, *41*, 10514-10517; h) J. S. Ward, J. T. W. Bray, B. J. Aucott, C. Wagner, N. E. Pridmore, A. C. Whitwood, J. W. B. Moir, J. M. Lynam, I. J. S. Fairlamb, *Eur. J. Inorg. Chem.* **2016**, *2016*, 5044-5051; i) C. C. Romao, W. A. Blattler, J. D. Seixas, G. J. Bernardes, *Chem. Soc. Rev.* **2012**, *41*, 3571-3583; j) J. Marhenke, K. Trevino, C. Works, *Coord. Chem. Rev.* **2016**, *306*, Part 2, 533-543; k) E. Kottelat, Z. Fabio, *Inorganics* **2017**, *5*, 24; l) S. H. Heinemann, T. Hoshi, M. Westerhausen, A. Schiller, *Chem. Commun. (Camb.)* **2014**, *50*, 3644-3660; m) I. Chakraborty, S. J. Carrington, P. K. Mascharak, *Acc. Chem. Res.* **2014**, *47*, 2603-2611; n) Y. Zhao, J. A. Woods, N. J. Farrer, K. S. Robinson, J. Pracharova, J. Kasparkova, O. Novakova, H. Li, L. Salassa, A. M. Pizarro, G. J. Clarkson, L. Song, V.

Brabec, P. J. Sadler, *Chem. Eur. J.* **2013**, *19*, 9578-9591; o) Y. Zhao, G. M. Roberts, S. E. Greenough, N. J. Farrer, M. J. Paterson, W. H. Powell, V. G. Stavros, P. J. Sadler, *Angew. Chem. Int. Ed.* **2012**, *51*, 11263-11266; p) Y. Zhao, N. J. Farrer, H. Li, J. S. Butler, R. J. McQuitty, A. Habtemariam, F. Wang, P. J. Sadler, *Angew. Chem. Int. Ed.* **2013**, *52*, 13633-13637; q) L. A. Wickramasinghe, P. R. Sharp, *Inorg. Chem.* **2014**, *53*, 1430-1442; r) E. Shaili, M. Fernández-Giménez, S. Rodríguez-Astor, A. Gandioso, L. Sandín, C. García-Vélez, A. Massaguer, G. J. Clarkson, J. A. Woods, P. J. Sadler, V. Marchán, *Chem. Eur. J.* **2015**, *21*, 18474-18486; s) F. S. Mackay, J. A. Woods, P. Heringova, J. Kasparkova, A. M. Pizarro, S. A. Moggach, S. Parsons, V. Brabec, P. J. Sadler, *Proc. Natl. Acad. Sci. U. S. A.* **2007**, *104*, 20743-20748; t) F. S. Mackay, N. J. Farrer, L. Salassa, H.-C. Tai, R. J. Deeth, S. A. Moggach, P. A. Wood, S. Parsons, P. J. Sadler, *Dalton Trans.* **2009**, 2315-2325; u) A. Gandioso, E. Shaili, A. Massaguer, G. Artigas, A. Gonzalez-Canto, J. A. Woods, P. J. Sadler, V. Marchan, *Chem. Commun.* **2015**, *51*, 9169-9172; v) N. J. Farrer, J. A. Woods, L. Salassa, Y. Zhao, K. S. Robinson, G. Clarkson, F. S. Mackay, P. J. Sadler, *Angew. Chem. Int. Ed.* **2010**, *49*, 8905-8908; w) L. Cubo, A. M. Pizarro, A. G. Quiroga, L. Salassa, C. Navarro-Ranninger, P. J. Sadler, *J. Inorg. Biochem.* **2010**, *104*, 909-918; x) C. F. Chin, Q. Tian, M. I. Setyawati, W. Fang, E. S. Q. Tan, D. T. Leong, W. H. Ang, *J. Med. Chem.* **2012**, *55*, 7571-7582; y) J. S. Butler, J. A. Woods, N. J. Farrer, M. E. Newton, P. J. Sadler, *J. Am. Chem. Soc.* **2012**, *134*, 16508-16511; z) E. Wachter, D. K. Heidary, B. S. Howerton, S. Parkin, E. C. Glazer, *Chem. Commun.* **2012**, *48*, 9649-9651; aa) V. H. S. van Rixel, B. Siewert, S. L. Hopkins, S. H. C. Askes, A. Busemann, M. A. Siegler, S. Bonnet, *Chem. Sci.* **2016**, *7*, 4922-4929; ab) T. N. Singh, C. Turro, *Inorg. Chem.* **2004**, *43*, 7260-7262; ac) M. A. Sgambellone, A. David, R. N. Garner, K. R. Dunbar, C. Turro, *J. Am. Chem. Soc.* **2013**, *135*, 11274-11282; ad) B. S. Howerton, D. K. Heidary, E. C. Glazer, *J. Am. Chem. Soc.* **2012**, *134*, 8324-8327; ae) R. E. Goldbach, I. Rodriguez-Garcia, J. H. van Lenthe, M. A. Siegler, S. Bonnet, *Chem. Eur. J.* **2011**, *17*, 9924-9929; af) S. Betanzos-Lara, L. Salassa, A. Habtemariam, O. Novakova, A. M. Pizarro, G. J. Clarkson, B. Liskova, V. Brabec, P. J. Sadler, *Organometallics* **2012**, *31*, 3466-3479; ag) A. Bahreman, B. Limburg, M.

- A. Siegler, E. Bouwman, S. Bonnet, *Inorg. Chem.* **2013**, *52*, 9456-9469; ah) U. Schatzschneider, *Eur. J. Inorg. Chem.* **2010**, *2010*, 1451-1467; ai) J. D. Knoll, C. Turro, *Coord. Chem. Rev.* **2015**, *282-283*, 110-126; aj) Y. Sun, L. E. Joyce, N. M. Dickson, C. Turro, *Chem. Commun.* **2010**, *46*, 6759-6761.
- [38] A. Bahreman, J.-A. Cuello-Garibo, S. Bonnet, *Dalton Trans.* **2014**, *43*, 4494-4505.
- [39] I. Chakraborty, S. J. Carrington, P. K. Mascharak, *ChemMedChem* **2014**, *9*, 1266-1274.
- [40] a) F. Zobi, *Future Med Chem* **2013**, *5*, 175-188; b) U. Schatzschneider, *Br. J. Pharmacol.* **2015**, *172*, 1638-1650; c) S. Garcia-Gallego, G. J. Bernardes, *Angew. Chem. Int. Ed.* **2014**, *53*, 9712-9721.
- [41] a) N. A. Kratochwil, M. Zabel, K.-J. Range, P. J. Bednarski, *J. Med. Chem.* **1996**, *39*, 2499-2507; b) M. Kubeil, R. R. Vernooij, C. Kubeil, B. R. Wood, B. Graham, H. Stephan, L. Spiccia, *Inorg. Chem.* **2017**, *56*, 5941-5952.
- [42] a) S. Bonnet, *Comments Inorg. Chem.* **2014**, *1-35*; b) C. Mari, V. Pierroz, S. Ferrari, G. Gasser, *Chem. Sci.* **2015**, *6*, 2660-2686; c) J. K. White, R. H. Schmehl, C. Turro, *Inorg. Chim. Acta* **2017**, *454*, 7-20; d) E. C. Glazer, *Isr. J. Chem.* **2013**, *53*, 391-400; e) M. Fanelli, M. Formica, V. Fusi, L. Giorgi, M. Micheloni, P. Paoli, *Coord. Chem. Rev.* **2016**, *310*, 41-79; f) K. Mitra, *Dalton Trans.* **2016**, *45*, 19157-19171.
- [43] a) G. Stochel, M. Brindell, W. Macyk, Z. Stasicka, K. Szaciłowski, in *Bioinorganic Photochemistry*, John Wiley & Sons, Ltd, **2009**, pp. 19-23; b) V. Balzani, G. Bergamini, S. Campagna, F. Puntoriero, in *Photochemistry and Photophysics of Coordination Compounds I* (Eds.: V. Balzani, S. Campagna), Springer Berlin Heidelberg, Berlin, Heidelberg, **2007**, pp. 1-36.
- [44] a) C. Latouche, D. Skouteris, F. Palazzetti, V. Barone, *J. Chem. Theory Comput.* **2015**, *11*, 3281-3289; b) C. Garino, A. Terenzi, G. Barone, L. Salassa, *J. Chem. Educ.* **2016**, *93*, 292-298; c) C. Adamo, D. Jacquemin, *Chem. Soc. Rev.* **2013**, *42*, 845-856; d) W. J. Hehre, L. Radom, P. v. R. Schleyer, J. A. Pople, *Ab initio molecular orbital theory*, New York : Wiley, New York, **1986**; e) P. S. Wagenknecht, P. C. Ford, *Coord. Chem. Rev.* **2011**, *255*, 591-616.

- [45] F. R. Hartley, *The chemistry of platinum and palladium: with particular reference to complexes of the elements*, Applied Science Publishers, London, **1973**.
- [46] a) E. Wexselblatt, D. Gibson, *J. Inorg. Biochem.* **2012**, *117*, 220-229; b) D. Gibson, *Dalton Trans.* **2016**, *45*, 12983-12991.
- [47] N. A. Kratochwil, P. J. Bednarski, *Arch. Pharm.* **1999**, *332*, 279-285.
- [48] A. Vogler, A. Kern, J. Hüttermann, *Angew. Chem. Int. Ed.* **1978**, *17*, 524-525.
- [49] a) F. S. Mackay, J. A. Woods, H. Moseley, J. Ferguson, A. Dawson, S. Parsons, P. J. Sadler, *Chem. Eur. J.* **2006**, *12*, 3155-3161; b) P. J. Bednarski, R. Grunert, M. Zielzki, A. Wellner, F. S. Mackay, P. J. Sadler, *Chem. Biol.* **2006**, *13*, 61-67.
- [50] S. Chang, S. H. Lamm, *Int. J. Toxicol.* **2003**, *22*, 175-186.
- [51] a) L. Ronconi, P. J. Sadler, *Dalton Trans.* **2011**, *40*, 262-268; b) L. Salassa, H. I. A. Phillips, P. J. Sadler, *PCCP* **2009**, *11*, 10311-10316.
- [52] a) Y. Min, J. Li, F. Liu, E. K. L. Yeow, B. Xing, *Angew. Chem. Int. Ed.* **2013**; b) V. Venkatesh, N. K. Mishra, I. Romero-Canelón, R. R. Vernooij, H. Shi, J. P. C. Coverdale, A. Habtemariam, S. Verma, P. J. Sadler, *J. Am. Chem. Soc.* **2017**, *139*, 5656-5659.
- [53] J. P. C. Coverdale, PhD thesis, University of Warwick **2017**.
- [54] P. Müller, B. Schröder, J. A. Parkinson, N. A. Kratochwil, R. A. Coxall, A. Parkin, S. Parsons, P. J. Sadler, *Angew. Chem. Int. Ed.* **2003**, *42*, 335-339.
- [55] J. B. Patrick, S. M. Fiona, J. S. Peter, *Anti-Cancer Agents Med. Chem.* **2007**, *7*, 75-93.
- [56] N. J. Farrer, J. A. Woods, V. P. Munk, F. S. Mackay, P. J. Sadler, *Chem. Res. Toxicol.* **2010**, *23*, 413-421.
- [57] N. J. Farrer, P. Gierth, P. J. Sadler, *Chem. Eur. J.* **2011**, *17*, 12059-12066.
- [58] L. Ronconi, A. M. Pizarro, R. J. McQuitty, P. J. Sadler, *Chem. Eur. J.* **2011**, *17*, 12051-12058.
- [59] A. Y. Sokolov, H. F. Schaefer lii, *Dalton Trans.* **2011**, *40*, 7571-7582.
- [60] J. Pracharova, L. Zerzankova, J. Stepankova, O. Novakova, N. J. Farrer, P. J. Sadler, V. Brabec, J. Kasparkova, *Chem. Res. Toxicol.* **2012**, *25*, 1099-1111.

- [61] H.-C. Tai, R. Brodbeck, J. Kasparkova, N. J. Farrer, V. Brabec, P. J. Sadler, R. J. Deeth, *Inorg. Chem.* **2012**, *51*, 6830-6841.
- [62] H.-C. Tai, Y. Zhao, N. J. Farrer, A. E. Anastasi, G. Clarkson, P. J. Sadler, R. J. Deeth, *Chem. Eur. J.* **2012**, *18*, 10630-10642.
- [63] A. F. Westendorf, J. A. Woods, K. Korpis, N. J. Farrer, L. Salassa, K. Robinson, V. Appleyard, K. Murray, R. Grunert, A. M. Thompson, P. J. Sadler, P. J. Bednarski, *Mol. Cancer Ther.* **2012**, *11*, 1894-1904.
- [64] A. M. Pizarro, R. J. McQuitty, F. S. Mackay, Y. Zhao, J. A. Woods, P. J. Sadler, *ChemMedChem* **2014**, *9*, 1169-1175.
- [65] X.-D. Yang, H.-J. Xiang, L. An, S.-P. Yang, J.-G. Liu, *New J. Chem.* **2015**, *39*, 800-804.
- [66] Y. Cong, Z. Wang, S. He, D. Zhou, J. Li, Z. Xie, X. Chen, X. Jing, Y. Huang, *RSC Adv.* **2016**, *6*, 20366-20373.
- [67] R. R. Vernooij, T. Joshi, E. Shaili, M. Kubeil, D. R. T. Appadoo, E. I. Izgorodina, B. Graham, P. J. Sadler, B. R. Wood, L. Spiccia, *Inorg. Chem.* **2016**, *55*, 5983-5992.
- [68] A. A. Shushakov, I. P. Pozdnyakov, V. P. Grivin, V. F. Plyusnin, D. B. Vasilchenko, A. V. Zadesenets, A. A. Melnikov, S. V. Chekalin, E. M. Glebov, *Dalton Trans.* **2017**, *46*, 9440-9450.
- [69] D. E. Lyon, J. M. Walter, A. R. Starkweather, C. M. Schubert, N. L. McCain, *BMC Res Notes* **2011**, *4*, 156.
- [70] a) S. J. Berners-Price, L. Ronconi, P. J. Sadler, *Prog. Nucl. Magn. Reson. Spectrosc.* **2006**, *49*, 65-98; b) R. Weissleder, M. J. Pittet, *Nature* **2008**, *452*, 580-589; c) M. Schirle, M. Bantscheff, B. Kuster, *Chem. Biol.* **2012**, *19*, 72-84.
- [71] D. E. Pivonka, J. M. Chalmers, P. R. Griffiths, *Applications of Vibrational Spectroscopy in Pharmaceutical Research and Development*, John Wiley & Sons, Ltd, **2007**.
- [72] a) G. Bellisola, C. Sorio, *Am. J. Cancer Res.* **2012**, *2*, 1-21; b) M. J. Baker, J. Trevisan, P. Bassan, R. Bhargava, H. J. Butler, K. M. Dorling, P. R. Fielden, S. W. Fogarty, N. J. Fullwood, K. A. Heys, C. Hughes, P. Lasch, P. L. Martin-Hirsch, B. Obinaju, G. D. Sockalingum, J. Sulé-Suso, R. J. Strong, M. J. Walsh, B. R. Wood, P. Gardner, F. L. Martin, *Nat. Protocols* **2014**, *9*, 1771-1791.

- [73] a) K. Nakamoto, in *Infrared and Raman Spectra of Inorganic and Coordination Compounds*, John Wiley & Sons, Inc., **2008**, pp. 1-147; b) M. Diem, in *Modern Vibrational Spectroscopy and Micro-Spectroscopy*, John Wiley & Sons, Ltd, **2015**, pp. 1-38.
- [74] a) C. V. Raman, *Indian J. Phys.* **1928**, 2, 387-398; b) C. V. Raman, K. S. Krishnan, *Nature* **1928**, 121, 501-502.
- [75] a) L. A. Averett, P. R. Griffiths, K. Nishikida, *Anal. Chem.* **2008**, 80, 3045-3049; b) N. J. Harrick, *J. Opt. Soc. Am.* **1965**, 55, 851-857; c) N. J. Harrick, F. K. du Pre, *Appl. Opt.* **1966**, 5, 1739-1743.
- [76] J. M. Chalmers, in *Handbook of Vibrational Spectroscopy*, John Wiley & Sons, Ltd, **2006**, pp. 2327-2347.
- [77] a) K. Nakamoto, in *Infrared and Raman Spectra of Inorganic and Coordination Compounds*, John Wiley & Sons, Inc., **2008**, pp. 149-354; b) J. R. Ferraro, *Low-Frequency Vibrations of Inorganic and Coordination Compounds*, Springer US, Boston, MA, **1971**.
- [78] A. Marcelli, A. Cricenti, W. M. Kwiatek, C. Petibois, *Biotechnol. Adv.* **2012**, 30, 1390-1404.
- [79] A. Marcelli, G. Cinque, in *Biomedical Applications of Synchrotron Infrared Microspectroscopy: A Practical Approach*, The Royal Society of Chemistry, **2011**, pp. 67-104.
- [80] Bruker, Application Note AN M92 Vacuum FT-IR Beamline Installations at e-Synchrotrons. https://www.bruker.com/fileadmin/user_upload/8-PDF-Docs/OpticalSpectroscopy/FT-IR/IFS125/AN/AN_M92_Vacuum_FT-R_Beamline_Installation_EN.pdf (15/09/2017), **2016**.
- [81] C. Cappelli, M. Biczysko, in *Computational Strategies for Spectroscopy*, John Wiley & Sons, Inc., **2011**, pp. 309-360.
- [82] A. P. Scott, L. Radom, *J. Phys. Chem.* **1996**, 100, 16502-16513.
- [83] D. Steele, in *Encyclopedia of Spectroscopy and Spectrometry (Third Edition)* (Eds.: G. E. Tranter, D. W. Koppenaal), Academic Press, Oxford, **2017**, pp. 463-468.
- [84] a) V. Barone, M. Cossi, *J. Phys. Chem. A* **1998**, 102, 1995-2001; b) M. Cossi, N. Rega, G. Scalmani, V. Barone, *J. Comput. Chem.* **2003**, 24, 669-681; c) J. Tomasi, B. Mennucci, R. Cammi, *Chem. Rev.* **2005**, 105, 2999-3094.

- [85] J. Shen, G. Chen, A.-M. Vu, W. Fan, O. S. Bilsel, C.-C. Chang, G. Han, *Adv. Opt. Mater.* **2013**, *1*, 644-650.
- [86] a) S. Perfahl, M. M. Natile, H. S. Mohamad, C. A. Helm, C. Schulzke, G. Natile, P. J. Bednarski, *Mol. Pharm.* **2016**, *13*, 2346-2362; b) B. Teng, P. a. Ma, C. Yu, X. Zhang, Q. Feng, L. Wen, C. Li, Z. Cheng, D. Jin, J. Lin, *J. Mater. Chem. B* **2017**, *5*, 307-317.
- [87] a) Y. Yang, J. Mu, B. Xing, *Wiley Interdiscip. Rev.: Nanomed. Nanobiotechnol.* **2017**, *9*, 1-19; b) H. Huang, J. F. Lovell, *Adv. Funct. Mater.* **2017**, *27*, 1616-3028; c) K. Zarschler, L. Rocks, N. Licciardello, L. Boselli, E. Polo, K. P. Garcia, L. De Cola, H. Stephan, K. A. Dawson, *Nanomed. Nanotechnol. Biol. Med.* **2016**, *12*, 1663-1701; d) X. Chen, D. Peng, Q. Ju, F. Wang, *Chem. Soc. Rev.* **2015**, *44*, 1318-1330; e) M. k. g. Jayakumar, N. M. Idris, K. Huang, Y. Zhang, *Nanoscale* **2014**, *6*, 8441-8443; f) L. Cheng, C. Wang, L. Feng, K. Yang, Z. Liu, *Chem. Rev.* **2014**, *114*, 10869-10939; g) X. Li, F. Zhang, D. Zhao, *Nano Today* **2013**, *8*, 643-676; h) S. Gai, C. Li, P. Yang, J. Lin, *Chem. Rev.* **2013**, *114*, 2343-2389.
- [88] a) X. Xie, N. Gao, R. Deng, Q. Sun, Q.-H. Xu, X. Liu, *J. Am. Chem. Soc.* **2013**, *135*, 12608-12611; b) D. Wang, B. Xue, X. Kong, L. Tu, X. Liu, Y. Zhang, Y. Chang, Y. Luo, H. Zhao, H. Zhang, *Nanoscale* **2015**, *7*, 190-197; c) X. Li, R. Wang, F. Zhang, L. Zhou, D. Shen, C. Yao, D. Zhao, *Sci. Rep.* **2013**, *3*; d) Q. Ju, X. Chen, F. Ai, D. Peng, X. Lin, W. Kong, P. Shi, G. Zhu, F. Wang, *J. Mater. Chem. B* **2015**, *3*, 3548-3555; e) F. He, G. Yang, P. Yang, Y. Yu, R. Lv, C. Li, Y. Dai, S. Gai, J. Lin, *Adv. Funct. Mater.* **2015**, *25*, 3966-3976; f) B. del Rosal, U. Rocha, E. C. Ximendes, E. Martín Rodríguez, D. Jaque, J. G. Solé, *Opt. Mater.* **2017**, *63*, 185-196.
- [89] V. Mahalingam, F. Vetrone, R. Naccache, A. Speghini, J. A. Capobianco, *Adv. Mater.* **2009**, *21*, 4025-4028.
- [90] a) S. Wilhelm, M. Kaiser, C. Wurth, J. Heiland, C. Carrillo-Carrion, V. Muhr, O. S. Wolfbeis, W. J. Parak, U. Resch-Genger, T. Hirsch, *Nanoscale* **2015**, *7*, 1403-1410; b) S. P. Pujari, L. Scheres, A. T. M. Marcelis, H. Zuilhof, *Angew. Chem. Int. Ed.* **2014**, *53*, 6322-6356; c) Q. Liu, W. Feng, F. Li, *Coord. Chem. Rev.* **2014**, *273-274*, 100-110; d) W. Zhang, B. Peng, F. Tian, W. Qin, X. Qian, *Anal. Chem.* **2013**, *86*, 482-

- 489; e) C. Yuan, G. Chen, L. Li, J. A. Damasco, Z. Ning, H. Xing, T. Zhang, L. Sun, H. Zeng, A. N. Cartwright, P. N. Prasad, H. Ågren, *ACS Appl. Mater. Interfaces* **2014**, *6*, 18018-18025; f) X. Wu, Y. Zhang, K. Takle, O. Bilsel, Z. Li, H. Lee, Z. Zhang, D. Li, W. Fan, C. Duan, E. M. Chan, C. Lois, Y. Xiang, G. Han, *ACS Nano* **2016**, *10*, 1060–1066; g) T. Ma, Y. Ma, S. Liu, L. Zhang, T. Yang, H.-R. Yang, W. Lv, Q. Yu, W. Xu, Q. Zhao, W. Huang, *J. Mater. Chem. C* **2015**, *3*, 6616-6620
- [91] a) E. Ruggiero, A. Habtemariam, L. Yate, J. Mareque Rivas, L. Salassa, *Chem. Commun.* **2013**, *50*, 1715-1718 ; b) Y. Dai, H. Xiao, J. Liu, Q. Yuan, P. a. Ma, D. Yang, C. Li, Z. Cheng, Z. Hou, P. Yang, J. Lin, *J. Am. Chem. Soc.* **2013**, *135*, 18920–18929.
- [92] a) H. Shi, T. Fang, Y. Tian, H. Huang, Y. Liu, *J. Mater. Chem. B* **2016**, *4*, 4746-4753; b) X. Ge, L. Sun, B. Ma, D. Jin, L. Dong, L. Shi, N. Li, H. Chen, W. Huang, *Nanoscale* **2015**, *7*, 13877-13887.
- [93] a) C. T. Xu, Q. Zhan, H. Liu, G. Somesfalean, J. Qian, S. He, S. Andersson-Engels, *Laser Photon. Rev.* **2013**, *7*, 663-697; b) Y. Sun, W. Feng, P. Yang, C. Huang, F. Li, *Chem. Soc. Rev.* **2015**; c) L. Xiong, T. Yang, Y. Yang, C. Xu, F. Li, *Biomaterials* **2010**, *31*, 7078-7085; d) L. Cheng, K. Yang, M. Shao, X. Lu, Z. Liu, *Nanomedicine* **2011**, *6*, 1327-1340; e) Y. Gao, X. Zhu, Y. Zhang, X. Chen, L. Wang, W. Feng, C. Huang, F. Li, *RSC Adv.* **2017**, *7*, 31588-31596.

Chapter 2

Comprehensive Vibrational Spectroscopic Investigation of *trans,trans,trans*-[Pt(N₃)₂(OH)₂(py)₂], a Pt(IV) Diazido Anticancer Prodrug Candidate

The potential of metal-based photoactivatable anticancer complexes as chemotherapeutic agents by local activation in selected cancerous areas to address the severe side effects of current clinical drugs have been discussed in Chapter 1.3. The promising candidate, *trans,trans,trans*-[Pt(N₃)₂(OH)₂(py)₂] (**1**, py = pyridine) shows biological activity resulting from its unique photophysical and photochemical properties, suggesting a multi-targeted biological activity originating from cleaved ligands and the platinum centre upon photoactivation (Chapter 1.4). Monitoring the reactive metal centre as well as the azido and hydroxido ligands of **1** remains challenging and the initial strategy, covered in Chapter 2, involved the vibrational spectroscopic screening of **1**, towards utilisation of vibrational spectroscopy as a tool to study such metal-based anticancer prodrug candidates. Solid theoretical and experimental methods were established using Attenuated Total Reflection Fourier Transform Infrared (ATR-FTIR), Raman spectroscopy and synchrotron radiation far-infrared (SR-FIR) complemented by density functional theory calculations to capture the vibrational fingerprint of **1**. Chapter 2 includes of the main manuscript text (section 2.1), supporting information (section 2.2) and a link to the ACS LiveSlides recordings of this publication (section 2.3).

2.1 Main Manuscript

Comprehensive Vibrational Spectroscopic Investigation of
trans,trans,trans-[Pt(N₃)₂(OH)₂(py)₂], a Pt(IV) Diazido Anticancer Prodrug
Candidate

Robbin R. Vernooij, Tanmaya Joshi, Evyenia Shaili, Manja Kubeil,
Dominique R. T. Appadoo, Ekaterina I. Izgorodina, Bim Graham,
Peter J. Sadler, Bayden R. Wood and Leone Spiccia

Inorg. Chem. **2016**, *55*, 5983-5992

American Chemical Society

DOI: 10.1021/acs.inorgchem.6b00476

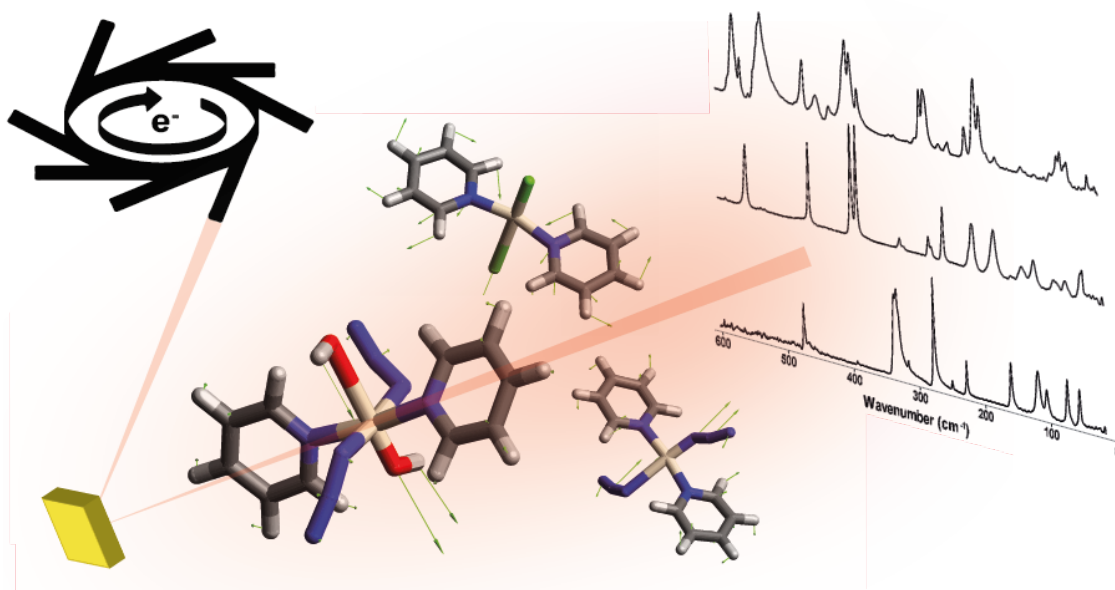


Figure 2.1 Table of contents graphic for the Comprehensive Vibrational Spectroscopic Investigation of *trans,trans,trans*-[Pt(N₃)₂(OH)₂(py)₂], a Pt(IV) Diazido Anticancer Prodrug Candidate.

Chapter 3

Photoinduced Studies of Metal-Based Anticancer Prodrug Candidates

A more detailed understanding of the underpinning mechanism of photoinduced reactions by photoactivatable drugs is an essential component in the development of future biologically active metal complexes. The vibrational spectroscopic acquisition techniques outlined in Chapter 2 were subsequently applied to study the photodecomposition and photoreaction of *trans,trans,trans*-[Pt(N₃)₂(OH)₂(py)₂] by Attenuated Total Reflection Fourier Transform Infrared (ATR-FTIR), transient electronic absorption and UV-Vis spectroscopy, complemented by theoretical calculations. Building on the same methodologies, a range of ruthenium-based CO-releasing complexes (Chapter 1.3.1) of the formula [RuLCl₂(CO)₂] (L = 4,4'-dimethyl-2,2'-bipyridine, 4'-methyl-2,2'-bipyridine-4-carboxylic acid or 2,2'-bipyridine-4,4'-dicarboxylic acid) were studied on account of the electron-withdrawing/donating properties of the carboxyl/methyl substituents attached to the bipyridine ligand. In both studies, the steady state and chemometric analysis of the resulting spectra allowed for extraction of mechanistic and quantitative kinetic information, revealing new insights into photochemical and photophysical properties of the photoactivatable prodrug candidates. Chapter 3 comprises of two manuscript texts and their corresponding supporting information. First the submitted manuscript; Spectroscopic Studies on Photoinduced Reactions of the Anticancer Prodrug, *trans,trans,trans*-[Pt(N₃)₂(OH)₂(py)₂] (section 3.1, 3.2 SI, 3.3 front cover, 3.4 cover profile), followed by the published manuscript; Studies of Carbon Monoxide Release from Ruthenium(II) Bipyridine Carbonyl Complexes upon UV-Light Exposure (section 3.5 and 3.6 SI).

3.1 Main Manuscript: Spectroscopic Studies on Photoinduced Reactions of the Anticancer Prodrug, *trans,trans,trans*-[Pt(N₃)₂(OH)₂(py)₂]

Spectroscopic Studies on Photoinduced Reactions of the Anticancer Prodrug, *trans,trans,trans*-[Pt(N₃)₂(OH)₂(py)₂]

Robbin R. Vernooij, Tanmaya Joshi, Michael D. Horbury, Bim Graham, Ekaterina I. Izgorodina, Vasilios G. Stavros, Peter J. Sadler, Leone Spiccia[†] and Bayden R. Wood

In memory of Leone Spiccia

Published online: 5 February 2018, awaiting issue assignment (front cover and cover profile)



Figure 3.1 Table of contents graphic for the Spectroscopic Studies on Photoinduced Reactions of the Anticancer Prodrug, *trans,trans,trans*-[Pt(N₃)₂(OH)₂(py)₂].

3.5 Main Manuscript: Studies of Carbon Monoxide Release from Ruthenium(II) Bipyridine Carbonyl Complexes upon UV-Light Exposure

Studies of Carbon Monoxide Release from Ruthenium(II) Bipyridine Carbonyl Complexes upon UV-Light Exposure

Manja Kubeil, Robbin R. Vernooij, Clemens Kubeil, Bayden R. Wood, Bim Graham, Holger Stephan, and Leone Spiccia

Inorg. Chem. **2017**, *56*, 5941-5952

American Chemical Society

DOI: 10.1021/acs.inorgchem.7b00599

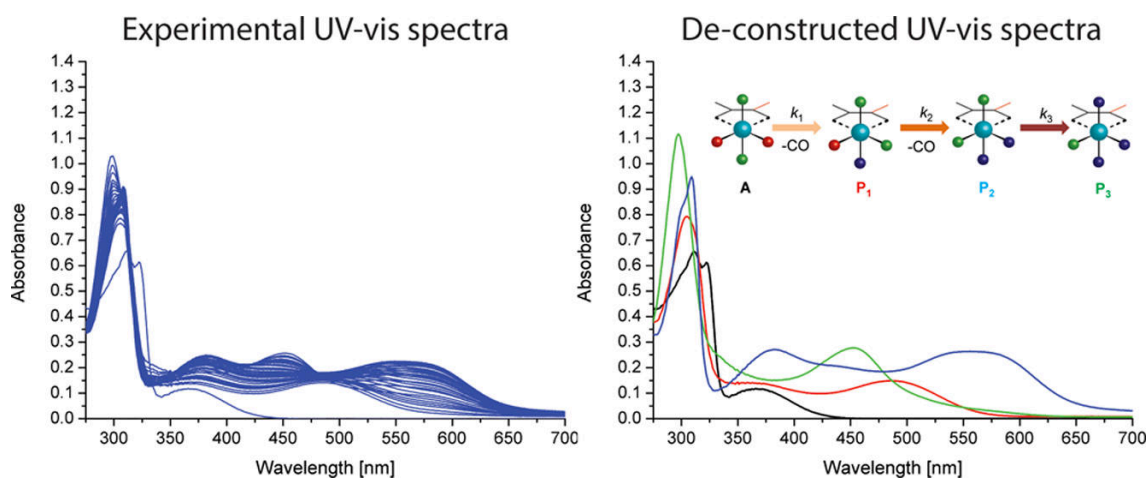


Figure 3.2 Table of contents graphic for Studies of Carbon Monoxide Release from Ruthenium(II) Bipyridine Carbonyl Complexes upon UV-Light Exposure.

Chapter 4

Synchrotron Infrared Beamline Studies

In this chapter, the use of synchrotron based infrared techniques to study metal-based anticancer complexes is discussed. At the heart of these studies is the photoactivatable anticancer prodrug candidate, *trans,trans,trans*-[Pt(N₃)₂(OH)₂(py)₂] (**1**, py = pyridine), which has been comprehensively characterised and studied using laboratory-based infrared spectrometers in Chapter 2 and Chapter 3.1-2. The use of state-of-the-art infrared equipment coupled to the high brilliance and collimation of synchrotron radiation has advanced our understanding of the photophysical and photochemical properties of this anticancer prodrug candidate and enabled the development of (new) synchrotron techniques. All the results presented in this chapter were obtained at the THz/Far-IR and the Infrared Microspectroscopy beamlines at the Australian Synchrotron in Melbourne, Australia. This chapter describes the infrared transmission and reflection studies undertaken on **1**, and consists of three parts: first, Synchrotron Radiation Far-Infrared (SR-FIR) transmission and Attenuated Total Reflection (ATR) studies to enable rapid screening of solid and evaporated liquid solutions of **1**, exposing the changes occurring to the metal to ligand vibrations upon irradiation (section 4.2.1, 4.3.1); second, SR-FIR transmission measurements of the prodrug in solution under *in situ* irradiation exposed the decrease in the ν Pt-OH and ν Pt-N₃ vibrations simultaneously (section 4.2.2, 4.3.2); the final part covers the mid-infrared single cell study of **1** on live acute myeloid leukaemia cells (K562) by Synchrotron Radiation Infrared Microspectroscopy (SR-IRMS). Significant changes to the DNA base stacking and lipid vibrations were observed four hours after a low dose of 350 nm irradiation (2.58 J cm⁻²), whereas this was not observed or to a lesser extent in the control cells (section 4.2.3, 4.3.3).

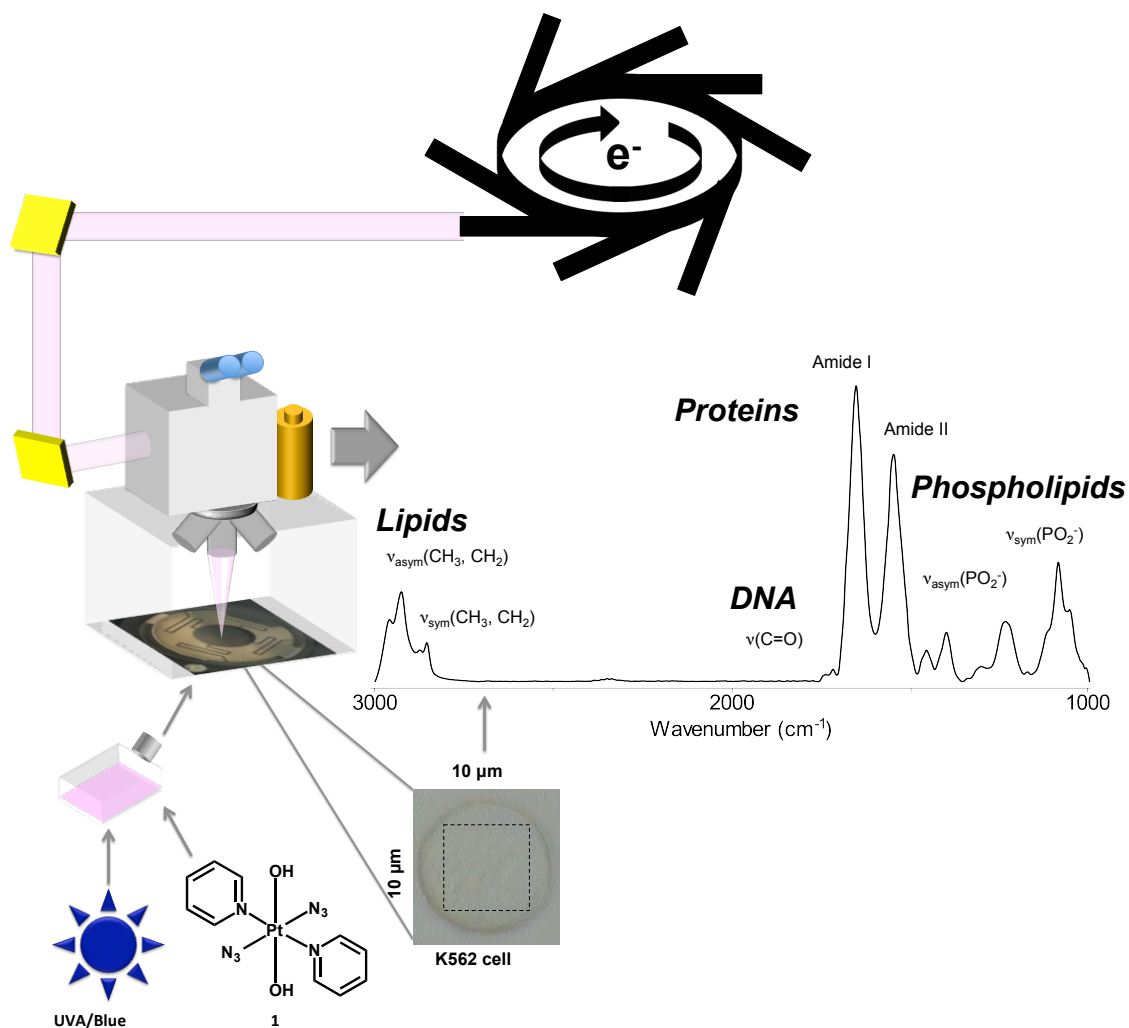


Figure 4.1. Graphical abstract for the mid-infrared single cell study of **1** on live acute myeloid leukaemia cells (K562) by synchrotron radiation infrared microspectroscopy.

4.1 Introduction

An introduction is provided below for the reader to familiarize themselves with the synchrotron based infrared techniques. The reader is kindly directed to Chapter 1.5.2 for a more detailed description of synchrotron light sources.

Chapter 3.1 and 3.2 covered the use of mid-infrared to study the mechanism of action of **1** by monitoring its chemical environment on its own and in presence of a DNA-base nucleotide. Herein, state-of-the-art infrared equipment coupled with the high brilliance and collimation of the synchrotron beam enable studies to be carried out with unprecedented signal-to-noise ratios and resolution throughout the far-infrared to mid-infrared spectral region.

4.1.1 Synchrotron Radiation Far-Infrared

The use and further development of SR-FIR techniques to study the photoactivatable metal-based anticancer complex **1**, studied throughout this thesis, is pursued in this chapter to revisit far-infrared spectroscopy as a tool to study the characteristics of inorganic complexes. These include ATR and transmission experiments to study **1** in its crystalline, solvated and dissolved state.

The usefulness of low-frequency spectra of inorganic and coordination compounds was already highlighted as early as the 1900's by Randall.^[1] The region below 650 cm^{-1} has vast amounts of metal to ligand vibrations and has been used throughout the years as a tool for structural analysis of such inorganic and coordination compounds. This, of course, is prior to the emergence of synchrotron radiation (SR) sources and Fourier transform interferometers as well as other analytical methods to carry out structural analysis of these compounds. Interestingly, the first use of Fourier transform interferometers in chemical applications was made in far-infrared spectroscopy.^[2] One of the major limits in traditional far-infrared spectroscopy was the lack of energy in the low-frequency region of the infrared blackbody emission sources, such as the Globar or mercury arc lamps. These conventional infrared sources are still used as mid- and far-infrared sources, but typically emit over 500 times less energy at 200 cm^{-1} compared to 5000 cm^{-1} .^[1d] SR and FEL's (free electron lasers) inspired the resurgence of far-infrared

studies with their unparalleled brilliance and collimation. This, together with more recent short pulse laser beam systems have led to the field of THz spectroscopy, covering the so called 'THz gap' ($300 - 3 \text{ cm}^{-1}$ or $10 - 0.1 \text{ THz}$) in the last decade or two, whereas acquiring significant intensity by infrared sources was difficult prior to this.^[2]

The use of water in far-infrared spectroscopy was avoided in the early stages, due to the strong broad absorbance in this region caused by intermolecular hydrogen stretching and libration modes of water, especially compared to the weak vibrations of the solute.^[3] This is further reflected in the design of the interferometers, which are the typically in vacuum to reduce interference of water vapour. However, following the advancements in equipment and SR, more recent studies have shown that these vibrations of water can be exploited to investigate the higher-order structures of proteins and biological molecules by studying the hydration layers and/or hydrogen bonding networks.^[4]

To date, THz/far-infrared spectroscopy has been used for a variety of applications. These include but are not limited to, astrophysical and atmospheric research on gas phase molecules, potential surface studies of small molecules and atoms, morphology investigations of polymers and materials, studying low wavenumber vibrations of inorganic materials, phonon/lattice mode and optical constants determination of molecular crystals and biomolecular investigations of DNA, proteins, cells and tissue.^[1d,2-5]

4.1.2 Synchrotron Radiation Infrared Microspectroscopy

The nature of vibrations in biological materials have been studied in great detail in the past decades leading to comprehensive descriptions of cellular vibration-bands in the mid-infrared region ($4000 - 400 \text{ cm}^{-1}$).^[6] A list of the main cellular, tissue and DNA related vibrations are tabulated in Table 4.1.

Changes occurring to these described vibrations (in absolute or relative intensity, ratio and/or wavenumber) can be used to deduce mechanistic information of a factor applied to the cell, such as light irradiation, drug uptake or oxygen deprivation.^[7]

A prime example is the effect of cisplatin (*cis*-[PtCl₂(NH₃)₂], CDDP) on cells, which is known to interact with DNA to form DNA adducts (primarily in the form of intra-strand crosslinking) leading to an extended signalling pathway cascade, usually leading to cell cycle arrest in its G2 phase and ultimately apoptosis

(Chapter 1.2.1).^[8] Bambery et al. studied the effect of cisplatin uptake in single rat glioma cells by synchrotron radiation infrared microspectroscopy (SR-IRMS).^[9] Multivariate data analysis of the infrared spectra of treated versus non-treated cells revealed a blue shift in the anti-symmetric phosphodiester stretching vibration (1241 – 1228 cm^{-1} region), which is characteristic of RNA (Table 4.1). These results were related to an increase of mRNA concentration inside the cell under these conditions. The indication of mRNA synthesis was assigned to a cellular response preceding protein synthesis in an apoptotic or repair event, in line with the mechanism of action of cisplatin. Interestingly, this shows that the largest effect of cisplatin on rat glioma cells, as monitored by infrared vibrations, is not related to nuclei condensation but rather a secondary response effect of the cell upon treatment with cisplatin. This technique proves to be an effective tool to study such drugs as cisplatin in cells on a single cellular basis, complementing the more conventional cytotoxicity assays.

Fourier Transform Infrared (FTIR) spectroscopy and imaging techniques are rapidly developing in terms of resolution and acquisition time, whereby single cellular level of detection is now possible using Global infrared sources.^[10] The main reason FTIR has not seen wide application in the study of live biological systems is the strong mid-IR absorption of water overlapping with the vibrations outlined in Table 4.1 (the broad vibrations: $\nu(\text{OH})$ between 3700 – 2800 cm^{-1} , centred at $\sim 3300 \text{ cm}^{-1}$ and $\delta(\text{H}_2\text{O})$ between 1700 – 1500 cm^{-1} , centred at $\sim 1640 \text{ cm}^{-1}$). Fixation methods, such as methanol or cryogenic fixation are commonly employed to circumvent this problem.

However, Tobin et al. reported the development of a microfluidic sample slide allowing infrared transmission through cellular samples by limiting the path length to 12 μm or less whilst being in a hydrated state (e.g. cell medium).^[11] This is where the high collimation and brilliance of SR offers advantage over the bench-top equipment. The aperture size of the SR can be reduced to $\geq 5 \times 5 \mu\text{m}$ while maintaining high signal-to-noise ratio, thus allowing the infrared beam to pass through single cells without passing through the surrounding medium or solvent. Any remaining intracellular water/medium signal can be subtracted by acquisition of background spectra in the surrounding cellular environment.^[11] Using a similar setup, Zobi et al. studied the uptake and cellular distribution of a metal-based photoactivatable carbon monoxide releasing complex (photoCORMs, Chapter 1.3.2) in fibroblasts (in growth medium) by SR-IRMS.^[7d]

The CO stretching vibrations of the metal-carbonyl complex between 2100 – 1800 cm^{-1} , which are at least 100 cm^{-1} separated from the cellular vibrations (*vide infra*), were used to track the internalisation, accumulation and subsequent photoactivation of the compound without the need of exogenous labelling. This demonstrates the potential power of synchrotron-based infrared techniques.

Table 4.1. Major infrared bands found in cells, tissues and nucleic acids. Reproduced from Ref.^[12] with permission from the Royal Society of Chemistry.

Wavenumber (cm^{-1})	Assignment
3600–3500	Amide A, proteins, $\nu(\text{N-H})$
3490	Water, $\nu_3, \nu_{\text{as}}\text{OH}$
3277	Water, $\nu_2, \nu_{\text{as}}\text{OH}$
2956	$\nu_{\text{as}}\text{CH}_3$ acyl chains lipids
2922	$\nu_{\text{as}}\text{CH}_2$ acyl chains lipids
2874	$\nu_s\text{CH}_3$ acyl chains lipids
2852	$\nu_s\text{CH}_2$ acyl chains lipids
1740	Lipids, $\nu(\text{C=O})$ ester carbonyl
1715	B-DNA base pairing vibration ($\nu\text{C=O}$ & $\nu\text{C=N}$)
1708	A-DNA base pairing vibration ($\nu\text{C=O}$ & $\nu\text{C=N}$)
1720–1666	$\nu\text{C=O}$ from purine and pyrimidine
1695	Z-DNA base pairing vibration ($\nu\text{C=O}$ & $\nu\text{C=N}$)
1690	RNA, $\nu_a(\text{C}_2=\text{O})$
1660–1665	DNA, $\nu(\text{C}_5=\text{O})$, $\delta(\text{N=H})$, RNA, $\nu(\text{C}_6=\text{O})$
1650	Amide I, protein, α -helical
1635	Amide I, proteins, β -pleated sheet
1642	Water, $\nu_2, \delta(\text{H}_2\text{O})$
1610	DNA and RNA, $\nu\text{C}_4=\text{C}_5$ imidazole
1605	DNA, δNH_2
1578	DNA and RNA, $\nu\text{C=N}$ imidazole ring
1545–1530	Proteins, amide II
1418, 1425, 1408	A-DNA, B-DNA, Z-DNA deoxyribose
1457	$\delta_{\text{as}}\text{CH}_3$ of cellular proteins
1450	Proteins, lipids, δCH_2
1400	νCOO_2^- of fatty acids and amino acid side chains
1300–1250	Proteins, amide III
1244	RNA, $\nu_{\text{as}}\text{PO}_2^-$
1240, 1225, 1215	A-DNA, B-DNA, Z-DNA, $\nu_{\text{as}}\text{PO}_2^-$
1185	A-DNA, ribose
1160, 1120	RNA, $\nu(\text{C=O})$ ribose
1080	DNA, $\nu_s\text{PO}_2^-$
1060, 1050	DNA, RNA, $\nu(\text{C-O})$ ribose
1038	RNA, $\nu(\text{C=O})$ ribose
1015	DNA and RNA, $\nu(\text{C-O})$ ribose
1014–1018	Z-DNA marker band
996	RNA, uracil ring motions
970, 915	DNA, RNA, ribose–phosphate skeletal motions
899, 894, 929	A-DNA, B-DNA, Z-DNA
806, 830–840	A-DNA, B-DNA

Notations used: ν = stretch, δ = in-plane angle bending, s = symmetric and as = anti-symmetric.

The effect of the diazido Pt(IV) anticancer prodrug candidate **1** on live K562 cells is investigated in this chapter and the corresponding infrared marker bands of K562 cells are listed below and a single cell infrared spectrum of K562 by SR-IRMS is shown in Figure 4.2.

CH₃ and CH₂ stretching vibrations (3000 – 2800 cm⁻¹) relate to all lipids inside the cell, as well as methyl containing parts of proteins and DNA. The weak carbonyl stretching vibrations ($\nu(\text{C}=\text{O})$) are related to phospholipids (~1740 cm⁻¹) and base stacking of purine and pyrimidine moieties (~1720 cm⁻¹). The latter provide information about the ratio of alpha (A) and beta (B) sheet DNA. The amide I peak (1650 – 1635 cm⁻¹) is the most intense absorption band. This is primarily governed by the in-plane carbonyl stretching vibration coupled to the carbon to nitrogen stretching vibration.^[6,13] The amide II band is more complex, but mainly consists of the in-plane R₂-N-H bending vibration with minor contributions (in potential energy terms) from carbon to nitrogen and carbon to carbon stretching vibrations.^[6,14] Furthermore, the CH₂ and CH₃ bending modes (~1450 cm⁻¹) from lipids and proteins, as well as the symmetric and anti-symmetric phosphate stretching vibrations (~1180 cm⁻¹ and ~1250 – 1215 cm⁻¹, respectively) clearly stand out in the spectrum. Whilst these spectral features look very clear, changes occurring to these vibrations are relatively minor (small shifts of 3 – 10 cm⁻¹ and minor peak ratio and/or peak intensity changes). Spectral and experimental replicates become highly essential in these cases and multivariate data analysis is almost a necessity to statistically verify observations.

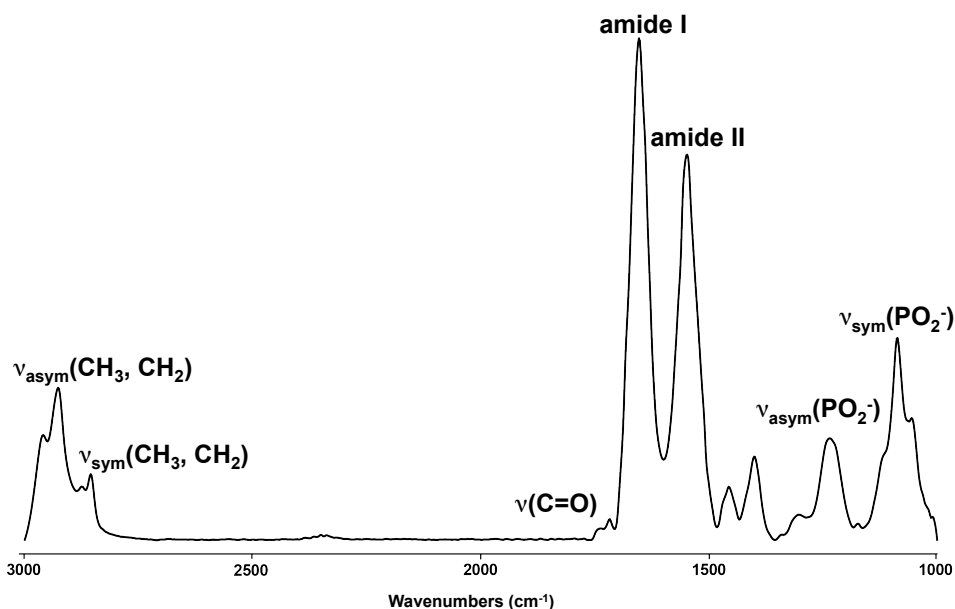


Figure 4.2. A synchrotron radiation infrared microspectroscopy spectrum of a single K562 cell including selected peak labels. Spectrum is background and rubberband baseline corrected. Notations used: ν = stretch, sym = symmetric and asym = anti-symmetric.

Partial Least Squares-Discriminant Analysis (PLS-DA) models are used to investigate the data obtained from by SR-IRMS. PLS-DA is a statistical classification tool to capture variation in a data set, like the Principal Component Analysis (PCA) mentioned and used in Chapter 3.1. The main difference between the two is that PCA is an unsupervised method whilst PLS-DA is a supervised method, i.e. PLS-DA has predefined classes and looks to reduce dimension of the data set between these classes whilst PCA does not attempt to discriminate between classes directly. Thus, PLS-DA allows to breakdown data sets affected by several conditions (classes), such as the influence of time, irradiation and treatment with a drug on cellular spectra. An example data set is provided in order to further rationalise how PLS-DA operates and can be used to interpret data sets. 50 random spectra are generated and a distinct spectral feature is applied (green class) to half of them at 850 a.u. where no predefined band shapes were generated (Figure 4.3). While to the other half (red class), a spectral feature is added underlying the randomly generated bands at 1220 a.u. (Figure 4.3). The green feature at 850 a.u. results in an obvious distinction between the two sets, whereas the changes to the red class are less obvious due to overlapping bands and pre-existing features.

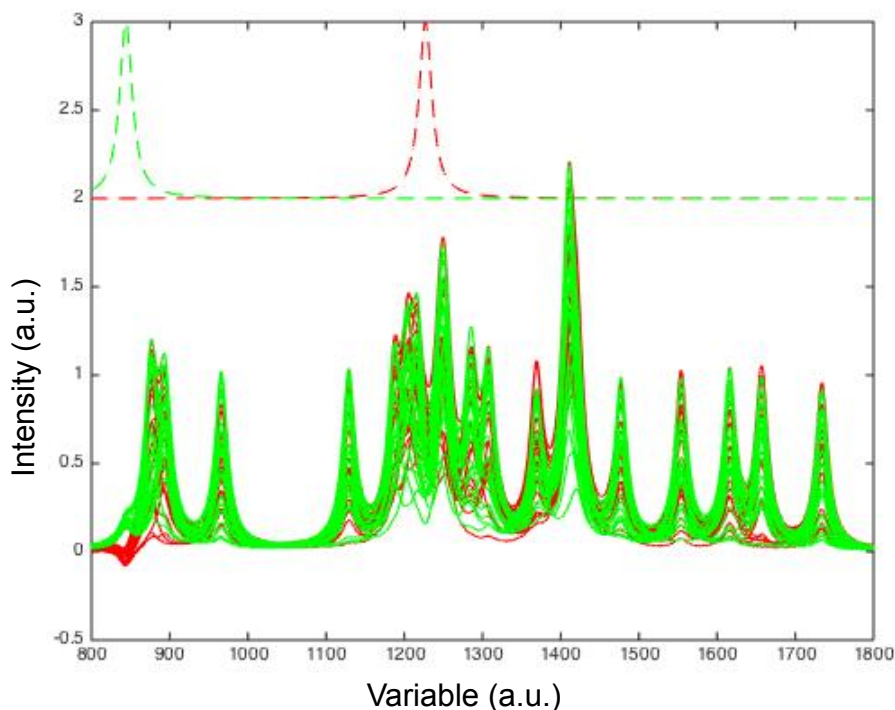


Figure 4.3. 50 randomly generated spectra separated into two classes (green and red) by introducing a spectral feature for the green spectra at 850 a.u. (next to the generated peaks) and a spectral feature for the red spectra at 1220 a.u (underlying the generated peaks).

A PLS-DA model is created which contains two regression vectors (in the case of two classes) and cross validation is applied by checking the difference between each sample and the regression vectors. The cross validation value and/or error are measures of the classification performance and the regression vector is a measure of the direction (positive or negative) and intensity of the spectral bands in each classification (Figure 4.4).

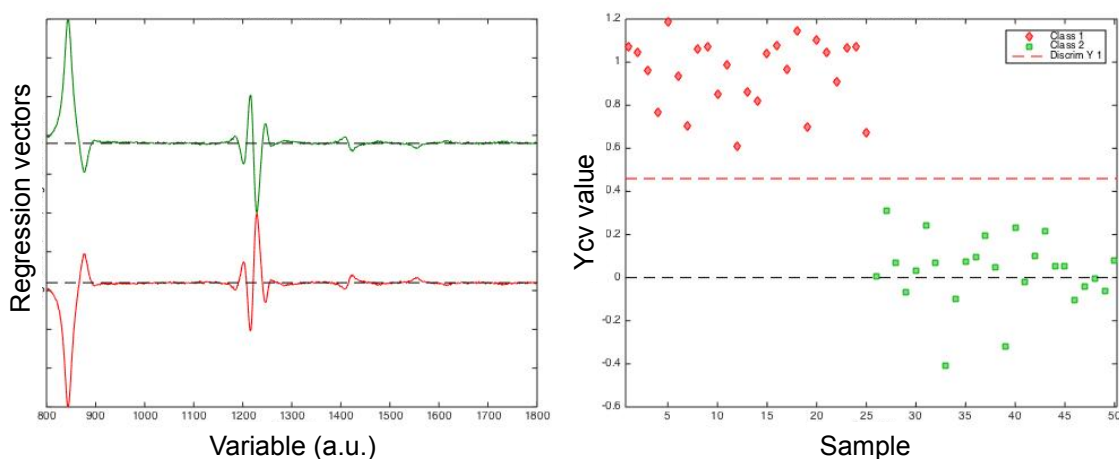


Figure 4.4. PLS-DA regression vectors (left) and Y cross validation error (right).

The classification captures both manually applied spectral features in the regression vectors (850 a.u.; green = positive, red = negative, 1220 a.u.; red = positive, green = negative). The separation of the green and red class by the cross validation error value (Ycv value) provides an approximation of how much the classes differ to each other and how well each sample performs in its class (green clusters around Ycv = 0 and red clusters around Ycv = 1). In a real time example, one would then investigate what changes to spectral features centred at 850 a.u. and 1220 a.u. could imply as described above.

4.2 Results

All studies were carried out at the Australian Synchrotron in Melbourne, Australia at the THz/Far-IR and Infrared Microspectroscopy beamlines. Beam time was acquired three times through the merit-based proposal scheme and once via an expert user application. A total of four days were spent at the Infrared Microspectroscopy beamline and twelve days at the THz/Far-IR beamline. In addition, the author has been involved with the development of the ATR technique for the THz/Far-IR beamline, which is now accessible for synchrotrons users as of application round 3, 2017.

4.2.1 Synchrotron Radiation Attenuated Total Reflection Far-Infrared

A feasibility study was carried out to test the potential application of attenuated total reflection in a synchrotron infrared setup, prior to the development and use of the Attenuated Total Reflection Synchrotron Radiation Far Infrared (SR-ATR-FIR).

Towards this end, a Specac golden gate diamond ATR accessory was used in both a bench top Bruker Equinox 55 FT-IR spectrometer (fixed beamspot size of ~30 mm) at Monash University and the IFS 125/HR Bruker FT spectrometer (variable beamspot size of 12.5 to 0.5 mm) at the Australian synchrotron. Different infrared sources, detectors and beamsplitters were used to test the capabilities of an ATR setup, which are listed in Table 4.2.

The Specac ATR accessory contains ZnSe condensing optics to focus the infrared beam onto the 4 mm x 4 mm ATR crystal, which do not transmit infrared radiation below $\sim 480\text{ cm}^{-1}$; this limited the spectral region to test. The entire IFS 125/HR Bruker FT spectrometer, including sample chamber, operates at $\leq 10^{-4}$ mbar to minimise H₂O and CO₂ interference. Therefore, all spectra were obtained under vacuum, regardless of the infrared source.

Solid polystyrene and Teflon™ samples (poly(1-phenylethene) and polytetrafluoroethylene) were used to carry out the spectral acquisitions and the reference spectra were obtained on the Bruker Equinox 55 FT-IR spectrometer. Infrared spectra of both materials at a resolution of 4 cm^{-1} using SR and the internal Globar source (12.5 mm beamspot size) at the Australian Synchrotron were compared to the spectra obtained at Monash University (Figure 4.5).

Identical peak positions and similar peak intensities confirmed the correct alignment of the setup. The feasibility of SR applied to ATR-FTIR was benchmarked vs. the internal Globar source by measuring the signal counts of the background (empty ATR), Telfon™ and polystyrene using the three different detectors (Figure 4.6). Figure 4.6A-C show, that in all cases, SR is superior to the Globar for beamspot sizes ≤ 2 mm. Figure 4.6D shows an example of the polystyrene ATR spectra obtained using the Si:B photodetector using different beamspot sizes for both the SR and Globar infrared sources. The high signal-to-noise ratio for SR is maintained throughout each beamspot size, as shown by the polystyrene peaks at 694 cm^{-1} and 536 cm^{-1} . The quality of the spectra recorded with the Globar source, however, clearly diminishes when the beamspot size is decreased (Figure 4.6D). This feasibility study of a SR-ATR-FIR setup proved to be successful and enabled the following studies using a far-infrared capable ATR accessory.

Table 4.2. Experimental setups used to test the potential of synchrotron radiation and ATR. A Specac golden gate diamond ATR accessory was used in all setups.

Spectrophotometer^a	Infrared source^b	Beamspot size (mm)	Detector^c	Beam splitter	Measurable spectral region (cm^{-1})
IFS 125/HR Bruker	SR or Globar	12.5 – 0.5	He-cooled Si bolometer	6 μm multilayer Mylar	650 – 40 ^d
			He-cooled Si:B photodetector	KBr	750 – 450 ^d
			N ₂ -cooled MCT _n	KBr	5000 – 700
Bruker Equinox 55	Globar	~30	N ₂ -cooled MCT	KBr	4000 – 600

^a Acquisition parameters: resolution = 4 cm^{-1} , 50 interferograms coadded, 40 kHz.

^b SR = synchrotron radiation, Globar = internal infrared source. ^c MCT_n = Mercury Cadmium Telluride narrow band, Si:B photodetector was not used for spectral acquisition, only for infrared signal counts. ^d Lower limit restricted to 480 cm^{-1} due to ZnSe optics in the golden gate ATR accessory, ordinary lower limits: Si bolometer = 10 cm^{-1} and Si:B photodetector = 300 cm^{-1} .

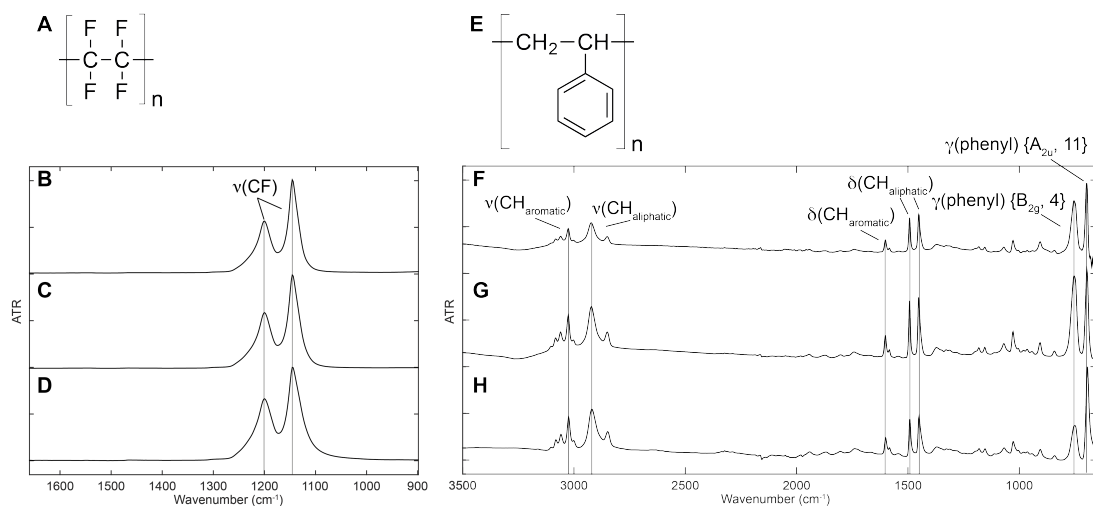


Figure 4.5. ATR-FTIR spectra of Teflon™ and polystyrene, including selected peak labels. A & E) Molecular structures of Teflon™ and polystyrene. B & F) Spectra obtained with SR (12.5 mm) and MCT_n detector. C & G) Spectra obtained with Globar (12.5 mm) and MCT_n using the IFS125 at the THz/Far-IR beamline. D & H) Reference spectra obtained with Globar and MCT using the Equinox 55 at Monash University. Notations used: ν = stretch, δ = in-plane angle bending and γ = out-of-plane angle bending. The descriptions of phenyl modes are given in Wilson's notations.^[15]

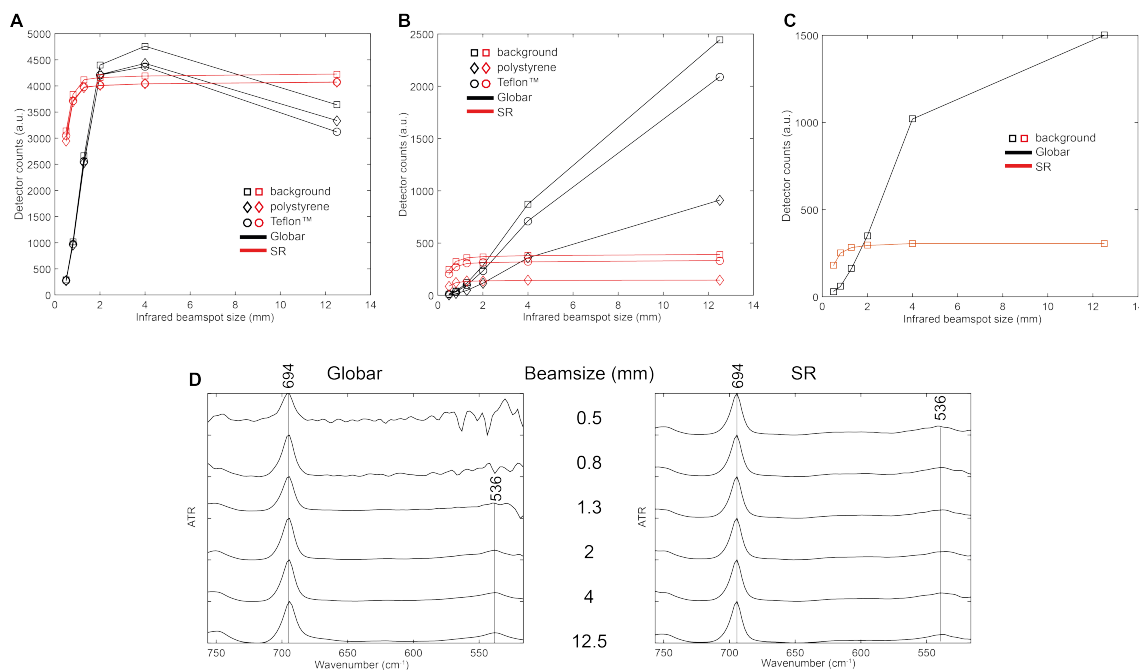


Figure 4.6. Comparison of SR and Globar infrared source in the IFS 125/HR Bruker FT spectrometer equipped with a Specac golden gate diamond ATR accessory with three different detectors. Please refer to Table 4.2 for experimental conditions. A) MCT_n detector counts using the Globar and SR infrared source at different beamspot sizes. B) Si:B photodetector counts using the globar and SR infrared source at different beamspot sizes. C) Si Bolometer detector counts using the Globar and SR infrared source at different beamspot sizes, please note that detector counts of TeflonTM and polystyrene could not be obtained due to limited offline synchrotron time. D) Example ATR spectra of polystyrene, including peak labels, at different beamspot sizes using the Globar and SR infrared sources with the Si:B photodetector, highlighting the diminishing quality of the spectra using the Globar source when decreasing the beamspot size whilst the high signal-to-noise ratio of the SR remains the same.

The above results allowed for a successful expert user time application at the Australian synchrotron to use a far-infrared capable ATR accessory for 48 hours to further test the capabilities of a SR-ATR-FIR setup. A Bruker platinum ATR accessory was kindly provided by Dr. Bobby Pejic from CSIRO in Western Australia. The two days of beamtime was allocated to several potential SR-ATR-FIR projects to support a funding application for a beamtime accessible SR-ATR-FIR setup. These included:

1. Investigation of *trans,trans,trans*-[Pt(N₃)₂(OH)₂(py)₂] (**1**) and its synthetic precursors *trans*-[Pt(N₃)₂(py)₂] (**2**) and *trans*-[Pt(Cl)₂(py)₂] (**3**) using SR-ATR-FIR vs. SR-FIR (transmission infrared, as described in Chapter 2).
2. The photodecomposition of **1** by SR-ATR-FIR.
3. Screening of solid DNA nucleobases for use in metal complex binding studies.
4. Investigation of potential far-infrared marker bands of malaria infected red blood cells.

Points 1 and 2 will be reported and discussed below. Points 3 and 4 can be found in section 4.8 at the end of this chapter to maintain focus of this work on complex **1**.

The Bruker platinum diamond ATR accessory was fitted into the IFS 125/HR Bruker FT spectrometer. This ATR accessory only contains gold-coated reflective mirrors and no condensing optics to obtain a spectral range of 8000 – 10 cm⁻¹. The synchrotron beamspot size was set to 2 mm, and no increase signal counts was observed beyond this diameter. Spectra were recorded at a resolution of 1 cm⁻¹, 128 interferograms co-added. Samples were either measured as solids with the ATR anvil pressed down to ensure proper contact between the sample and the diamond (Figure 4.7A), or deposited onto the ATR diamond from solution followed by evaporation under a gentle N₂ flow resulting in a thin layer of sample (Figure 4.7B). A custom built cover was placed over the ATR accessory to seal the spectrometer and allow for measurements *in vacuo* (Figure 4.7C).

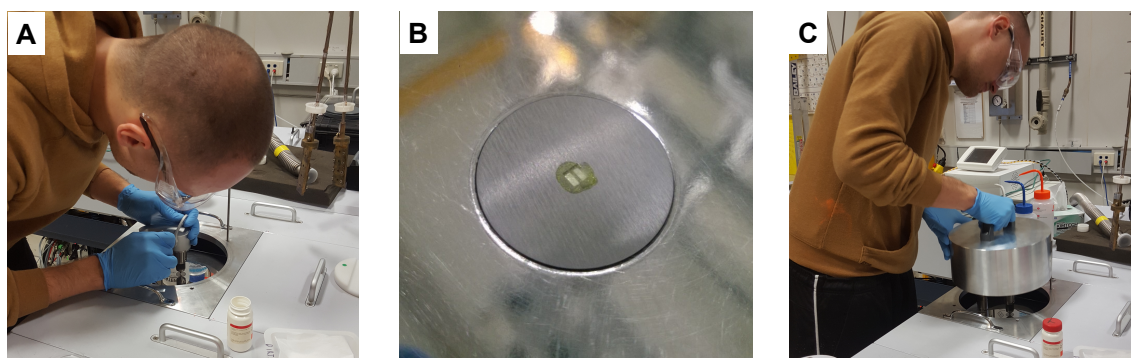


Figure 4.7. A Bruker platinum ATR accessory inside an IFS 125/HR Bruker FT spectrometer with a custom built cover at the Australian Synchrotron. A) ATR anvil pressed down in a solid sample. B) A thin layer of sample (**1**) on the ATR diamond from solution after evaporation of solvent. C) Custom built lid to allow vacuum sealing inside the sample chamber whilst the ATR accessory is aligned.

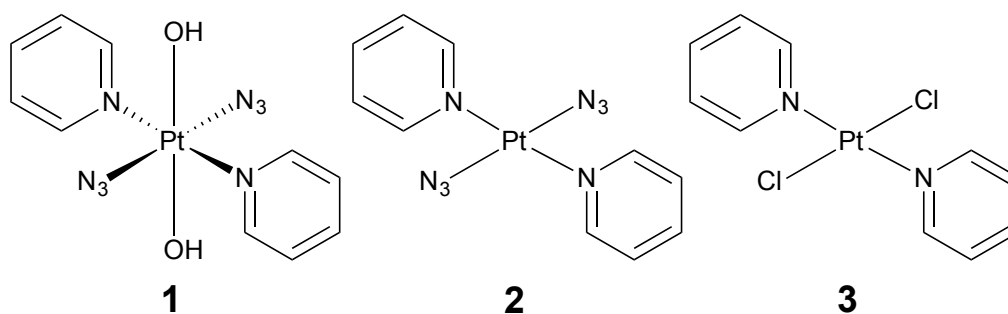


Figure 4.8. Structures of *trans,trans,trans*-[Pt(N₃)₂(OH)₂(py)₂] (**1**), *trans*-[Pt(N₃)₂(py)₂] (**2**) and *trans*-[PtCl₂(py)₂] (**3**).

Initial comparison was made between the previously obtained transmission spectra at ~301 K of **1** and its synthetic precursors **2** and **3** (Figure 4.8), as reported in Chapter 2.^[16] Figure 4.9 shows the ATR vs. transmission spectra, with peak labels and assignments in line. Extended ATR correction was carried out on the SR-ATR-FIR spectra of the solids of **1**, **2** and **3** to correct for the artefacts caused by anomalous dispersion, as described previously in Chapter 2.^[16-17]

A typical ATR spectra of solid samples took 5 – 10 min to acquire (majority of the time consists of pumping down the sample chamber to $\leq 10^{-4}$ mbar), whereas transmission spectra took ~30 min – 2 h to acquire (with sample preparation being the most time consuming step).

Identical sample preparation as described in Chapter 3.1 was used to carry out the ATR measurements of the photodecomposition of **1** in water under 420 nm

irradiation (small quantities of solution were deposited onto the ATR crystal, followed by evaporation under a gentle N₂ flow, prior to measurement). Figure 4.10 depicts the SR-ATR-FIR spectra of crystalline **1** (Figure 4.10A), **1** from solution prior to irradiation (Figure 4.10B), **1** after 10 min of irradiation (Figure 4.10C) and **1** completely photodecomposed after 22 h of irradiation (Figure 4.10D).

First, going from the crystalline solid of **1** to **1** evaporated from solution strongly effects the intermolecular interactions of **1** resulting in shifts of vibrational peaks mainly affecting the hydroxide and azide related vibrations, with less significant effects on the pyridine vibrations. The out-of-plane bending mode of azide, $\gamma(\text{N}_3)$, at 583 cm⁻¹ and 574 cm⁻¹ shifts to lower wavenumber values, merging together with the platinum to oxygen stretching vibration, $\nu(\text{Pt-OH})$, shifting to higher energies from 540 cm⁻¹ to the combination band at 574 cm⁻¹, 569 cm⁻¹ and 559 cm⁻¹. The out of plane pyridine bending mode, $\gamma(\text{py}, 16\text{b})$, shifts slightly from 476 cm⁻¹ to 472 cm⁻¹. Furthermore, the platinum to nitrogen (azido) stretching vibration, $\nu(\text{Pt-N}_3)$, shows less splitting in bands with the two main vibrations at 411 cm⁻¹ and 406 cm⁻¹ (solid) remaining at 410 cm⁻¹ and 406 cm⁻¹. Platinum to oxygen bending modes, $\text{scr}(\text{HO-Pt-OH})$ at 299 cm⁻¹ and 290 cm⁻¹ split up to 299 cm⁻¹, 286 cm⁻¹ and 278 cm⁻¹. Lastly, the platinum to nitrogen (pyridine) stretching mode, $\nu(\text{Pt-py})$, shifts to lower wavenumber values from 257 cm⁻¹ to 244 cm⁻¹ with other combinational modes below 240 cm⁻¹ effected slightly by the dissolution and evaporation of solvent of **1** (Figure 4.10A, B).

Time restrictions only allowed for two time points to be investigated. 10 min was selected, at which time considerable changes were observed in the mid-infrared to the $\nu(\text{OH})$ and $\nu_{\text{asym}}(\text{N}_3)$ by ATR-FTIR without the complete removal of $\nu(\text{OH})$. While at 22 h the spectrum of the final photoproduct is obtained, which only contained pyridine and water related vibrations. Upon 10 min of irradiation, the azido related vibrations show a reduction in wavenumber values and several shifts and splitting of bands (Figure 4.10B). Most importantly, the platinum to nitrogen (azido) stretching vibration, $\nu(\text{Pt-N}_3)$, splits up into three main vibrations at 440 cm⁻¹, 419 cm⁻¹ and 384 cm⁻¹, with $\gamma(\text{N}_3)$ still present at 578 cm⁻¹. Further expanding on the hydroxido ligand vibrations, the broad platinum to oxygen (hydroxyl) stretching vibrations, $\nu(\text{Pt-OH})$, peaking at 559 cm⁻¹ prior to irradiation splits into two bands at 555 cm⁻¹ and 507 cm⁻¹, with the related platinum to oxygen bending modes reducing in intensity. The pyridine related

vibrations are mainly affected in terms of intensity. The $\gamma(\text{py}, 16\text{b})$ remains at 473 cm^{-1} and the majority of vibrations below 230 cm^{-1} become too weak to observe apart from the vibrations at 222 cm^{-1} and 101 cm^{-1} . Upon full photodecomposition of **1** after 22 h, the SR-ATR-FIR spectra consist solely of platinum to oxygen (OH/H₂O) and pyridine vibrations as shown in Figure 4.10D. Namely, the broad platinum to oxygen stretching vibration, $\nu(\text{Pt-OH/H}_2\text{O})$, at 545 cm^{-1} , $\gamma(\text{py}, 16\text{b})$ at 468 cm^{-1} , $\nu(\text{HO-Pt-OH})$ at 295 cm^{-1} and $\nu(\text{Pt-py})$ at 237 cm^{-1} .

These results and those outlined in the Supporting Information were presented to the infrared beamline staff, which supported the successful internal synchrotron application by the THz/Far-IR beamline to purchase a custom built SR-ATR-FIR setup. This consisted of modifying a commercial ATR accessory to fit in the IFS 125/HR Bruker FT spectrometer, whereby the sample area above the ATR diamond would lie outside at ambient pressure while its optics remained in vacuum. A summary of the development of this ATR setup, which was finalised in June 2017 and is now available for beamtime applications, is shown in Figure 4.11. The SR-ATR accessory is a modified Pike GladiATR™ single reflection, heated (< 300 °C), ATR accessory, with several optional adapters such as a digital high-pressure clamp and a liquid flow cell.

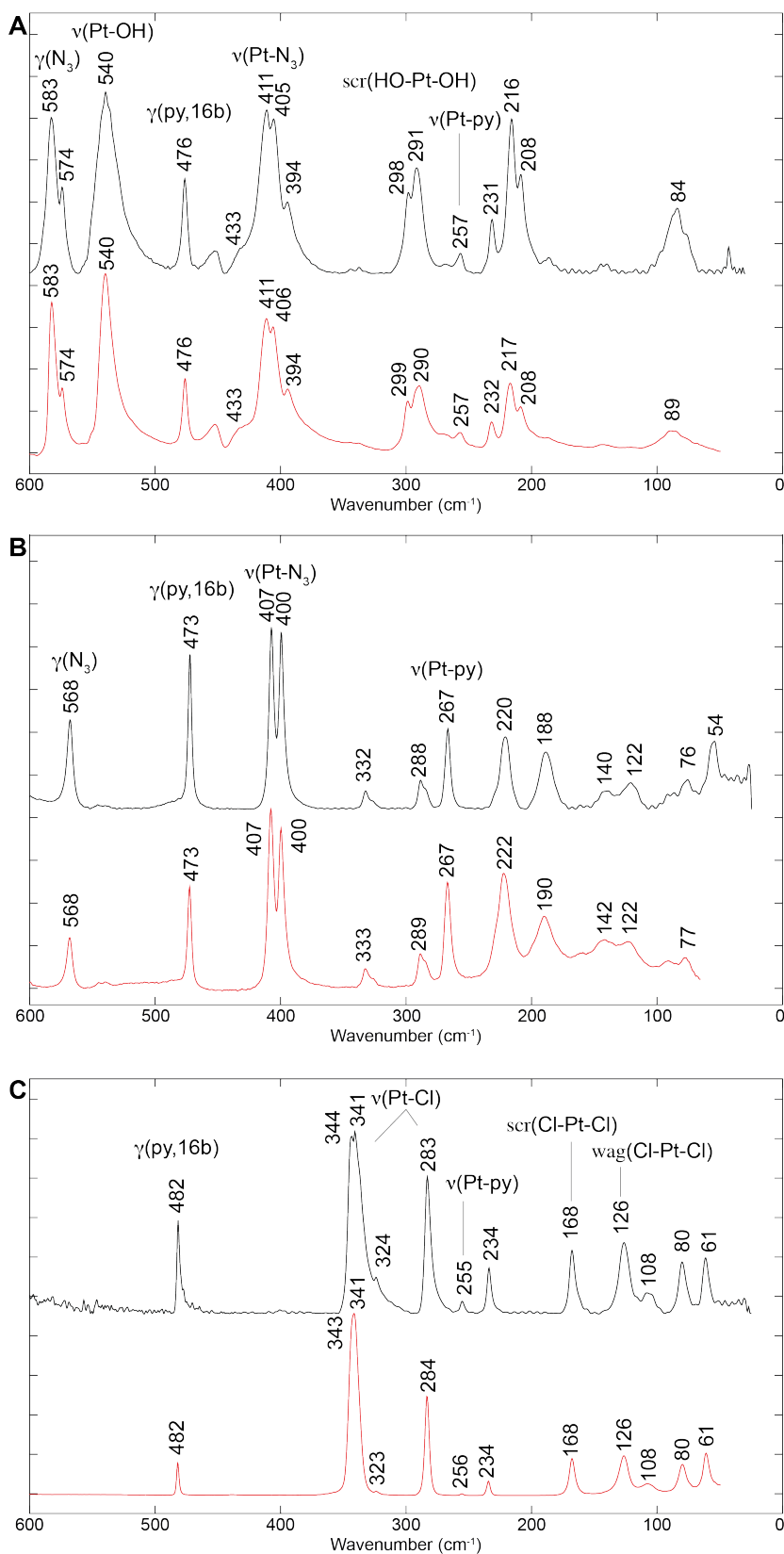


Figure 4.9. Transmission SR-FIR (black) and SR-ATR-FIR (red) spectra of **1** (A), **2** (B) and **3** (C) including peak labels and selected peak assignments.^[16] Resolution = 1 cm^{-1} . Notations used: ν = stretch, γ = out-of-plane angle bending, scr = scissoring, wag = wagging. The descriptions of pyridine modes are given in Wilson's notations, as described previously.^[15-16]

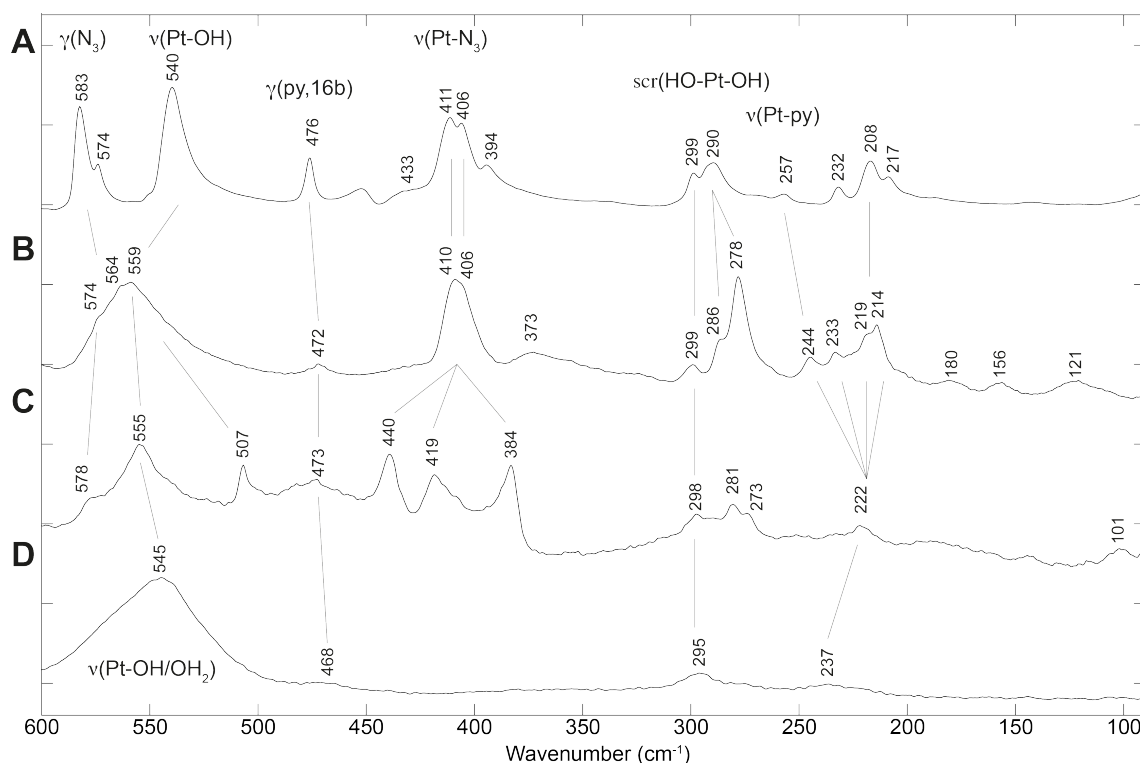


Figure 4.10. SR-ATR-FIR spectra of the photodecomposition of **1** (2 mM) under 420 nm irradiation. A) **1** solid. B) **1** after dissolution in water followed by evaporation prior to measurement. C) 10 min of 420 nm irradiation. D) 22 h of irradiation. Resolution = 1 cm⁻¹. Notations used: ν = stretch, γ = out-of-plane angle bending, scr = scissoring, wag = wagging. The descriptions of pyridine modes are given in Wilson’s notations, as described previously.^[15-16]

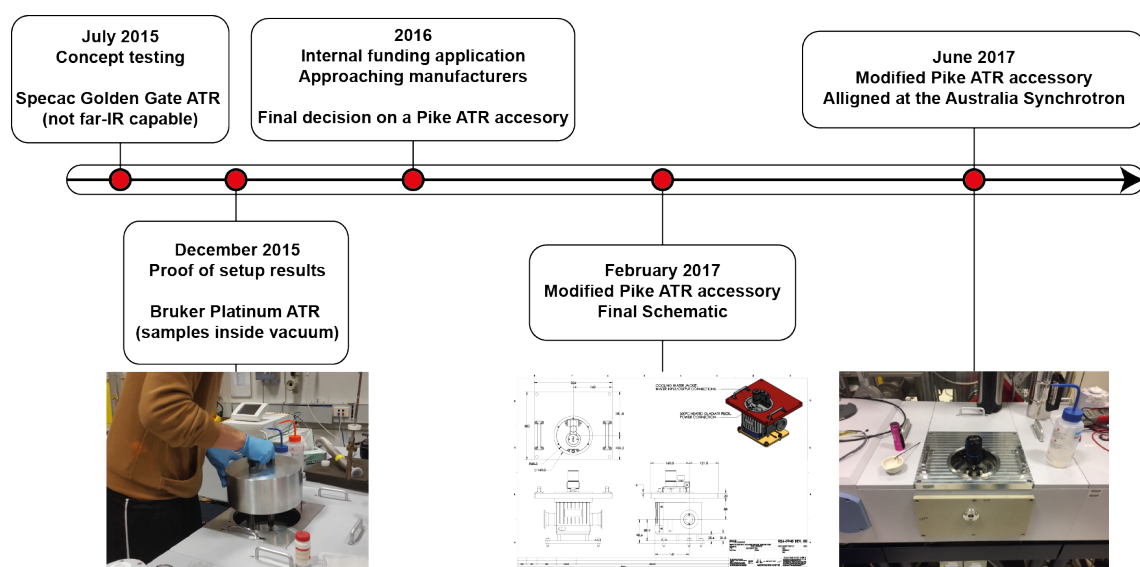


Figure 4.11. Timeline of the development of the SR-ATR-FIR accessory for the THz/Far-IR beamline at the Australian Synchrotron. Pike ATR accessory schematic and picture of the finalised setup (right) were kindly supplied by Dr. Dominique Appadoo.

4.2.2 Transmission Synchrotron Radiation Far-Infrared – Liquid cell *in situ* Irradiation

The same spectrometer at the THz/Far-IR beamline at the Australian Synchrotron was used to work on a new transmission liquid cell far-infrared setup with a Surelite Nd:YAG pulsed laser (variable wavelength, beamsplitter set to 355 nm for these experiments in particular) aligned to the sample chamber to allow for *in situ* irradiation. Figure 4.12 shows a picture and a schematic representation of the setup. In short, the laser was aligned at a 90° angle to the SR, passing through a UV grade CaF₂ window on the side of the sample chamber. By rotation of the sample holder, the sample can be exposed to irradiation and measured afterwards without breaking vacuum. The liquid cells are a custom design to be operated under vacuum, and are equipped with wedged diamond windows (1°) to attempt to minimise spectral artefacts caused by internal reflections from the window. These artefacts are further referred to as fringing, and will be considered in more detail below and in section 4.3.2.^[18] Pictures of the diamond window liquid cells are shown in Figure 4.13. Different spacers can be used to achieve the desired path length (5 – 300 µm, Figure liquid 4.13A). One O-ring is used to seal the liquid from the vacuum (Figure 4.13B) and allow for tight closure of the compressed windows (Figure 4.13C,D). The liquid cells allow for small excess sample volumes to be removed between the edge of the window and the O-ring upon tightening of the cell. Exact cell volumes and volumes used throughout the experiments are shown in Table 4.3.

Table 4.3. Diamond window liquid cell volumes and volumes used according to spacer size.

Spacer size (µm)	Cell volume (µL)	Volume used (µL)
5	0.32	0.5
10	0.64	-
15	0.95	1.5
20	1.27	1.5
25	1.59	-
50	3.18	4.0
100	6.36	7.0
200	12.72	-
300	19.09	20.0

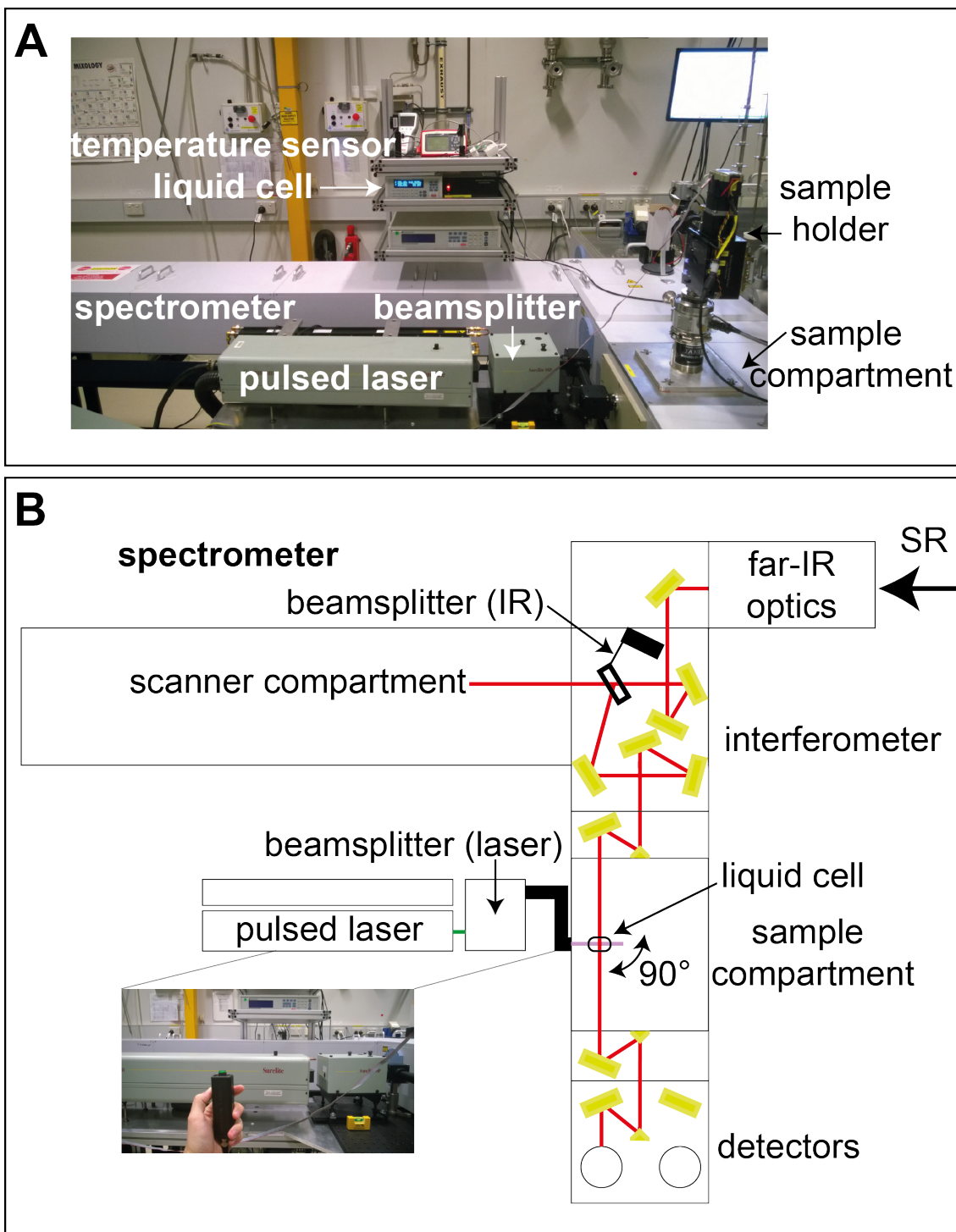


Figure 4.12. Picture (A) and simplified schematic representation (B) of the IFS 125/HR Bruker FT spectrometer with a Surelite Nd:YAG pulsed laser aligned at a 90° of the synchrotron radiation (SR). Rotation of the sample holder allows for sample exposure to irradiation without breaking vacuum. Please note that one sample compartment is left out for clarity.

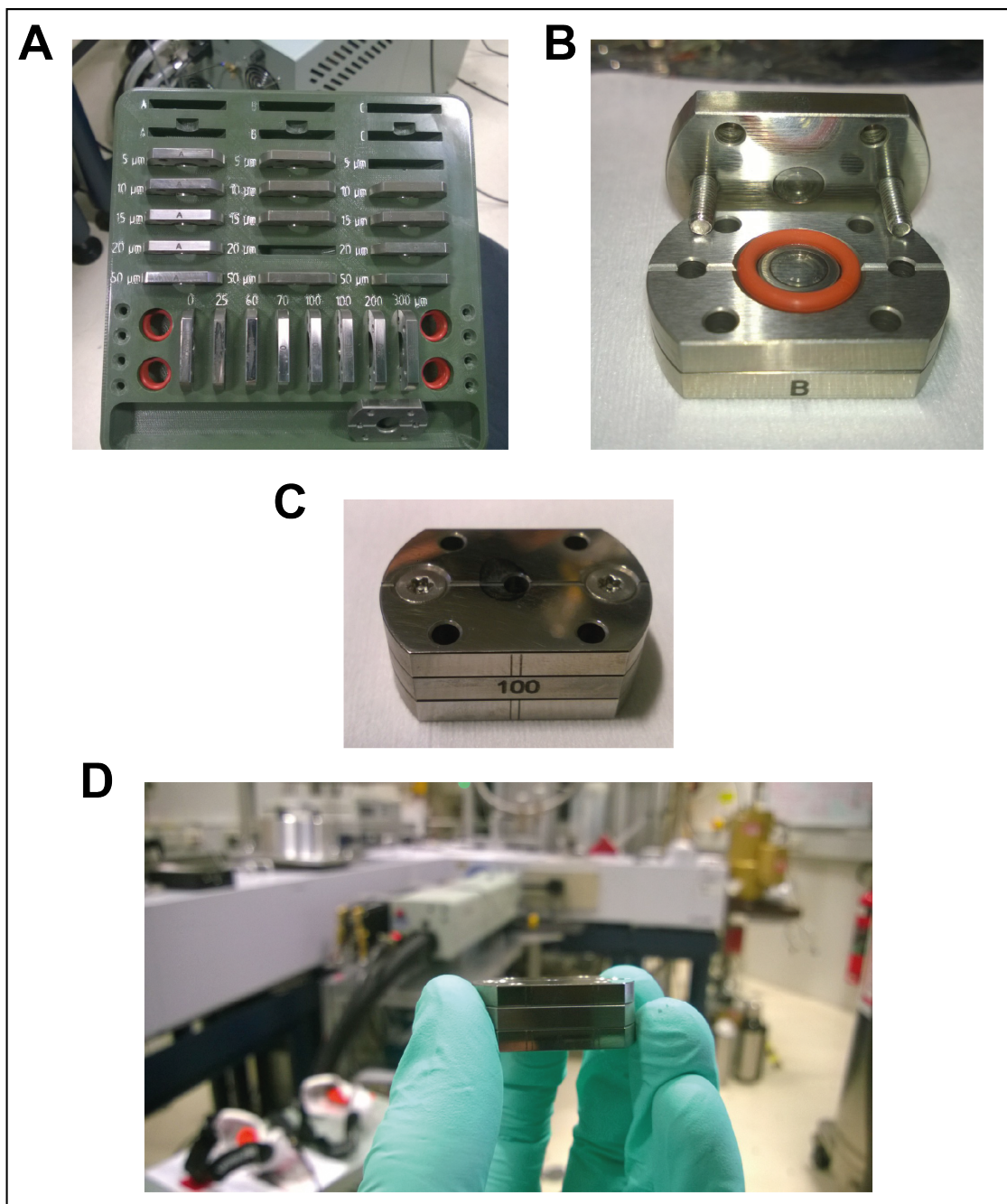


Figure 4.13. Pictures of diamond window liquid infrared cells. A) Set holder with multiple spacers (5 - 300 μm) to vary the pathlength. B) Bottom and top window of a liquid cell to hold the liquid in between the O-ring. C/D) Assembled and sealed liquid cell with a 100 μm spacer.

Initial tests of the liquid cells were carried out using different solvents: water, acetonitrile (MeCN) and dimethyl sulfoxide (DMSO). Fringing artefacts were found to be present, varying with solvent, sample, pathlength and within replicates (Figure 4.14A). Therefore, fringing corrections were carried out for each individual spectrum as reported previously.^[18b,18c] The process provided below is supported by the example in Figure 4.14 of a 20 μm pathlength cell with MeCN:

1. Inverse Fourier transformation of the single-channel sample spectrum (Figure 4.14B).
2. Identify regions outside the centreburst in the interferogram that cause the fringing (Figure 4.14B, box 1 and 2).
3. Straight line generation on those regions.
4. Fourier transformation of the interferogram to the single-channel sample spectrum (Figure 4.14C).
5. Single-channel sample spectrum divided by the single-channel reference spectrum (vacuum) gives the transmittance spectrum and is transformed to the absorbance spectrum (Figure 4.14D).

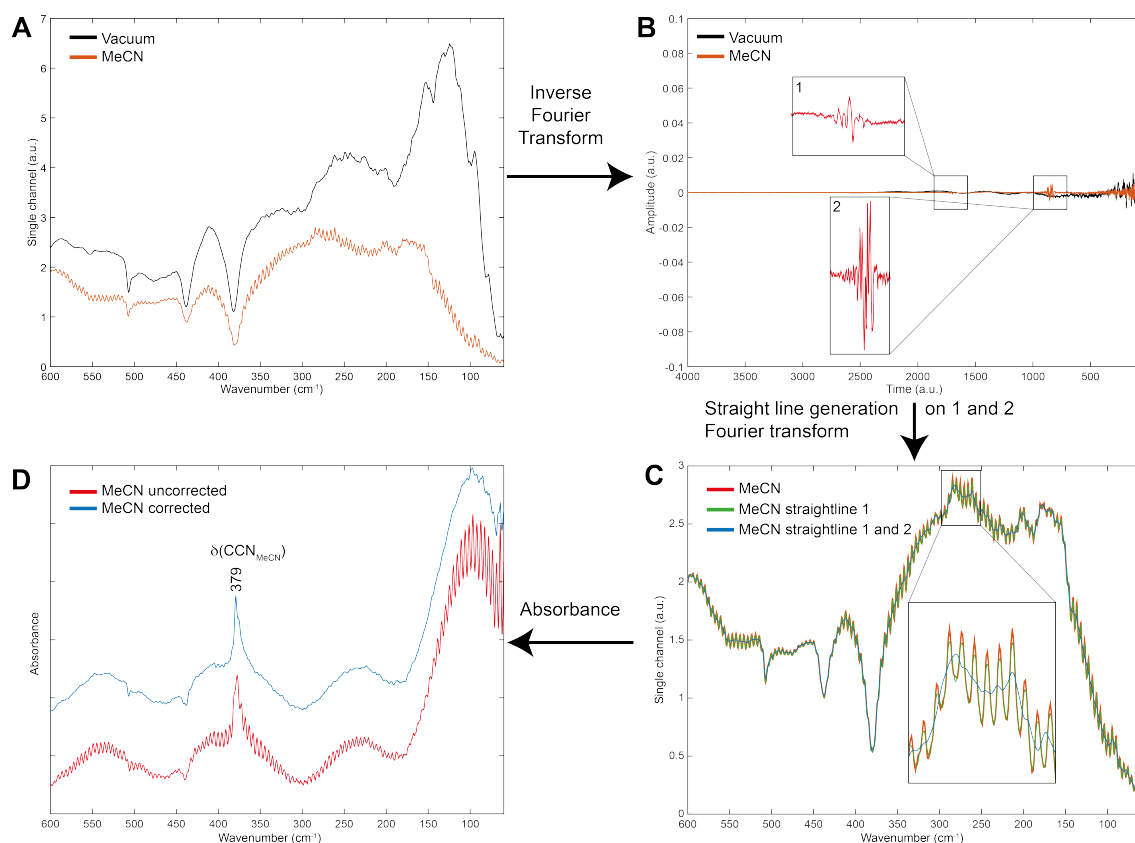


Figure 4.14. Processing schematic used to correct for fringing artefacts. **A)** Single-channel sample spectra of vacuum (no fringes) and MeCN (sinusoidal fringes observed). **B)** Resulting interferograms after inverse Fourier transformation, highlighting the artefacts of MeCN (box 1 and 2). **C)** Fourier transformed interferograms before (red), after one straight line generated on box 1 (green) and after two straight line generations on box 1 and 2 (blue). **D)** Absorbance spectra (single-channel MeCN \div single-channel vacuum, transform transmission to absorbance) of corrected (blue) and uncorrected (red) MeCN single-channels. Notation used: δ = in-plane angle bending.

After this correction, depending on the sample, some artefacts still remained in the spectrum (Figure 4.14D, corrected MeCN) in the form of broader sinusoidal artefacts and non-smooth baselines. This prevented the use of water (strong far-infrared absorber) to study compounds at low concentration, at which one cannot distinguish between noise and signal with certainty. Therefore, DMSO was used as a solvent to study the *in-situ* photodecomposition of **1** to allow for elevated concentrations and longer pathlengths.

The SR-FIR spectrum of DMSO using a 20 μm pathlength is shown in Figure 4.15 with corresponding peak labels. Two methyl rocking modes are present at 954 cm^{-1} and 933 cm^{-1} , both in-plane and out-of-plane angle bending of CSO at

383 cm^{-1} and 334 cm^{-1} , the out-of-plane CSC bending mode at 309 cm^{-1} and the broad peak at 97 cm^{-1} corresponding to intermolecular vibrations of several hundreds of DMSO molecules. These peaks are in line with previously reported results.^[5n,19] Note that the CSC stretching vibrations cannot be observed, reported between 700 – 650 cm^{-1} , due to absorption of the polyethylene window in the detector.

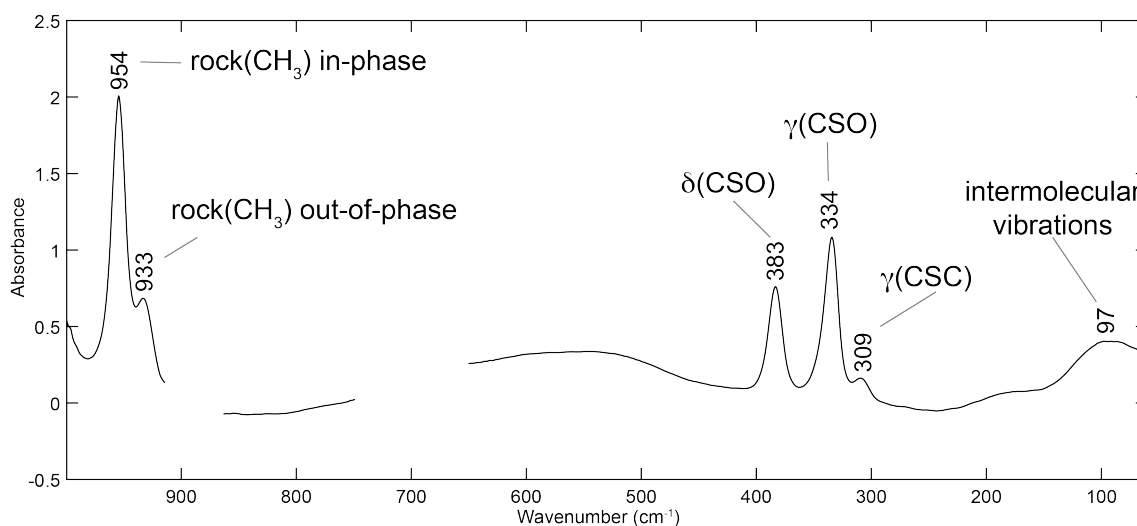


Figure 4.15. SR-FIR spectrum of DMSO in a 20 μm pathlength diamond window liquid cell. Beamsplitter (Mylar) and detector (polyethylene window) are cut ($\sim 920 - 870 \text{ cm}^{-1}$ and $\sim 740 - 650 \text{ cm}^{-1}$, respectively) and the spectrum is smoothed (31 points). Resolution = 1 cm^{-1} . Notations used: rock = rocking mode, δ = in-plane angle bending, γ = out-of-plane angle bending.

Elevated concentrations had to be used to observe clear absorption for **1** (76 mM, 35.8 mg mL^{-1} , 0.54 mol%) and its synthetic precursor **2** (54 mM, 23.6 mg mL^{-1} , 0.38 mol%). The spectra of **1** and **2** in a 100 μm pathlength cell are shown in Figure 4.16. The pyridine bending mode, $\gamma(\text{py}, 4)$, is located at 777 cm^{-1} and 772 cm^{-1} for **1** and **2** respectively. The platinum to oxygen stretching vibration, $\nu(\text{Pt-OH})$, can be clearly observed at 567 cm^{-1} for **1**. The platinum to nitrogen stretching vibration for **1** and **2**, $\nu(\text{Pt-N}_3)$, are located at 410 cm^{-1} and 408 cm^{-1} on the shoulder of the DMSO vibration, $\delta(\text{CSO})$. The out-of-plane bending mode of DMSO, $\gamma(\text{CSC})$, at 309 cm^{-1} can be used as a reference and allows for the normalisation of spectra. Please note that the other stronger vibrations of DMSO ($\delta(\text{CSO})$ at $\sim 380 \text{ cm}^{-1}$ and $\gamma(\text{CSO})$ at $\sim 330 \text{ cm}^{-1}$) are not considered due to line saturation caused by the 100 μm pathlength and are therefore not true values.

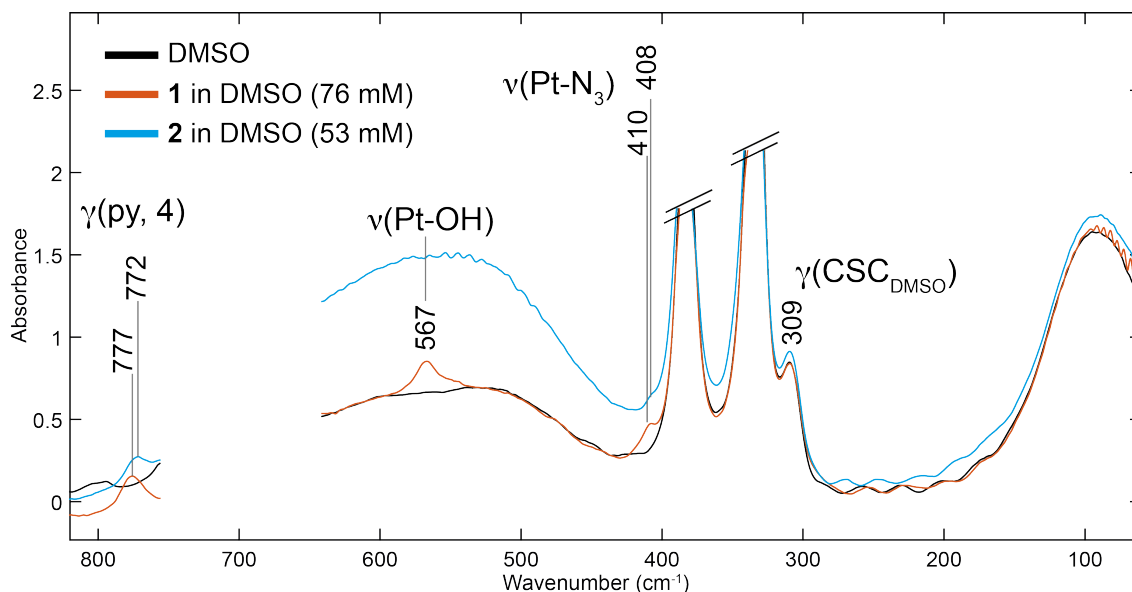


Figure 4.16. SR-FIR spectra of DMSO, **1** (76 mM in DMSO) and **2** (53 mM in DMSO) in a 100 μm pathlength diamond window liquid cell. Spectral regions are cut to remove absorption of the polyethylene window in the detector and the spectra are smoothed (15 points). Resolution = 1 cm^{-1} . Notations used: ν = stretch, γ = out-of-plane angle bending. The description of the pyridine mode is given in Wilson's notations, as described previously.^[15-16]

The raw and second derivative spectra of the photodecomposition of **1** in DMSO (76 mM) are shown in Figure 4.17. Second derivative spectra are acquired to enhance the separation of overlapping peaks and exclude broad background features. Please note that in second derivative spectra, peak minimum correspond to peak maxima in the un-derivatised spectra. Rapid decrease of the $\nu(\text{Pt-N}_3)$ vibration is observed in the first five minutes, after which it slows down and the peak shifts from 410 to 409 cm^{-1} (insignificant as spectra were recorded at a resolution of 1 cm^{-1}). After 1 h and 15 min of irradiation, a new peak is gleaned at 419 cm^{-1} , which continues to evolve until the last spectrum is recorded, 7 h 15 min later (Figure 4.17B). The $\nu(\text{Pt-OH})$ vibration continues to decrease throughout irradiation, with complete removal observed after 7 hours 15 minutes. Furthermore, the $\gamma(\text{py}, 4)$ shifts from 777 cm^{-1} to 772 cm^{-1} during irradiation. The average peak intensities (four replicates) of the $\nu(\text{Pt-OH})$ and $\nu(\text{Pt-N}_3)$ vibrations during irradiation are plotted in Figure 4.18 (567 cm^{-1} , 419 cm^{-1} and 409 cm^{-1} normalized second derivative). A near identical trend is observed for the 567 cm^{-1} and 409 cm^{-1} vibrations, which indicates a same rate of removal for the $\nu(\text{Pt-OH})$ and $\nu(\text{Pt-N}_3)$ vibrations

in terms of peak intensity and sharpness of the band. Irradiation of DMSO in 20 μm and 100 μm pathlength liquid cells was carried out and no changes were observed (section 4.8, Figure S4.6).

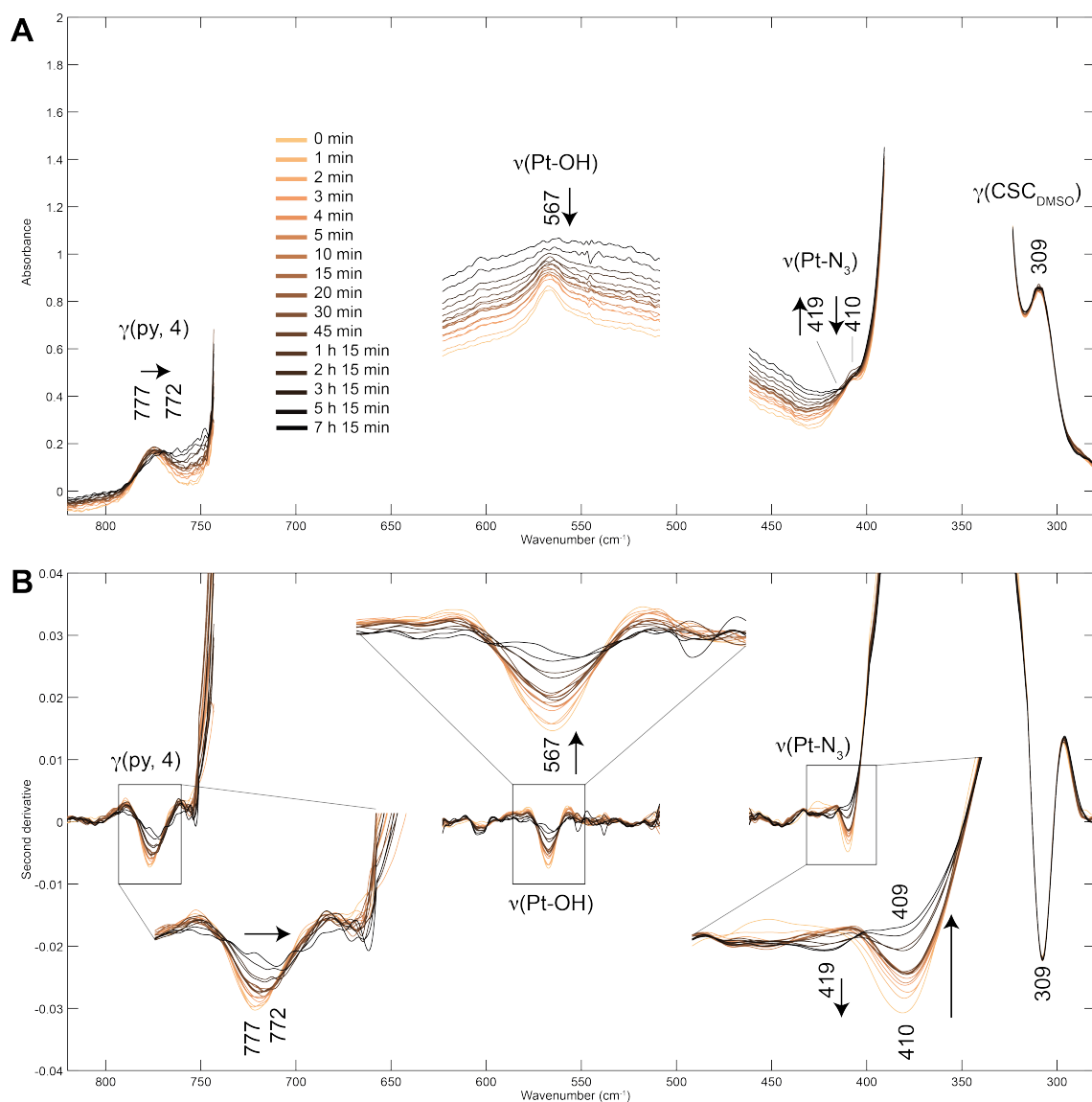


Figure 4.17. SR-FIR spectra (A) and second derivative spectra (B) of the photodecomposition of **1** in DMSO (76 mM) under 355 nm irradiation, including selected peak labels. A) Raw spectra are cut to highlight peaks. B) Second derivative (65 smoothing points, weighted tails), normalized to 309 cm^{-1} . Arrows indicate increase, decrease or shift direction of the vibration during irradiation. Resolution = 1 cm^{-1} . Notations used: ν = stretch, γ = out-of-plane angle bending. The description of the pyridine mode is given in Wilson's notations, as described previously.^[15-16]

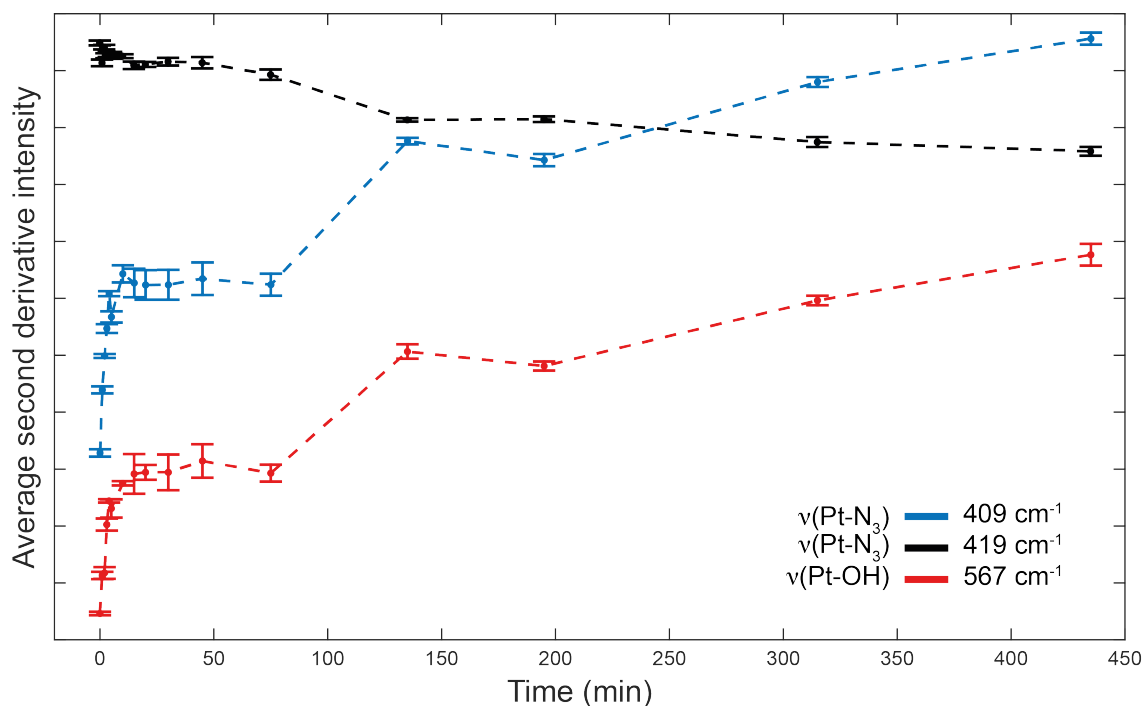


Figure 4.18. Average second derivative intensities of the $\nu(\text{Pt-OH})$ and $\nu(\text{Pt-N}_3)$ vibrations (567 , 419 and 409 cm^{-1}) of four measurements. Standard deviations are depicted as error bars, relative second derivative intensities shown.

The next set of experiments was carried out to study the effect of **1** on DNA by SR-FIR. Deoxyribonucleic acid sodium salt from calf thymus (CT-DNA) was used, and samples were freshly dissolved in water (15.8 mg/mL) prior to each measurement. The smallest spacer ($5 \mu\text{m}$) was used due to the strong absorption of water, allowing a spectral window between $300 - 45 \text{ cm}^{-1}$. Figure 4.19 shows the spectrum of water (MiliQ) by SR-FIR, highlighting the broad band peaking at $\sim 194 \text{ cm}^{-1}$ which corresponds to the restricted translation mode of stretching hydrogen bonds ($\nu(\text{O-H}\cdots\text{O})$).^[3,5g] A second broad feature can be observed at $\sim 64 \text{ cm}^{-1}$, which has been previously attributed to a β -band (bending of the intermolecular hydrogen bonds).^[3,20]

Multiple spectra of water, CT-DNA in water and CT-DNA + **1** were recorded in the dark and after exposure to irradiation (355 nm). A list of recorded spectra and experimental replicates is tabulated in Table 4.4. No considerable differences can be observed between individual spectra, as shown in Figure 4.20, containing six selected spectra showing slight intensity differences.

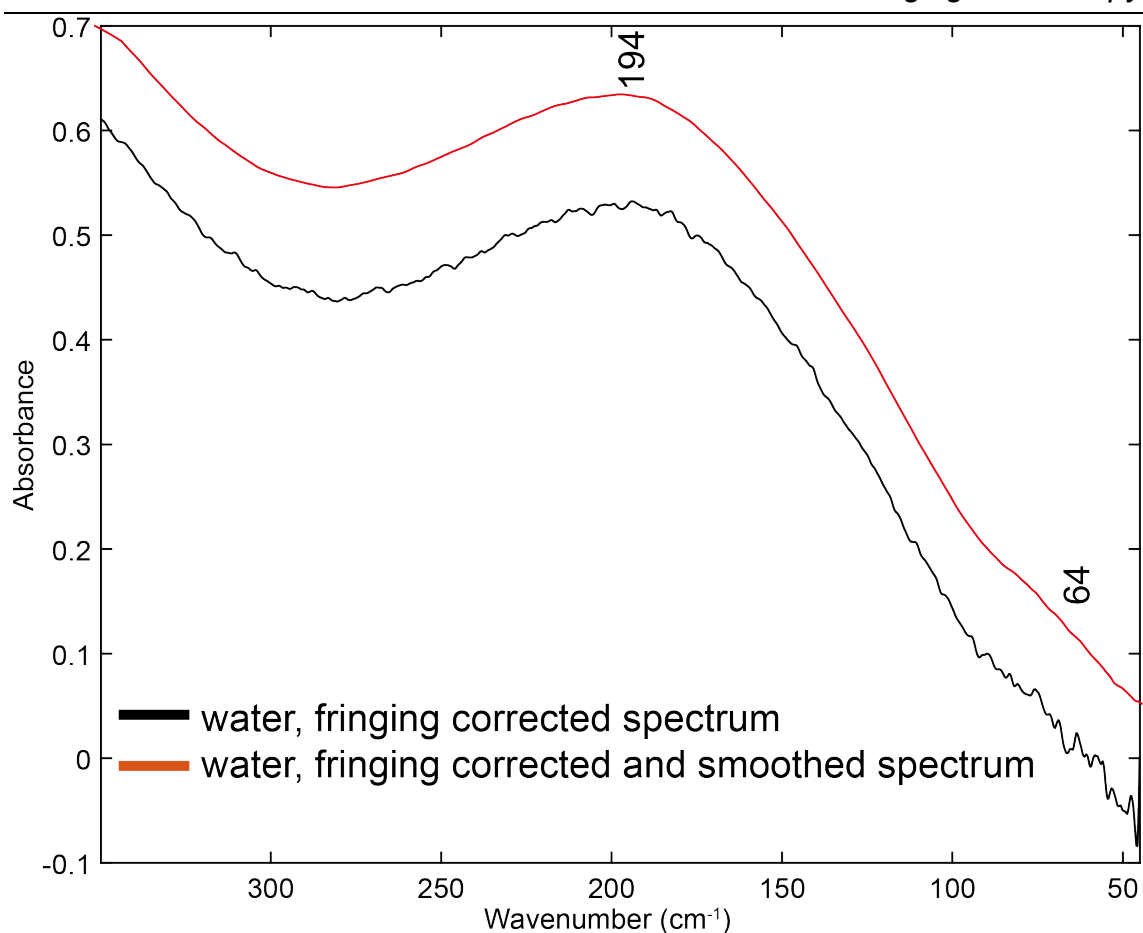


Figure 4.19. SR-FIR spectra of water (black = fringing corrected, red = smoothed, 65 points) in a 5 μm pathlength diamond window liquid cell. Offset between smoothed and raw spectra is artificially created for clarity. Peak labels indicate the stretching and bending mode of intermolecular hydrogen bonding at $\sim 194\text{ cm}^{-1}$ and $\sim 64\text{ cm}^{-1}$ respectively.

Table 4.4. SR-FIR spectra recorded of liquid/solution samples. CT-DNA in water (15.8 mg/mL), **1** (3.0 mM, 1.5 mg/mL).

Component	Irradiation , 355 nm (min)	Experimental replicates	Total spectra obtained
water	-	10	27
	5	1	4
	30	1	4
CT-DNA	-	7	59
	5	2	8
	30	2	8
CT-DNA + 1	-	2	11
	5	1	12

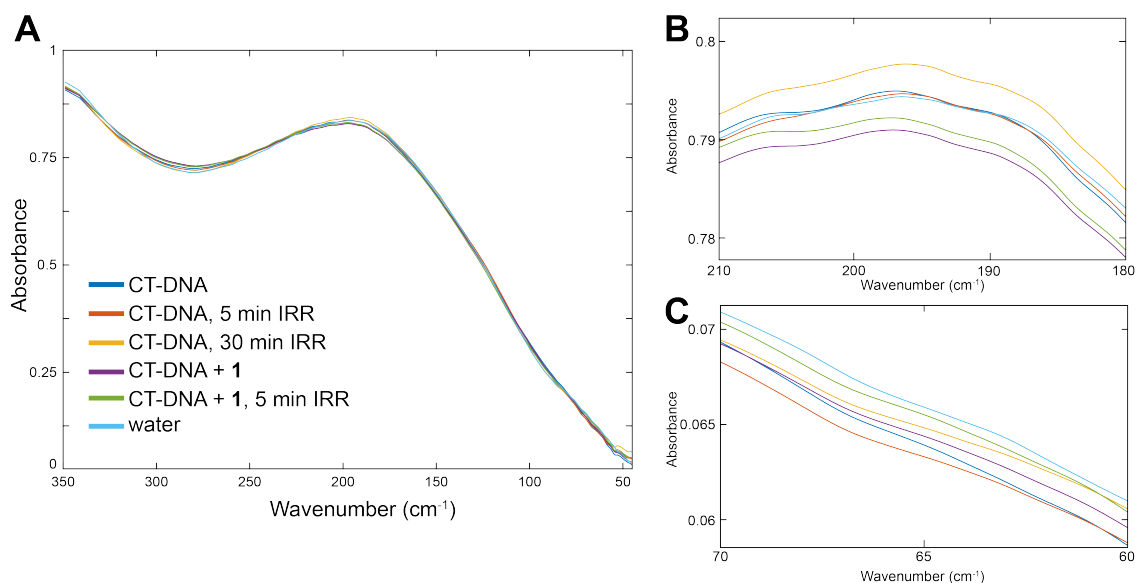


Figure 4.20. SR-FIR spectra of water, CT-DNA and CT-DNA+1 with and without 355 nm irradiation (IRR) in a 5 μm pathlength diamond window liquid cell. Spectra are fringing corrected, smoothed (65 points) and normalized (SNV). A) full spectral region. B,C) 210 – 180 cm^{-1} and 70 – 60 cm^{-1} highlighting the minor differences between spectra.

Principal Component Analysis (PCA) was carried out in an effort to identify any variation between spectra, samples and experiments. Three Principal Components (PCs) were selected, capturing 95% of the variance. The resulting PCA scores and loading plots of PC1 and PC2 are shown in Figure 4.21, whereas PC1 and PC2 vs. PC3 plots can be found in section 4.8, Figure S4.7. Spectral replicates cluster well in the score plot of PC1 vs. PC2. However, experimental replicates do not, as shown by the selected bold symbol labels in Figure 4.21A. Experimental replicates were found on opposite sites of the plots in all cases. The loading plots corresponding to PC1 and PC2 reveal that the

variation captured by the PCA is due to difference in offsets between spectra, mainly at $\sim 280\text{ cm}^{-1}$ (negative in PC1, positive in PC2) and between $120 - 50\text{ cm}^{-1}$ (Figure 4.21B). These results are further elaborated on in the discussion.

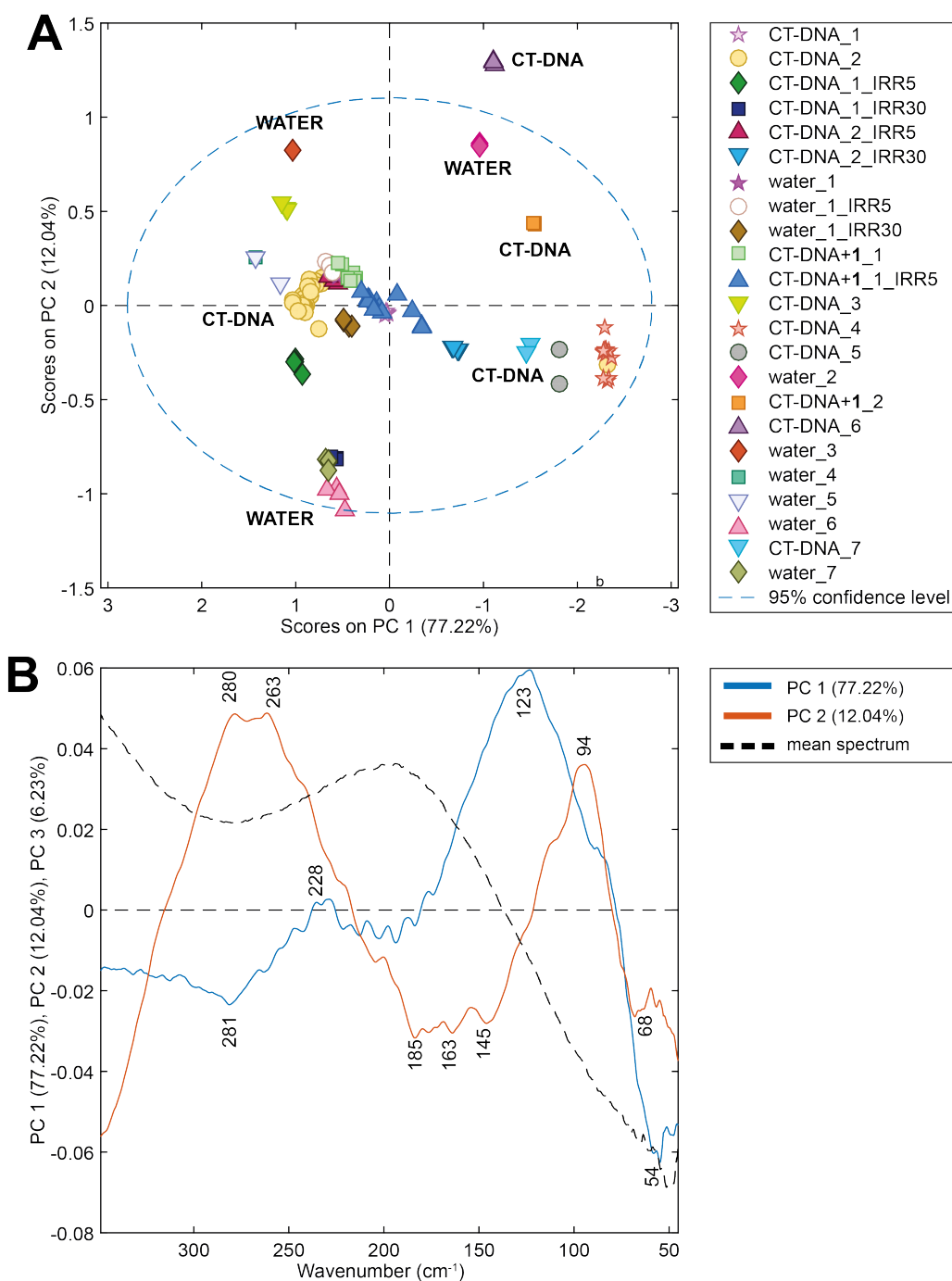


Figure 4.21. PCA score and loading plots for the SR-FIR spectra of water, CT-DNA and CT-DNA+1 with and without 355 nm irradiation (IRR) in a $5\ \mu\text{m}$ pathlength diamond window liquid cell. A) Score plot PC1 vs. PC2, bold labels of water and CT-DNA highlight the variation between experimental replicates. B) Loading plots and peak labels of PC1 (blue), PC2 (red) and the mean spectrum of the data set (black dashed line) for comparison. IRR = irradiation time of 5 or 30 minutes.

4.2.3 Synchrotron Radiation Infrared Microspectroscopy – Live Single Cell Study

The acute myeloid leukaemia cell line, K562, was used to study the effect of **1** on live cells by synchrotron radiation infrared microspectroscopy (SR-IRMS) in the mid-infrared region ($3800 - 900 \text{ cm}^{-1}$). Cells were treated as described in the experimental section and an overview of the measured samples is shown in Figure 4.22.

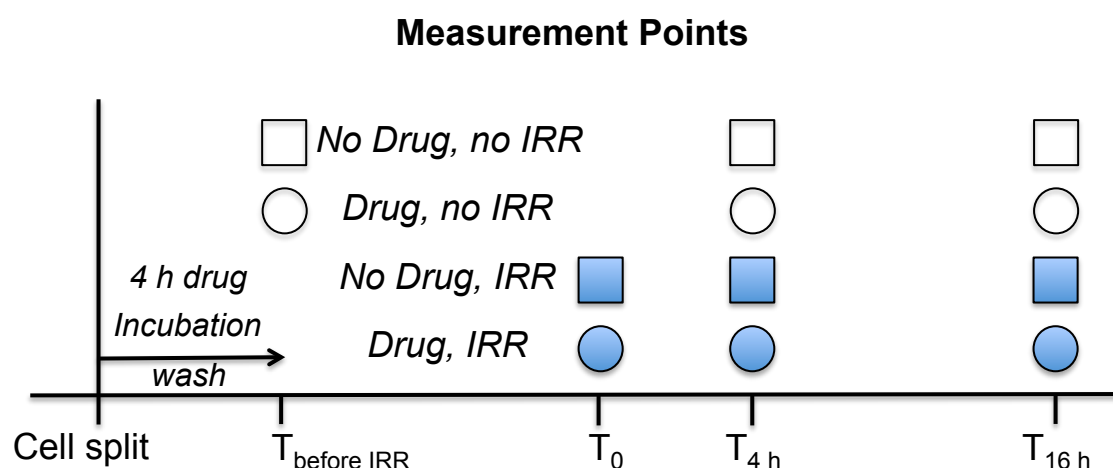


Figure 4.22. Overview of K562 cell treatment and SR-IRMS measurement points (60 single cell spectra per point, carried out in triplicate). Drug = **1**, IRR = irradiation, square = no addition of **1**, circle = addition of **1**, white = cells not exposed to irradiation, blue = cells exposed to 350 nm irradiation.

The average second derivative spectra (to enhance spectral features) of each time point were investigated prior to statistical analysis. As an example, differences between the spectra are outlined in Figure 4.23 showing the average second derivative spectra of cells not treated with **1** at time point 0 and no irradiation vs. cells treated with **1** and irradiated at time point 0, 4 h and 16 h. Other average spectra were omitted for clarity and will be discussed in more detail below. Selected peak labels are included in Figure 4.23, covering potential marker bands to monitor throughout the full spectral analysis (please note that in second derivative spectra, peak minimum correspond to peak maxima in the un-derivatised spectra).

In the high wavenumber region (Figure 4.23A), there is a change in ratio to the $\nu_{\text{sym}}(\text{CH}_3)$ vibration related to cellular lipids at 2893 cm^{-1} and 2875 cm^{-1} . Furthermore, a decrease in intensity of lipid vibrations at 2924 cm^{-1} and 2852

cm^{-1} ($\nu_{\text{asym}}(\text{CH}_3)$ and $\nu_{\text{sym}}(\text{CH}_2)$) is observed four hours after irradiation, whereas these vibrations become equal to untreated cells after 16 hours. Several differences can be observed between 1800 cm^{-1} and 1040 cm^{-1} (Figure 4.23B): the B-DNA base pairing vibration at 1716 cm^{-1} , several of the amide I vibrations (1655 cm^{-1} , 1645 cm^{-1} 'water', 1628 cm^{-1}), the amide II vibration at 1552 cm^{-1} , the A-DNA and ribose vibration at 1173 cm^{-1} and the RNA vibrations at 1173 cm^{-1} , 1124 cm^{-1} and 1119 cm^{-1} .

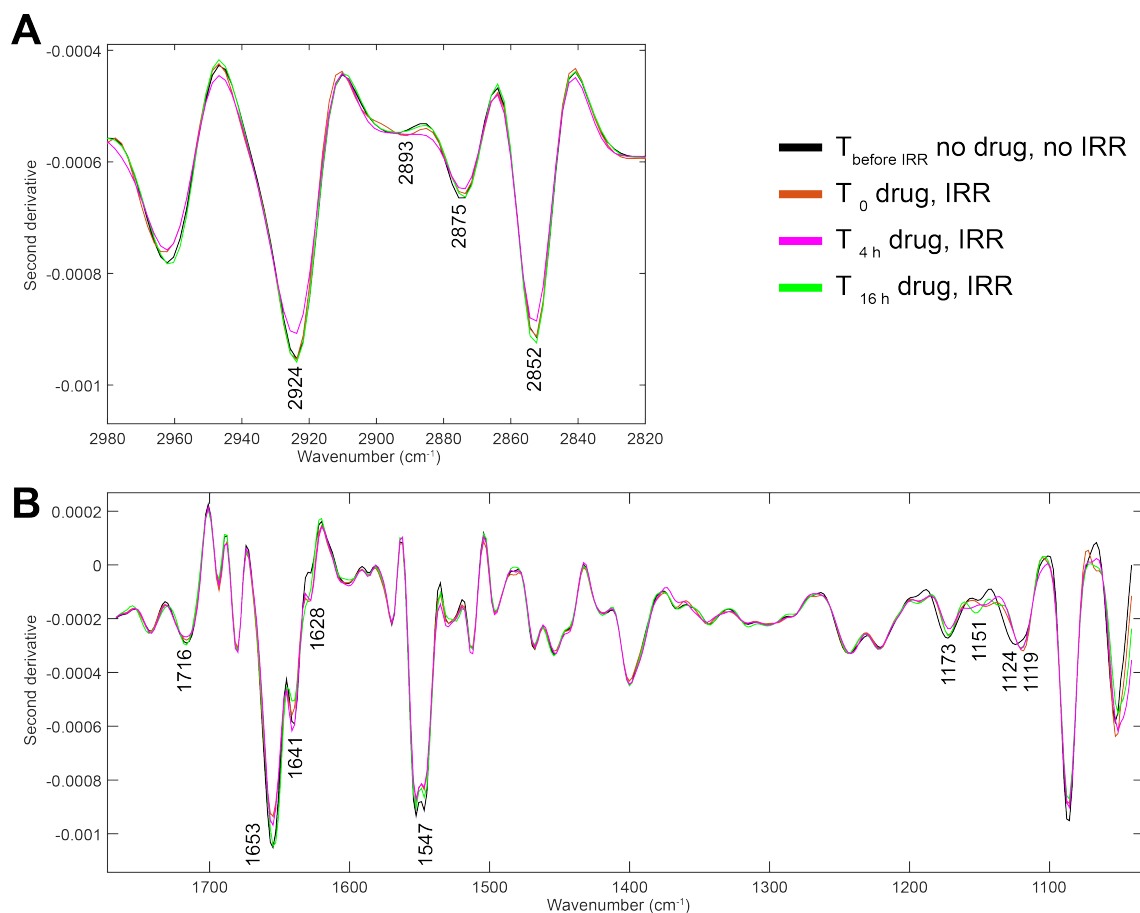


Figure 4.23. Average second derivative spectra of K562 cells by SR-IRMS including selected peak labels (A: $2980 - 2820 \text{ cm}^{-1}$, B: $1800 - 1040 \text{ cm}^{-1}$). Four measurement points are depicted for comparison: time point before irradiation, no drug and no irradiation vs. time points 0, 4 h, 16 h with treatment of 1 and irradiation.

Pre-processing was applied to the raw spectra as outlined in the experimental section and outliers were removed with at least 50 spectra per time point per replicate remaining. Six individual PLS-DA's were setup to discriminate between the different factors applied to the cell: time, drug, irradiation and combinations of the three. Each factor was compared vs. cells not exposed to irradiation, drug and time.

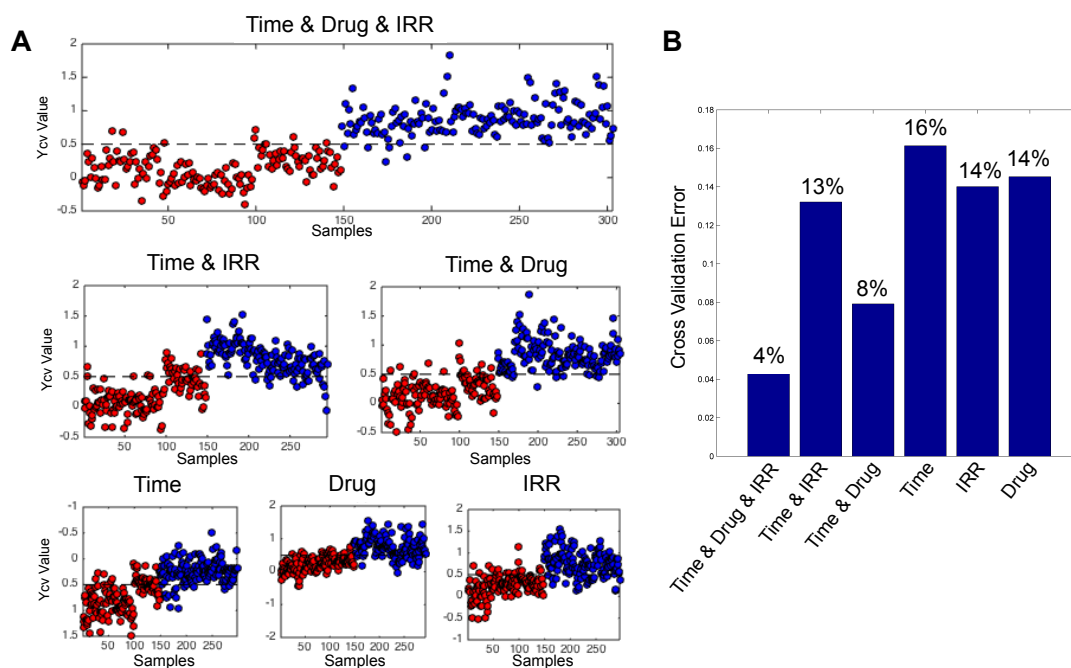


Figure 4.24. Ycv values (A) and cross validation errors (B) of the PLS-DA's of the effect of time, irradiation and/or drug (blue) vs. no time, no irradiation and no drug (red). IRR = irradiation, drug = 1 and time = 4 hours.

The Ycv values and cross validation errors of the PLS-DA's are depicted in Figure 4.24. The largest separation between 0 and 1 for the Ycv values is observed for the cells affected by time, drug and irradiation. The cross validation errors similarly reflect this with the lowest percentage obtained for time, drug and irradiation, whereas larger cross validation errors are obtained for the independent and control factors (> 8%) on the cells.

The regression vectors for each PLS-DA are shown in Figure 4.25. Inspection of the regression vectors from the PLS-DA reveal the main contributions of the Ycv value plots of the control factors (time, drug, irradiation and time and drug) to be related to the DNA vibration underlying the amide I at 1662 cm^{-1} and the symmetric phosphate vibration ($\nu_{\text{sym}}(\text{PO}_2^-)$) at 1084 cm^{-1} . The regression vector for the time and irradiation factor has one main additional contribution that stands out at 1564 cm^{-1} (shoulder of the amide II vibration) and two minor contributions from the B-DNA basepairing vibration and water from the amide I vibration at 1713 cm^{-1} and 1639 cm^{-1} , respectively. Time, drug and irradiation factor, however, clearly have additional main spectral contributions in the regression vector. These include, $\nu_{\text{sym}}(\text{CH}_3)$ at 2875 cm^{-1} , the more prominent B-DNA and A-DNA basepairing vibrations at 1713 cm^{-1} and 1705 cm^{-1}

respectively, the amide II vibration at 1558 cm^{-1} , 1367 cm^{-1} on the shoulder of the $\nu(\text{COO}^{2-})$ vibration of fatty acids and amino acid side chains and the A-DNA and ribose vibration at 1178 cm^{-1} .

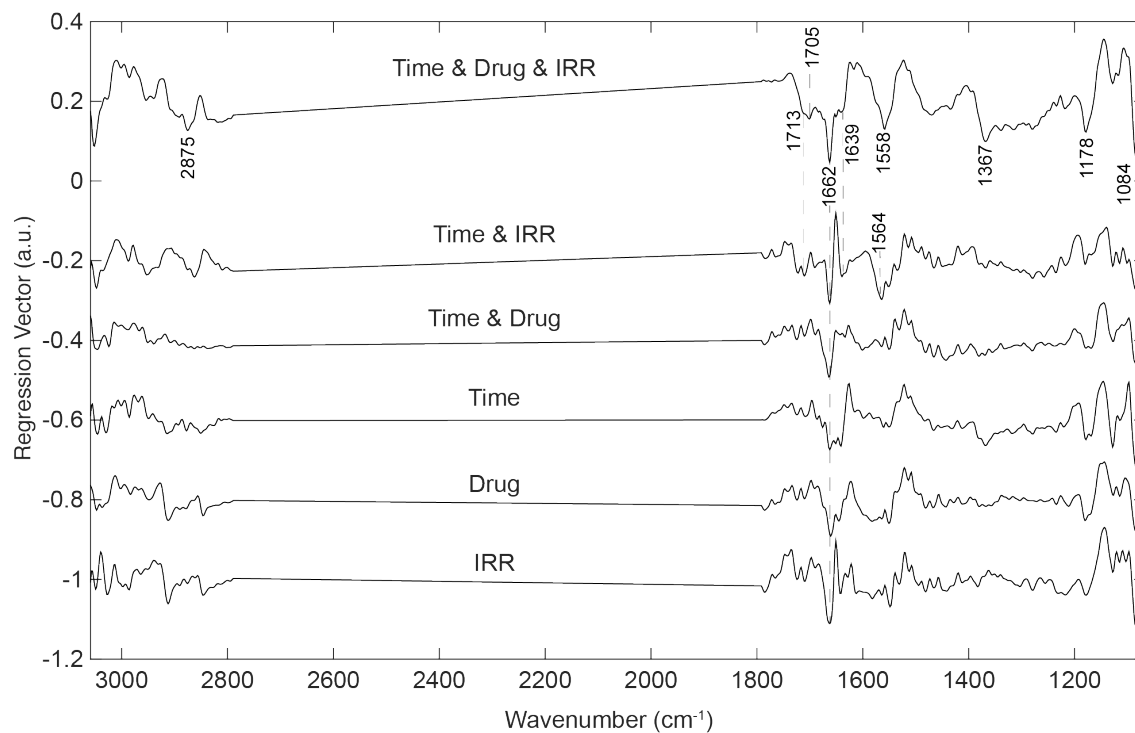


Figure 4.25. Regression vectors obtained for each PLS-DA, including selected peak labels. IRR = irradiation, drug = 1 and time = 4 hours.

4.3 Discussion

4.3.1 Synchrotron Radiation Attenuated Total Reflection Far-Infrared

New experimental setups for the THz/Far-IR beamline were pursued to allow for faster measurements and reduced sample preparation times. ATR is a commonly used infrared method allowing for a range of sample compositions (solid, liquid, film) to be measured without prior sample preparation. Prior to this work, only one such SR-ATR setup was known to exist, at the SOLEIL synchrotron in France.^[21]

Alignment of an ATR accessory (Specac golden gate ATR) was possible using SR and Global infrared sources, with reference material spectra obtained using a bench-top ATR setup matching the SR spectra. The Specac golden gate ATR accessory limited the spectral range to 480 cm^{-1} (lowest) due to the ZnSe condensing optics which focus the infrared beam on the 4 mm x 4 mm ATR crystal. The feasibility of a SR ATR setup was tested by comparison of the internal Global to the SR infrared source by varying the infrared beamspot size. Global infrared sources are typically weaker in the far-infrared region ($< 400\text{ cm}^{-1}$), unfortunately, this could not be tested with this particular setup. Nevertheless, it showed the superiority of SR over Global at beamspot sizes smaller than 2 mm. Furthermore, far-infrared capable ATR accessories typically do not contain condensing optics and would therefore not limit the spectral region and the high collimation of SR starts to become key with smaller sample areas. The outcome of this study enabled the follow up studies using a far-infrared capable ATR accessory.

The Bruker platinum ATR accessory was used to obtain rapid collection of solid sample spectra of metal complexes, DNA nucleobases and malaria infected red blood cells. The previously measured SR-FIR spectra of **1**, **2** and **3** could be matched with the SR-ATR-FTIR spectra. Furthermore, the photodecomposition using identical experimental preparations as in Chapter 3.1 was attempted. SR-ATR-FIR spectra of irradiated time points of **1** were limited to two time points (10 min and 22 h) due to time restrictions caused by extended amounts of time the spectrometer took to reach an adequate vacuum level to use the SR after samples were deposited (~3 – 5 h). This is likely caused by extended

periods of time (~1 h) to deposit liquid samples on the ATR followed by evaporation, allowing water and CO₂ accumulation inside the sample chamber (ultimately circumvented with the out-of-vacuum sample setup). The deposition of samples using a mid-infrared ATR-FTIR setup as outlined in Chapter 3.1 took considerably less amount of time (1 – 5 min). This is due to two factors, first the Si-ATR accessory used in Chapter 3.1 has a cavity that allows for samples to be deposited effortlessly under a N₂ flow on the ATR crystal, whereas the platinum ATR crystal is on a flat surface allowing solution to evaporate outside the measurable area (Figure 4.7). Second, the penetration depth of far-infrared beam is considerably larger than in the mid-infrared by a factor of at least 2 (depending on the refraction index of the sample and ATR crystal, Chapter 1, Figure 1.14). Therefore, deposition of several layers of sample was required in order to obtain high quality spectra.

Initially, the effect of dissolving **1** in water, followed by evaporation prior to measurement showed the effect on the platinum to azide and platinum to hydroxide related vibrations. The changes effecting the hydroxide and azide vibrations are in line with our previously reported results the mid-infrared ATR studies of **1** in Chapter 2.1, with evident changes to the intermolecular interactions effecting the shifts of the main vibrations.^[16] The pyridine vibrations in the far-infrared are combination bands with platinum to azide and platinum to hydroxide vibrations, such as the $\nu(\text{Pt-py})$ (complete description: $\nu_{\text{asym}}(\text{py-Pt-py})$, $\text{scr}(\text{N}_3\text{-Pt-N}_3)$, $\text{rot}(\text{Pt-OH})$ out-of-phase). Thus, in turn these vibrations are more significantly affected (from 257 cm⁻¹ to 244 cm⁻¹) than the pyridine vibrations in the mid-infrared region as reported in Chapter 2.1 (± 5 cm⁻¹).

The time points of 420 nm irradiation investigated were 10 min and 22 h. 10 min was selected as it showed the presence of hydroxide vibrations ($\nu(\text{OH}_{\text{Pt-OH}})$), as well as multiple azide vibrations ($\nu_{\text{asym}}(\text{N}_3)$) in the mid-infrared region (Chapter 3.1). Whereas, 22 h was selected to investigate the final product postulated to be *trans*-[Pt(py)₂(OH/H₂O)₂]^{0/1+/2+} (Chapter 3.1). Interestingly, after 10 min of irradiation, both the platinum to azide, $\nu(\text{Pt-N}_3)$, and platinum to hydroxide, $\nu(\text{Pt-OH})$, vibrations split up into multiple vibrations shifting both to lower and higher wavenumber vibrations ($\nu(\text{Pt-OH})$, from 559 cm⁻¹ to 555 cm⁻¹ and 507 cm⁻¹, $\nu(\text{Pt-N}_3)$ from 410 cm⁻¹ and 406 cm⁻¹ to 440, 419 and 384 cm⁻¹). This confirms that multiple platinum species are present in the first 20 minutes of irradiation (after which $\nu(\text{OH}_{\text{Pt-OH}})$ is completely removed according to mid-infrared

spectra). The difference in the $\nu(\text{Pt-OH})$ vibrations (-47 cm^{-1}) and the $\nu(\text{Pt-N}_3)$ vibrations ($+21 \text{ cm}^{-1}$ and -35 cm^{-1}), going from 0 to 10 min of irradiation, are substantially larger compared to the changes observed in the mid-infrared region ($\Delta \text{ cm}^{-1} \leq 15 \text{ cm}^{-1}$, Chapter 3.1). Increasing and decreasing bond lengths, geometry changes and/or ligand release could result in the observed changes. However, only educated guesses can be made at this point, as more irradiation time points and accompanied computational studies have to be carried out in order to provide more definite results. The $\nu(\text{Pt-OH})$ vibration at 507 cm^{-1} could be the result of a single hydroxide ligand release or substantial elongation of the platinum to oxygen bond length. The $\nu(\text{Pt-N}_3)$ vibration at 440 cm^{-1} could be the result of single azido ligand release, in line with the increase in the mid-infrared for $\nu_{\text{asym}}(\text{N}_3)$ for the *trans*-[Pt(N₃)(py)₂(OH/H₂O)] species. The $\nu(\text{Pt-N}_3)$ vibration at 384 cm^{-1} could be related to the previously observed decrease in $\nu_{\text{asym}}(\text{N}_3)$ in the first 10 minutes, as highlighted by the principal component analysis of the mid-infrared spectra of the photodecomposition of **1** (Chapter 3.1). The spectra of **1** after 22 h of irradiation confirmed our suspected final product of *trans*-[Pt(py)₂(OH/H₂O)₂]^{0/1+/2+}, with one broad platinum to oxygen (water) vibration present at 545 cm^{-1} , the out-of-plane pyridine bending mode at 468 cm^{-1} , the scissoring mode of oxygen to platinum to oxygen at 295 cm^{-1} and the platinum to nitrogen (pyridine) stretching vibration at 237 cm^{-1} .

The above limitations of increased system evacuation to vacuum were to be circumvented by the manufacture of an ATR accessory with the sample area remaining outside of vacuum. The modified Pike GladiATR™ single reflection, heated ($< 300 \text{ }^\circ\text{C}$) ATR was finalized in June 2017 with additional adapters (high-pressure and liquid cell), opening up the far-infrared field to rapid analysis of otherwise difficult to obtain spectra. Unfortunately, this work could not be progressed further within this PhD candidature.

4.3.2 Transmission Synchrotron Radiation Far-Infrared – Liquid cell *in situ* Irradiation

A set of new liquid cells (first users) was investigated together with a novel SR and pulsed laser setup to allow for irradiation of liquid samples without breaking vacuum. Several experimental difficulties were encountered, which needed to be addressed. As outlined in the results, one of the major problems met was the interference phenomenon called fringes caused by internal in-phase

reflections.^[18,22] The custom built diamond windows of the liquid cells were wedged in order to reduce such fringing effects, whereby the out-of-phase reflections should not interfere, as shown in Figure 4.26. Unfortunately, fringes were still present and it is possible that additional fringes are introduced due to angled reflections. Furthermore, the infrared reflections are dependent on the substance in between the windows, as well as the pathlength. There is extensive literature reported attempting to address these artefacts, with results shown to completely negate these artefacts by optimising wedge angle to pathlength and refractive index of the measured substance.^[18,23] Time, nor the liquid cells, allowed for such optimisations and these would be recommended to be carried out separately in the future by the THz/Far-IR beamline at the Australian Synchrotron.

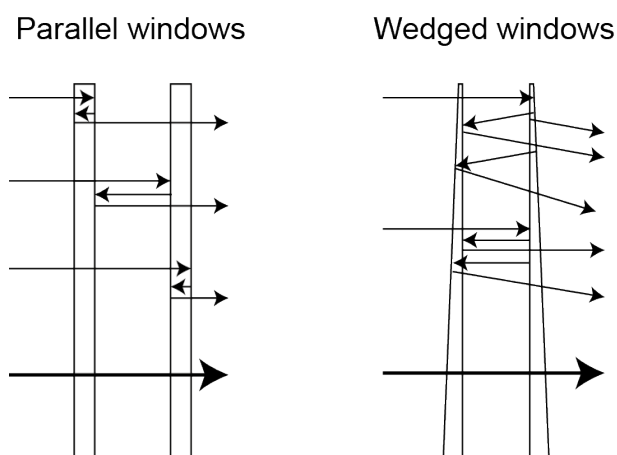


Figure 4.26. Schematic representation of parallel and wedged windows showing possible in-phase (straight) and out-of-phase (angled) reflections. The angle of the wedged windows is exaggerated for clarity.

The fringing artefacts were not reproducible within experimental replicates. This could be due to leakage of the cell and/or slight differences in pathlength caused by the tightening of the cell. In turn, this meant that solvent spectra could not be used as a background reference. The fringes were corrected for as described in the section 4.2.2 and vacuum background (no liquid cell, no fringing artefact) was used to obtain absorbance spectra. While a majority of the fringes could be accounted for with the corrections, it is likely that other interferences were recorded inside or too close to the spectral part of the interferogram to allow for corrections. This in turn resulted in noisy baselines, whereby one cannot distinguish between noise and weak signal of solutes.

Other issues encountered were leakage of the cells inside the spectrometer and cracks developing in the windows of the diamond liquid cell.

The use of water to study the photodecomposition of **1** *in situ* was not feasible due to the pathlength limitations (5 μm) when using water (due to its strong far-infrared absorption). This in turn, did not allow for distinguishing between noise and infrared absorptions of **1**. Therefore, it was decided to use DMSO to allow higher concentrations and longer pathlengths to monitor the photodecomposition. The SR-FIR spectra of **1** and its synthetic precursor **2** in DMSO were obtained, revealing their platinum to oxygen, $\nu(\text{Pt-OH})$, and platinum to nitrogen, $\nu(\text{Pt-N}_3)$, stretching vibrations as well as a pyridine bending mode ($\gamma(\text{py}, 4)$). The $\nu(\text{Pt-OH})$ vibration can be clearly observed at 567 cm^{-1} for **1**, slightly shifted compared to the SR-ATR-FIR (559 cm^{-1}) of hydrated **1** and SR-FIR (540 cm^{-1}) of crystalline **1**. The platinum to nitrogen stretching vibration of **1** and **2**, $\nu(\text{Pt-N}_3)$, are located at 409 cm^{-1} and 408 cm^{-1} on the shoulder of the DMSO vibrations. These are within 2 cm^{-1} of the main vibrations of the spectra by both transmission SR-FIR (crystalline) and SR-ATR-FIR (crystalline and hydrated) and could be insignificant as spectra were recorded at a resolution of 1 cm^{-1} . However, the possibility of other $\nu(\text{Pt-N}_3)$ vibrations underlying DMSO cannot be ruled out. The pyridine bending mode, $\gamma(\text{py}, 4)$, located at 777 cm^{-1} and 772 cm^{-1} for **1** and **2** respectively, has not been recorded before by SR-FIR prior to this. Their corresponding solids show identical wavelengths for this vibration by ATR-FTIR at 777 cm^{-1} for **1** and 772 cm^{-1} for **2** (Chapter 2.1).

Upon irradiation of **1**, $\gamma(\text{py}, 4)$ shifts from 777 cm^{-1} to 772 cm^{-1} , in line with the photodecomposition results described in Chapter 3.1 by ATR-FTIR. The decrease of both $\nu(\text{Pt-N}_3)$ and $\nu(\text{Pt-OH})$ of **1** in DMSO (76 mM) could be monitored *in situ* upon 355 nm irradiation. Both vibrations appeared to decrease rapidly in the first five minutes and no apparent difference in rate of removal was observed. A new peak is observed at 419 cm^{-1} , which is identical to one of the $\nu(\text{Pt-N}_3)$ vibrations of **1** observed after 10 minutes of irradiation by SR-ATR-FTIR. In Chapter 3.1, an increase in $\nu_{\text{asym}}(\text{N}_3)$ vibration of **1** is observed and is assigned to one of the photodecomposition intermediates, *trans*-[Pt(N₃)(py)₂(solvent)]. This could be a possible intermediate formed in this work. The work described in Chapter 3.1 monitors the photodecomposition based on the individual ligand vibrations rather than metal to ligand vibrations.

This revealed the complete removal of the $\nu(\text{OH}_{\text{Pt-OH}})$ at a rapid rate, whereas it took extended times of irradiation to remove $\nu_{\text{asym}}(\text{N}_3)$ completely. Both results are not directly comparable due to the use of different solvents, concentrations and irradiation wavelength and do require further investigation in order to draw any conclusions. However, the SR-FIR results might suggest that the hydroxido ligand undergoes chemical changes prior to release, which cannot be monitored by the $\nu(\text{OH}_{\text{Pt-OH}})$ in the mid-infrared region.

Further studies on **1** were attempted by investigation of its effect on DNA in the far-infrared region. While there are reports of dried and partly hydrated DNA and protein spectra in the far-infrared region that reveal potential marker bands, spectral reproducibility remains a problem.^[4c-f,5e,24] The hydration layers around such biomolecules can be a used study higher-order structures. Furthermore, Globus et al. reported the correlation between oscillator strength and hydration levels of herring DNA films prepared at different water-to-DNA concentrations.^[5e] Whilst not completely understood, the observed spectral bands reduce in intensity when the amount of water used to prepare the films is reduced. This suggests that the vibrational modes in the far-infrared region of DNA occur at the interface between DNA and the surrounding media.^[5e] Their reported DNA spectra are in line with our results for CT-DNA, revealing the broad intermolecular hydrogen vibrations at $\sim 194 \text{ cm}^{-1}$ and $\sim 64 \text{ cm}^{-1}$. The fine structure of these spectra was not further investigated due to the uncertainty between noise caused by fringing artefacts or weak DNA vibrations. Instead, smoothing of spectra was carried out to obtain clean broad peaks for the intermolecular hydrogen stretching and bending modes of water. No apparent variation between water, CT-DNA or CT-DNA+**1** spectra with or without 355 nm irradiation could be observed in the smoothed spectra. Further examination of the data by principal component analysis showed the reproducibility within spectral replicates, although no significant changes to the intermolecular hydrogen bond vibrations could be observed. It could be that the hydration layers around CT-DNA were too large in order to identify any differences even though very high concentrations of CT-DNA in water were used (leading to viscous solutions). The improvement of better liquid cells might improve the feasibility of such studies and could reveal exciting new ways to study the biochemistry of life.

4.3.3 Synchrotron Radiation Infrared Microspectroscopy – Live Single Cell Study

Cells were treated for four hours to allow uptake of **1** into the cell, prior to washing away remaining **1** in the growth medium. This was chosen to reflect the clinical application of **1**, in which cancerous areas would be irradiated locally. Therefore, relatively high concentrations of **1** (50 μM) were used to promote uptake in short times to fit within the limited amount of continuous experimental time that can be obtained at synchrotrons. **1** is known to show rapid platinum accumulation in cells in the dark in just an hour.^[25] Pizarro et al. reported an uptake of ~ 20 ng of platinum per 10^6 cells for **1**, whereas ~ 8 ng of platinum per 10^6 cells was found for cisplatin (*cis*-[PtCl₂(NH₃)₂]) in the A2780 human ovarian carcinoma cell line. In this case, irradiation prior to removing **1** (at lower concentrations) resulted in a low viability of cells and an inability to study the effect of **1** on cells that were still intact. The protocol used in this study allowed for plentiful viable cells at all time points regardless of the factors applied.

Initial examination of the average second derivative spectra of the infrared data revealed potential marker bands to explore further by PLS-DA, including lipid, DNA base pairing and ribose vibrations (Figure 4.23). The effect of **1** on the K562 cell line was divided into three different factors to investigate by PLS-DA; time, drug (exposure to **1**) and irradiation. Whilst measurements were obtained for 0, 4 and 16 h after irradiation, only 0 and 4 h were investigated in the PLS-DA, as the majority of changes occurred in this time.

The PLS-DA model classification performances vs. the sample prediction (Y_{cv} values), revealed the best separation when all three factors were applied together (time, drug and irradiation). Furthermore, the cross validation error verifies this with the lowest value (4%) found for this model (the lower the percentage, the better the model). It is expected that the worst model fits are obtained for the three independent factors, which are expected to have little to no effect on the cells (controls).

The corresponding regression vectors revealed the two main vibrations contributing to the separation in the PLS-DA models for the controls (time, drug, irradiation and time & drug). The vibration at 1662 cm^{-1} , underlying the amide I, and the symmetric phosphate vibration, $\nu_{\text{sym}}(\text{PO}_2^-)$, at 1084 cm^{-1} . Increased intensity of the symmetric phosphate vibration has been reported to occur in live

cell infrared studies compared to dried cells and the amount of short-lived phosphate containing components in metabolically active cells could account for this strong intensity.^[26] Components such as adenine triphosphate, proteins and phosphorylated carbohydrates are especially prominent in active metabolic cells and are expected to change over time or when any other external or internal factor is applied, such as irradiation or drug ingestion. Therefore, it is challenging to relate changes to this particular vibration with confidence to any of the factors. The other main contribution to the controls is the vibration at 1662 cm^{-1} , which shows a slight increase in intensity when comparing the controls: time, drug and time & drug.

More significant is the effect by irradiation and irradiation & time factors. The low dose of 350 nm irradiation (2.58 J cm^{-2}) applied to the cells resulted in an initial increase in intensity of the 1662 cm^{-1} vibration upon irradiation. Upon including time (four hours after irradiation), this increase is accompanied by the increase in intensity of the shoulder of the amide II vibration at 1564 cm^{-1} . Intensity increases of the amide II vibration have been previously reported in live cells upon exposure to UV radiation by SR-IRMS, which might be related to the cellular repair response and therefore increase in protein content.^[7b] Nevertheless, the irradiation did not result in an apoptotic event as this would result in a significant decrease of amide I intensity.^[27]

The most noteworthy alterations were obtained when time, drug and irradiation are applied to the cells concurrently. Significant changes to the symmetric methyl vibration, $\nu_{\text{sym}}(\text{CH}_3)$, at 2875 cm^{-1} were picked up by both the PLS-DA as well as the average second derivative spectra. This is indicative of alterations to the lipid saturation inside the cell, a potential effect of **1** that has not been reported before. The PLS-DA further suggest changes to the $\nu(\text{COO}^{2-})$ vibration of fatty acids and amino acid side chains at 1367 cm^{-1} , supporting the observed changes on the lipid vibrations.

Secondly, the B-DNA and A-DNA base pairing vibrations at 1713 cm^{-1} and 1705 cm^{-1} considerably increase in intensity, with the A- to B-DNA ratio increasing in favour of A-DNA. Furthermore, the A-DNA and ribose vibration at 1178 cm^{-1} in the regression vector suggest a shift from 1173 cm^{-1} as shown in the average second derivative spectra (Figure 4.23, 4.25). Previous studies have shown that **1** rapidly accumulates inside tumour cells whereupon it penetrates the nucleus after irradiation, strongly binding to nuclear DNA. The major DNA adducts

formed proved capable of efficiently stalling RNA polymerase II and in turn inhibit DNA transcription.^[28] The observed changes to the DNA basepairing and A-DNA and ribose vibrations support that in these live conditions, **1** alters the conformational structures of DNA significantly already four hours after irradiation.

Whilst the average second derivative spectra suggested possible shifts occurring to the RNA vibrations at $\sim 1120\text{ cm}^{-1}$, this did not significantly stand out in the regression vector of the PLS-DA.

Please note, that background subtraction should allow for an accurate infrared spectrum of intracellular material only, although, the presence of external water (growth medium) cannot be 100% ruled out. This has to be taken into account when drawing conclusions based on the amide I signal. Shifts occurring in the amide I vibration can normally be assigned to a result of intramolecular changes. However, the average spectra and PLS-DA only suggest changes in intensity including increase in intensity for the water bending mode at 1639 cm^{-1} (Figure 4.25). Therefore, I refrain from drawing further conclusions on the strong signal at 1662 cm^{-1} without further investigation by additional experimental methods.

Further studies on K562 cells with **1** were attempted at both Monash University and the University of Warwick to backup our observations but poor sustainability of the cell line did not allow for successful studies by ATR or cell viability studies.

Lastly, attempts were carried out to obtain imaging maps of single cells in order to detect vibrational signatures of **1** (in particular the strong anti-symmetric azido vibration at $\sim 2050\text{ cm}^{-1}$) at similar and elevated concentrations (up to $500\text{ }\mu\text{M}$ for four hours) compared to the single cell spectra, however, no signal could be uncovered. This could be due several reasons, namely, detection limitations, the influence of water inside the cell and/or related to the mechanism of uptake and accumulation of **1** prior to irradiation.

4.4 Conclusion

Attempts were undertaken to exploit the high brilliance and collimation of Synchrotron Radiation (SR) using infrared spectroscopy at the Australian Synchrotron. The development of a new beamline accessory, Synchrotron Radiation Attenuated Total Reflection Far-Infrared (SR-ATR-FIR), for the THz/Far-IR beamline was instigated and proof of concept studies provided the necessary evidence of SR spectral range superiority over conventional sources whilst allowing for rapid screening of samples. Particular to this thesis is the groundwork on the SR-ATR-FIR spectra of **1** and synthetic precursors, highlighting the in line vibrations to the transmission SR-FIR spectra as well as the capabilities to carry out photodecomposition studies with an out-of-vacuum SR-ATR-FIR system. This particular system has been funded, designed and is now available as of application round 3, 2017 at the Australian Synchrotron.

New liquid diamond window cells were tested at the THz/Far-IR beamline with a laser source aligned to the sample chamber to allow for *in situ* irradiation of samples. Reflection artefacts of the liquid cells, referred to as fringes, hampered the detection of weak and low intensity vibrations in solution due to noise in the baselines. Nevertheless, elevated concentrations of **1** in DMSO allowed for the photodecomposition to be monitored by SR-FIR. Rapid rate of removal of the $\nu(\text{Pt-OH})$ and $\nu(\text{Pt-N}_3)$ vibrations was observed in the first five minutes, with similar rates of removal followed throughout 7 hours and 15 minutes. A new $\nu(\text{Pt-N}_3)$ vibration appears overtime, which might correspond to the *trans*-[Pt(N₃)(py)₂(solvent)] formed throughout irradiation as described in Chapter 3.1. Further liquid cell work on CT-DNA and **1** was studied by monitoring the intermolecular hydrogen vibrations. Whilst inconclusive at this stage, the improvement of better liquid cells could open up the field to these types of studies.

Lastly, Synchrotron Radiation Infrared Microspectroscopy (SR-IRMS) was carried out to study effect of **1** on live cells. With the unique microfluidic setup available at the Infrared Microspectroscopy beamline it is possible to study the effect of **1** on the K562 suspension cell line in a live state by SR-IRMS whilst obtaining spectra of single cells. Partial Least Square – Discriminant Analysis (PLS-DA) of the live single cell spectra reveals significant changes to the DNA

base stacking and lipid vibrations, already at 4 hours after drug treatment and irradiation, whilst this is not observed or to a lesser extent for the controls. The observed changes to the DNA basepairing, A-DNA and ribose vibrations support that **1** alters the conformational structures of DNA significantly and rapidly, in line with previous studies where rapid accumulation of platinum inside the nucleus is observed upon irradiation of **1**.^[28-29]

4.5 Experimental

4.5.1 Chemicals

All reactions were performed under nitrogen atmosphere using standard Schlenk techniques. Chemicals, deoxyribonucleic acid sodium salt from calf thymus, cell culture products and other solvents were purchased from Sigma-Aldrich, BioScientific or ThermoFisher and used as such.

4.5.2 Synthesis

The synthesis of *trans,trans,trans*-[Pt(N₃)₂(OH)₂(py)₂] (**1**, py = pyridine) was carried out as described in Chapter 2 with characterisation data in agreement with those reported previously.^[16,30]

4.5.3 External Illumination source

A Rayonet RPR-200 photoreactor equipped with six 420 nm lamps ($\lambda_{em\ max}$: 420 nm, spectral distribution: 390 – 460 nm, 3.6 mW cm⁻²) or six 350 nm lamps ($\lambda_{em\ max}$: 350 nm, spectral distribution: 300 – 400 nm, 4.3 mW cm⁻²) was used for irradiation. Solutions for 420 nm irradiation were placed in a 3 mL, 1 cm pathlength fluorescent quartz cuvette with a PTFE stopper. Multi well cell cultures plates, including their top plates (68% transmission at 350 nm) were irradiated for 13 minutes to reach a total of 2.58 J cm⁻².

4.5.4 The Australian Synchrotron

The Australian synchrotron light source runs at 200 mA in top-up mode.

4.5.5 Far-Infrared spectroscopy

Spectra were acquired on a Bruker IFS 125/HR FT spectrometer equipped with a 6 μ m multilayer Mylar beamsplitter and a helium-cooled Si bolometer detector, unless otherwise stated.

A Specac golden gate diamond ATR accessory was used to carry out initial alignments and to acquire spectra of test samples (poly(1-phenylethene) and polytetrafluoroethylene, also known as polystyrene and Teflon™). A Bruker Platinum ATR accessory was used to acquire spectra of all other solids and

evaporated solutions of **1**. Unless otherwise stated, spectra were recorded at a resolution of 1 cm^{-1} , 128 interferograms co-added.

For liquid samples, automated motorised cryostat sample holder (ST-100, Janis Research), holding three sample holders, was used to hold diamond window liquid cell holders with variable spacers (described in more details in section 4.2.2). A Nd:YAG pulsed laser (Surelite, 355 nm, 3rd harmonic, 12.0 mW) was used to irradiate the samples at a 90° angle of incidence relative to the infrared beam. 3.5 mW transmitted through the diamond cell window onto the liquid. A Lakeshore model 335 cryogenic temperature controller was set to 296.5 K and maintained the temperature of the sample holder between 296.5 and 298.2 K throughout irradiation of the samples over continuous periods of irradiation.

4.5.6 Synchrotron Infrared Microspectroscopy

Single cell spectra were acquired on a modified Bruker V80v spectrometer with a narrow band MCT detector. Transmission spectra were recorded between $3800 - 900\text{ cm}^{-1}$ with 64 interferograms co-added at a spectral resolution of 6 cm^{-1} . 2 μL of a cell pellet suspension (section 4.5.8) was placed on a microfluidic sample slide (CaF_2), purposely built for hydrated sample measurements.^[11] A top window (CaF_2) is gently placed on top of the microfluidic slide and held stationary during measurement allowing for a fully hydrated state for 30 to 60 min. The aperture was set to $10 \times 10\text{ }\mu\text{m}$ to cover the majority of the inside of the cell ($12 - 16\text{ }\mu\text{m}$). Background spectra (cell medium next to the live cells) were taken every 5th scan to subtract non-cellular contributions and account for synchrotron current and signal fluctuations. A total of three experimental replicates were carried out; three time points, four sets per time points, a minimum of 60 single cell spectra per set ≥ 2160 spectra.

4.5.7 Cell Culture

The acute myeloid leukaemia suspension cell line (K562) was cultured in RPMI 1640 medium (containing L-Glutamine) supplemented with 10% (v/v) fetal bovine serum (FBS) and 1% (v/v) penicillin-streptomycin at $37\text{ }^\circ\text{C}$ with 5% CO_2 . Cells were transported to the Australian synchrotron one week prior to the experiment and maintained at exponential growth ($\pm 1 \times 10^6$ cells/mL).

4.5.8 Cell Treatment and Irradiation

All cell treatment was carried out under dim light conditions to prevent unwanted activation of **1**. All cells were pooled before each experiment out of which three T75 cell cultures flasks were seeded ($\pm 0.25 \times 10^6$ cells/mL) and remaining cells were maintained at exponential growth in T75 cell cultures flasks until the next replicate experiment. The three T75 flasks were incubated for 48 hours at 37 °C with 5% CO₂, after which two T75 flask were seeded ($\pm 0.5 \times 10^6$ cells/mL). **1** (2 mM stock in Mili-Q water) was added to one T75 flask at a final concentration of 50 µM, with equal quantities of Mili-Q water added to the other flask and incubated for four hours at 37 °C with 5% CO₂. The cells in growth media were centrifuged at 500 × g for five minutes, supernatant discarded and resuspended in fresh growth medium. Two multi well plates (6 wells ea.) were filled with 3 mL aliquots of re-suspended cells (three treated with **1** and three untreated) to undergo irradiation. Both plates were put in the photoreactor for 13 minutes (350 nm, 2.58 J cm⁻²), with one plate covered in aluminium foil to prevent exposure to light. The aluminium foil was removed and both multi well plates were placed in the incubator at 37 °C with 5% CO₂ until measurement time points were reached (0, 4 and 16 h). Samples at each time point were centrifuged at 500 × g for five minutes, supernatant discarded, leaving a small volume of growth medium in the cell pellet and placed on the sample holder as described in section 4.5.6.

4.5.9 Data Processing

SR-ATR-FIR

Data was cut as indicated and extended ATR correction was carried out only on the SR-ATR-FIR spectra of the solids of **1**, **2** and **3** to correct for the artefacts caused by anomalous dispersion, as described previously in Chapter 2.2.^[16-17]

Transmission SR-FIR – Liquid cell

Data was cut as indicated and fringing corrections were carried out by straight-line generation in the interferogram, caused by interferences of the infrared beam with the surfaces of the liquid cell, when possible as outlined in the results. Principal Component Analysis (PCA) was carried out in MATLAB using PLS-Toolbox 8.2 (Eigenvector Research). Preprocessing prior to PCA: 1) data

was cut ($350 - 45 \text{ cm}^{-1}$), 2) smoothed (65 smoothing points), 3) standard normal variate (SNV) normalization and 5) mean centred.

Synchrotron Infrared Microspectroscopy

Partial Least Squares-Discriminant Analysis (PLS-DA) was carried out in MATLAB using the PLS_Toolbox 8.2 (Eigenvector Research). Preprocessing prior to PLS-DA: 1) data was cut, $3050 - 2750 \text{ cm}^{-1}$ and $1800 - 1040 \text{ cm}^{-1}$, 2) second derivative (9 smoothing points, weighted tails), 3) SNV normalization, 4) Pareto scaling and 5) mean centred. Separate PLS-DA's were carried out to compare the individual and combined effect of three factors on the cells (1, time and irradiation) to that of cells not treated with 1, at time zero and no irradiation.

4.6 Acknowledgments

I would like to thank the beamline scientists, Dr. Dom Appadoo, Dr. Keith Bambery and Dr. Mark Tobin for their support during and after beamtime at the THz/Far-IR and Infrared Microspectroscopy beamlines at the Australian Synchrotron. Furthermore, I would like to acknowledge Mrs. Clare Scott for her assistance to setup and supply experimental necessities prior and during beamtime access.

The AILES beamline at SOLEIL, France, is kindly acknowledged for providing their ATR schematics to help in the modification of the present ATR system at the Australian Synchrotron. Likewise, I kindly thank Dr. Bobby Pejic from CSIRO in Western Australia for the use of their Bruker platinum ATR accessory to obtain the ATR-SR-FTIR data.

4.7 References

- [1] a) H. M. Randall, *Science* **1927**, *65*, 167-173; b) H. M. Randall, *Reviews of Modern Physics* **1938**, *10*, 72-85; c) H. M. Randall, *J. Appl. Phys.* **1939**, *10*, 768-779; d) J. R. Ferraro, *Low-Frequency Vibrations of Inorganic and Coordination Compounds*, Springer US, Boston, MA, **1971**.
- [2] J. R. Durig, S. S. Panikar, J. J. Klaassen, in *Encyclopedia of Spectroscopy and Spectrometry (Third Edition)* (Eds.: G. E. Tranter, D. W. Koppenaal), Academic Press, Oxford, **2017**, pp. 558-565.
- [3] N. Miura, H. Yamada, A. Moon, *Spectrochim. Acta Mol. Biomol. Spectros.* **2010**, *77*, 1048-1053.
- [4] a) C. Zhang, S. M. Durbin, *J. Phys. Chem. B* **2006**, *110*, 23607-23613; b) D. M. Leitner, M. Gruebele, M. Havenith, *HFSP Journal* **2008**, *2*, 314-323; c) R. J. Falconer, H. A. Zakaria, Y. Y. Fan, A. P. Bradley, A. P. J. Middelberg, *Appl. Spectrosc.* **2010**, *64*, 1259-1264; d) T. Ding, T. Huber, A. P. J. Middelberg, R. J. Falconer, *J. Phys. Chem. A* **2011**, *115*, 11559-11565; e) T. Ding, A. P. J. Middelberg, T. Huber, R. J. Falconer, *Vib. Spectrosc* **2012**, *61*, 144-150; f) R. J. Falconer, A. G. Markelz, *Journal of Infrared, Millimeter, and Terahertz Waves* **2012**, *33*, 973-988.
- [5] a) A. E. Pekary, *J. Phys. Chem.* **1974**, *78*, 1744-1746; b) S. A. Lee, A. Anderson, W. Smith, R. H. Griffey, V. Mohan, *J. Raman Spectrosc.* **2000**, *31*, 891-896; c) S. A. Lee, J. Li, A. Anderson, W. Smith, R. H. Griffey, V. Mohan, *J. Raman Spectrosc.* **2001**, *32*, 795-802; d) B. Fischer, M. Walther, P. U. Jepsen, in *Proceedings, IEEE Tenth International Conference on Terahertz Electronics*, **2002**, pp. 74-76; e) B. M. Fischer, M. Walther, P. U. Jepsen, *Physics in Medicine & Biology* **2002**, *47*, 3807; f) H. Kitahara, M. Tani, M. Hangyo, Y. Miura, T. Sawai, J. Nishizawa, in *2005 Joint 30th International Conference on Infrared and Millimeter Waves and 13th International Conference on Terahertz Electronics, Vol. 2*, **2005**, pp. 644-645 vol. 642; g) V. I. Gaiduk, D. S. F. Crothers, *J. Mol. Liq.* **2006**, *128*, 145-160; h) S. Wietzke, C. Jansen, M. Reuter, T. Jung, D. Kraft, S. Chatterjee, B. M. Fischer, M. Koch, *J. Mol. Struct.* **2011**, *1006*, 41-51; i) I. Bergonzi, L. Mercury, J.-B. Brubach, P. Roy, *PCCP*

- 2014**, 16, 24830-24840; j) C. J. Evans, J. P. Carter, D. R. T. Appadoo, A. Wong, D. McNaughton, *J. Mol. Spectrosc.* **2015**, 316, 32-37; k) L. L. Ng, T. L. Tan, A. Wong, D. R. T. Appadoo, D. McNaughton, *Mol. Phys.* **2016**, 114, 2798-2807; l) S. Yamaguchi, Y. Fukushi, O. Kubota, T. Itsuji, T. Ouchi, S. Yamamoto, **2016**, 6, 30124; m) X. Yang, X. Zhao, K. Yang, Y. Liu, Y. Liu, W. Fu, Y. Luo, *Trends Biotechnol.* **2016**, 34, 810-824; n) M. K. Hazra, B. Bagchi, *J. Chem. Phys.* **2017**, 146, 024505; o) P. R. Griffiths, in *Handbook of Vibrational Spectroscopy*, John Wiley & Sons, Ltd, **2006**.
- [6] Z. Movasaghi, S. Rehman, D. I. ur Rehman, *Appl. Spectrosc. Rev.* **2008**, 43, 134-179.
- [7] a) A. L. M. Batista de Carvalho, M. Pilling, P. Gardner, J. Doherty, G. Cinque, K. Wehbe, C. Kelley, L. A. E. Batista de Carvalho, M. P. M. Marques, *Faraday Discuss.* **2016**, 187, 273-298; b) E. Lipiec, K. R. Bambery, P. Heraud, W. M. Kwiatek, D. McNaughton, M. J. Tobin, C. Vogel, B. R. Wood, *Analyst* **2014**, 139, 4200-4209; c) L. M. Miller, P. Dumas, *BBA-Biomembranes* **2006**, 1758, 846-857; d) F. Zobi, L. Quaroni, G. Santoro, T. Zlateva, O. Blacque, B. Sarafimov, M. C. Schaub, A. Y. Bogdanova, *J. Med. Chem.* **2013**, 56, 6719-6731.
- [8] Z. H. Siddik, *Oncogene* **2003**, 22, 7265-7279.
- [9] K. R. Bambery, B. R. Wood, E. Schultke, B. H. J. Juurlink, T. May, D. McNaughton, in *Biomedical Applications of Synchrotron Infrared Microspectroscopy: A Practical Approach*, The Royal Society of Chemistry, Cambridge, UK, **2011**, pp. 339-350.
- [10] D. Perez-Guaita, D. Andrew, P. Heraud, J. Beeson, D. Anderson, J. Richards, B. R. Wood, *Faraday Discuss.* **2016**, 187, 341-352.
- [11] M. J. Tobin, L. Puskar, R. L. Barber, E. C. Harvey, P. Heraud, B. R. Wood, K. R. Bambery, C. T. Dillon, K. L. Munro, *Vib. Spectrosc* **2010**, 53, 34-38.
- [12] B. R. Wood, *Chem. Soc. Rev.* **2016**, 45, 1980-1998.
- [13] R. Eckel, H. Huo, H.-W. Guan, X. Hu, X. Che, W.-D. Huang, *Vib. Spectrosc* **2001**, 27, 165-173.
- [14] a) Y. Fukuyama, S. Yoshida, S. Yanagisawa, M. Shimizu, *Biospectroscopy* **1999**, 5, 117-126; b) J.-G. Wu, Y.-Z. Xu, C.-W. Sun, R. D. Soloway, D.-F. Xu, Q.-G. Wu, K.-H. Sun, S.-F. Weng, G.-X. Xu,

- Biopolymers* **2001**, 62, 185-192; c) Q.-B. Li, X.-J. Sun, Y.-Z. Xu, L.-M. Yang, Y.-F. Zhang, S.-F. Weng, J.-S. Shi, J.-G. Wu, *Clin. Chem.* **2005**, 51, 346-350.
- [15] E. B. Wilson, *Phys. Rev.* **1934**, 45, 706-714.
- [16] R. R. Vernooij, T. Joshi, E. Shaili, M. Kubeil, D. R. T. Appadoo, E. I. Izgorodina, B. Graham, P. J. Sadler, B. R. Wood, L. Spiccia, *Inorg. Chem.* **2016**, 55, 5983-5992.
- [17] J. M. Chalmers, in *Handbook of Vibrational Spectroscopy*, John Wiley & Sons, Ltd, **2006**, pp. 2327-2347.
- [18] a) G. C. Hayward, *Appl. Spectrosc.* **1969**, 23, 620-621; b) T. Hirschfeld, A. W. Mantz, *Appl. Spectrosc.* **1976**, 30, 552-553; c) F. R. S. Clark, D. J. Moffatt, *Appl. Spectrosc.* **1978**, 32, 547-549; d) T. Hirschfeld, *Appl. Opt.* **1978**, 17, 1400-1412; e) E. Knözinger, *Ber Bunsenges Phys Chem* **1986**, 90, 1240-1241; f) T. Konevskikh, A. Ponossov, R. Blumel, R. Lukacs, A. Kohler, *Analyst* **2015**, 140, 3969-3980.
- [19] W. N. Martens, R. L. Frost, J. Kristof, J. Theo Kloprogge, *J. Raman Spectrosc.* **2002**, 33, 84-91.
- [20] a) H. R. Zelsmann, *J. Mol. Struct.* **1995**, 350, 95-114; b) F. Sacchetti, J. B. Suck, C. Petrillo, B. Dorner, *Phys Rev E* **2004**, 69, 061203.
- [21] The AILES beamline, SOLEIL. <https://www.synchrotron-soleil.fr/en/beamlines/ailles> (18 September 2017), **2016**.
- [22] T. R. Globus, D. L. Woolard, A. C. Samuels, B. L. Gelmont, J. Hesler, T. W. Crowe, M. Bykhovskaia, *J. Appl. Phys.* **2002**, 91, 6105-6113.
- [23] a) C. W. Robertson, D. Williams, *J. Opt. Soc. Am.* **1971**, 61, 1316-1320; b) K. F. Palmer, D. Williams, *J. Opt. Soc. Am.* **1974**, 64, 1107-1110; c) I. L. Tyler, G. Taylor, M. R. Querry, *Appl. Opt.* **1978**, 17, 960-963; d) P. Bassan, P. Gardner, in *Biomedical Applications of Synchrotron Infrared Microspectroscopy: A Practical Approach*, The Royal Society of Chemistry, **2011**, pp. 260-276.
- [24] G. Tatiana, B. Maria, W. Dwight, G. Boris, *J. Phys. D: Appl. Phys.* **2003**, 36, 1314.
- [25] A. M. Pizarro, R. J. McQuitty, F. S. Mackay, Y. Zhao, J. A. Woods, P. J. Sadler, *ChemMedChem* **2014**, 9, 1169-1175.
- [26] a) M. Miljkovic, M. Romeo, C. Matthäus, M. Diem, *Biopolymers* **2004**, 74, 172-175; b) C. Matthäus, B. Bird, M. Miljković, T. Chernenko, M. Romeo,

-
- M. Diem, *Methods Cell Biol.* **2008**, *89*, 275-308; c) L. Chen, H.-Y. N. Holman, Z. Hao, H. A. Bechtel, M. C. Martin, C. Wu, S. Chu, *Anal. Chem.* **2012**, *84*, 4118-4125.
- [27] a) F. Gasparri, M. Muzio, *Biochem. J* **2003**, *369*, 239-248; b) M. Jimenez-Hernandez, M. D. Brown, C. Hughes, N. W. Clarke, P. Gardner, *Analyst* **2015**, *140*, 4453-4464.
- [28] J. Pracharova, L. Zerzankova, J. Stepankova, O. Novakova, N. J. Farrer, P. J. Sadler, V. Brabec, J. Kasparkova, *Chem. Res. Toxicol.* **2012**, *25*, 1099-1111.
- [29] Y. Zhao, J. A. Woods, N. J. Farrer, K. S. Robinson, J. Pracharova, J. Kasparkova, O. Novakova, H. Li, L. Salassa, A. M. Pizarro, G. J. Clarkson, L. Song, V. Brabec, P. J. Sadler, *Chem. Eur. J.* **2013**, *19*, 9578-9591.
- [30] N. J. Farrer, J. A. Woods, L. Salassa, Y. Zhao, K. S. Robinson, G. Clarkson, F. S. Mackay, P. J. Sadler, *Angew. Chem. Int. Ed.* **2010**, *49*, 8905-8908.
- [31] A. Messinger, J. W. Powell, T. Weidlich, L. Genzel, *J. Biomol. Struct. Dyn.* **1993**, *10*, 841-852.
- [32] C. J. L. Murray, L. C. Rosenfeld, S. S. Lim, K. G. Andrews, K. J. Foreman, D. Haring, N. Fullman, M. Naghavi, R. Lozano, A. D. Lopez, *The Lancet* **2012**, *379*, 413-431.
- [33] a) B. R. Wood, E. Bailo, M. A. Khiavi, L. Tilley, S. Deed, T. Deckert-Gaudig, D. McNaughton, V. Deckert, *Nano Lett.* **2011**, *11*, 1868-1873; b) A. Khoshmanesh, M. W. A. Dixon, S. Kenny, L. Tilley, D. McNaughton, B. R. Wood, *Anal. Chem.* **2014**, *86*, 4379-4386; c) B. R. Wood, K. R. Bambery, M. W. A. Dixon, L. Tilley, M. J. Nasse, E. Mattson, C. J. Hirschmugl, *Analyst* **2014**; d) R. Puntharod, K. J. Haller, E. G. Robertson, E. S. H. Gwee, E. I. Izgorodina, B. R. Wood, *J. Raman Spectrosc.* **2017**, *48*, 1148-1157.
- [34] S. Dörr, U. Schade, P. Hellwig, *Vib. Spectrosc* **2008**, *47*, 59-65.
- [35] J. G. Menting, L. Tilley, L. W. Deady, K. Ng, R. J. Simpson, A. F. Cowman, M. Foley, *Mol. Biochem. Parasitol.* **1997**, *88*, 215-224.

4.8 Supporting Information

4.8.1 SR-ATR-FIR – DNA Nucleobases

DNA nucleobases, including deoxyribose and monophosphate derivatives were measured by SR-ATR-FIR to record their spectra for potential metal complex binding studies. Figure S4.1 shows the SR-ATR-FIR spectra of thymine, guanine, cytosine and adenine. The spectra shown below, including the deoxyribose (Figure S4.2) and monophosphate derivatives (Figure S4.3), are in line with previously reported transmission spectra of the corresponding compounds.^[5b-e,31]

The peaks present in the far-infrared region mainly consist of out-of-plane ring deformations, torsional and lattice modes. These vibrations are extremely sensitive to conformational changes and can be used to monitor effect to geometry like hydration, isomerisation and/or binding of other molecules. For example, the effect of changing anions and the state (crystal or gel) of guanosine 5'-monophosphate disodium salt (5'-GMP) showed to have large effects of the far-infrared spectra, including large differences in intensities (very strong to weak and *vice versa*) and wavenumber shifts of $\pm 20 \text{ cm}^{-1}$.^[31]

Increasing amount of rotational and lattice vibrations are observed going from guanine to guanosine to 5'-GMP (Figure S4.2). The crystal lattice of the disodium salts have a large effect on the rotational and lattice vibrations, resulting in multiple broad peaks with underlying features, as shown in Figure S4.3.

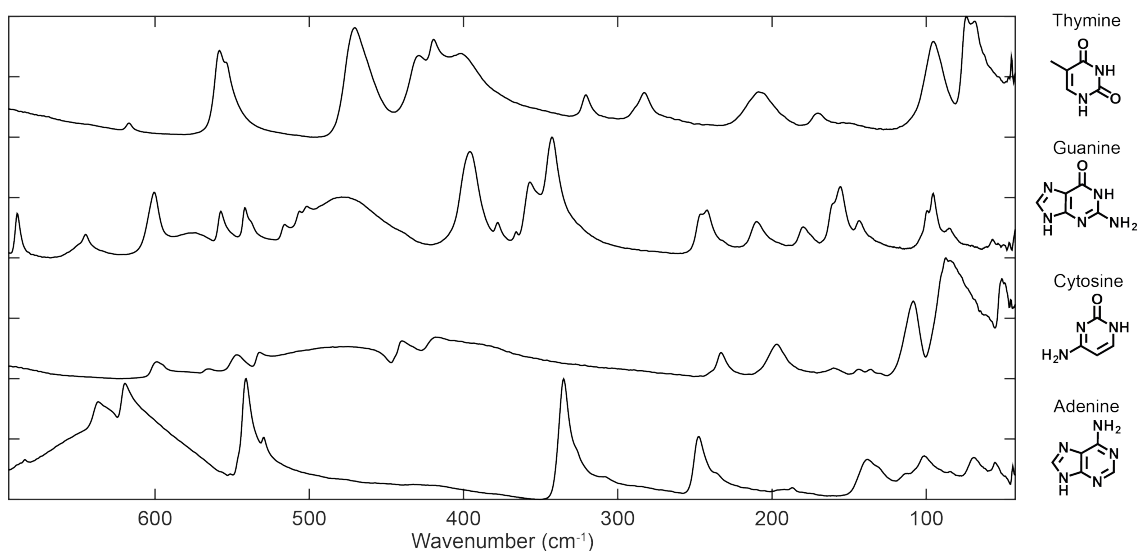


Figure S4.1. SR-ATR-FIR spectra of thymine, guanine, cytosine and adenine, including molecular structures.

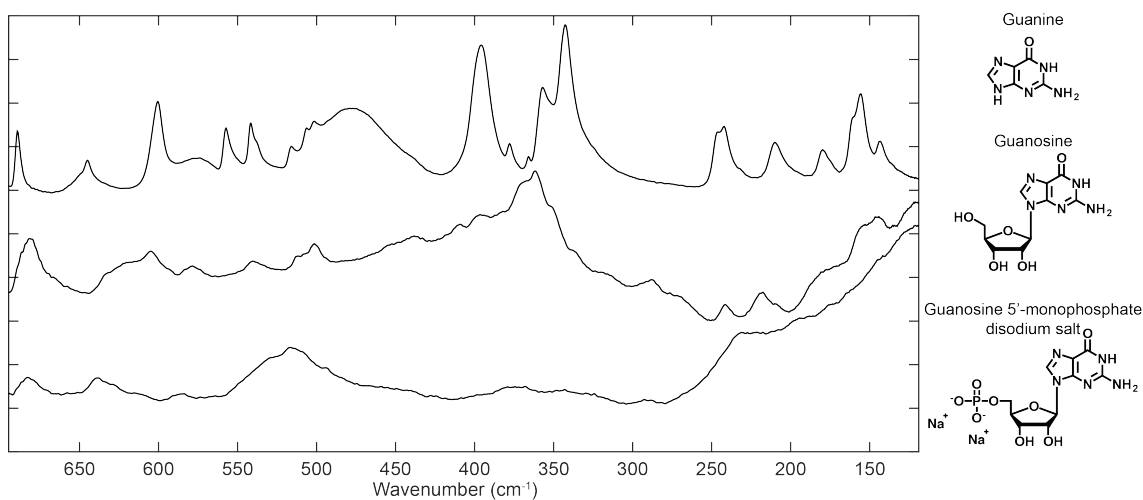


Figure S4.2. SR-ATR-FIR spectra of guanine, guanosine and guanosine 5'-monophosphate disodium salt, including molecular structures.

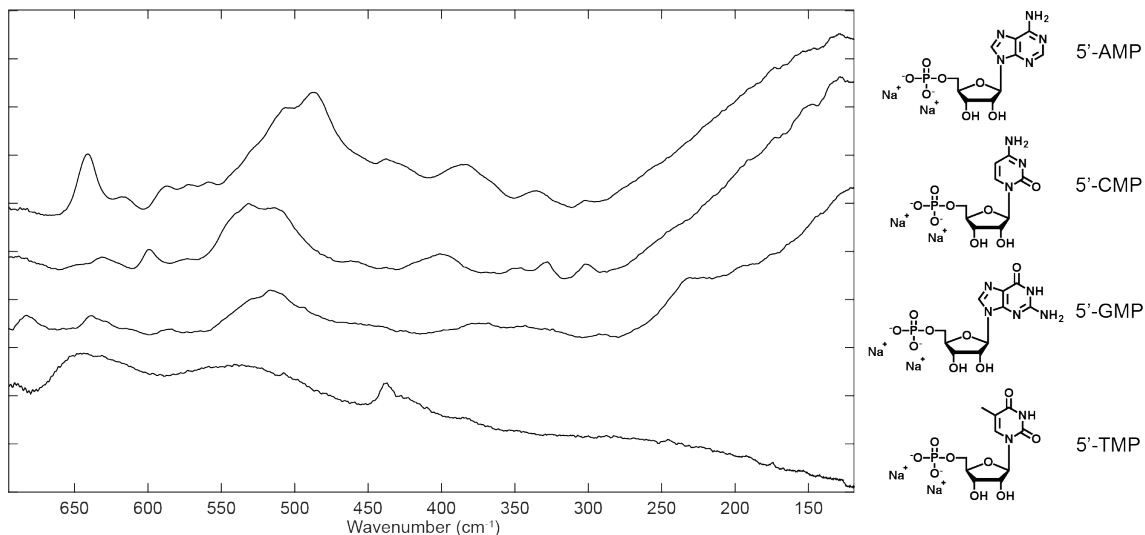


Figure S4.3. SR-ATR-FIR spectra of 5'-AMP, 5'-CMP, 5'-GMP and 5'-TMP disodium salts, including molecular structures. Abbreviations used: 5'-A/C/G/TMP = adenosine/cytidine/guanosine/thymidine 5'-monophosphate disodium salt.

4.8.2 SR-ATR-FIR – Malaria Infected Red Blood Cells

Malaria has one of the highest yearly human mortality rates in the world, with up to 1.2 million reported deaths per annum.^[32] Continuous effort is placed on the development of new highly sensitive diagnostic techniques to detect low-density parasite infections in asymptomatic carriers (infected people without symptoms). Development of vibrational spectroscopic techniques has been highlighted in recent years as a potential diagnostic tool and to better understand the different stages of malaria.^[33]

SR-ATR-FTIR could allow for a fast screening method of the far-infrared spectra of marker molecules associated with detecting malaria, such as haemoglobin and haematin, containing metal to ligand vibrations in this region. Furthermore, screening red blood cells fixed in methanol at different stages of malaria infection (on glass slides or as a solution) would be a new approach to investigate malaria.

The spectra obtained by SR-ATR-FTIR and molecular structures for the haemoglobin protein, β -haematin, haematin, haemin and protoporphyrin ix are shown in Figure S4.4. Starting at Haemin, the protoporphyrin ix ligand vibrations remain present (such as at 475 cm^{-1}) and a strong new band is observed for the iron to chloride stretching vibration at 349 cm^{-1} . Furthermore, the iron to nitrogen (protoporphyrin ix) stretching vibration emerges at 259 cm^{-1} , which remains present throughout haematin and β -haematin at 267 cm^{-1} and 264 cm^{-1} respectively. Haematin contains the single strong iron to oxygen (hydroxide) stretching vibration at 342 cm^{-1} , whereas β -haematin contains several iron to oxygen (carboxylate) stretching vibrations at 383 cm^{-1} , 361 cm^{-1} , 343 cm^{-1} and 326 cm^{-1} . β -haematin consists of several haematin stacked dimers, as shown in Figure S4.4, resulting in different iron to oxygen bond lengths and angles, intermolecular hydrogen bonding and longer distance interactions. This results in the factor group splitting observed for the iron to oxygen stretching vibration, which is in line with previous reports.^[33d,34] Furthermore, several other marker bands are clearly present in the spectra, namely at, 625 cm^{-1} , 558 cm^{-1} , 516 cm^{-1} , 461 cm^{-1} , 264 cm^{-1} , 174 cm^{-1} and 150 cm^{-1} .

The iron to oxygen stretching vibrations can be gleaned in the spectra of the haemoglobin protein at 348 cm^{-1} , including other weak vibrations (Figure S4.4). The malaria parasite catabolizes haemoglobin into toxic haeme inside red blood

cells, which it sequesters into the insoluble pigment haemozoin. β -haematin is the synthetic precursor of haemozoin and therefore, the observed vibrations could be used to detect malaria in red blood cells.

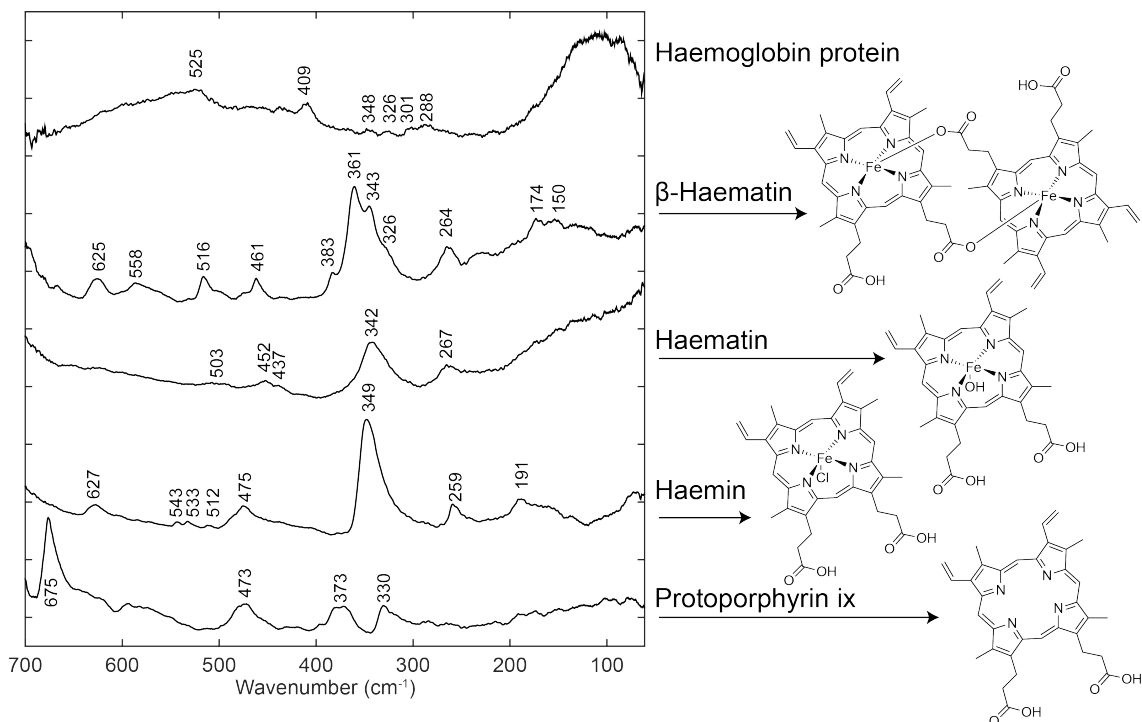


Figure S4.4. SR-ATR-FIR spectra of haemoglobin, β -haematin, haematin, haemin and protoporphyrin ix, including selected peak labels and molecular structures (apart from haemoglobin).

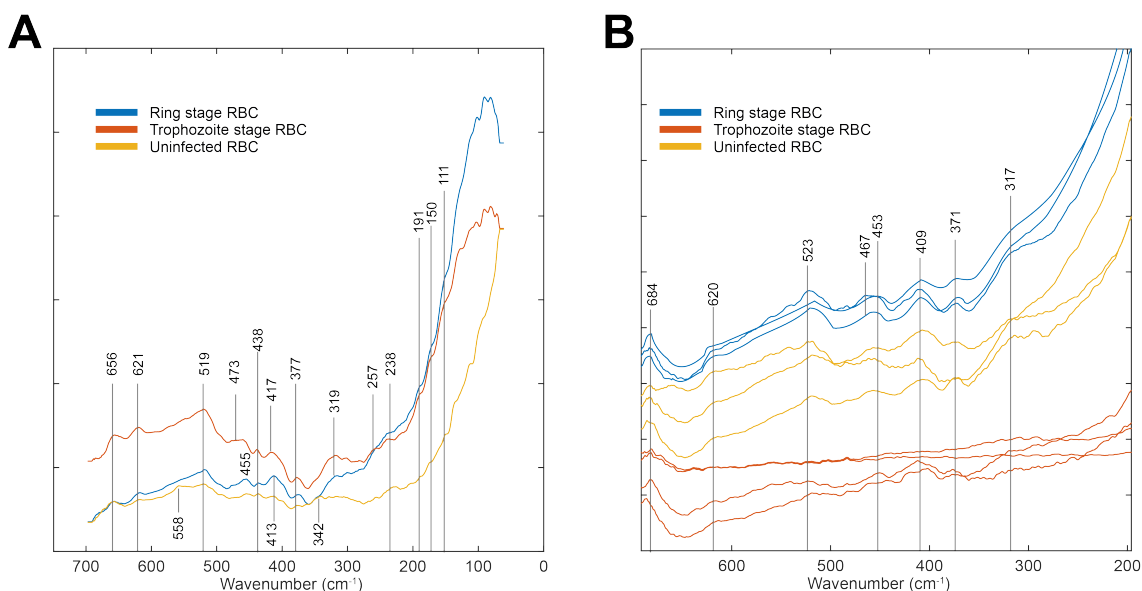


Figure S4.5. SR-ATR-FIR spectra of uninfected and infected RBC (ring or trophozoite phase), including selected peak labels. A) Fixed RBC in methanol were deposited on the ATR diamond and evaporated prior to measurement (average spectra of four sample replicates, with four spectral replicates each). B) Methanol fixed RBC on glass microscopy slides, placed on the ATR diamond (each spectrum is a different sample, four spectral replicates each).

Methanol fixed Red Blood Cells (RBC) were kindly supplied by Prof. Leann Tilly from the University of Melbourne for this study and were prepared as reported previously.^[10,35] Two different (morphological) phases of malaria parasite infection were studied and uninfected RBC were measured as controls. The ring phase (immature asexual stage of the parasite, present in circulation) and the trophozoite phase (later asexual stage of the parasite, still present in circulation), where increasing amounts of haemozoin is present going from the ring to the trophozoite phase.^[33b]

RBC in methanol were deposited onto the ATR crystal and evaporated using a gentle N₂ flow. Average SR-ATR-FIR spectra (four sample replicates, four spectral replicates each) of the RBC are shown in Figure S4.5A, which includes selected peak labels. Several vibrational signatures could be obtained present in all three spectra, with a few vibrations only present in either the uninfected or infected RBC. These include the vibrations at 558 cm⁻¹ (uninfected), 473 cm⁻¹ (trophozoite), 455 cm⁻¹ (ring), 473 cm⁻¹ (trophozoite), 413 cm⁻¹ (uninfected and ring), 342 cm⁻¹ (uninfected), 319 cm⁻¹ (ring and trophozoite) and 257 cm⁻¹ (ring and trophozoite). Interestingly, an increase in the vibration at 377 cm⁻¹ is observed for the infected RBC compared to uninfected RBC. This could be due to increasing quantities of β-haematin present in the RBC.

Intriguingly, the peak at 558 cm⁻¹ of the uninfected RBC is present in the spectra of β-haematin (Figure S4.4), whilst this peak doesn't stand out in either of the infected RBC spectra or Haemoglobin. Haemoglobin is a main component of RBC, however, other proteins and membrane lipids are present in RBC. These should be screened in the future in order to fully characterise the SR-ATR-FIR vibrational signature of RBC.

Furthermore, previously fixed RBC on glass slides were measured by placing them facedown on the ATR crystal with spectra shown in Figure S4.5B. Each spectrum corresponds to a different sample, with four spectral replicates each sample. Spectral acquisition was limited to 700 – 200 cm⁻¹ due to the strong infrared absorption of the glass slides (SiO₂) below 200 cm⁻¹. Comparable vibrational signatures could be obtained compared to the RBC in methanol, such as the matching vibrations (methanol/glass slides) at 621/620 cm⁻¹, 523/519 cm⁻¹, 377/371 cm⁻¹ present in all RBC. However, the inconsistency between the previously fixed RBC were too excessive to allow for spectral

averaging between samples (and the small amount of samples measured). Therefore, further investigation of spectral replicates is necessary in the future. Nevertheless, these results provide an outlook to a potential new area to pursue in SR far-infrared spectroscopy.

4.8.3 Transmission Synchrotron Radiation Far-Infrared – Liquid cell *in situ* Irradiation

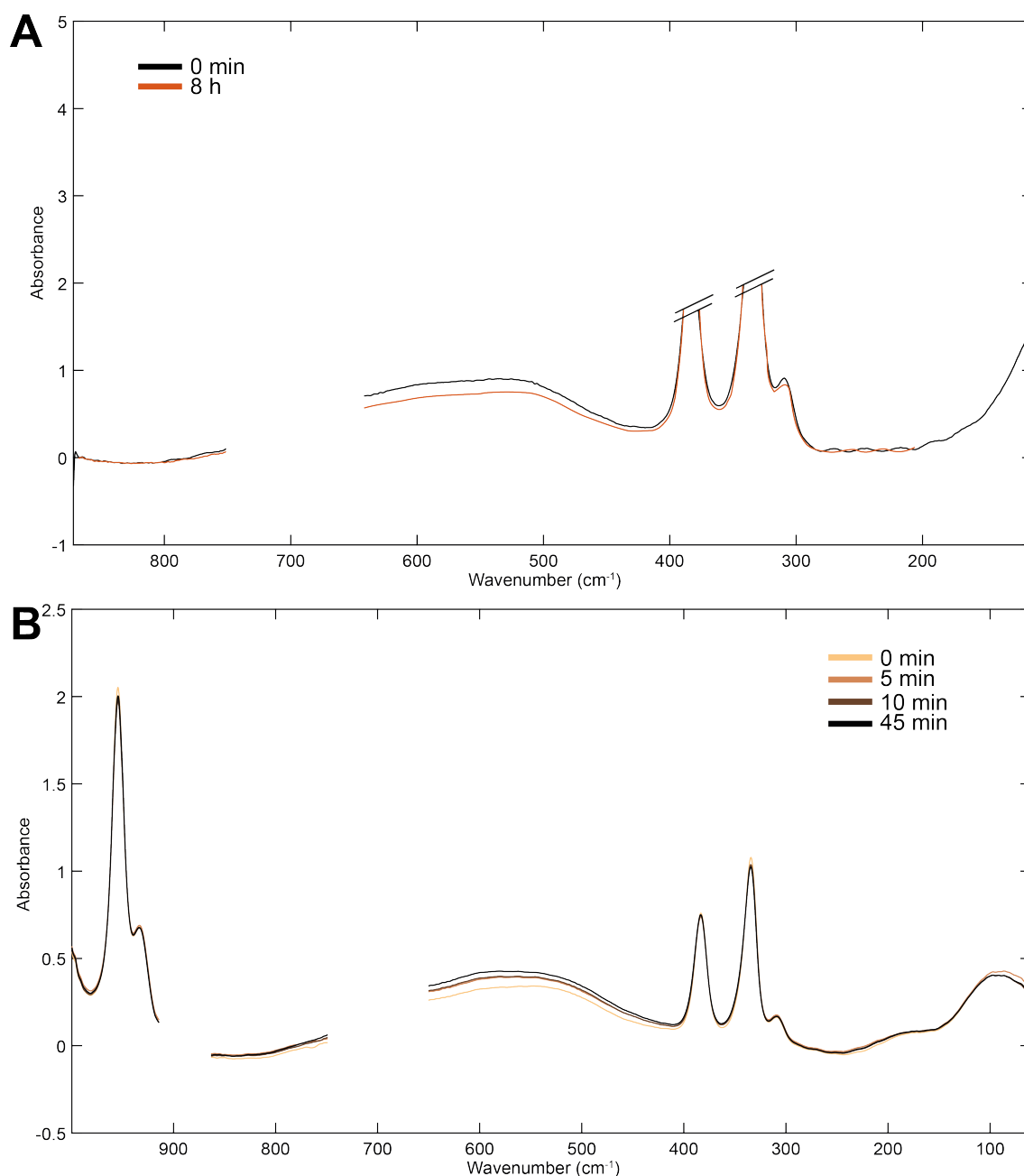


Figure S4.6. SR-FIR spectra of DMSO upon 355 nm irradiation at selected time points using a 20 μm (A) and 100 μm (B) pathlength diamond window liquid cell. Beamsplitter (Mylar) and detector (polyethylene window) absorptions are cut ($\sim 920 - 870 \text{ cm}^{-1}$ and $\sim 740 - 650 \text{ cm}^{-1}$, respectively), line saturations are cut ($\sim 380 \text{ cm}^{-1}$ and $\sim 330 \text{ cm}^{-1}$) and the spectra are smoothed (15 points).

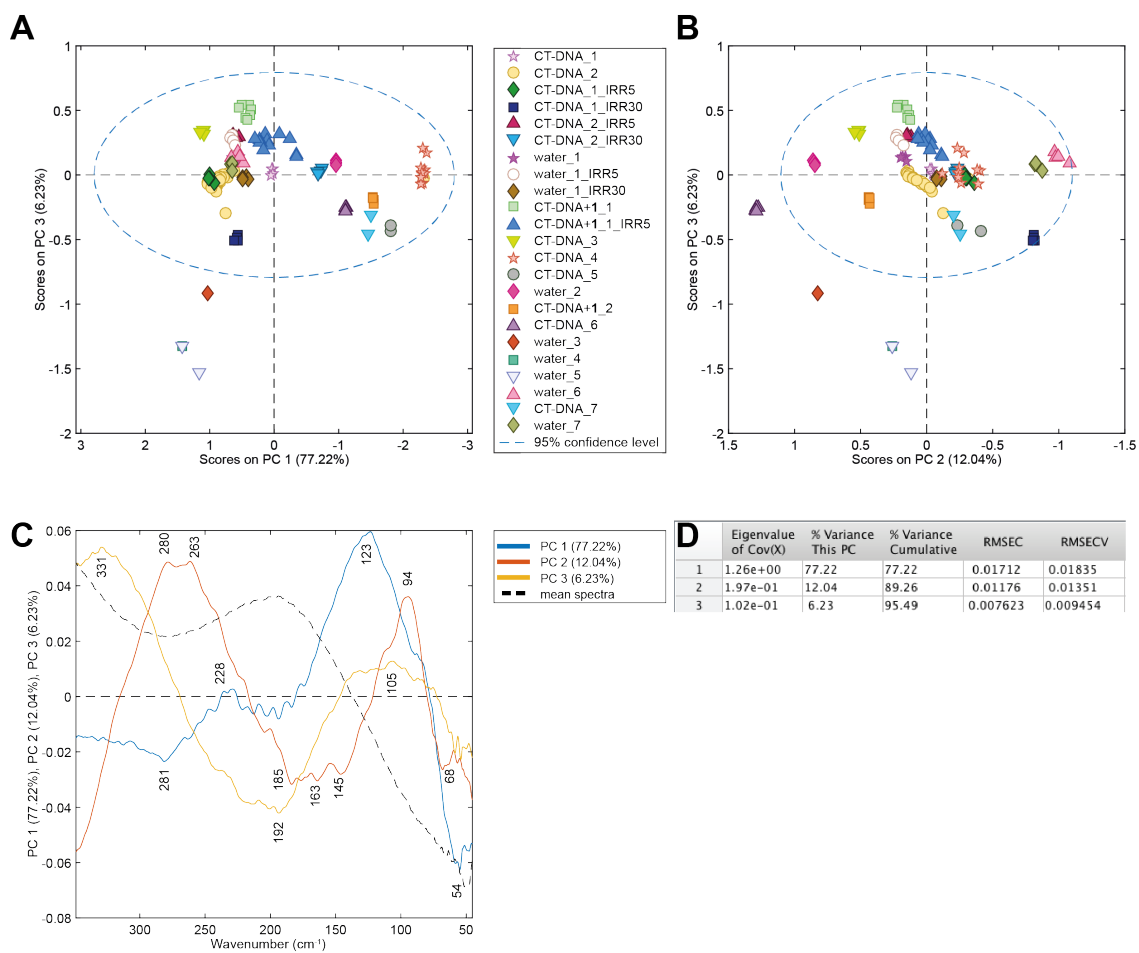


Figure S4.7. PCA analysis results for the SR-FIR spectra of water, CT-DNA and CT-DNA+1 with and without 355 nm irradiation (IRR) in a 5 μm pathlength diamond window liquid cell. A) PC1 vs. PC3 score plot. B) PC2 vs. PC3 score plot. C) Loading plot including mean spectra, including peak labels. D) Eigenvalues, variance captured, Root Mean Square Error of Calibration (RMSEC) and Root Mean Square Error of Cross Validation (RMSECV) of the Principal components (PC).

Chapter 5

Upconverting Nanoparticles

Chapter 5 covers the efforts made towards the development of new lanthanide-doped upconverting nanoparticles (UCNPs) to address the low wavelength excitation of the earlier described photoactivatable metal-based anticancer prodrug candidates (Chapters 1 – 3), which currently hamper their clinical feasibility. This involves the preparation of a range of highly defined, narrow-sized UCNPs by variation of doping materials, inorganic host lattices, capping agents and physical parameters (reaction time and temperature). Preliminary characterisation of UCNPs was carried out using Transmission Electron Microscopy (TEM), X-ray powder diffraction (XRD) and UV-Vis absorption spectroscopy. Attempts were made to further expand the excitation wavelengths of these nanoparticles to the clinically relevant optical window by coupling of near-infrared dyes to their surface to match wavelengths accessible by clinically used lasers. Lastly, a custom-made setup was build to screen the emission profiles of such UCNPs.

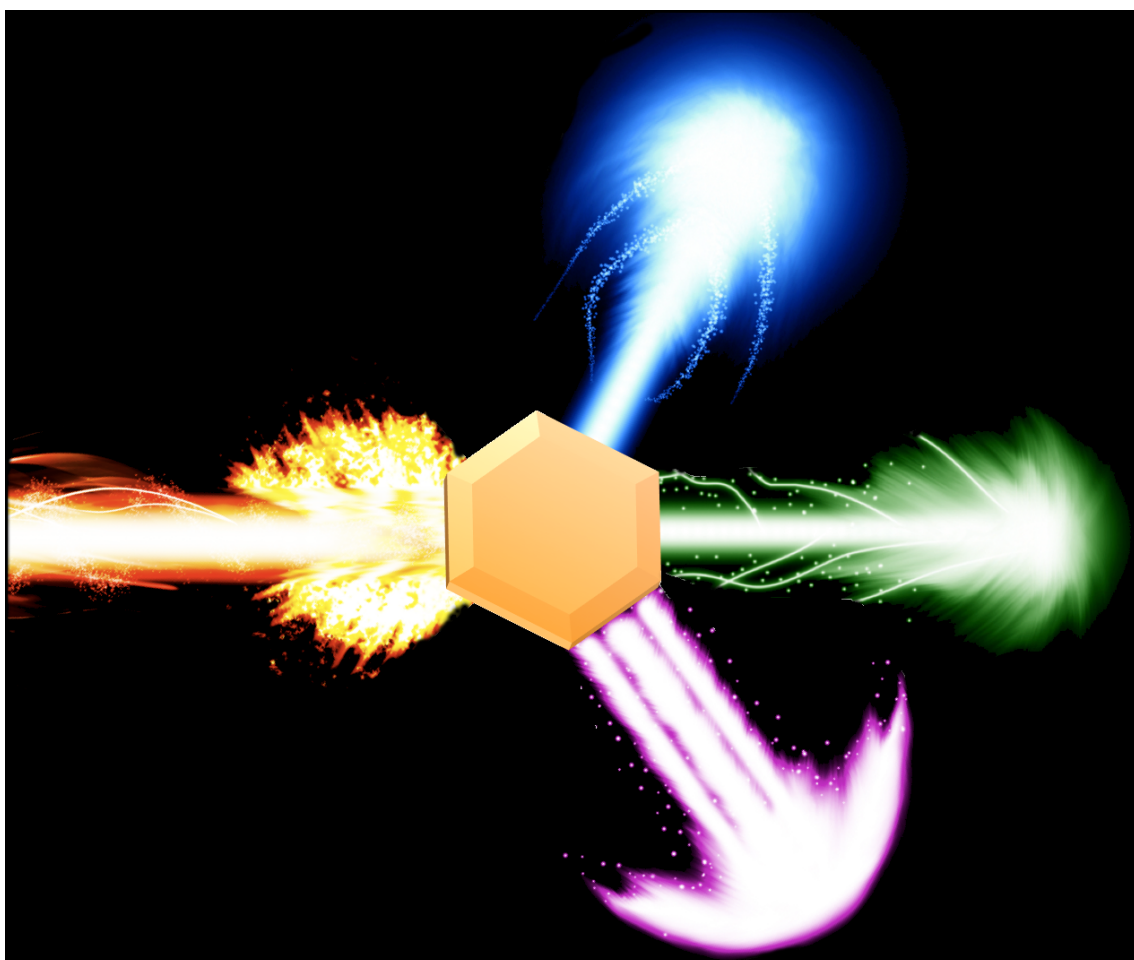


Figure 5.1. Graphical representation of a hexagonal upconverting nanoparticle excited with an NIR (red) laser, emitting visible (blue, green) and UVA (pink) light.

5.1 Introduction

A brief outline on upconverting nanoparticles (UCNPs) is covered below, concentrating on the physical and (photo)chemical requirements to make them clinically relevant. The reader is kindly directed to Chapter 1.6 for a more detailed overview on UCNPs.

UCNPs are well known for their anti-Stokes type upconversion (near-infrared excitation, visible light emission) that originates from the lanthanides doped at different ratios into a host lattice (e.g. NaYF₄, CaF₂, LiYF₄) in a core or core/shell nanoparticle assembly.^[1] They display unique optical, structural and chemical properties. This includes different absorption and emission bandwidths, different extents of water solubility, a diverse range of surface functionalities and varying size distributions. The challenge remains to utilise and improve previous results to develop the core/shell UCNPs best suited for their biomedical application as a drug-delivery and drug-activation system. The opportunity of having multiple imaging and therapeutic modalities on UCNPs makes them ideally suited as drug-delivery systems, allowing for possible new diagnostic therapy on an individual basis (theranostics). However, before that, a systematic and reproducible approach is much-needed for synthesising water-dispersible UCNPs of uniform size and shape with an easy to functionalise surface to allow for efficient covalent binding of multiple modalities.

5.1.1 Physical and (Photo)Chemical Requirements

Optimal size. Size distribution displays an important role in the uptake, distribution and accumulation of nanoparticles in *in vivo* testing.^[2] “Larger” nanoparticles (>100nm) are easily cleared by the reticuloendothelial system (RES) or mononuclear phagocytic system (MPS), thus providing an upper size threshold for this research in particular.^[3] A lower size threshold can be set by taking the kidney clearance (8 nm), glomerular filtration of the blood (5 nm) and renal excretion (5.5 nm) cut-off pore sizes into account.^[4] More recent *in vivo* studies show that UCNPs with an average size between 10 and 50 nm can still accumulate rapidly in the liver and spleen.^[2,5] Based on these research findings, the ultimate aim for this project was to synthesise sub-20 nm UCNPs (this includes the core/shell, coating and surface functionalities). At the same time, it is important to increase the blood circulation half-lives in order to prevent premature clearance and still allow for the utilisation of the enhanced permeability and retention (EPR) effect of leaky tumour cells.^[6] For this, several working strategies have already been reported. For example polyethylene glycol (PEG), citric acid or polyphosphoric acid incorporation on the surface of the UCNPs has been reported to increase blood circulation half-lives of the NPs.^[7]

Hexagonal Structure. Hexagonal-phase NaYF₄ (β -NaYF₄) crystals have been reported to be the most efficient host materials for upconverting lanthanide ions due to the low phonon energy of the crystal lattice, compared to the other commonly obtained cubic-phase NaYF₄ (α -NaYF₄).^[8] It is important to synthesise phase-pure hexagonal UCNPs to achieve high quantum yields.

Excitation band at or below 800 nm. The majority of UCNPs reported have an excitation band centred at 980 nm, which can in most cases be allocated to the peak absorption of Yb³⁺ ions.^[1,9] However, the excitation band overlaps with the maximum absorption peak of water molecules (Figure 5.2). The absorption of 980 nm light is expected to limit deep tissue penetration and induce thermal damage to cells and tissues.^[9] Thus, UCNPs with excitation bands at or below 800 nm will be the aim in this project to increase tissue penetration and reduce potential thermal damage.

Water-dispersible. The majority of as-synthesised UCNPs are hydrophobic. There are several coating strategies to render them water-dispersible, such as polymer, silica, phospholipid and zwitterionic coatings.^[10] For this work, coating with octylamine-modified polyacrylic acid (OPA) polymer was used as a starting point as the Spiccia and Graham groups have studied it intensively.^[11] OPA coating has shown little effect on the size and shape of UCNPs without the formation of UCNP aggregates.^[11]

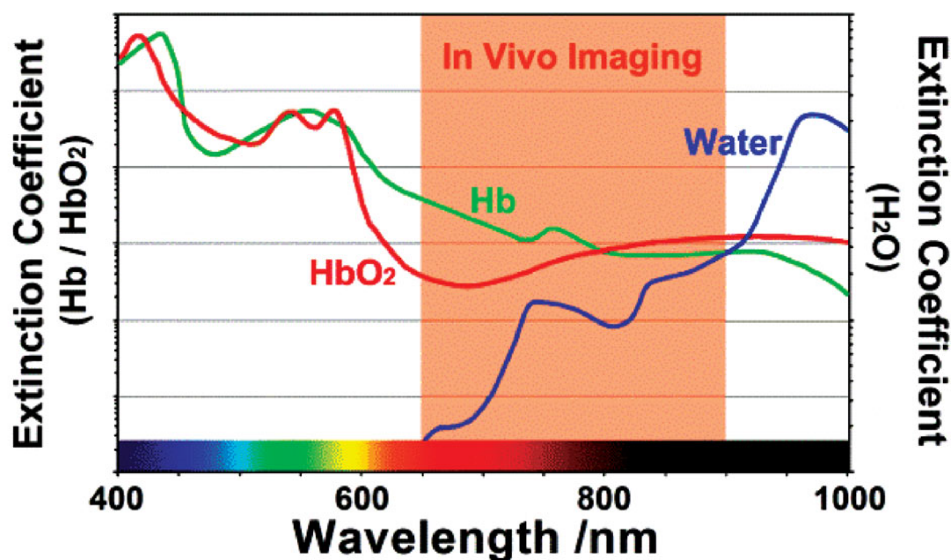


Figure 5.2. Spectral profiles of tissue optical window. The extinction coefficient of water at 800 nm is about 20 times lower than that at 980 nm (Hb = haemoglobin, HbO₂ = oxyhemoglobin). Adapted from Han et al.^[12] Reprinted by permission of John Wiley & Sons, Inc. 2013 Copyright WILEY-VCH Verlag GmbH & Co. KGaA, Weinheim.

Throughout the last decade, examples of Nd³⁺-doped core/shell NaYF₄ UCNPs with absorption wavelengths around 800 nm have been reported using the thermal decomposition synthesis method.^[12-13] Low concentrations of Nd³⁺ (doping ratio ≤ 2%) in the core are used to reduce self-quenching, whereas high concentrations of Nd³⁺ (~20%) in the shell are essential to synthesise UCNPs with absorption at 800 nm.^[13]

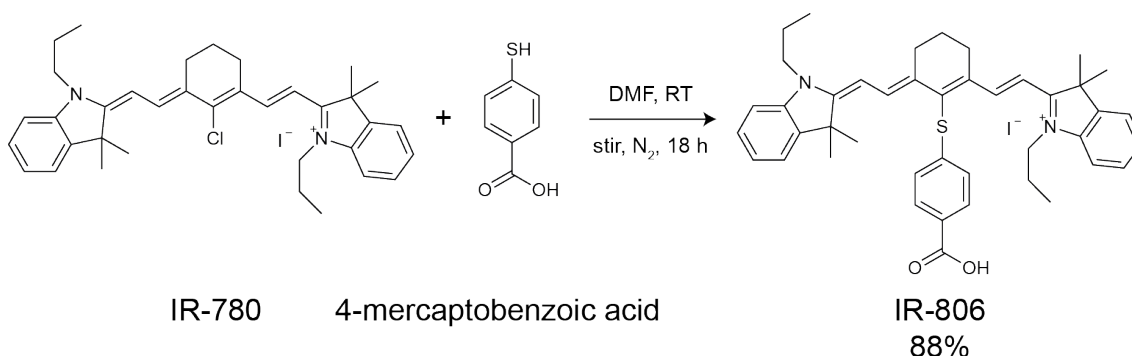
It is important to keep in mind that lasers most commonly used in clinics for photodynamic therapy (PDT) are pulsed dye lasers (595 nm) and diode lasers (ranging from 630 nm to 670 nm). Furthermore, when aiming for ultrasmall UCNPs, the already poor quantum yields of UCNPs will be further reduced, which would increase the irradiation time required for these particles to be

effective.^[14] Clinical laser irradiation times can vary between 5-45 minutes, therefore, it is of importance to synthesise UCNPs with high quantum yields to minimise irradiation times.^[15] Embedding dyes onto the UCNPs might overcome the above mentioned limitations, i.e. increasing quantum yields to reduce irradiation times, reducing UCNP sizes towards the ultimate objective of nanoparticle renal clearance, and broadening of the absorption spectrum for the use of clinical grade lasers.^[16]

Therefore, initial strategies involved the synthesis of hexagonal neodymium doped UCNPs and embedding dyes into well defined UCNPs with absorption peaks around 800 nm. Appropriate core/shell ratios were selected based on the surface functionalities.

5.2 Results and Discussion

5.2.1 IR-806



Scheme 5.1. Synthesis of IR-806.

IR-806 was synthesised from a commercially available dye IR-780 following a slight modification from literature.^[16] The reaction is shown in Scheme 5.1. Several batches of IR-806 (gold coloured crystals) were synthesised and stored in the fridge protected from light. The UV-Vis and emission spectra of IR-780 ($\lambda_{\text{abs max}}$ 790 nm, $\lambda_{\text{em max}}$ 826 nm) and IR-806 ($\lambda_{\text{abs max}}$ 805 nm, $\lambda_{\text{em max}}$ 837 nm) are shown in Figure 5.3, matching the previously reported results.^[16] Equipment limitations only allowed for emission spectra measurements up until 850 nm, but did not hinder the observation of the emission maxima.

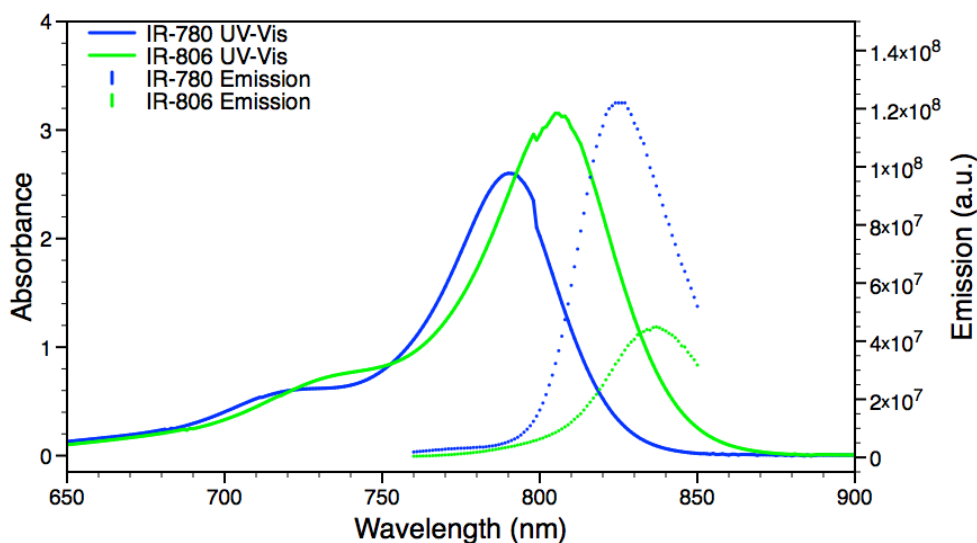


Figure 5.3. UV-Vis (solid) and Emission spectra (dotted, $\lambda_{\text{excitation}}$ 750 nm) of IR-780 and IR-806.

5.2.2 IR-806 dye adsorption to $\text{LiYF}_4: \text{Yb}^{3+}/\text{Tm}^{3+}$ nanoparticles

For initial trials, the adsorption/attachment of IR-806 to the surface of $\text{LiYF}_4: \text{Yb}^{3+}/\text{Tm}^{3+}$ nanoparticles was attempted. $\text{LiYF}_4: \text{Yb}^{3+}/\text{Tm}^{3+}$ nanoparticles (OG39) have an average size of 122 ± 14 nm, $\lambda_{\text{abs max}}$ at 977 nm (Yb^{3+}), are diamond shaped and were synthesised by Olga Gazukin.^[17] The UV-Vis spectrum in CHCl_3 and a TEM image of OG39 are shown in Figure 5.4. The UV-Vis spectrum of the bare UCNPs shows the characteristic absorption profile for the ${}^2\text{F}_{7/2} \rightarrow {}^2\text{F}_{5/2}$ transition of Yb^{3+} .^[18]

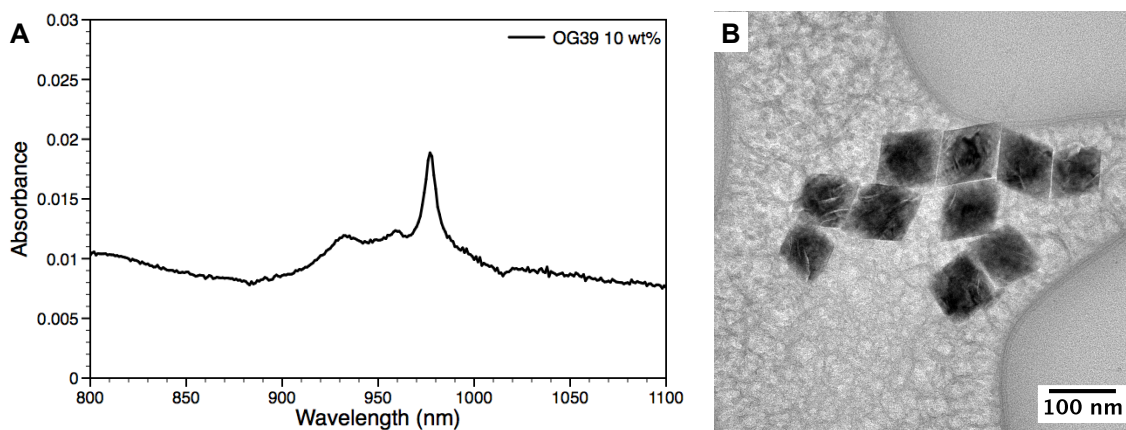


Figure 5.4. OG39; A) UV-Vis spectrum in CHCl_3 , B) TEM image.

IR-806 adsorption to OG39 (weight ratio 1:5) was carried out in CHCl_3 and the adsorption was followed by UV-Vis spectroscopy, recording the spectra after 4 h, 1, 4 and 7 days (Figure 5.5). A slight red shift from $\lambda_{\text{abs max}}$ 805 to 810 nm was observed after 4 h, indicative of the interaction of IR806 and OG39, and did not significantly change beyond this point.

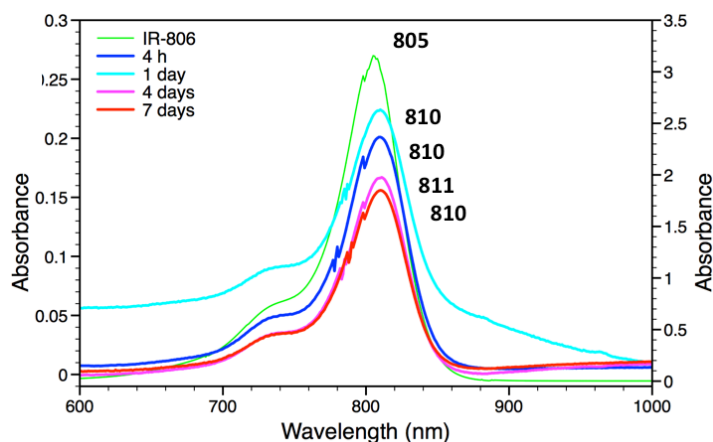


Figure 5.5. UV-Vis spectra of IR-806 and IR-806 adsorption to OG39 after 4 h, 1, 4 and 7 days. Y-axis left; Abs IR-806 and OG39 in CHCl_3 , y-axis right; IR-806 in CHCl_3 .

Following this, the IR-806 coated UCNP were further encapsulated with octylamine-modified polyacrylic acid (OPA), an amphiphilic polymer, to render them water-dispersible. The obtained nanoparticles are green in solution (Figure 5.6C) and can be obtained as a green solid when lyophilised. UV-Vis spectra of the final materials measured in water, showed an $\lambda_{\text{abs max}}$ at 805 nm for dye/UCNP ratio 1:50 (w/w) and a $\lambda_{\text{abs max}}$ at 807 nm for all other ratios (1:25, 1:100, 1:150 w/w) (Figure 5.6A). The UV-Vis spectrum of the nanoparticles were further referenced against dye-free OPA-coated OG39 nanoparticles in water ($\lambda_{\text{abs max}}$ 922 nm) in Figure 5.6B. IR-806 is not water soluble and the UV-Vis spectrum was therefore recorded in CHCl_3 .

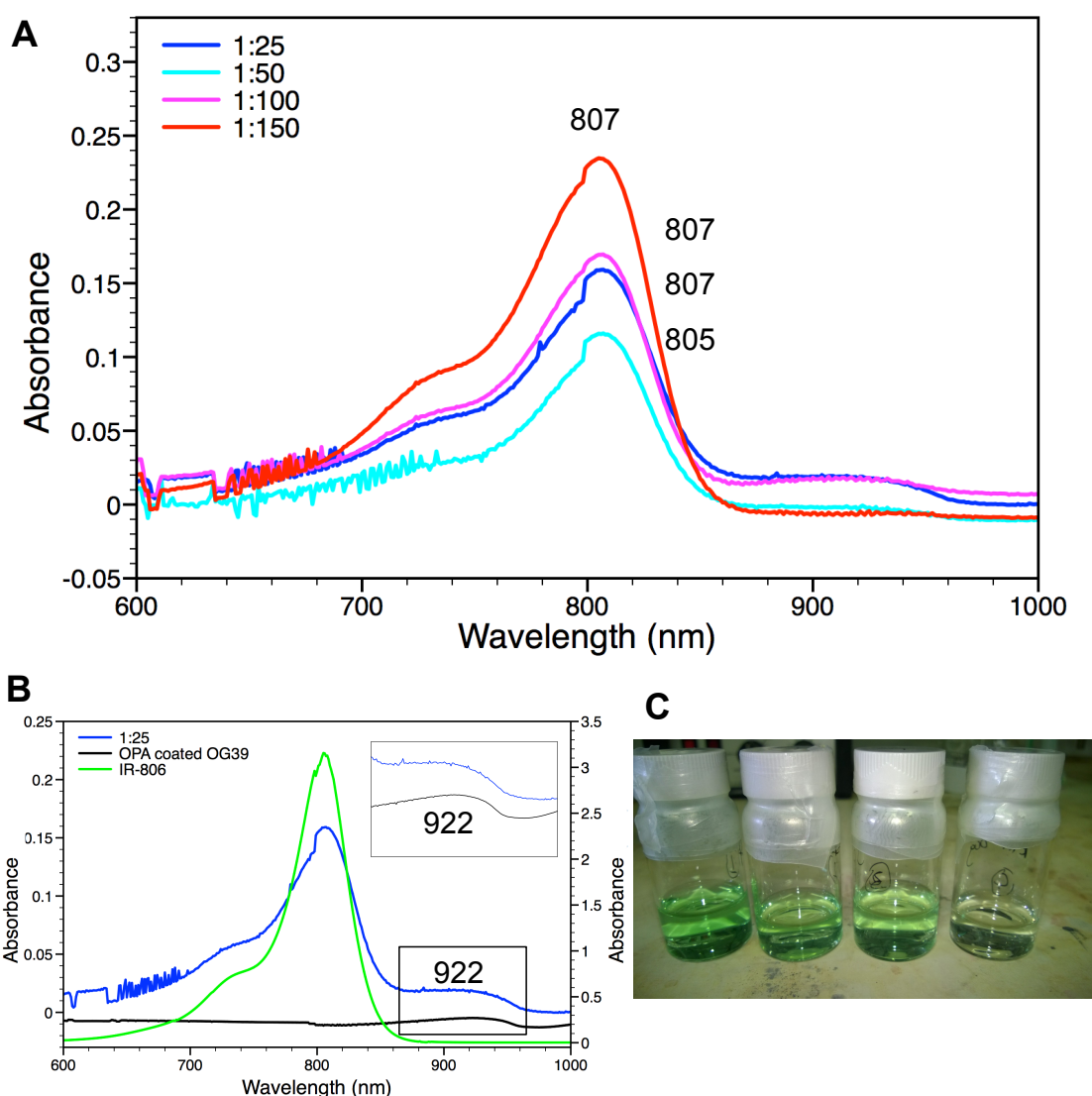


Figure 5.6. A) UV-Vis spectra of OPA coated OG39-IR-806 in water at different weight ratios (dye:OG39). B) UV-Vis spectra of OPA coated OG39-IR-806 (weight ratio 1:25) in water (LHS Abs. scale), OPA coated OG39 in water (LHS Abs. scale) and IR-806 in CHCl_3 (RHS Abs. scale). C) OPA coated OG39-IR-806 solutions in water.

In the absorption spectrum of the dye-loaded nanoparticles, characteristic absorption bands ascribable to the OPA coated nanoparticles as well as to the IR-806 were observed, providing clear evidence for the adsorption of IR-806 onto $\text{LiYF}_4: \text{Yb}^{3+}/\text{Tm}^{3+}$ nanoparticles. The resulting green solutions provide a visual proof for this. Moreover, the slight red shift in $\lambda_{\text{abs max}}$ for IR-806 from 805 nm to 810 nm is indicative of interaction between the two.

However, previously reported studies on interaction of IR-806 with $\text{NaYF}_4: \text{Yb}, \text{Er}$ nanoparticles mention a Dye:UCNP ratio dependent blue shift of $\lambda_{\text{abs max}}$ from 806 to 800 nm.^[16] Ratio dependent results originating in that case were carried out in CHCl_3 , on the dye samples and UCNPs simply mixed together in solution, whereas our UV-Vis studies were carried out in water, which may account for the difference in observations. Whether or not our particles behave differently to reported results remains unclear as changes in $\lambda_{\text{abs max}}$ in such a small range can be highly influenced by instrumental error (1 nm), which cannot be ruled out at this stage.

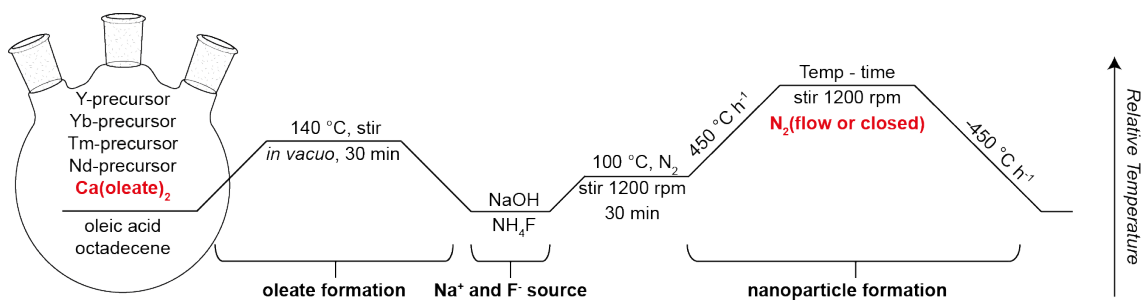
Evidence for IR-806 increasing the quantum yield of the nanoparticles has yet to be obtained. Emission spectra could not be recorded due to the lack of and technical challenges with appropriate instrumental setups (refer to Chapter 5.2.4). Collaboration should be established when these particles are pursued in the future.

5.2.3 Neodymium (Nd^{3+}) doped UCNP

Synthesis of Nd^{3+} -doped UCNP ($\text{NaYF}_4: \text{Yb}^{3+}/\text{Tm}^{3+}/\text{Nd}^{3+}$) involved a series of experiments to optimise the size and shape, adapting a synthetic procedure previously reported by Xie *et al.*^[13] A typical reaction involves a series of steps as shown in Scheme 5.2. In short, the lanthanide salts ($\text{Y}^{3+}:\text{Yb}^{3+}:\text{Tm}^{3+}:\text{Nd}^{3+} = 80.5:18:0.5:1$ mol%) in methanol are added to a three-neck round-bottom flask containing oleic acid (capping agent) and octadecene (high boiling point solvent). Methanol, water traces and oxygen are removed under vacuum at 140 °C, before cooling to 50 °C and addition of the fluoride and sodium source (NH_4F and NaOH in methanol). Evaporation of methanol is followed by an increase of temperature to 270 or 290 °C, at a rate of 450 °C h^{-1} and the solution was maintained at this temperature for a set time under N_2 or by applying a flow of N_2 allowing for nanoparticle formation. The resulting solution is then cooled to room temperature at 450 °C h^{-1} and the UCNP are collected

by addition of ethanol. Please refer to the experimental section for a more detailed description of synthetic procedure.

The size and shape of the Nd^{3+} -doped UCNPs were tuned by varying the temperature and time in an effort to yield small hexagonal-phase UCNPs, whereby higher temperatures restrict the formation of the thermodynamically less stable cubic-phase but favour the formation of larger nanoparticles.^[19] Size and uniformity control was further tested by introducing $\text{Ca}(\text{oleate})_2$, which has been reported to yield more reproducible and uniform UCNPs.^[20] Table 5.1 shows the summary of synthetic outcomes.



Scheme 5.2. Synthesis of neodymium doped nanoparticles, $\text{NaYF}_4: \text{Yb}^{3+}/\text{Tm}^{3+}/\text{Nd}^{3+}$ ($\text{Y}^{3+}:\text{Yb}^{3+}:\text{Tm}^{3+}:\text{Nd}^{3+} = 80.5:18:0.5:1$ mol%).

The synthesis of $\text{NaYF}_4: \text{Yb}^{3+}/\text{Tm}^{3+}/\text{Nd}^{3+}$ (18/0.5/1 mol%) UCNPs was carried out at 290 °C for 1.5 h (RRV-001), during which $\text{Ca}(\text{oleate})_2$ was introduced to yield RRV-011 and a gentle N_2 flow was used during the nanoparticle formation of RRV-017. RRV-001 UCNPs were characterised by TEM and have an average size of 59 ± 3.4 nm (Figure 5.7A). Addition of $\text{Ca}(\text{oleate})_2$ resulted in UCNPs (RRV-011) with an average size of 46 ± 3.1 nm and pure hexagonal-phase (X-ray diffraction and TEM, Figure 5.7B, 5.8). The average size of the particles was further reduced to 39 ± 1.6 nm when nitrogen was allowed to flow through the reaction vessel while heating (RRV-017, Scheme 5.2, Figure 5.7C).

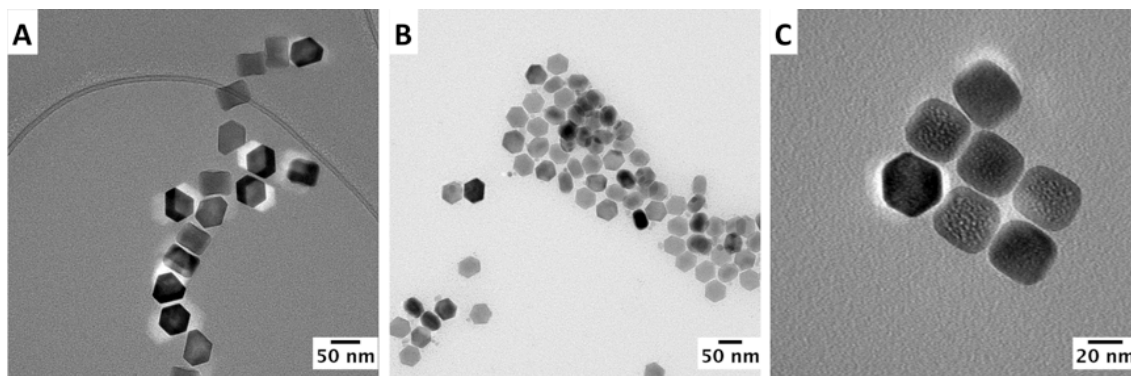


Figure 5.7. TEM images of $\text{NaYF}_4: \text{Yb}^{3+}/\text{Tm}^{3+}/\text{Nd}^{3+}$ (18/0.5/1 mol%) UCNPs; A) RRV-001, B) RRV-011, C) RRV-017.

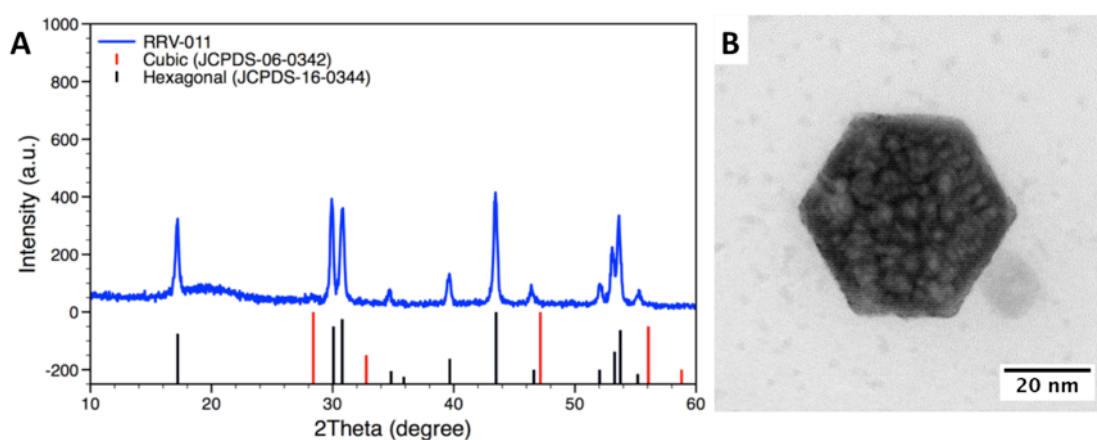


Figure 5.8. X-ray diffraction (A) and HR TEM (B) of $\text{NaYF}_4: \text{Yb}^{3+}/\text{Tm}^{3+}/\text{Nd}^{3+}$ UCNPs; RRV-011.

Synthesis of similarly doped $\text{NaYF}_4: \text{Yb}^{3+}/\text{Tm}^{3+}/\text{Nd}^{3+}$ UCNPs was carried out at a maximum temperature of 270 °C, in an effort to attain smaller sized nanoparticles, whilst varying the reaction time at this temperature (1.5 h RRV-003, 1.5 h RRV-007, 15 min RRV-012, 15 min RRV-013, 3h RRV-015 and 45 min OG111). However, non-uniform mixtures of UCNPs were obtained with size distributions ranging between 4 – 30 nm (Figure 5.9, Table 5.1).

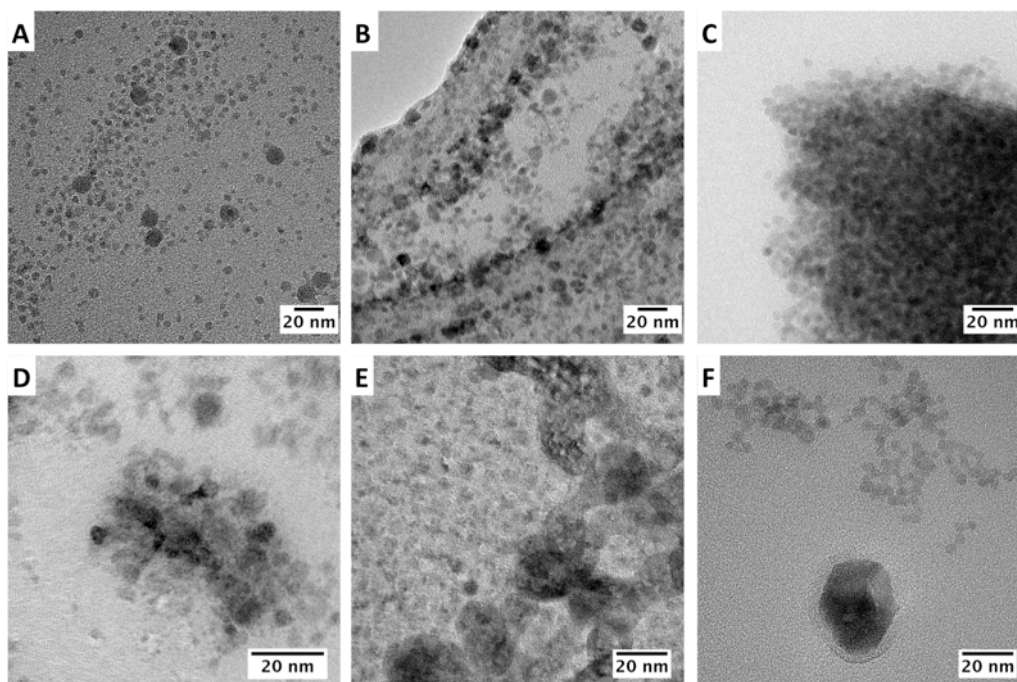


Figure 5.9. TEM images of NaYF₄: Yb³⁺/Tm³⁺/Nd³⁺ UCNPs synthesised at 270 °C maintained for: A) 1.5 h, RRV-003, B) 1.5 h, RRV-007, C) 15 min, RRV-012. D) 15 min, RRV-013. E) 3 h, RRV-015, F) 45 min, OG111.

UV-Vis spectra were recorded for all nanoparticles in n-hexane or cyclohexane and are identical for all ($\lambda_{\text{abs max Yb}}$ 977 nm). Representative UV-Vis spectra of RRV-011 in cyclohexane at different UCNP/solvent weight ratios (2.5, 5, 10 wt%) are shown in Figure 5.10.

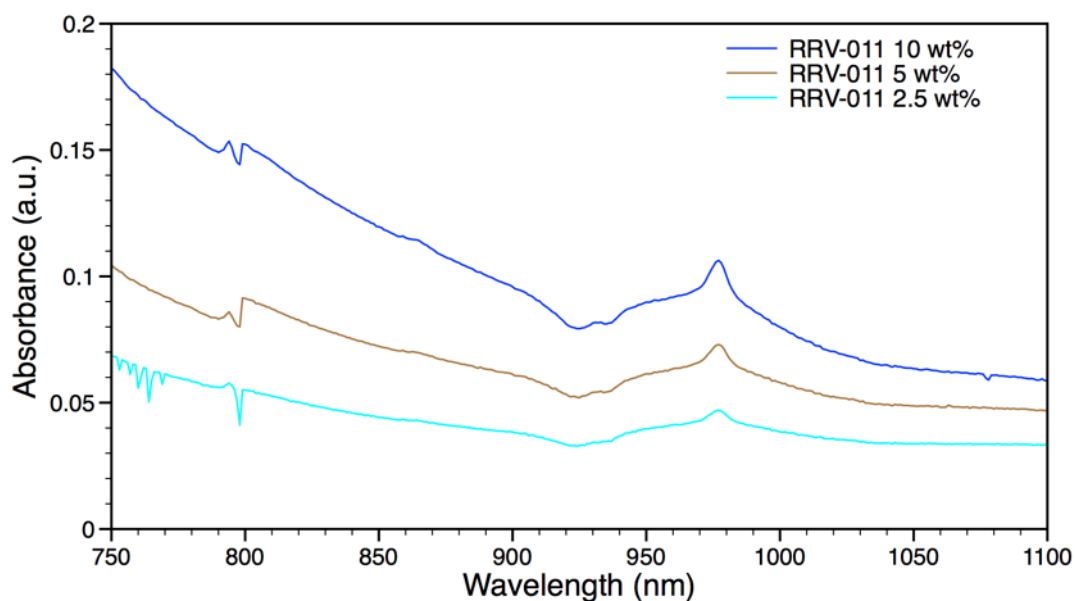


Figure 5.10. UV-Vis spectra of RRV-011 in cyclohexane at different UCNP/solvent weight ratios (wt%).

A variety of shape and size of neodymium doped nanoparticles was obtained by varying experimental conditions. Procedures carried out at 290 °C resulted in more uniform size distributions while reactions carried out at 270 °C resulted in two different sized nanoparticles in the same batch.

Introduction of Ca^{2+} ions into the nanoparticle lattice decreased the size of the nanoparticles by approximately 12 nm and resulted in pure hexagonal nanoparticles, as revealed by X-ray diffraction studies. The introduction of alkali ions into the UCNPs is believed to introduce F^- vacancies in the host matrix due to their lower valence. Previous reports have shown that this can potentially accelerate the crystal growth of UCNPs and turn it into a diffusion-controlled process tolerating shorter reaction times whilst maintaining a small unimodal size distribution of UCNPs.^[20-21]

The introduction of a N_2 flow during the heating process reduced the size of the nanoparticles by approximately 18 nm. The N_2 flow might be influencing the heating rate and create more stable maximum temperatures.

Very minor changes in the experimental conditions for synthesis of these nanoparticles can have a large effect on the shape and size of these particles. Therefore, emission profiles of the nanoparticles have to be measured followed by optimisation of the Ln^{3+} ion ratios to obtain the desired emission profiles, before continuing the size and shape optimisation.

It remains unclear whether the characteristic $\lambda_{\text{abs max}}$ of Nd^{3+} is present in the absorption profiles of the nanoparticles (Figure 5.10). A filter changeover at 800 nm of the spectrophotometer results in a measurement error in this region. Mathematical corrections were applied to correct the spectra. Nevertheless, a $\lambda_{\text{abs max}}$ at 800 nm was not evident. Recording emission profiles under 800 nm excitation would reveal whether neodymium doping of the nanoparticles led to the desired outcome.

5.2.4 Fluorescence Spectroscopy Setup for Upconverting Nanoparticles

The development of custom-made equipment was endeavoured in order to measure emission profiles of the recently developed UCNPs. A single cell holder for a Cary Eclipse Fluorescence Spectrophotometer was modified to hold single wavelength diode lasers (class 3b). Figure 5.11 illustrates a simplified overview of the setup as well as a top view picture, in which diode lasers of different diameters could be inserted using custom cut O-rings and connected

to the 3 VDC power supply. The build-in monochromators of the spectrophotometer were turned off and covered with a detector card for NIR light to focus the NIR diode lasers. The power switch of the diode lasers is placed outside the spectrophotometer to allow for control of the laser whilst the spectrophotometer is closed. Initial testing was carried out using ultrasmall UCNP particles obtained from our collaborators at Helmholtz-Zentrum Dresden-Rossendorf, Dr. Julia Hesse and Dr. Holger Stephan. Core particles, Core/Shell (C/S) particles and Core/Shell particles coated with OPA of the composition: NaYF₄: Nd³⁺/Yb³⁺/ Tm³⁺ (Core, 18/0.5/1 mol%) and NaYF₄: Nd³⁺ (Shell, 20 mol%) were used. TEM images of the core (11.71 ± 0.76 nm) and Core/Shell (C/S, 14.87 ± 0.61 nm) particles were taken before recording the emission spectra, confirming the average sizes obtained through dynamic light scattering measurements in *n*-hexane (Core: 13.78 ± 2.46 nm, C/S: 17.02 ± 2.92 nm) (Figure 5.12). The emission spectra, including selected peak labels, are depicted in Figure 5.13. Core, C/S and OPA coated C/S UCNP particles exhibit emission peaks at 290 nm (Tm³⁺, ¹I₆ → ³H₆), 346 nm (Tm³⁺, ¹I₆ → ³F₄), 363 nm (Tm³⁺, ¹D₂ → ³H₆), 452 nm (Tm³⁺, ⁴D₂ → ³F₄), 476 nm (Tm³⁺, ¹G₄ → ³H₆), 541 nm (impurity Er³⁺, ⁴S_{3/2} → ⁴I_{15/2}), 652 nm (Tm³⁺, ¹G₄ → ³F₄) and 804 nm (Nd³⁺, ³F_{4/2} → ⁴I_{9/2}) under 980 nm excitation (~200 mW). The emission profiles match those of similarly doped UCNP particles reported previously, confirming the presence of the lanthanide dopants and cover the excitation wavelengths for both the platinum (Chapter 2, 3.1, 3.2) and ruthenium (Chapter 3.5, 3.6) complexes discussed in this thesis.^[12-13] Different concentrations were used to obtain signal, as the emission from the water soluble UCNP particles suffered from a decrease in intensity as expected due to the absorption of NIR light by water and the OPA coating. This setup does not allow for additional photophysical measurements. Determination of life-time or quantum yield is not possible, as diode lasers are continuous wave and have to be refocused after each sample, i.e. identical power and focus on each sample is difficult to achieve.

This setup was developed, tested and approved initially with the use of a relatively weak (200 mW, 3 VDC) 980 nm diode laser (class 3b), due to stringent regulations regarding the use of (NIR) lasers. Approval was obtained over a year after synthesis of the UCNP particles, whilst approval of an 800 nm laser could not be obtained before travel to the University of Warwick. This setup, however, allows for fast screening of the emission profiles under different

excitation wavelengths directly after synthesis and is available at Monash University, School of Chemistry.

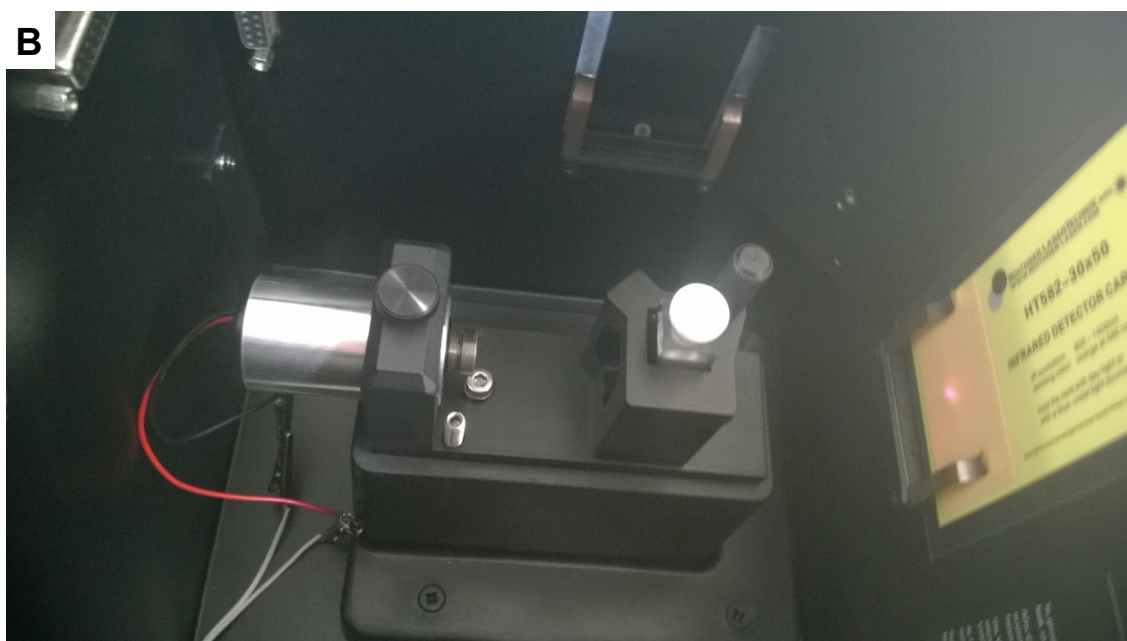
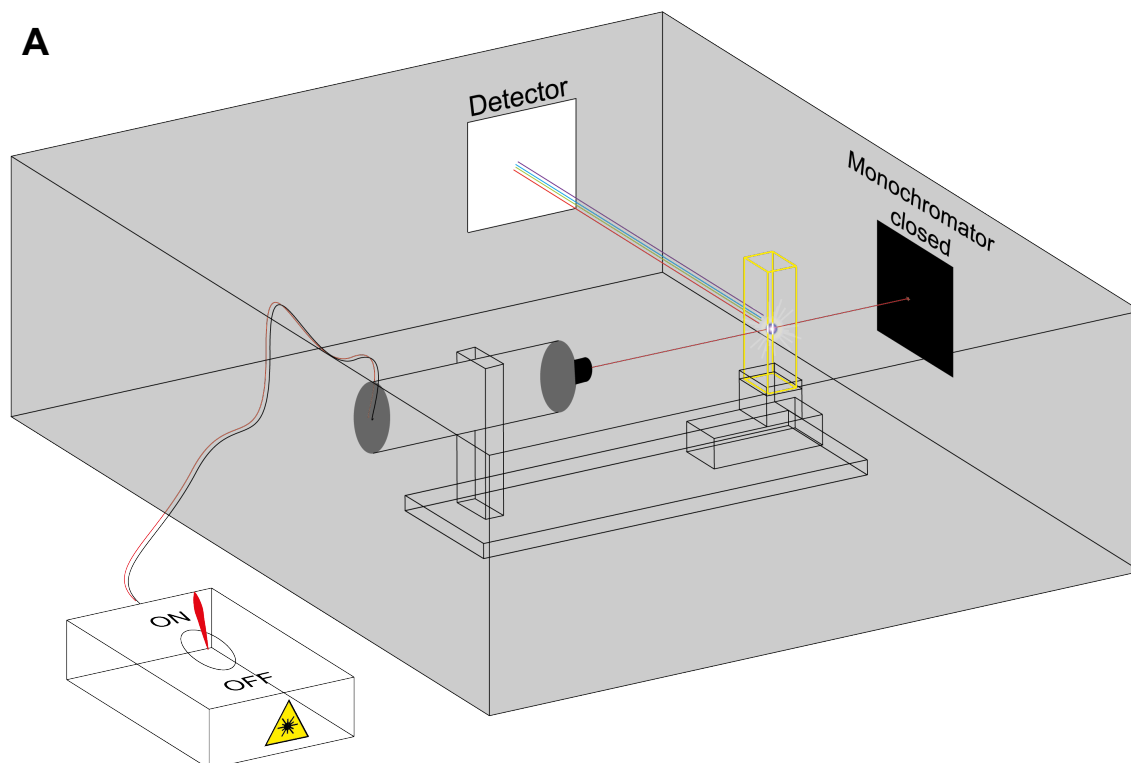


Figure 5.11. Simplified representation (A) and top view picture (B) of the custom sample and laser holder in a Cary Eclipse Fluorescence Spectrophotometer.

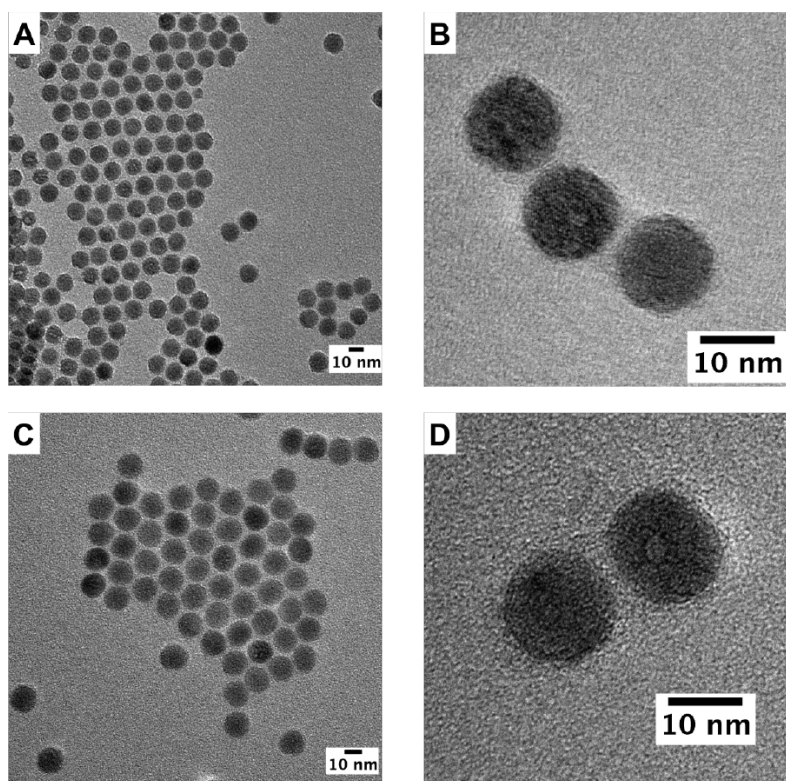


Figure 5.12. TEM images of $\text{NaYF}_4: \text{Nd}^{3+}/\text{Yb}^{3+}/\text{Tm}^{3+}$ (A, B Core) and $\text{NaYF}_4: \text{Nd}^{3+}@ \text{NaYF}_4: \text{Nd}^{3+}/\text{Yb}^{3+}/\text{Tm}^{3+}$ (C, D Core/Shell) particles synthesised by Dr. Julia Hesse.

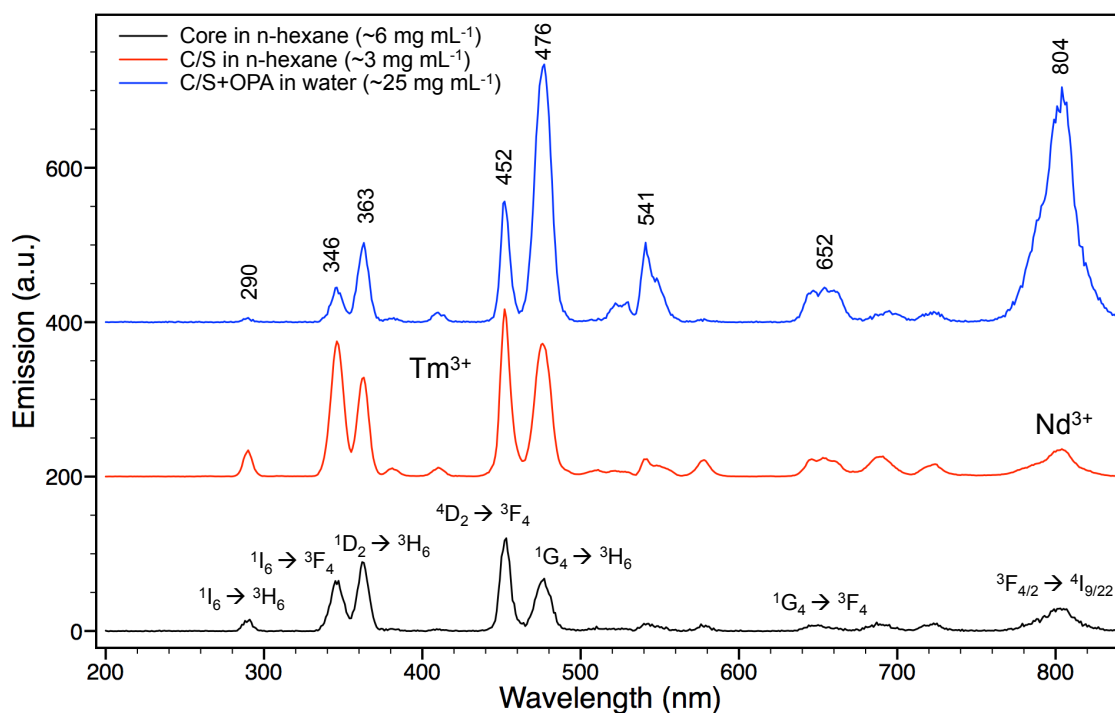


Figure 5.13. Emission spectra including selected peak labels of $\text{NaYF}_4: \text{Nd}^{3+}/\text{Yb}^{3+}/\text{Tm}^{3+}$ UCNPs in *n*-hexane (black), $\text{NaYF}_4: \text{Nd}^{3+}@ \text{NaYF}_4: \text{Nd}^{3+}/\text{Yb}^{3+}/\text{Tm}^{3+}$ UCNPs in *n*-hexane (red) and OPA coated $\text{NaYF}_4: \text{Nd}^{3+}@ \text{NaYF}_4: \text{Nd}^{3+}/\text{Yb}^{3+}/\text{Tm}^{3+}$ UCNPs in water (blue) under 980 nm excitation (~ 200 mW).

5.3 Conclusion

A range of NaYF₄: Nd³⁺/Yb³⁺/Tm³⁺ upconverting nanoparticles were synthesised, with measurement and sampling methods optimised.

A commercially available NIR dye, IR-780, was suitably modified to incorporate a carboxylate functionality (IR-806). This allowed for its coupling to LiYF₄: Yb³⁺/Tm³⁺ upconverting nanoparticles in an effort to increase emission intensity and broaden the window of excitation wavelengths of these particles. Nanoparticles were later coated with octylamine-modified polyacrylic acid to render them water-dispersible.

A range of neodymium (Nd³⁺) doped nanoparticles were synthesised with a theoretical intrinsic property of 800 nm excitation. Perfect hexagonal particles with a size of 46.3 ± 3.1 nm were synthesised, which were further optimised to a size of 39.0 ± 1.6 nm. Attempts to synthesise ultrasmall nanoparticles (< 10 nm) resulted in mixed population of ultrasmall and small (10 – 40 nm) nanoparticles. The above mentioned UCNPs would need to be studied by fluorescence spectroscopy before further optimisation of dye coupled, core and core-shell neodymium doped nanoparticles can be carried out as minor changes to the experimental procedure of these nanoparticles can have a large effect on their shape and size. Therefore, it is essential to measure the emission profiles and lifetimes before further size and shape optimisation. Collaboration was sought throughout the candidature but to no avail, thus far.

In order to progress, the development of custom-made equipment was endeavoured to measure emission profiles of the neodymium doped and dye coupled upconverting nanoparticles in-house. A single cell holder for a Cary Eclipse Fluorescence Spectrophotometer was modified to hold single wavelength diode lasers. Due to stringent regulations, the approval of this setup was obtained for one 980 nm laser over a year after the particle synthesis and optimised core/shell neodymium doped nanoparticles from our collaborators at Helmholtz-Zentrum Dresden-Rossendorf were used as a proof of principle. The setup enabled fast screening of the emission profiles under different excitation wavelengths using inexpensive NIR diode lasers. However, this setup does not allow for photophysical measurements, such as life-times and quantum yield determination, due to the limitations of diode lasers.

5.4 Experimental

5.4.1 Chemicals

All reactions were performed under nitrogen atmosphere using standard Schlenk techniques. Chemicals and other solvents were purchased from Sigma-Aldrich or BioScientific and used as such.

5.4.2 Instrumentation

¹H-NMR spectra were acquired on a Bruker DRX400 (400 MHz) spectrometer. Chemical shifts were referenced to the residual ¹H-NMR of deuterated solvents in ppm (δ) and the coupling constants are given in Hz.

UV-Vis spectra were acquired on a Varian Cary 5G UV-Vis-NIR spectrophotometer for NIR measurements and on a Varian Cary 300 BIO UV-Vis spectrophotometer equipped with a Varian Cary temperature controller.

Emission spectra were acquired on a Horiba Scientific FluoroMax4 fluorescence spectrophotometer.

ESI MS was carried out on a Micromass Platform II coupled to an ESI source with a capillary voltage of 3.5 keV and cone voltage of 35 V.

TEM images were acquired on a FEI Tecnai G2 T20 transmission electron microscope operated at an acceleration voltage of 200 kV at the Monash Centre for Electron Microscopy. ImageJ was used to process TEM images and calculate size distributions.^[22]

X-ray diffraction (XRD) patterns were acquired on a Philips X-ray diffractometer with Cu K α radiation.

DLS measurements were undertaken on a Brookhaven Instruments Corporation (BIC) Zetaplus Zeta Potential Analyzer and processed with BIC particle sizing software.

5.4.3 Synthesis

IR-806

Synthesis of IR-806 was adapted from literature.^[16]

A green solution of IR-780 (50 mg, 0.075 mmol) and 4-mercaptobenzoic acid (27 mg, 0.18 mmol) in DMF (5 mL) was stirred for 18 h at RT. Removal of DMF under reduced pressure at 50 °C resulted in a dark red residual with a green edge. The residue was dissolved in DCM (1 mL) and filtered through a 0.20 µm PTFE syringe filter followed by slow addition of diethyl ether (50 mL). Gold coloured crystals were collected by centrifugation, washed with diethyl ether over a glass frit and dried under vacuum (52 mg, 88%). ¹H-NMR (400 MHz, δ in CDCl₃, 298 K): 8.59 (d, *J* = 14.1 Hz, 2H), 7.97 (d, *J* = 8.1 Hz, 2H), 7.34 (t, *J* = 8.2 Hz, 2H), 7.26 (t, *J* = 6.9 Hz, 4H), 7.19 (t, *J* = 7.4 Hz, 2H), 7.11 (d, *J* = 8.0 Hz, 2H), 6.24 (d, *J* = 14.1 Hz, 2H), 4.10 (t, *J* = 7.2 Hz, 4H), 2.80 (t, *J* = 5.7 Hz, 4H), 2.06 (t, *J* = 5.6 Hz, 2H), 2.06 (t, *J* = 5.6 Hz, 2H), 1.88 (sext, 7.4 Hz, 4H), 1.43 (s, 12H), 1.04 (t, *J* = 7.4 Hz, 6H). ESI MS *m/z* (calcd.): 679.4 (679.333 [M – H + Na]⁺), 657.4 (657.351 [M]⁺).

Calcium di((9Z)-9-octadecenoate) (Ca(oleate)₂)

NaOH (0.9 g, 22 mmol) in 100 mL methanol was added drop wise to a solution of CaCl₂ (1.1 g, 10 mmol) and oleic acid (7.0 mL, 22 mmol) in 30 mL methanol. The reaction mixture was stirred at RT overnight. The white precipitate was washed three times with methanol, collected by centrifugation and dried under vacuum (2.9 g, 48%).

NaYF₄: Yb³⁺/Tm³⁺/Nd³⁺ Nanoparticles

A range of conditions has been investigated towards the synthesis of the nanoparticles. Experimental details are shown in Table 5.1. In a typical experiment the rare earth (RE) salts, yttrium, ytterbium, thulium and neodymium (80.5:18:0.5:1 mol%) were transferred into a 50 or 100 mL three neck round bottom flask using minimal amounts of methanol. After evaporation of methanol, oleic acid and 1-octadecene were added followed by heating at 140 °C under vacuum until a clear yellow solution was formed. The resulting mixture was cooled to 50 °C before NH₄F and NaOH (RE:NH₄F:NaOH, 1:4:2.5 mol%) was added and stirred for 30 min. The reaction temperature was increased to 100 °C

to remove methanol. Upon removal of methanol, the temperature was increased to 270 or 290 °C at a rate of 450 °C h⁻¹ and maintained at this temperature for a set time under N₂. The resulting solution was cooled to room temperature at 450 °C h⁻¹. The resulting nanoparticles were precipitated out by addition of ethanol, collected by centrifugation and washed three times with ethanol resulting in a brown oil. The nanoparticles were redispersed in n-hexane or cyclohexane (~10 wt%) and stored in the fridge.

NaYF₄: Ca²⁺/Yb³⁺/Tm³⁺/Nd³⁺ Nanoparticles

NaYF₄: Ca²⁺/Yb³⁺/Tm³⁺/Nd³⁺ nanoparticles (80.5:10:18:0.5:1 mol%) were synthesised using the same procedure as NaYF₄: Yb³⁺/Tm³⁺/Nd³⁺ nanoparticles where Ca(oleate)₂ was added simultaneously with the RE methanol mixture to the round bottom flask. Experimental details are shown in Table 5.1.

LiYF₄: Yb³⁺/Tm³⁺ Nanoparticles

Synthesis of LiYF₄: Yb³⁺/Tm³⁺ nanoparticles was carried out in collaboration with Olga Gazukin (Monash University),^[17] and adapted from literature.^[23]

Yttrium trifluoroacetate (856 mg, 2.00 mmol), ytterbium trifluoroacetate (276 mg, 0.539 mmol), thulium trifluoroacetate (5.08 mg, 0.0100 mmol) and lithium trifluoroacetate (300 mg, 2.50 mmol) were added to a three-necked round bottom flask followed by addition of oleic acid (20 mL) and 1-octadecene (20 mL). The mixture was heated to 110 °C at a rate of 450 °C h⁻¹ at 1200 rpm under vacuum for 3 hours. The flask was placed under nitrogen and heated to 322 °C at a rate of 450 °C h⁻¹ and kept at the temperature for one hour before cooling down to RT. The resulting nanoparticles were precipitated out by addition of ethanol, collected by centrifugation, redispersed in minimal amounts of chloroform and washed three times with ethanol resulting in a yellow oil. Size(TEM) = 122±14 nm. λ_{abs max Yb} 977 nm.

IR-806 dye adsorption to LiYF₄: Yb³⁺/Tm³⁺ nanoparticles

IR-806 (0.049 mg in 2.04 mL CHCl₃) was added to a round bottom flask containing LiYF₄: Yb³⁺/Tm³⁺ nanoparticles (6.5 mg) in 0.39 mL CHCl₃. The reaction was stirred at RT under N₂ for 2 hours before addition of 20 mL ethanol. The nanoparticles were collected by centrifugation and washed three

times with ethanol before drying under vacuum at 40 °C. The green solid was stored in the fridge and protected from light.

In another batch, IR-806 (1.36 mg in 2.00 mL CHCl₃) was added to a round bottom flask containing LiYF₄: Yb³⁺/Tm³⁺ nanoparticles (6.5 mg) in 0.80 mL CHCl₃. The reaction was stirred at RT under N₂ for a week, where samples were taken for UV-Vis at 4 h, 1, 4 and 7 days before addition of 80 mL of ethanol. The nanoparticles were collected by centrifugation and washed three times with ethanol before drying under vacuum at 40 °C (13 mg). The green solid was stored in the fridge and protected from light.

Table 5.1. Experimental details of NaYF₄: (Ca²⁺) Yb³⁺/Tm³⁺/Nd³⁺ nanoparticle synthesis.

Sample	Scale	RE	Temp & Time ^a	Yield	TEM (nm) ^b
RRV-001	0.4 mmol RE 9.5 mmol OA (3 mL) 21.9 mmol ODE (7 mL) 1.6 mmol NH ₄ F 1.0 mmol NaOH	Y(CH ₃ CO ₂) ₃ • xH ₂ O Yb(CH ₃ CO ₂) ₃ • xH ₂ O Tm(CH ₃ CO ₂) ₃ • xH ₂ O Nd(CF ₃ SO ₂) ₃	290 °C 1.5 h 450 °C h ⁻¹ heating, stir 450 °C h ⁻¹ cooling, stir	0.17 g	58.5 ± 3.4 nm
RRV-011	0.4 mmol RE 9.5 mmol OA (3 mL) 21.9 mmol ODE (7 mL) 1.6 mmol NH ₄ F 1.0 mmol NaOH	Y(CH ₃ CO ₂) ₃ • xH ₂ O Yb(CH ₃ CO ₂) ₃ • xH ₂ O Tm(CH ₃ CO ₂) ₃ • xH ₂ O Nd(CF ₃ SO ₂) ₃ Ca(Oleate) ₂	290 °C 1.5 h 450 °C h ⁻¹ heating, stir 450 °C h ⁻¹ cooling, stir	0.18 g	46.3 ± 3.1 nm
RRV-017	0.4 mmol RE 9.5 mmol OA (3 mL) 21.9 mmol ODE (7 mL) 1.6 mmol NH ₄ F 1.0 mmol NaOH	Y(CH ₃ CO ₂) ₃ • xH ₂ O Yb(CH ₃ CO ₂) ₃ • xH ₂ O Tm(CH ₃ CO ₂) ₃ • xH ₂ O Nd(CH ₃ CO ₂) ₃ • xH ₂ O	290 °C 1.5 h 450 °C h ⁻¹ heating, stir, N ₂ flow 450 °C h ⁻¹ cooling, stir	0.30 g	39.0 ± 1.6 nm
RRV-003	1.0 mmol RE 10 mmol OA (3.2 mL) 37.5 mmol ODE (7 mL) 4.0 mmol NH ₄ F 2.5 mmol NaOH	Y(CH ₃ CO ₂) ₃ • xH ₂ O Yb(CH ₃ CO ₂) ₃ • xH ₂ O Tm(CH ₃ CO ₂) ₃ • xH ₂ O Nd(CF ₃ SO ₂) ₃	270 °C 1.5 h 450 °C h ⁻¹ heating, stir No controlled cooling, no stirring	0.24 g	~4-12 nm
RRV-007	1.0 mmol RE 10 mmol OA (3.2 mL) 37.5 mmol ODE (7 mL) 4.0 mmol NH ₄ F 2.5 mmol NaOH	Y(CH ₃ CO ₂) ₃ • xH ₂ O Yb(CH ₃ CO ₂) ₃ • xH ₂ O Tm(CH ₃ CO ₂) ₃ • xH ₂ O Nd(CF ₃ SO ₂) ₃	270 °C 1.5 h 450 °C h ⁻¹ heating, stir 450 °C h ⁻¹ cooling, stir	0.10 g	~4-20 nm
OG111	1.0 mmol RE 10 mmol OA (3.2 mL) 37.5 mmol ODE (7 mL) 4.0 mmol NH ₄ F 2.5 mmol NaOH	Y(CH ₃ CO ₂) ₃ • xH ₂ O Yb(CH ₃ CO ₂) ₃ • xH ₂ O Tm(CH ₃ CO ₂) ₃ • xH ₂ O Nd(CF ₃ SO ₂) ₃	270 °C 45 min 450 °C h ⁻¹ heating, stir 450 °C h ⁻¹ cooling, stir	-	~4-40 nm
RRV-012	1.0 mmol RE 10 mmol OA (3.2 mL) 37.5 mmol ODE (7 mL) 4.0 mmol NH ₄ F 2.5 mmol NaOH	Y(TFA) ₃ Yb(Cl) ₃ Tm(CH ₃ CO ₂) ₃ • xH ₂ O Nd(CF ₃ SO ₂) ₃	270 °C 15 min 450 °C h ⁻¹ heating, stir 450 °C h ⁻¹ cooling, stir	0.14 g	~3-10 nm
RRV-013	1.0 mmol RE 10 mmol OA (3.2 mL) 37.5 mmol ODE (7 mL) 4.0 mmol NH ₄ F 2.5 mmol NaOH	Y(CH ₃ CO ₂) ₃ Yb(Cl) ₃ Tm(CH ₃ CO ₂) ₃ • xH ₂ O Nd(CF ₃ SO ₂) ₃	270 °C 15 min 450 °C h ⁻¹ heating, stir 450 °C h ⁻¹ cooling, stir	0.19 g	~3-10 nm
RRV-015	1.0 mmol RE 10 mmol OA (3.2 mL) 37.5 mmol ODE (7 mL) 4.0 mmol NH ₄ F 2.5 mmol NaOH	Y(CH ₃ CO ₂) ₃ Yb(Cl) ₃ Tm(CH ₃ CO ₂) ₃ • xH ₂ O Nd(CF ₃ SO ₂) ₃	270 °C 3 h 450 °C h ⁻¹ heating, stir 450 °C h ⁻¹ cooling, stir	0.80 g	~3-30 nm

^a stirring is set to 1200 rpm. ^b Average sizes were calculated using at least 100 individual nanoparticles when particles were uniform, ~ = indicates the range of sizes observed by TEM when more than one average particle size was present.

Octylamine-Modified Polyacrylic Acid (OPA)

Octylamine-modified polyacrylic acid (OPA) was synthesised as described elsewhere.^[24]

OPA coating of LiYF₄: Yb³⁺/Tm³⁺ nanoparticles

A five-fold excess of OPA (25 mg) in 5 mL CHCl₃ was added to a round bottom flask containing LiYF₄: Yb³⁺/Tm³⁺ nanoparticles (5 mg) in 1 mL CHCl₃. The reaction mixture was stirred at RT under N₂ for 2 hours followed by solvent removal under reduced pressure. 20 mL of water was added to the white solid, the pH was adjusted to ~ 9 and the mixture was sonicated until fully suspended. The resulting reaction mixture was filtered through a 0.2 µm PTFE syringe filter, spin dialysed using a 50 kDa centrifugal filters and washed three times with water using the same filter. The transparent concentrated solutions were stored in the fridge.

OPA coating and IR-806 dye adsorption to LiYF₄: Yb³⁺/Tm³⁺ nanoparticles

IR-806 was attached to LiYF₄: Yb³⁺/Tm³⁺ nanoparticles at different ratios and coated with OPA (Table 5.2). A stock solution of IR-806 (4.16 mg in 5 mL CHCl₃) was used. IR-806 was added to a solution of LiYF₄: Yb³⁺/Tm³⁺ nanoparticles in 15 mL CHCl₃ and the resulting green mixtures were stirred at RT under N₂ for 3 hours. An excess of OPA in 1.2 mL CHCl₃ was added to the reaction mixture and stirred at RT under nitrogen for 2 hours followed by solvent removal under reduced pressure. 15 mL of water was added to the green solid, the pH was adjusted to ~ 9 and the mixture was sonicated until fully suspended. The resulting reaction mixture was filtered through a 0.2 µm PTFE syringe filter, spin dialysed using a 50 kDa centrifugal filter and washed three times with water using the same filter. Note that the filtrate of sample 1 and 2 was slightly green after the final third wash. The green concentrated solutions were stored in the fridge and protected from light.

Table 5.2. Experimental details of OPA coating and IR-806 dye adsorption to $\text{LiYF}_4: \text{Yb}^{3+}/\text{Tm}^{3+}$ nanoparticles.

Sample	Ratio (NP:IR-806)	NP (mg)	IR-806 (mg)	OPA (mg)
1	25:1	5.91	0.24	24
2	50:1	7.48	0.15	31
3	100:1	12.46	0.12	52
4	150:1	5.96	0.04	25

5.5 References

- [1] X. Chen, D. Peng, Q. Ju, F. Wang, *Chem. Soc. Rev.* **2015**, *44*, 1318-1330.
- [2] a) L. Xiong, T. Yang, Y. Yang, C. Xu, F. Li, *Biomaterials* **2010**, *31*, 7078-7085; b) L. Cheng, K. Yang, M. Shao, X. Lu, Z. Liu, *Nanomedicine* **2011**, *6*, 1327-1340.
- [3] C. J. Sunderland, M. Steiert, J. E. Talmadge, A. M. Derfus, S. E. Barry, *Drug Dev. Res.* **2006**, *67*, 70-93.
- [4] a) J. H. Rao, *ACS Nano* **2008**, *2*, 1984-1986; b) F. Alexis, E. Pridgen, L. K. Molnar, O. C. Farokhzad, *Mol. Pharm.* **2008**, *5*, 505-515; c) E. Gullotti, Y. Yeo, *Mol. Pharm.* **2009**, *6*, 1041-1051; d) S. D. Li, L. Huang, *Mol. Pharm.* **2008**, *5*, 496-504; e) H. S. Choi, W. Liu, P. Misra, E. Tanaka, J. P. Zimmer, B. I. Ipe, M. G. Bawendi, J. V. Frangioni, *Nat. Biotechnol.* **2007**, *25*, 1165-1170; f) M. E. Davis, Z. Chen, D. M. Shin, *Nat. Rev. Drug Discovery* **2008**, *7*, 771-782.
- [5] Y. Gao, X. Zhu, Y. Zhang, X. Chen, L. Wang, W. Feng, C. Huang, F. Li, *RSC Adv.* **2017**, *7*, 31588-31596.
- [6] a) I. Brigger, C. Dubernet, P. Couvreur, *Adv. Drug Del. Rev.* **2002**, *54*, 631-651; b) P. S. Williams, F. Carpino, M. Zborowski, *Mol. Pharm.* **2009**, *6*, 1290-1306; c) F. M. Kievit, M. Zhang, *Adv. Mater.* **2011**, *23*, H217-H247.
- [7] a) N. M. Idris, M. K. Gnanasammandhan, J. Zhang, P. C. Ho, R. Mahendran, Y. Zhang, *Nat. Med.* **2012**, *18*, 1580-U1190; b) J. Peng, Y. Sun, L. Zhao, Y. Wu, W. Feng, Y. Gao, F. Li, *Biomaterials* **2013**, *34*, 9535-9544; c) P. Lei, P. Zhang, S. Yao, S. Song, L. Dong, X. Xu, X. Liu, K. Du, J. Feng, H. Zhang, *ACS Appl. Mater. Interfaces* **2016**, *8*, 27490-27497.
- [8] a) J. F. Suyver, A. Aebischer, S. García-Revilla, P. Gerner, H. U. Güdel, *Phys. Rev. B* **2005**, *71*, 125123; b) J. H. Burns, *Inorg. Chem.* **1965**, *4*, 881-886; c) A. Aebischer, M. Hostettler, J. Hauser, K. Krämer, T. Weber, H. U. Güdel, H.-B. Bürgi, *Angew. Chem. Int. Ed.* **2006**, *45*, 2802-2806; d) H.-S. Qian, Y. Zhang, *Langmuir* **2008**, *24*, 12123-12125.

- [9] a) Q. Zhan, J. Qian, H. Liang, G. Somesfalean, D. Wang, S. He, Z. Zhang, S. Andersson-Engels, *ACS Nano* **2011**, *5*, 3744-3757; b) H. Kobayashi, M. Ogawa, R. Alford, P. L. Choyke, Y. Urano, *Chem. Rev.* **2009**, *110*, 2620-2640; c) X. Xie, X. Liu, *Nat. Mater.* **2012**, *11*, 842-843.
- [10] a) S. Wilhelm, M. Kaiser, C. Wurth, J. Heiland, C. Carrillo-Carrion, V. Muhr, O. S. Wolfbeis, W. J. Parak, U. Resch-Genger, T. Hirsch, *Nanoscale* **2015**, *7*, 1403-1410; b) S. L. Gai, P. P. Yang, C. X. Li, W. X. Wang, Y. L. Dai, N. Niu, J. Lin, *Adv. Funct. Mater.* **2010**, *20*, 1166-1172; c) L.-L. Li, R. Zhang, L. Yin, K. Zheng, W. Qin, P. R. Selvin, Y. Lu, *Angew. Chem. Int. Ed.* **2012**, *51*, 6121-6125; d) K. P. García, K. Zarschler, L. Barbaro, J. A. Barreto, W. O'Malley, L. Spiccia, H. Stephan, B. Graham, *Small* **2014**, *10*, 2516–2529.
- [11] a) K. Pombo-Garcia, K. Zarschler, J. A. Barreto, J. Hesse, L. Spiccia, B. Graham, H. Stephan, *RSC Adv.* **2013**, *3*, 22443-22454; b) K. Pombo-García, S. Weiss, K. Zarschler, C.-S. Ang, R. Hübner, J. Pufe, S. Meister, J. Seidel, J. Pietzsch, L. Spiccia, H. Stephan, B. Graham, *ChemNanoMat* **2016**, *2*, 959-971.
- [12] J. Shen, G. Chen, A.-M. Vu, W. Fan, O. S. Bilsel, C.-C. Chang, G. Han, *Adv. Opt. Mater.* **2013**, *1*, 644-650.
- [13] X. Xie, N. Gao, R. Deng, Q. Sun, Q.-H. Xu, X. Liu, *J. Am. Chem. Soc.* **2013**, *135*, 12608-12611.
- [14] a) F. Wang, D. Banerjee, Y. Liu, X. Chen, X. Liu, *Analyst* **2010**, *135*, 1839-1854; b) X. Xue, S. Uechi, R. N. Tiwari, Z. Duan, M. Liao, M. Yoshimura, T. Suzuki, Y. Ohishi, *Opt. Mater. Express* **2013**, *3*, 989-999.
- [15] a) The American Cancer Society, <https://www.cancer.org/treatment/treatments-and-side-effects/treatment-types/photodynamic-therapy.html> (03/08/2017), **2015**; b) NHS UK, [http://www.nhs.uk/conditions/photodynamic-therapy-ngpdt-sonodynamic-therapy/pages/introduction.aspx - what-happens](http://www.nhs.uk/conditions/photodynamic-therapy-ngpdt-sonodynamic-therapy/pages/introduction.aspx-what-happens) (03/08/2017), **2016**.
- [16] W. Zou, C. Visser, J. A. Maduro, M. S. Pshenichnikov, J. C. Hummelen, *Nat Photon* **2012**, *6*, 560-564.
- [17] O. Gazukin, Masters Thesis, Monash University (<https://doi.org/10.4225/03/58ab82fe830ac>), **2016**.
- [18] K. V. Krishnaiah, E. Soares de Lima Filho, Y. Ledemi, G. Nemova, Y. Messaddeq, R. Kashyap, **2016**, *6*, 21905.

- [19] L. Zhengquan, Z. Yong, *Nanotechnology* **2008**, *19*, 345606.
- [20] L. Lei, D. Chen, P. Huang, J. Xu, R. Zhang, Y. Wang, *Nanoscale* **2013**, *5*, 11298-11305.
- [21] a) W. Zheng, S. Y. Zhou, Z. Chen, P. Hu, Y. S. Liu, D. T. Tu, H. M. Zhu, R. F. Li, M. D. Huang, X. Y. Chen, *Angew. Chem. Int. Ed.* **2013**, *52*, 6671-6676; b) A. Pandey, V. K. Rai, K. Kumar, *Spectrochim. Acta Mol. Biomol. Spectros.* **2014**, *118*, 619-623.
- [22] W. S. Rasband, U. S. National Institutes of Health, Bethesda, Maryland, USA, **1997-2014**.
- [23] V. Mahalingam, F. Vetrone, R. Naccache, A. Speghini, J. A. Capobianco, *Adv. Mater.* **2009**, *21*, 4025–4028.
- [24] M. Zhou, E. Nakatani, L. S. Gronenberg, T. Tokimoto, M. J. Wirth, V. J. Hruby, A. Roberts, R. M. Lynch, I. Ghosh, *Bioconjugate Chem.* **2007**, *18*, 323-332.

Chapter 6

Conclusion and Future Perspectives

The requirement for more effective anticancer drugs is clear, and new classes of metal-based photoactivatable prodrugs might provide the necessary means to overcome the current drawbacks, on account of their novel mechanism(s) of action. However, a viable and improved chemotherapeutic agent is very rarely revealed in the first round of discovery. Studying the mechanisms of action can provide invaluable information for the development of more potent prodrugs and yield experimental evidence on how to modify screened candidates.

Vibrational spectroscopic approaches were used throughout this thesis to study the photophysical and photochemical properties of metal-based photoactivatable anticancer prodrugs, centred around the potent diazido Pt(IV) prodrug candidate. These techniques reasserted the excellent capabilities of vibrational spectroscopy to study such prodrugs whilst being non-destructive and label-free.

In this thesis, the comprehensive vibrational spectroscopic screening of *trans,trans,trans*-[Pt(N₃)₂(OH)₂(py)₂] (**1**, py = pyridine) followed by the subsequent mechanism of action studies of **1** have been described (Chapter 2 and Chapter 3.1, 3.2 respectively). Alike methodologies were applied to study a series of ruthenium CO releasing complexes (Chapter 3.5, 3.6). The high-brilliance of synchrotron radiation was exploited by infrared spectroscopy further examining the photoactivation and *in vitro* activity of **1** (Chapter 4). Finally, the preparation of upconverting nanoparticles (UCNPs) was examined towards their potential application in combination with photoactivatable prodrug candidates (Chapter 5).

The work presented in this thesis can be summarised based on the previously noted research objectives in Chapter 1.7. Where appropriate, further work is also suggested.

1. *Explore the vibrational fingerprint of the photoactivatable Pt(IV) prodrug candidate, trans,trans,trans-[Pt(N₃)₂(OH)₂(py)₂] (**1**, py = pyridine), with a series of vibrational spectroscopic techniques as the essential first step towards monitoring the photoactivation pathways.*

The ligand (pyridine, hydroxide and azide) and Pt-ligand vibrations of **1** were recorded by Attenuated Total Reflection Fourier Transform Infrared (ATR-FTIR), Raman and transmission synchrotron radiation far-infrared (SR-FIR) and were assigned by comparison to the synthetic precursors *trans*-[Pt(N₃)₂(py)₂] and *trans*-[PtCl₂(py)₂] (Chapter 2). Assignments of vibrational modes were aided by Density Functional Theory (DFT) calculations, with experimental data consistent with the predicted values. Notably, are the strong platinum to oxygen stretching vibrations, $\nu(\text{OH}_{\text{Pt-OH}})$ (540 cm⁻¹) and the platinum to nitrogen stretching vibrations, $\nu(\text{Pt-N}_3)$ (415 – 395 cm⁻¹) by SR-FIR, which are likewise Raman active. Furthermore, multiple strong anti-symmetric azido stretching vibrations, $\nu_{\text{asym}}(\text{N}_3)$ (2048 cm⁻¹ and 2033 cm⁻¹) and a sharp hydroxido stretching vibration, $\nu(\text{OH}_{\text{Pt-OH}})$ (3551 cm⁻¹) were observed by ATR-FTIR after the deposition of **1** in water (2 mM).

This essential first step allowed for translation of the described methodologies into further application in photodecomposition and photoreaction studies.

2. *Translation of the vibrational signatures to support photodecomposition and photoinduced binding studies of **1** and subsequently apply these methods to other metal-based PACT candidates.*

New insights into the mechanism of action of **1** were elucidated by a combination of ATR-FTIR, transient electronic absorption spectroscopy (TEAS) and UV-Vis spectroscopy (Chapter 3.1, 3.2). Following the selected results in Figure 6.1, a multistep mechanism could be assigned to the photodecomposition of **1** in water upon 420 nm irradiation. Principal Component

Analysis (PCA) correlated the removal of $\nu(\text{OH}_{\text{Pt-OH}})$ at 3550 cm^{-1} to a -10 cm^{-1} decrease to $\nu_{\text{asym}}(\text{N}_3)$, prior to an increase of 21 cm^{-1} upon complete disappearance of $\nu(\text{OH}_{\text{Pt-OH}})$. At the same time, the formation of a new broad $\delta(\text{OH}_{\text{Pt-OH/OH}_2})$ vibration at 1381 cm^{-1} and 1334 cm^{-1} correlates to the single $\nu_{\text{asym}}(\text{N}_3)$ vibration at 2044 cm^{-1} , with gradual increase of $\delta(\text{OH}_{\text{Pt-OH/OH}_2})$ until $\nu_{\text{asym}}(\text{N}_3)$ is completely removed. Additional HPLC and Multi Curve Resolution Alternating Least Squares (MCR-ALS) on ATR-FTIR and UV-Vis spectra suggested the formation of a *trans*-[Pt(N₃)(py)₂(OH/H₂O)] intermediate and a final product, *trans*-[Pt(py)₂(OH/H₂O)₂]. Studies carried out in acetonitrile for **1** and its synthetic precursor *trans*-[Pt(N₃)₂(py)₂] showed similar photodecomposition pathways with analogous intermediate species, verified by the pure components obtained with MCR-ALS. TEAS to study the fast photomechanics of **1** provided a plausible switching mechanism where the excited state complex has access to a dissociative ³MC state only when it is vibrationally hot. Consecutively, **1** gets trapped in a vibrationally cool state resulting in a long-lived absorption ($\gg 2\text{ ns}$). Extending on reactivity of **1** were the photoinduced reactions in the presence of the DNA nucleotide, 5'-guanosine monophosphate (5'-GMP). These studies revealed the faster removal of $\nu(\text{OH}_{\text{Pt-OH}})$ compared to the photodecomposition ($\leq 5\text{ min}$ vs. 20 min) and increased hydrogen bonding between the hydroxide ligands of **1** and 5'-GMP and/or water prior to irradiation. HPLC separation of the photoproducts allowed for the mass spectrometry and ATR-FTIR characterisation. Aided by frequency calculations of DFT optimised photoproducts, marker bands for the major photoproducts *trans*-[Pt(N₃)(py)₂(5'-GMP)] and *trans*-[Pt(py)₂(5'-GMP)₂] were deduced and marker bands at 1772 cm^{-1} , for example, could be used to follow the formation of the latter product in the reaction mixture by ATR-FTIR.

Successful translation of the ATR-FTIR methodology to study the steady state photodecomposition showed evidence of subsequent azido dissociation from platinum, which suggests that at least one hydroxyl radical is formed in the reduction of Pt(IV) to Pt(II) under such conditions. TEAS revealed several characteristics of the complicated fast photodynamics. However, TEAS is blind to the formation of photoproducts, thus paving the way for more comprehensive ultrafast photodynamic studies (transient vibrational spectroscopy) in combination with DFT calculations. The optimisation of singlet and triplet

excited state structures by TD-DFT via vertical excitation of the corresponding ground states could provide essential information on excited state energies, which can potentially be measured with transient infrared spectroscopy, focussing on the azido and hydroxido ligand vibrations. The photoinduced reactions with 5'-GMP can contribute to understanding the chemical basis for the mechanism of action of **1** with DNA bases. This could be followed up with studies using short oligonucleotides as a DNA model to complement previous DNA binding studies of **1**, opening up the option to detect the interactions of released ligands as potential azide anions or radicals.

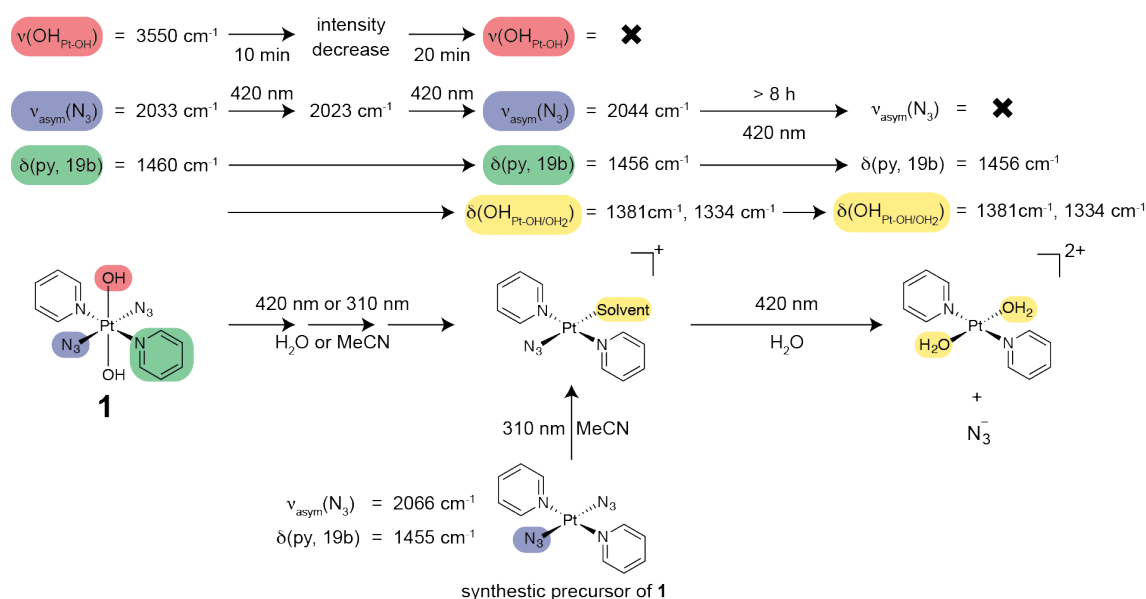


Figure 6.1 Summary of the photodecomposition pathway of *trans,trans,trans*-[Pt(N₃)₂(OH)₂(py)₂] (**1**) derived from ATR-FTIR and UV-Vis spectroscopy complemented by PCA and MCR-ALS analysis as outlined in Chapter 2, 3.1 and 3.2. Only selected ATR-FTIR vibrations are shown for clarity. Notations used: ν = stretch, δ = in-plane angle bending, \times = complete removal of vibration, MeCN = acetonitrile. The description of the pyridine mode is given in Wilson's notations, as described previously in Chapter 2.

Likewise, the methods described above for ATR-FTIR and UV-Vis spectroscopy were essential for the exploration of the fundamental understanding of the photodecarbonylation of a series of ruthenium complexes of the formula [RuLCl₂(CO)₂] (L = 4,4'-dimethyl-2,2'-bipyridine, 4'-methyl-2,2'-bipyridine-4-carboxylic acid or 2,2'-bipyridine-4,4'-dicarboxylic acid). Decarbonylation of the first CO ligand in acetonitrile occurred on a rapid time-scale ($k_1 \gg 3 \text{ min}^{-1}$), to an extent that the steady state UV-Vis spectroscopy did not allow for

determination of the influence of the electron-donating/withdrawing groups attached to the bipyridine ligand by MCR-ALS. Subsequent release of the second CO ligand proved to be substantially slower ($k_2 = 0.099 - 0.17 \text{ min}^{-1}$) exposing the reduction in rates caused by the electron withdrawing carboxyl substituents on bipyridine. These groups increase the absorption wavelength maxima, thus potentially enabling more "biologically friendly" longer-wavelength excitation (red – near-infrared). However, careful consideration is required when using acetonitrile, as the rate of CO release was found to be significantly slower in aqueous media using identical protocols ($k_1 = 0.46 - 2.0 \text{ min}^{-1}$, $k_2 = 0.026 - 0.035 \text{ min}^{-1}$), once more emphasising results obtained with organic solvents might be an incomplete model for biological applications.

3. Methodological plus instrumental development and utilisation of synchrotron based infrared techniques to study metal-based PACT candidates, outlined by 1, in an effort trying to overcome the limitations of bench-top infrared equipment.

Synchrotron based infrared studies were undertaken to acquire otherwise difficult to obtain spectra of far-infrared metal to ligand vibrations and mid-infrared live cells with unprecedented signal-to-noise levels. The results obtained with transmission SR-FIR outlined in Chapter 2 and the maintained focus on the mechanism of action of **1** instigated the combination of ATR and SR-FIR. A custom built *in vacuo* Synchrotron Radiation Attenuated Total Reflection Far-Infrared (SR-ATR-FIR) setup was developed, which significantly reduced the turnover time between samples, from ~30 min – 2 h, to 5 – 10 min, of which the majority of the time now consisted of pumping down to $\leq 10^{-4}$ mbar rather than sample preparation. SR-ATR-FIR spectra for **1** and its synthetic precursors were directly compared to the transmission SR-FIR spectra and are in good agreement. The *in vacuo* setup and limited beamtime restricted a full study, as described in Chapter 3.1, due to extended amounts of time to reach adequate vacuum level to use SR after samples were deposited on the ATR crystal. This could eventually be circumvented with the out-of-vacuum SR-ATR-FIR setup, but this setup was not completed prior to the end of PhD candidature. Nevertheless, the development of a new beamline accessory, funded, built and available for use by all synchrotron applicants as of round 3,

2017 at the THz/Far-Infrared beamline (Australian Synchrotron), is a reflection of the efforts made throughout this thesis.

Testing of new diamond window liquid cells for the *in situ* irradiation of samples by transmission SR-FIR revealed reflection artefacts, which hampered the detection of weak and low intensity vibrations in solution due to noise in the baselines. Elevated concentrations of **1** in dimethyl sulfoxide (DMSO, 76 mM) did allow for *in situ* photodecomposition to be carried out under 355 nm irradiation. The decrease of both the $\nu(\text{Pt-N}_3)$ at 559 cm^{-1} and $\nu(\text{Pt-OH})$ at 409 cm^{-1} occurred rapidly in the first five minutes and no apparent difference in rate of removal was observed. A new peak was observed at 419 cm^{-1} , which is identical to one of the $\nu(\text{Pt-N}_3)$ vibrations of **1** observed after 10 minutes of irradiation by SR-ATR-FTIR. In Chapter 3.1, an increase in $\nu_{\text{asym}}(\text{N}_3)$ vibration of **1** was assigned to one of the photodecomposition intermediates, $[\text{Pt}(\text{N}_3)(\text{py})_2(\text{solvent})]$. This could be a possible intermediate formed in this work. Live cell studies of **1** on acute myeloid leukaemia cells (K562) by Synchrotron Radiation Infrared Microspectroscopy (SR-IRMS) revealed significant changes to the DNA base stacking and lipid vibrations, already at 4 hours after drug treatment and irradiation. This was not observed or to a lesser extent for the controls. The observed changes to the DNA basepairing, A-DNA and ribose vibrations support the proposition that **1** alters the conformational structures of DNA significantly and rapidly, in line with previous studies in which rapid accumulation of platinum inside the nucleus is observed upon irradiation of **1**.

The apparent next study should be photodecomposition studies by out-of-vacuum SR-ATR-FIR, to allow for substantial complementary evidence of the outlined mechanism of action by mid-infrared ATR-FTIR in Figure 6.1. Furthermore, the results outlined in Chapter 3 are not directly comparable to the transmission SR-FIR studies due to use of different solvents, concentrations and irradiation wavelength and do require further investigation in order to draw any conclusions. However, the SR-FIR results might suggest that the hydroxido ligands undergo chemical changes prior to release, which cannot be monitored by the $\nu(\text{OH}_{\text{Pt-OH}})$ in the mid-infrared region. Therefore, further optimisation of the diamond window liquid cell is essential, also highlighted by the work carried out on CT-DNA, suffering from irreproducibility. The artefacts could potentially be overcome by the development of algorithms that can correct for the fringes in

the case of pattern recognition and/or in combination of reducing the fringing effects by systematic increase/decrease of the angles between the windows. Additional cell study attempts were carried out at both Monash University and the University of Warwick in order to complement the obtained results of **1** in K562 cells by SR-IRMS. However, poor sustainability of the cell line did not allow for successful studies by ATR-FTIR or cell viability studies. At the same time, cell studies on different cell lines are of interest to compare reported antiproliferative activities to the observed vibrational changes in an effort to identify possible intracellular targets of **1**. Raman spectroscopy, infrared microspectroscopy, ATR-FTIR and Atomic Force Microscopy IR are potentially powerful techniques to carry out such studies.

4. Synthesis and optimisation of UCNPs as a platform for addressing the wavelength activation of PACT candidates to a clinically-relevant window.

Current clinically available light sources commonly include photodynamic therapy lasers ranging from red to near-infrared wavelengths. Optimum penetration depths into tissue can be achieved using approx. 800 nm light. Thus, a range of lanthanide-doped UCNPs were synthesised to allow for visible light emission matching the absorbance of photoactivatable metal-based complexes. Emphasis was placed on the clinical relevance of UCNPs by targeting water-dispersible, ultrasmall (< 10 nm to reduce spleen and liver accumulation), hexagonal shaped (highest quantum yields) nanoparticles that allow for 800 nm excitation. Perfect hexagonal UCNPs were obtained at a smallest size of 39.0 ± 1.6 nm; mixed populations of 10 – 40 nm UCNPs were obtained when attempting to go ultrasmall sizes (< 10 nm). Both neodymium doping and coupling of a near-infrared dye to the nanoparticles afforded water-dispersible UCNPs theoretically capable of 800 nm excitation and UV and blue light emission. Minor changes to the synthesis procedures have a large effect on the resulting shape and size. Therefore, confirming the theoretical emission with experimental proof was essential. In the absence of available equipment, an in-house setup was developed to measure the emission of UCNPs using diode lasers and experimental emission wavelengths of thulium (290 nm, 346 nm, 363 nm, 452 nm, 476 nm, 541 nm and 652 nm) and neodymium (804 nm).

Previous reported studies, as outlined in Chapter 1.6, revealed the retained *in vitro* and *in vivo* antiproliferative activity of diazido Pt(IV) complexes when incorporated onto UCNPs, allowing for near-infrared activation of the prodrugs. However, the *in vivo* effectiveness of nanoparticles has mainly been hampered by accumulation of UCNPs in the liver and spleen. Therefore, continued effort is essential to address the factors effecting accumulation, such as size and surface (charge) modifications.